

CHARACTERIZATION OF Zn-Ti OXIDE NANOPOWDER SYNTHESIZED BY  
SONOCHEMICAL METHOD



A THESIS SUBMITTED IN PARTIAL FULFILLMENT  
OF THE REQUIREMENT FOR THE DEGREE OF  
DOCTOR OF PHILOSOPHY IN NANOSCIENCE AND NANOTECHNOLOGY  
COLLEGE OF NANOTECHNOLOGY  
KING MONGKUT'S INSTITUTE OF TECHNOLOGY LADKRABANG  
2017  
KMITL-2017-NT-D-001-005

CHARACTERIZATION OF Zn-Ti OXIDE NANOPOWDER SYNTHESIZED BY  
SONOCHEMICAL METHOD



A THESIS SUBMITTED IN PARTIAL FULFILLMENT  
OF THE REQUIREMENT FOR THE DEGREE OF  
DOCTOR OF PHILOSOPHY IN NANOSCIENCE AND NANOTECHNOLOGY  
COLLEGE OF NANOTECHNOLOGY  
KING MONGKUT'S INSTITUTE OF TECHNOLOGY LADKRABANG  
2017  
KMITL-2017-NT-D-001-005



COPYRIGHT 2017

COLLEGE OF NANOTECHNOLOGY

KING MONGKUT'S INSTITUTE OF TECHNOLOGY LADKRABANG

This material is reserved for educational use only, not allowed for commercial use.

Forbidden to modify the content, and cite the document when use.

หัวข้อวิทยานิพนธ์	การหาลักษณะเฉพาะของผงนาโนซิงค์-ไททาเนียมออกไซด์ที่เตรียมโดยวิธีโซโนเคมี
นักศึกษา	นายจักรพันธ์ วัฒนวิทย์กรรม
รหัสประจำตัว	57607004
ปริญญา	ปรัชญาดุษฎีบัณฑิต
สาขา	นาโนวิทยาและนาโนเทคโนโลยี
พ.ศ.	2560
อาจารย์ที่ปรึกษาวิทยานิพนธ์	รศ.ดร. วิษณุ เพชรภา

### บทคัดย่อ

จุดมุ่งหมายหลักของงานวิจัยนี้คือการสังเคราะห์และวิเคราะห์สมบัติของผงนาโนซิงค์-ไททาเนียมออกไซด์ที่เตรียมโดยวิธีโซโนเคมี ตัวอย่างที่สังเคราะห์ประกอบด้วยสองกลุ่มหลัก คือกลุ่มสารประกอบที่มีไททาเนียมไดออกไซด์เป็นองค์ประกอบหลักและกลุ่มสารประกอบเพอรอกไซด์ซิงค์ไททาเนต โดยกลุ่มของไททาเนียมไดออกไซด์นั้นมีการเจือทั้งแบบเดี่ยวด้วยไอออนซิงค์และการเจือแบบร่วมด้วยซิงค์-โคบอลต์ และซิงค์-แมงกานีส เพื่อปรับปรุงสมบัติของผงนาโน สารประกอบกลุ่มที่สองคือกลุ่มผงนาโนซิงค์ไททาเนต โดยมีการเจือแบบเดี่ยวด้วยไอออนโคบอลต์และแมงกานีส ศึกษาสมบัติทางโครงสร้างเฟส สัณฐานวิทยา และสมบัติทางแสงของตัวอย่างที่สังเคราะห์ด้วยเทคนิคการเลี้ยวเบนของรังสีเอ็กซ์ กล้องจุลทรรศน์อิเล็กตรอนแบบส่องกราด และเครื่องวิเคราะห์การดูดกลืนแสง ตามลำดับ ศึกษาองค์ประกอบทางเคมีและโครงสร้างเชิงลึกด้วยเทคนิคการดูดกลืนรังสีเอ็กซ์ ศึกษาสมบัติการเป็นตัวเร่งปฏิกิริยาทางแสงโดยการทดสอบการย่อยสลายสีย้อมโรดามีนบีภายใต้การกระตุ้นด้วยแสงอัลตราไวโอเลตและแสงที่ตามองเห็น

ไททาเนียมไดออกไซด์ที่มีการเจือแบบเดี่ยวด้วยไอออนซิงค์โดยไม่ผ่านกระบวนการแคลไซน์แสดงโครงสร้างผลึกแบบอนาเทสและค่าความเป็นผลึกเพิ่มขึ้นหลังจากผ่านกระบวนการให้ความร้อน ขนาดอนุภาคเฉลี่ยมีค่าประมาณ 20 นาโนเมตร การเจือแบบเดี่ยวด้วยซิงค์ส่งผลให้ค่าพลังงานต้องห้ามของตัวอย่างมีค่าลดลงเล็กน้อยเมื่อเปรียบเทียบกับไททาเนียมไดออกไซด์บริสุทธิ์ สำหรับการเจือแบบร่วมด้วยไอออนซิงค์-โคบอลต์และซิงค์-แมงกานีสนั้น ตัวอย่างที่สังเคราะห์ได้มีโครงสร้างเฟสแบบอนาเทสไททาเนียมไดออกไซด์ เมื่อเตรียมด้วยวิธีโซโนเคมีเป็นเวลา 30 นาที โดยไม่อาศัยกระบวนการให้ความร้อน การวิเคราะห์โครงสร้างเชิงลึกด้วยเทคนิคการดูดกลืนของรังสีเอ็กซ์แสดงให้เห็นว่าไอออนของสารเจือมีการแทนที่โครงสร้างของไททาเนียม การวิเคราะห์สมบัติทางแสงแสดงให้เห็นว่าตัวอย่างมีการตอบสนองต่อแสงในย่านที่ตามองเห็นมากขึ้น การทดสอบการย่อยสลายสีย้อมโรดามีนบีภายใต้การกระตุ้นด้วยแสงที่ตามองเห็นพบว่า การเจือด้วยไอออนแบบร่วมมีประสิทธิภาพในการย่อยสลายสีย้อมดีกว่าการเจือแบบเดี่ยวและไม่มีการ

This material is reserved for educational use only, not allowed for commercial use.

Forbidden to modify the content, and cite the document when use.

เจือ อัตราการย่อยสลายสีย้อมสูงสุดพบในตัวอย่างที่เจือด้วยโคบอลต์ความเข้มข้น 3 เปอร์เซ็นต์ และแมงกานีส 2 เปอร์เซ็นต์ จากการศึกษาแสดงให้เห็นว่าวิธีโซโนเคมีเป็นที่ไม่ซับซ้อนและมีความเป็นมิตรต่อสิ่งแวดล้อมสามารถใช้ในการสังเคราะห์ผงนาโนสำหรับการย่อยสลายมลพิษอินทรีย์ได้อย่างมีประสิทธิภาพ

สำหรับกลุ่มเพอโรฟสไกต์ที่มีซิงค์ไททาเนตเป็นองค์ประกอบหลัก ตัวอย่างสังเคราะห์ด้วยวิธีโซโนเคมีและผ่านกระบวนการให้ความร้อนเพื่อเพิ่มความเป็นผลึก ผลการวิเคราะห์ด้วยเทคนิคการเลี้ยวเบนของรังสีเอ็กซ์แสดงให้เห็นว่า เมื่อเผาแคลไซน์ที่อุณหภูมิ 600 และ 700 องศาเซลเซียส ตัวอย่างมีโครงสร้างแบบคิวบิกและเฮกซะโกนัล เมื่ออุณหภูมิแคลไซน์เพิ่มถึง 800 องศาเซลเซียส พบว่าโครงสร้างแบบคิวบิกและเฮกซะโกนัลเริ่มเปลี่ยนสภาพเป็นโครงสร้างแบบสปีเนลและรูไทล์ การวิเคราะห์ด้วยเทคนิคการดูดกลืนด้วยรังสีเอ็กซ์แสดงสถานะออกซิเดชันของซิงค์และไททาเนียมมีค่า 2+ และ 4+ ตามลำดับ ขนาดอนุภาคเฉลี่ยมีค่าอยู่ในระดับนาโนเมตรซึ่งมีขนาดเพิ่มขึ้นเมื่ออุณหภูมิสูงขึ้น การทดสอบการย่อยสลายสีย้อมภายใต้การกระตุ้นด้วยแสงอัลตราไวโอเล็ตและแสงขาวพบว่าตัวอย่างที่แคลไซน์ที่อุณหภูมิ 700 องศาเซลเซียส มีประสิทธิภาพการย่อยสลายสูงสุด ในกรณีของการเจือด้วยธาตุโลหะทรานสิชันโคบอลต์และแมงกานีสลงในผงนาโนซิงค์ไททาเนตนั้นตัวอย่างสังเคราะห์ด้วยวิธีโซโนเคมีและเผาแคลไซน์ที่อุณหภูมิ 700 องศาเซลเซียส การวิเคราะห์ด้วยเทคนิคการเลี้ยวเบนของรังสีเอ็กซ์พบว่าตัวอย่างมีโครงสร้างแบบผสมระหว่างคิวบิกและเฮกซะโกนัลซึ่งปราศจากเฟสปลอมปนอื่นๆ ผลการวิเคราะห์ด้วยเทคนิคการดูดกลืนของรังสีเอ็กซ์แสดงสถานะออกซิเดชันของซิงค์ ไททาเนียม และโคบอลต์คือ 2+ 4+ และ 2+ ตามลำดับ และสถานะออกซิเดชันของแมงกานีสมีค่าผสมระหว่าง 3+ และ 4+ การวิเคราะห์ด้วยเทคนิคการดูดกลืนของรังสีเอ็กซ์แบบขยายออกอย่างละเอียดแสดงให้เห็นว่าไอออนสารเจือโคบอลต์มีการแทนที่บริเวณซิงค์และเริ่มมีการรวมตัวเป็นกลุ่มโคบอลต์ออกไซด์ภายในโครงสร้างซิงค์ไททาเนต การเจือด้วยแมงกานีสพบว่าไอออนส่วนหนึ่งของแมงกานีสเข้าไปแทนที่บริเวณของซิงค์และส่วนหนึ่งเกิดการก่อตัวเป็นสารประกอบไดแมงกานีสไดรอกไซด์ภายในโครงสร้าง การทดสอบพฤติกรรมเร่งปฏิกิริยาทางแสงโดยการทดสอบการย่อยสลายสีย้อมภายใต้การกระตุ้นด้วยแสงที่ตามองเห็นพบว่าอนุภาคที่เจือด้วยธาตุโคบอลต์และแมงกานีสมีประสิทธิภาพการย่อยสลายสูงกว่าตัวอย่างที่ไม่ได้เจือ จากการศึกษาแสดงให้เห็นว่าการรวมตัวของไอออนโลหะทรานสิชันโคบอลต์และแมงกานีสมีประสิทธิภาพในการปรับปรุงตัวเร่งปฏิกิริยาทางแสงของสารกลุ่มเพอโรฟสไกต์

คำสำคัญ : ไททาเนียมไดออกไซด์ การเจือแบบร่วม ซิงค์ไททาเนต วิธีโซโนเคมี ผงนาโน เซนส์ เอกซพอส ตัวเร่งปฏิกิริยาทางแสง

Thesis title	Characterization of Zn-Ti Oxide Nanopowder Synthesized by Sonochemical Method
Student	Mr. Chakkaphan Wattanawikkam
Student ID	57607004
Degree	Doctor of Philosophy
Program	Nanoscience and Nanotechnology
Year	2017
Thesis Advisor	Assoc. Prof. Dr. Wisanu Pecharapa

### ABSTRACT

The principle aim of this research is to synthesize and analyze Zn-Ti oxide nanopowders fabricated by the sonochemical method. The prepared samples are composed of two main groups, including TiO<sub>2</sub>-based and perovskite ZnTiO<sub>3</sub>-based compounds. The single-doping of Zn-ion and co-doping of Co-Zn and Mn-Zn were incorporated in the TiO<sub>2</sub> to modify the properties of nanoparticles. The second system, perovskite ZnTiO<sub>3</sub> nanoparticles were individually doped with Co and Mn ions. To study the properties of the prepared samples, X-ray diffraction (XRD), field emission scanning electron microscope (FESEM) and UV-VIS diffuse spectroscopy were employed to investigate their structural phase, morphology and optical properties, respectively. Their chemical composition and local structure were analyzed by X-ray absorption spectroscopy (XAS) using X-ray absorption near edges structure (XANES) and extended X-ray absorption fine structure (EXAFS) technique. Photocatalytic activity of TiO<sub>2</sub>-based and ZnTiO<sub>3</sub>-based catalysts was evaluated by the Rhodamine B (RhB) dye degradation under both ultraviolet and visible light irradiation.

Zn-singly doped TiO<sub>2</sub> sample reveals that the as-synthesized samples are in the anatase phase and their crystallinity increase after annealing process. The particle size of as-synthesized powders is around 20 nm. The Zn-dopant slightly affects the reduction of energy band gap of the samples compared with pure TiO<sub>2</sub> samples. For doubly-doped TiO<sub>2</sub>, the structural analysis exhibits that the pure anatase TiO<sub>2</sub> phase was found in all Co-Zn and Mn-Zn doped samples using sonication time for 30 min without heat treatment process. FESEM images can induce the nano-size of particle and uniform distribution. XANES and EXAFS analysis confirms that some Ti<sup>4+</sup> lattice of TiO<sub>2</sub> were substituted by dopant ions. The optical analysis reveals the significant shift of absorption spectra to visible light region. The photocatalytic activity of samples was tested by the degradation of Rhodamine B dye solution under visible light irradiation. The doubly-doped

This material is reserved for educational use only, not allowed for commercial use.

Forbidden to modify the content, and cite the document when use.

samples presents highly efficient and rapid degradation of dye compared with singly-doped and bare titania. The highest degradation rate was achieved in the sample with 3% for Co- and 2% for Mn-doping concentration. The uncomplicated and eco-environmental method can be useful for synthesizing the potential catalysts for highly efficient degradation of organic pollutants for environmental renewal.

For perovskite  $\text{ZnTiO}_3$ -based compounds, the samples were prepared by sonochemical method accompanying the annealing process for crystallinity improvement. XRD results of pure  $\text{ZnTiO}_3$  samples show that the phase of cubic and hexagonal are observed in sample calcined at  $600^\circ\text{C}$  and  $700^\circ\text{C}$ , respectively. In further, increasing calcination temperature up to  $800^\circ\text{C}$ , the cubic/hexagonal phase would decompose into cubic spinel  $\text{Zn}_2\text{TiO}_4$  and rutile  $\text{TiO}_2$  phase. The XANES analysis exhibits the oxidation state of  $\text{Zn}^{2+}$  and  $\text{Ti}^{4+}$  in the  $\text{ZnTiO}_3$  nanoparticles. The average particle size is in the nanoscale and its size increases with increasing annealing temperature. The superior photodegradation of RhB under UV and visible irradiation is found in the sample calcined at  $700^\circ\text{C}$  representing the highest percentage of hexagonal phase. In case of transition metal ions of Co- and Mn-doped  $\text{ZnTiO}_3$  samples, the samples were prepared by sonochemical method with the calcination temperature of  $700^\circ\text{C}$ . XRD results represent that the mixing phase of cubic and hexagonal structures are obtained in all prepared samples without impurity phase of metal oxides. The existence of Co and Mn in  $\text{ZnTiO}_3$  host was confirmed by XANES technique. The XANES results confirm the  $\text{Co}^{2+}$  of oxidation state in Co-ZTO and the mixing of  $\text{Mn}^{3+}$  and  $\text{Mn}^{4+}$  in Mn-ZTO samples. The optical studies exhibit that the extended visible light absorption are found in all doped samples. EXAFS analysis of Co-ZTO presents that the Zn site is occupied by Co-dopants. For Mn-ZTO sample, some Mn-dopants occupy in Zn-site of ZTO and some Mn-ions form small cluster of  $\text{Mn}_2\text{O}_3$ . The photocatalytic behavior for RhB dye decomposition under visible light irradiation indicates that the doped samples have the superior degradation compared to pure-ZTO sample. The results suggest that the incorporation of transition metal ions of Co and Mn dopants is an effective way to improve the catalytic efficiency of perovskite ZTO structure.

**Keywords:**  $\text{TiO}_2$ , co-doped  $\text{TiO}_2$ ,  $\text{ZnTiO}_3$ , Sonochemical method, nanopowder, XANES, EXAFS, Photocatalyst

This material is reserved for educational use only, not allowed for commercial use.

Forbidden to modify the content, and cite the document when use.

## ACKNOWLEDGEMENTS

First and foremost, I would like to express my deepest gratitude to Assoc. Prof. Dr. Wisanu Pecharapa, who has my advisor, for his excellent guidance, caring, patience and providing me with an opportunity for doing the PhD. I would like to thank to Prof. Keiichi N. Ishihara at Kyoto University, Japan who has accepted me as an oversea exchange student. I also would like to thank Asst. Prof. Dr. Wanichaya Mekprasart and Dr. Kanokthip Boonyarattanakalin, for guiding my research for several years. Also thank to the Nano-Materials Research Laboratory (NMRL) members, who were supporting in the experiment and also in many wonderful activities.

In addition, this research has been supported by Thailand Research Fund (TRF) through the Royal Golden Jubilee Ph.D. Program (grant no. PHD/0193/2556).

I greatly appreciate the facilities and experiments support by the College of Nanotechnology, King Mongkut's Institute of Technology Ladkrabang (KMITL), Graduate School of Energy Science, Kyoto University and the BL-8 at Synchrotron Light Research Institute (SLRI), Nakhon Rachasima.

Finally, but by no means least, I would like to thank my family for almost unbelievable support. They are the most important people in my world and I dedicate this thesis for them.

Chakkaphan Wattanawikkam

## LIST OF CONTENTS

Content	Page
ABSTRACT (THAI).....	i
ABSTRACT (ENGLISH).....	iii
ACKNOWLEDGEMENTS.....	v
LIST OF CONTENTS.....	vi
LIST OF TABLES.....	viii
LIST OF FIGURES.....	ix
CHAPTER 1 INTRODUCTION.....	1
1.1 Motivation.....	1
1.2 Objective of the study.....	3
1.3 Scope of the study.....	3
CHAPTER 2 THEORETICAL BACKGROUND.....	5
2.1 TiO <sub>2</sub> and ZnO based semiconductor.....	5
2.2 Perovskite materials.....	7
2.3 Photocatalytic activity.....	8
2.4 Sonochemical method.....	10
2.5 Materials Characterization technique.....	12
2.5.1 X-ray diffraction (XRD).....	12
2.5.2 X-ray absorption spectroscopy (XAS).....	13
2.5.3 UV-visible spectroscopy.....	16
2.5.4 Field emission scanning electron microscope (FESEM).....	17
2.5 Literature review.....	18
CHAPTER 3 EXPERIMENTAL PROCEDURES.....	29
3.1 Materials and equipment.....	29
3.2 Experimental procedure.....	30
3.2.1 Synthesis of Zn doped TiO <sub>2</sub> nanoparticle.....	30
3.2.2 Synthesis of Zn-Co and Zn-Mn co-doped TiO <sub>2</sub> nanoparticles.....	31
3.2.3 Synthesis of ZnTiO <sub>3</sub> nanoparticles.....	32
3.2.4 Synthesis of ZnTiO <sub>3</sub> doped with Co and Mn.....	33
3.3 Characterization methods.....	34
3.3.1 X-ray diffraction (XRD).....	34
3.3.2 X-ray Absorption Spectroscopy.....	35
3.3.3 UV-visible spectroscopy.....	35
3.3.4 Field Emission Scanning Electron Microscope.....	36
3.3.5 Photocatalytic system.....	36

This material is reserved for educational use only, not allowed for commercial use.

Forbidden to modify the content, and cite the document when use.

Content	Page
CHAPTER 4 RESULTS AND DISCUSSION.....	38
4.1 Zn doped TiO <sub>2</sub> nanoparticles .....	38
4.1.1 Structural phase.....	38
4.1.2 Morphology.....	40
4.1.3 Optical properties.....	40
4.2 Zn-Mn and Zn-Co co-doped TiO <sub>2</sub> nanoparticles .....	43
4.2.1 Structural phase.....	43
4.2.2 Chemical composition and local structure .....	45
4.2.4 Morphology.....	48
4.2.5 Optical properties.....	48
4.2.6 Photocatalytic activity .....	52
4.3 ZnTiO <sub>3</sub> .....	56
4.3.1 Structural phase.....	56
4.3.2 Chemical composition.....	58
4.3.3 Morphology.....	59
4.3.4 Optical properties.....	59
4.3.4 Photocatalytic behavior.....	61
4.4 ZTO doped with Co and Mn ion.....	65
4.4.1 Structural phase.....	65
4.4.2 Chemical composition.....	66
4.4.3 Local structure.....	68
4.4.4 Optical properties.....	73
4.4.5 Morphology.....	76
4.4.6 Photocatalytic activity.....	77
CHAPTER 5 CONCLUSION.....	79
REFERENCES.....	81
APPENDIX.....	88

## LIST OF TABLES

Content	Page
Table 2.1 Potential elemental combinations for the perovskite system $ABO_3$ and possible valence pairings that conform the charge neutrality.....	7
Table 4.1 Crystalline size of Zn doped $TiO_2$ samples.....	42
Table 4.2 Crystalline size, Energy band gap and LCF of as-synthesized samples.....	46
Table 4.3 Percentage of hexagonal phase.....	57



## LIST OF FIGURES

Content	Page
Figure 2.1 Representation of the TiO <sub>2</sub> (a) anatase, (b) rutile and (c) brookite.....	5
Figure 2.2 A representation of the different structures of ZnO; (a) cubic rock salt, (b) cubic zinc Blende (c) hexagonal wurtzite. The shaded black and gray spheres denote O and Zn respectively.....	6
Figure 2.3 Ideal cubic perovskite structures (a) showing the equivalence of both the A and B site cations as the origin. The dimensions of the cubic unit cell, including bond lengths, are shown in (b). The A site is shown in blue, the B site in beige, and oxide ions in red.....	7
Figure 2.4 The principle of photocatalysis in case of TiO <sub>2</sub> .....	9
Figure 2.5 Band Edge Positions of Common Semiconductor Photocatalyst.....	10
Figure 2.6 Diagram of ultrasound range.....	10
Figure 2.7 Growth and implosion of cavitation bubbles in aqueous solution under ultrasonic irradiation. ....	10
Figure 2.8 Cavitation bubble formation, growth and collapse.....	11
Figure 2.9 Schematic of X-ray reflection on the crystal planes.....	12
Figure 2.10 The schematic diagram showing the process of X-ray absorption.....	13
Figure 2.11 The schematic view of X-ray absorption.....	14
Figure 2.12 The XAS spectrum of Ti K-edge and Ba L <sub>3</sub> -edge for BaTiO <sub>3</sub> .....	15
Figure 2.13 A schematic of XAS spectrum.....	16
Figure 2.14 Interaction of light with solid samples.....	17
Figure 2.15 A Schematic for FESEM.....	18
Figure 2.16 The effect of zinc content on photocatalytic activity and The effect of initial concentration of ZnSO <sub>4</sub> on photo- catalytic activity.....	19
Figure 2.17 UV-visible transmittance spectrum T% of TiO <sub>2</sub> and Co.....	19
Figure 2.18 Typical cross-sectional micrographs of 100 nm thick (a) undoped and (b) Mn-doped TiO <sub>2</sub> .....	20

Content	Page
Figure 2.19 N <sub>2</sub> selectivity and catalytic performance of Mn-M/TiO <sub>2</sub> anatase catalyst: NH <sub>3</sub> =400 ppm.....	21
Figure 2.20 XRD patterns of the calcined samples at different temperatures (the standard diffraction XRD pattern of ZnTiO <sub>3</sub> is shown as a reference) .....	22
Figure 2.21 (A and B) TEM images of ZnTiO <sub>3</sub> powders calcined at 600 °C. (C) UV/vis diffuse reflectance spectra of samples calcined at different temperatures.....	22
Figure 2.22 XRD patterns of the samples calcined at different temperatures (a) 600 °C, (b) 700 °C (c) 800 °C and (d) 900 °C.....	23
Figure 2.23 Optical properties of ZTO (a) absorption as a function wavelength and (b) energy band gap.....	24
Figure 2.24 Excitation spectrum of the doped sample (Ni <sup>2+</sup> ion is 1%). Emission spectra of the doped sample excited at different wavelength.....	25
Figure 2.25 Photocatalytic activities under solar irradiation of the ZnTiO <sub>3</sub> :Ag(5%) photocatalysts for the degradation of RhB for five cycles and (b) XRD pattern of ZnTiO <sub>3</sub> :Ag(5%) after five cycles.....	26
Figure 2.26 Powder XRD spectra of TiO <sub>2</sub> prepared by sonication for 150min at temperature (a) 30°C, (b) 50°C, (c) 70°C, (d) 80°C and (e) sample d calcined at 400°C for 120 min. Powder XRD spectra of TiO <sub>2</sub> prepared at 80 °C after sonication (a) 60 min, (b) 120 min, (c) 150 min and (d) 180 min.....	26
Figure 2.27 XRD patterns of TiO <sub>2</sub> nanoparticles.....	27
Figure 2.28 TEM images of TiO <sub>2</sub> nanoparticles synthesized by (a) hydrothermal at 120°C, (b) sonochemical for 30 minute, (c) sonochemical-hydrothermal at 80°C, (d) sonochemical-hydrothermal at 100°C, (e) sonochemical-hydrothermal at 120°C.....	28
Figure 3.1 Schematic of preparation for Zn-doped TiO <sub>2</sub> nanoparticles.....	30
Figure 3.2 Schematic of preparation for Co-Zn and Mn-Zn co-doped TiO <sub>2</sub> nanoparticles.....	31
Figure 3.3 Schematic of preparation for ZnTiO <sub>3</sub> nanoparticles.....	32
Figure 3.4 Schematic of preparation for ZnTiO <sub>3</sub> nanoparticles doped with Co and Mn.....	33

Content	Page
Figure 3.5 schematic of photocatalytic system in UV- and visible light illumination.....	37
Figure 4.1 XRD patterns of as-synthesized and after calcined of Zn-doped TiO <sub>2</sub> nanoparticles....	39
Figure 4.2 TEM image of as-synthesized Zn-doped powder synthesized by sonochemical method with sonication for 30 min.....	41
Figure 4.3 UV-vis absorbance spectra of Zn-doped TiO <sub>2</sub> nanoparticles.....	41
Figure 4.4 Powder XRD pattern of Zn-TiO <sub>2</sub> , Co-Zn and Mn-Zn co-doped TiO <sub>2</sub> nanoparticles.....	44
Figure 4.5 Schematic for the possibly formation mechanisms of nanoparticles by sonication process: Top represents TiO <sub>2</sub> formation mechanism, Bottom is for low transition metal ions dopant concentration.....	45
Figure 4.6 Normalized XANES spectra of Co-Zn co-doped TiO <sub>2</sub> with (a) Ti K-edge, (b) Zn K-edge and (c) Co K-edge.....	47
Figure 4.7 Normalized XANES spectra of Co-Zn co-doped TiO <sub>2</sub> with (a) Ti K-edge, (b) Zn K-edge and (c) Co K-edge.....	47
Figure 4.8 FE-SEM images of co-doped TiO <sub>2</sub> nanoparticles with (a) TiO <sub>2</sub> , (b)TiO <sub>2</sub> :Zn-Co1%, (c) TiO <sub>2</sub> :Zn-Co3% and (d) TiO <sub>2</sub> :Zn-Co5% .....	50
Figure 4.9 FE- SEM images of co-doped TiO <sub>2</sub> nanoparticles with (a)TiO <sub>2</sub> :Zn-Mn1%, (b) TiO <sub>2</sub> :Zn-Mn3% and (c) TiO <sub>2</sub> :Zn-Mn5%.....	50
Figure 4.10 UV-vis diffuse reflectance spectra of (a) Mn-Zn and (b) Mn-Zn co-doped TiO <sub>2</sub> .....	51
Figure 4.11 Photocatalytic degradation curve for different catalysts in the presence of RhB dye for Co-Zn co-doped TiO <sub>2</sub> catalyst, (b) absorption kinetic of RhB over Co-Zn co-doped TiO <sub>2</sub> catalyst (c) time independent variation of UV-vis spectra for RhB degradation of 2% Co-dopant and (d) Visual comparison of color fading in the degradation of RhB solution subsequent to being subjected to various degradation time for 0-90 min.....	53

Content	Page
Figure 4.12 Photocatalytic degradation curve for different catalysts in the presence of RhB dye for Mn-Zn co-doped TiO <sub>2</sub> catalyst, (b) absorption kinetic of RhB over Mn-Zn co-doped TiO <sub>2</sub> catalyst and (c) Visual comparison of color fading in the degradation of RhB solution subsequent to being subjected to various degradation time for 0-90 min.....	54
Figure 4.13 the possible mechanism of photocatalytic activity for co-doped TiO <sub>2</sub> .....	55
Figure 4.14 XRD pattern of perovskite ZnTiO <sub>3</sub> nanoparticles calcined at 500-900 °C for 2 h.....	57
Figure 4.15 Measured XANES spectra of ZTO nanoparticle for (a) Zn K-edge and (b) Ti K-edge....	58
Figure 4.16 FE-SEM micrograph of ZTO nanoparticles calcined at (a) 600, (b) 700 and (c) 900 °C.....	60
Figure 4.17 Optical absorption spectra of ZnTiO <sub>3</sub> nanoparticle at difference annealing temperature and (b) the plot of $(\alpha h\nu)^{1/2}$ as a function of photon energy for ZnTiO <sub>3</sub> nanoparticle.....	61
Figure 4.18 (a) Photocatalytic behavior for RhB degradation as a function of time of ZnTiO <sub>3</sub> Calcined at 500-900 °C under UV irradiation.....	63
Figure 4.19 Time dependent variation of UV-vis spectra for RhB degradation of ZnTiO <sub>3</sub> calcined at 600-900 °C.....	63
Figure 4.20 (a) Photocatalytic behavior for RhB degradation as a function of time for ZTO calcined at 700 °C under visible irradiation and (b) Time dependent variation of UV-vis spectra for RhB degradation for ZTO calcined at 700 °C.....	64
Figure 4.21 Adsorption kinetic of RhB over ZTO catalyst (a) under UV irradiation and (b) samples calcined at 700 °C under UV and visible irradiation .....	64
Figure 4.22 XRD patterns of ZTO doped with Co and Mn at various concentrations .....	65
Figure 4.23 Measured XANES spectra of Co-ZTO and Mn-ZTO for Co K-edge and Mn K-edge with reference standard in fluorescent mode.....	67

Content	Page
Figure 4.24 The Fourier transform magnitudes of EXAFS spectra of $k^2$ -weighted data with fit at Zn K-edge into $R$ -space and EXAFS function $k^2\chi(k)$ with fit for Zn K-edge (small picture) of Co-ZTO.....	69
Figure 4.25 The Fourier transform magnitudes of EXAFS spectra of $k^2$ -weighted data with fit at Zn K-edge into $R$ space and EXAFS function $k^2\chi(k)$ with fit for Zn K-edge (small picture) of Mn-ZTO.....	70
Figure 4.26 EXAFS oscillations and their corresponding Fourier transform of dopant spectra compared to -site, B-site and their reference standard for Co-ZTO.....	71
Figure 4.27 EXAFS oscillations and their corresponding Fourier transform of dopant spectra compared to A-site, B-site and their reference standard.....	72
Figure 4.28 Diffuse reflectance spectra versus wavelength of Co-ZTO and Mn-ZTO.....	74
Figure 4.29 Direct and indirect energy band gap determination for Co-ZTO and Mn-ZTO.....	75
Figure 4.30 SEM images of ZTO doped by Co and Mn.....	76
Figure 4.31 (a) Photocatalytic degradation curve for different catalyst in the presence of RhB dye for Co-ZTO catalyst and (b) Adsorption kinetic of RhB over Co-ZTO catalyst.....	78
Figure 4.32 (a) Photocatalytic degradation curve for different catalyst in the presence of RhB dye for Co-ZTO catalyst and (b) Adsorption kinetic of RhB over Mn-ZTO catalyst.....	78

# CHAPTER 1

## INTRODUCTION

### 1.1 Motivation

In the past decade, the development of nanomaterials has been the focus of considerable attention with photocatalysis being used in a variety of products across a broad range of research areas, including especially environmental and energy-related fields [1-2]. Among the photocatalyst materials, titania ( $\text{TiO}_2$ ) nanoparticles has been widely studied and utilized in many applications due to its strong oxidizing abilities, for the decomposition of organic pollutants, super-hydrophobicity, long durability, nontoxicity, low cost and transparency to visible light [3-5]. After first time for discovery of titania for photo-electrolysis of water by Fujishima and Honda [6], titania has been widely investigated and modified for the environmental application as a photo-catalyst. However, the major limitation of titania catalyst includes its rather wide band gap indicating that only ultraviolet spectrum can be harvested for excitation and the high recombination rate between electron ( $e^-$ ) and hole ( $h^+$ ) pairs which results in low quantum yield. Recently, many studies have been dedicated to modify titania by substitutional doping of metal or non-metal element such as V, Cr, Mn, Fe, Co, Ni, Cu, Zn, N and C in order to extend its absorption edge to visible light region and to enhance the photocatalytic properties [7-23]. Among these, metal doping shows the shift of optical response from UV to visible spectral range and the reduction of recombination rate of electron ( $e^-$ ) and hole ( $h^+$ ) pairs during the photocatalytic process [24]. Previous studies suggested that the Zn-doping is one of the potential candidate dopant ions which can enhance the physical and chemical properties of  $\text{TiO}_2$  nanoparticles. For example, G. Marci *et al.* [25] found that Zn ions can considerably enhance the photocatalytic performance of  $\text{TiO}_2$  under UV irradiation, which is attributed to the increase in the separation rate of photo-induced charge due to the difference in the energy band position. The dynamic processes of photo-induced charges are affected by the oxygen vacancies, which can be determined sometimes on the metal ions doped in the surface of  $\text{TiO}_2$  nanoparticles. Moreover, other recent examples have demonstrated the studies of effect of different transition magnetic metal ions doping on  $\text{TiO}_2$  nanoparticles such as Co and Mn-doping. It exhibits that the doping ions are able to introduce new intrabands within the forbidden band gap of  $\text{TiO}_2$  which narrows the band gap of titania [26]. Lately, an approach to dope  $\text{TiO}_2$  with more than one transition metal ion has received attention since it could provide a finer control for tuning capability of its energy gap [27-28]. Moreover, compared with single metal doping, it

This material is reserved for educational use only, not allowed for commercial use.

Forbidden to modify the content, and cite the document when use.

also improves the photocatalytic performance of host materials. Zhi *et. al.* studied and compared the pure-, singly- and doubly-doped of Fe-Zn into TiO<sub>2</sub> nanoparticles prepared by alcohol-thermal method [29]. The results represented that the presence of co-doping exhibited two folds improvement in photocatalytic efficiency, which could be attributed to the enriched electronic properties of TiO<sub>2</sub>.

Recently, researchers have also focused on the titanium-based oxide with a general formula ATiO<sub>3</sub>, which have a wide range of application and are regarded as functional inorganic materials [30]. ZnTiO<sub>3</sub> (ZTO) is one of ABO<sub>3</sub> perovskite oxide materials having BO<sub>6</sub> octahedral with cations A<sup>2+</sup> inserting in the framework. This compound belongs to the binary system of ZnO-TiO<sub>2</sub>, including perovskite ZnTiO<sub>3</sub>, spinel Zn<sub>2</sub>TiO<sub>4</sub> and defect spinel Zn<sub>2</sub>Ti<sub>13</sub>O<sub>8</sub>. [31]. The cubic structure ZnTiO<sub>3</sub> has a thermodynamic stability at low temperature and it would decompose to spinel structure and rutile phase around 945°C [32]. Perovskite structure great interesting has been paid for wide range applications, which is precious nanostructure for practical industrial application such as regenerable catalyst, pigment, CO and NO sensor and dielectric material in microwave frequency region [33-39]. The properties of perovskite ZTO nanostructure could be improved by the adaptability in the electronic structure which arises from the change in content of cation dopant with different valence states. Doping with transition metal ion is one of effective routes to modify the structural and relevant properties of perovskite ZTO nanostructure. Y. W. Wang group [40] prepared ZTO nanopowders by a sol-gel process combined with calcinations at 800°C and investigated their photocatalytic behavior in the photodegradation of humic acid. The Ag-doped and Ag-dispersed nano ZTOs were studied by D. P. Dutta and it was revealed that the prepared nanoparticles showed high efficiency for antibacterial activity [41].

One of challenge for materials synthesis is to find a processing method for preparation process. Sonochemical synthesis is one candidate for nanomaterial fabrication. It has been proven to be a useful technique for generating novel nanomaterials with unusual properties and environmental-friendly [42-43]. The sonochemistry typically provides high frequency and energy of ultrasonic wave to initials chemical reaction of starting precursor, and induces particle formation during the irradiation. The sonication acoustic cavitation phenomenon abruptly generates cavities in the liquid solution of reactant. In general, the cavitation process consists of reaction, growth and implosive collapse of gas vacuoles in the solution. Regarding the hot-spot theory, extreme temperature and high pressure occur in the bubbles during cavitation collapse [44-45]. In synthesis process of metal nanoparticles, sonochemical method gains several advantages. No chemical reducing agent is necessary when using sonochemistry. Also due to the

This material is reserved for educational use only, not allowed for commercial use.

Forbidden to modify the content, and cite the document when use.

extreme conditions, reaction rates are reasonably fast and very small metal nanoparticles are typically formed. Sonochemical process, however, generally only produces spherical metal nanoparticles which limits its use in applications that require shape tuning.

In this present study, the sonochemical method was employed to prepare the  $\text{TiO}_2$ -based and ZTO-based materials. The singly-doping of Zn- and co-doping of Zn-Co and Zn-Mn ions were provided in  $\text{TiO}_2$  at various concentrations. In addition, Co and Mn dopant were individually doped into perovskite ZTO. The structural phase and microstructure of prepared samples were investigated the by X-ray diffraction and Field emission scanning electron microscope. The X-ray absorption spectroscopy including both X-ray absorption near edge structure and extended X-ray absorption fine structure was used to determine the chemical composition and the local structure of prepared samples. The optical properties were studied by UV-visible spectroscopy. The Rhodamine-B dye was used as a model to evaluate to photocatalytic performance under the visible and ultraviolet (UV) light irradiation. The effect of dopant concentration on physical, chemical, optical and photocatalytic properties were also proposed in this work.

## 1.2 Objective of the study

This work has conducted with its main goals including following aspects:

1.2.1 To obtain the nanopowders of  $\text{TiO}_2$ -based compound doped with Zn-, Zn-Co and Zn-Mn ions prepared by sonochemical method.

1.2.2 To obtain the nanopowders of ZTO-based compound doped with Co and Mn ions prepared by sonochemical method.

1.2.3 To study the crystal structure, morphology, chemical composition, local structure, optical properties and photocatalytic activity of prepared nanopowders.

1.2.4 To study the effect of sonochemical process on properties of prepared samples.

1.2.5 To study the functionality of prepared samples for photocatalytic application.

1.2.6 To understand the effect of different amounts of divalent cations, Zn, Co and Mn in each oxide-based compound on properties of prepared samples.

## 1.3 Scope of the study

The aim of this work is presented as following:

1.3.1 Use the sonochemical method for synthesizing  $\text{TiO}_2$ -based nanoparticles doped with Zn-, Zn-Co and Zn-Mn ions at various concentrations.

This material is reserved for educational use only, not allowed for commercial use.

Forbidden to modify the content, and cite the document when use.

1.3.2 Using the sonochemical method for synthesizing ZTO-based nanoparticles doped with Co- and Mn-ions at various concentrations.

1.3.3 Investigating the crystal structure, morphology, chemical composition, local structure, optical properties and photocatalytic activity of the prepared samples.

1.3.4 Utilizing the prepared samples as a photo-catalyst for organic pollutants in a water.

1.3.5 Examining the effect of different dopant ions on structural, chemical, local, optical and photocatalytic properties of the prepared samples.



## CHAPTER 2

### THEORETICAL BACKGROUND

In this chapter, a brief introduction to theoretical background of this research is given. The  $\text{TiO}_2$  and  $\text{ZnO}$  semiconductor theories and their application are presented. Then, a perovskite structure material is introduced. A brief history of photocatalytic process and details of the sonochemical synthesis are described. A review of  $\text{TiO}_2$ ,  $\text{ZnTiO}_3$  and sonochemical preparation was reported. Finally, the materials characterization used in this work are represented.

#### 2.1 $\text{TiO}_2$ and $\text{ZnO}$ based semiconductor

##### Titanium dioxide ( $\text{TiO}_2$ )

$\text{TiO}_2$  was singled out as an important oxide material in the wide-ranging review of future application, including especially in environmental and energy-related fields, because of its strong oxidizing abilities for degradation of organic pollutants, chemical stability, long durability, non toxicity, low cost and transparency to visible light [46]. Titania consists of oxygen (O) and titanium (Ti) ions arranged in a way that one Ti ion is surrounded by six ions bonded to create a distorted structure with majority carriers being electrons.  $\text{TiO}_2$ , naturally occurring oxide of titanium, was discovered in 1795, which generally have three phases including brookite, anatase and rutile [47] as seen in figure 2.1. Rutile is the most stable phase at ambient pressure and temperature in macroscopic sizes while, anatase is more stable in nanoscopic size. The more compact structure of rutile relative to anatase causes important differences in physical properties. Rutile has a higher refractive index, higher specific gravity and greater chemical stability than anatase. Rutile melts at  $1825^\circ\text{C}$  while anatase irreversibly transforms to rutile beginning at about  $500^\circ\text{C}$ . Brookite is the rarest naturally occurring form of  $\text{TiO}_2$  and is difficult to produce in pure form. Brookite has the same color and luster as rutile. Its hardness and density are nearly the same as those of rutile [48].

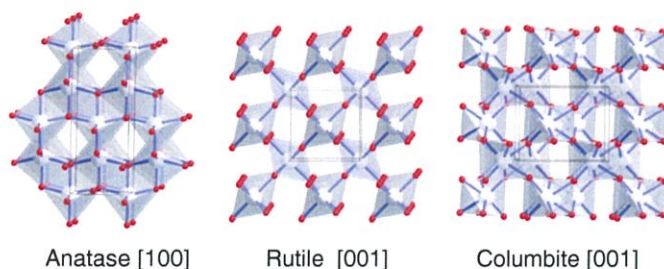


Figure 2.1 Representation of the  $\text{TiO}_2$  (a) anatase, (b) rutile and (c) brookite [48].

This material is reserved for educational use only, not allowed for commercial use.

Forbidden to modify the content, and cite the document when use.

## Zinc oxide (ZnO)

ZnO is an amphoteric oxide which is either a covalent or an ionic semiconductor. ZnO has three crystal structures; hexagonal wurtzite, cubic rock salt, and cubic zinc blende [49]. The most common structure is the hexagonal wurtzite structure since it is the most stable at ambient conditions. Rock salt can be formed at relatively high pressures at approximately 10GPa and a substantial decrease in volume of about 17%. However, cubic substrates can be used to synthesize zinc blende structure. Figure 2.2 shows the three different ZnO crystal structures. ZnO nanostructures have been synthesized and proven versatility and applicability in numerous applications since 1930 [50]. ZnO has intriguing properties, and hence its wide applicability. Researchers report that the direct band gap of 3.44eV exhibited by ZnO at low temperatures and 3.37eV at room temperature allows luminescent and high optical transparency properties in the visible and near ultraviolet regions [38]. ZnO can be applied in optoelectronic and electronic industries such as liquid crystal displays and solar cells due to this property. Additionally, ZnO has a large exciton binding energy of 60meV hence it permits its excitonic emissions to occur at room temperature and higher temperatures. Since ZnO exhibits large exciton binding energy, it can be used as various optical device materials [51].



Figure 2.2 A representation of the different structures of ZnO; (a) cubic rock salt, (b) cubic zinc blende (c) hexagonal wurtzite. The shaded black and gray spheres denote Zn respectively [52].

## 2.2 Perovskite materials

Perovskites have the general formula  $ABO_3$ , where A and B are both cations and O is typically an oxide ( $O^{2-}$ ) or halide ( $X^-$ ). It is well known that the diverse range of properties of perovskites that can exhibit derived from the fact that almost 90% of the metallic natural elements in the periodic table are known to be stable within the structure [53-55], with possible combinations listed in Table 2.1.

**Table 2.1** Potential elemental combinations for the perovskite system  $ABO_3$  and possible valence pairings that conforms the charge neutrality [55].

Site	Occupant	Valence
A	Alkali, alkaline-earth, post-transition or rare earth metal	$A^+$ , $A^{2+}$ or $A^{3+}$
B	Transition metal	$B^{5+}$ , $B^{4+}$ or $B^{3+}$
O	Oxide or halide anions	$O^{2-}$ or $X^-$

The ideal perovskite structure can be described by the cubic space group  $Pm\bar{3}m$ , with one formula unit ( $Z=1$ ) enclosed within the unit cell. The A site cation is the larger ion and requires twelve-fold coordination to neighboring anions, whereas the B site is much smaller and occupies the central position of a six-coordinate octahedron. The cubic structure of this unit cell is perhaps thought of most simply consisting of a network of  $BO_6$  octahedra with the larger A site cation residing in the interstitial site [56], as shown by Figure 2.3. The cubic arrangement means that either A or B site can be treated as the origin of the unit cell, with the  $BO_6$  octahedron or the A site cation occupying the body center of the unit cell, respectively. This equivalency is shown in figure 2.3. Alternatively, the structure can be described as the A cation being close-packed in layers with oxide ions, with the smaller B site metal situated in octahedrally coordinated holes between these  $AO_3$  layers.

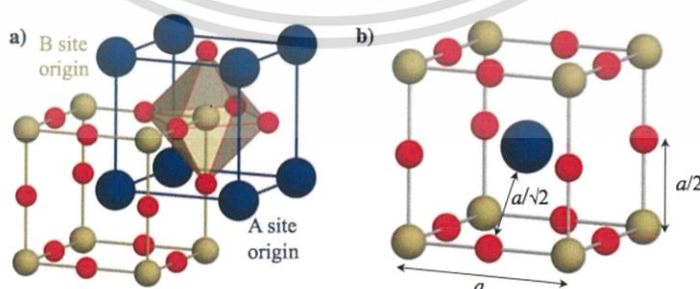


Figure 2.3 Ideal cubic perovskite structures (a) showing the equivalence of both the A and B site cations as the origin. The dimensions of the cubic unit cell, including bond lengths, are shown in (b). The A site is shown in blue, the B site in beige, and oxide ions in red [41].

This material is reserved for educational use only, not allowed for commercial use.

Forbidden to modify the content, and cite the document when use.

The ideal structure model is shown in Figure 2.3 (b) and with A–O and B–O bonds at equilibrium distances, the ions are treated as hard spheres and can be thought of as touching one another. This therefore makes the B–O distance equal to half of the unit cell length,  $a/\sqrt{2}$ , where  $a$  is the cubic lattice parameter. The A–O distance diagonally across the face of the unit cell is longer and is equal to  $a/\sqrt{2}$ , producing the following relationship between the ionic radii of the A and B site cations:

$$r_A + r_O = \sqrt{2}(r_B + r_O) \quad (2.1)$$

First observed by Goldschmidt in 1926 [57], it was used to show that the A site cations fit precisely into the twelve-coordinate site when they were of equal size to the anions. The O–A–O distance from one cell edge to the other would be exactly equal to  $\sqrt{2}$  times that of the cubic cell length. Goldschmidt realised that, by taking the ratio between the two, it was possible to use just the ionic radii of the two cations to quantify the deviation away from the ideal structure. This ratio, known as the tolerance factor [58], is shown by Equation:

$$t = \frac{r_A + r_O}{\sqrt{2}(r_A + r_O)} \quad (2.2)$$

where  $r_A$ ,  $r_B$  and  $r_O$  are the ionic radii of A, B and O, respectively.

### 2.3 Photocatalytic activity

TiO<sub>2</sub> is considered as the most efficient photocatalyst for the degradation of various organic and inorganic pollutants in water and air. The commonly studied principle of the photocatalysis reaction mechanisms is given in Figure 2.4. Upon absorption of photons with energies larger than the band gap of TiO<sub>2</sub>, electrons are excited from the valence band to the conduction band, creating electron-hole pairs [59]. These photogenerated charge carriers undergo recombination, become trapped in metastable states, or migrate to the surface of the TiO<sub>2</sub>, where they can react with adsorbed molecules. In an air-saturated aqueous environment, the photogenerated electrons and holes participate in reacting with dissolved molecular oxygen, surface hydroxyl groups, and adsorbed water molecules to form hydroxyl and superoxide radicals [60]. Although the detailed mechanism of TiO<sub>2</sub> photocatalysis reactions differs from one pollutant to another, it has been widely recognized that superoxide and, specifically, •OH hydroxyl radicals typically act as active reagents in the degradation of organic compounds. These

This material is reserved for educational use only, not allowed for commercial use.

Forbidden to modify the content, and cite the document when use.

radicals are formed by scavenging of the electron-hole pair by molecular oxygen and water, through the following:

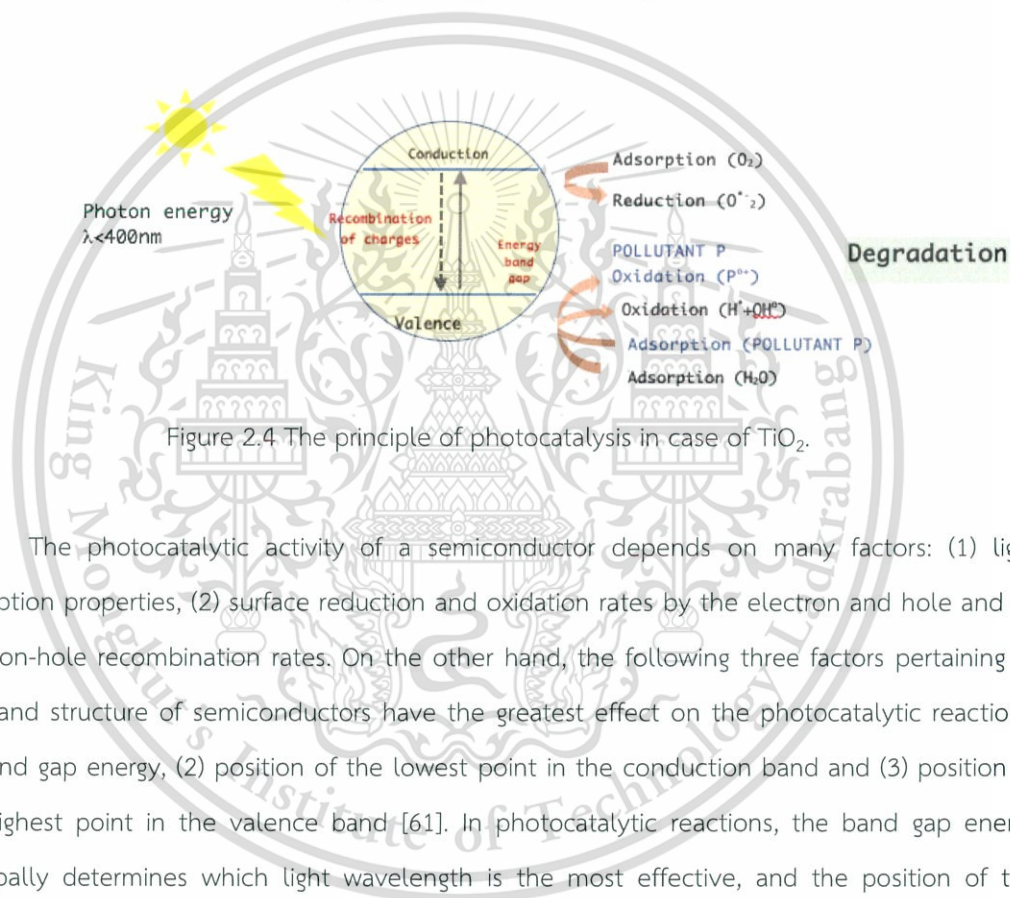
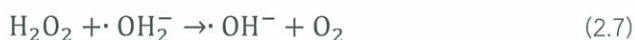


Figure 2.4 The principle of photocatalysis in case of  $\text{TiO}_2$ .

The photocatalytic activity of a semiconductor depends on many factors: (1) light absorption properties, (2) surface reduction and oxidation rates by the electron and hole and (3) electron-hole recombination rates. On the other hand, the following three factors pertaining to the band structure of semiconductors have the greatest effect on the photocatalytic reactions: (1) band gap energy, (2) position of the lowest point in the conduction band and (3) position of the highest point in the valence band [61]. In photocatalytic reactions, the band gap energy principally determines which light wavelength is the most effective, and the position of the highest point in the valence band is the main determinant of the oxidative decomposition power of the photocatalyst.

As noted, the mechanism for a photo-induced electron to transfer to an adsorbed pollutant on a semiconductor catalyst is controlled by the band energy position and the redox potential of the adsorbed species. Referring to the Normal Hydrogen Electrode (NHE) scale on figure 2.5, for an oxidation reaction to occur the potential level of the donor species must be above (more negative) than the valence band position of the semiconductor catalyst. Likewise, for a reduction reaction to take place the potential level of the acceptor species must be below

This material is reserved for educational use only, not allowed for commercial use.

Forbidden to modify the content, and cite the document when use.

(more positive) than the conduction band position of the semiconductor catalyst. It should be noted that the band edge position of the semiconductor catalysts shown in figure 2.5 are given for a pH=1, and that the pH of the solution influences the band edge position of the semiconductor [62].

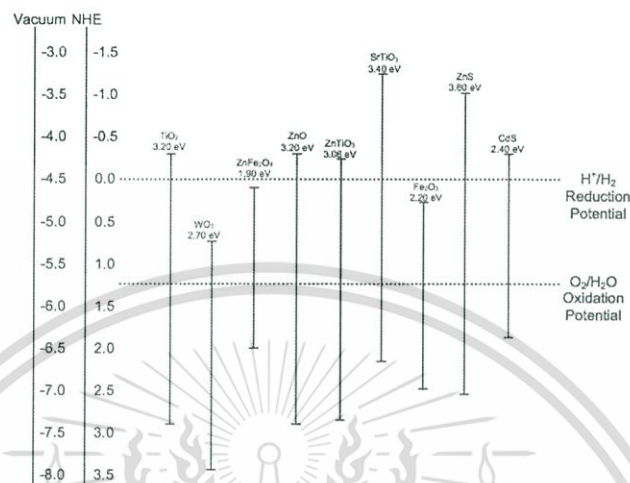


Figure 2.5 band edge positions of common semiconductor photocatalyst [62].

## 2.4 Sonochemical method

Ultrasonic waves at frequencies above 20 kHz are a branch of sound waves and it exhibits all the characteristics properties of sound waves. Depending on the frequency, ultrasound is divided into three categories, with power ultrasound (20–100 kHz), high frequency ultrasound (100 kHz–1 MHz), and diagnostic ultrasound (1–500 MHz) [63]. Ultrasound ranging from 20 to 100 kHz is used in chemically important systems, in which chemical and physical changes are desired as it has the ability to cause cavitation of bubbles. The cavitations are created when it reaches rarefaction cycle where a negative acoustic pressure is sufficiently large to pull the water molecules from each other. As a result, ‘voids’ are created in the liquid. On the other hand, the acoustic pressure is positive during compression cycle of ultrasonic wave to push molecules apart [65].

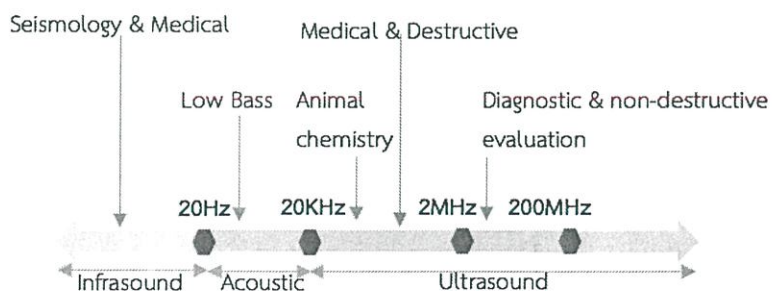


Figure 2.6 Diagram of ultrasound range. [64].

This material is reserved for educational use only, not allowed for commercial use.

Forbidden to modify the content, and cite the document when use.

(more positive) than the conduction band position of the semiconductor catalyst. It should be noted that the band edge position of the semiconductor catalysts shown in figure 2.5 are given for a pH=1, and that the pH of the solution influences the band edge position of the semiconductor [62].

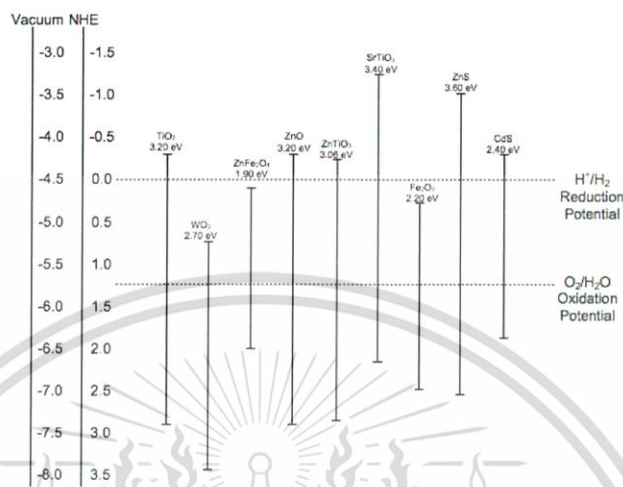


Figure 2.5 band edge positions of common semiconductor photocatalyst [62].

## 2.4 Sonochemical method

Ultrasonic waves at frequencies above 20 kHz are a branch of sound waves and it exhibits all the characteristics properties of sound waves. Depending on the frequency, ultrasound is divided into three categories, with power ultrasound (20–100 kHz), high frequency ultrasound (100 kHz–1 MHz), and diagnostic ultrasound (1–500 MHz) [63]. Ultrasound ranging from 20 to 100 kHz is used in chemically important systems, in which chemical and physical changes are desired as it has the ability to cause cavitation of bubbles. The cavitations are created when it reaches rarefaction cycle where a negative acoustic pressure is sufficiently large to pull the water molecules from each other. As a result, 'voids' are created in the liquid. On the other hand, the acoustic pressure is positive during compression cycle of ultrasonic wave to push molecules apart [65].

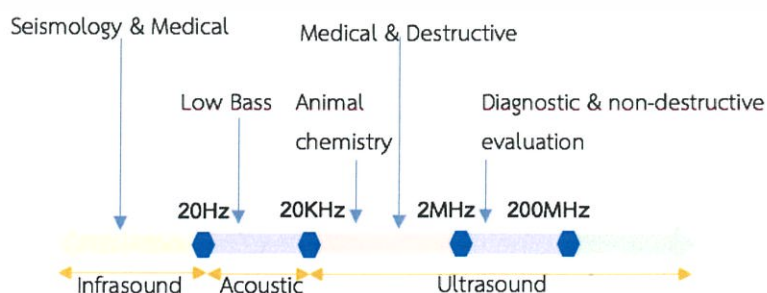


Figure 2.6 Diagram of ultrasound range. [64].

This material is reserved for educational use only, not allowed for commercial use.

Forbidden to modify the content, and cite the document when use.

depending on the technique used and experimental conditions. Meanwhile, the temperature of the interfacial region of cavitation bubbles in the water supercritical phase is only 647 K. Hence, the sonochemical method is a potential technique for preparation various nanomaterials in both lab scale and large scale [68].

## 2.5 Materials Characterization technique

### 2.5.1 X-ray diffraction (XRD)

Powder XRD is one of the primary techniques used to characterize solid state materials. It can provide valuable information about the crystalline phase and average crystallite size. The crystal size measured by this technique is smaller than the measurement limit of the optical or electronic microscope [69]. The structure of a crystal is analyzed by the X-ray diffraction patterns. The X-ray diffraction of a crystal can be formulated by means of Bragg's law [70] as in figure 2.9:

$$2d\sin\theta = n\lambda \quad (2.8)$$

when  $d$  is the d-spacing, perpendicular distance between pairs of adjacent planes in the crystal,  $\theta$  is the incident angle,  $n$  is the layer of planes, and  $\lambda$  is the wavelength of the X-rays.

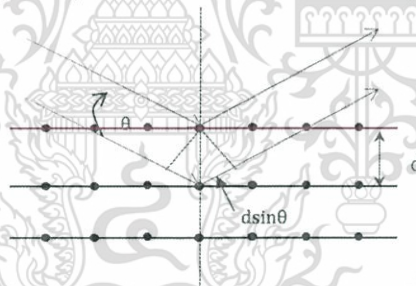


Figure 2.9 Schematic of X-ray reflection on the crystal planes.

In the cubic systems, the plane spacing is related to the lattice parameter and the Miller indices [71] by the following relation:

$$d_{hkl} = \frac{a}{\sqrt{h^2+k^2+l^2}} \quad (2.9)$$

On the other hand, the non cubic systems such as hexagonal system, the Miller indices can be calculated by using the lattice parameter from Bravais lattice:

$$\frac{1}{d^2} = \frac{4}{3} \frac{h^2+hk+k^2}{a^2} + \frac{l^2}{c^2} \quad (2.10)$$

This material is reserved for educational use only, not allowed for commercial use.

Forbidden to modify the content, and cite the document when use.

where,  $d$  is the d-spacing;  $a$ ,  $b$ ,  $c$  are sides of the unit cell; and  $h$ ,  $k$ , and  $l$  are the Miller indices, which are used to describe the lattice planes and directions in a crystal.

## 2.5.2 X-ray absorption spectroscopy (XAS)

X-ray absorption spectroscopy (XAS) is a powerful technique to determine the local structure around the absorbing atom. The XAS spectra are found to be sensitive to the oxidation state, coordination number and distance, type of neighboring atoms and their configurations. Since XAS is an atomic probe (around 6 Å from absorbing atom), the crystalline property is not required for XAS measurement. This makes XAS applicable to non-crystalline and highly disorder systems such as solution and doped sample. In many cases, including this work, XAS can be performed on elements of minority and even trace abundance, giving a unique and direct measurement of chemical and physical states of dilute species in a variety of systems [73-74]. The absorption process occurs when x-ray photon energy is higher than binding energy of core electrons. The core electron will be excited to a continuum state and leave the hole on the core shell. To keep the stability of the atom, the electron from the outer shell will be relaxed to replace the vacancy. The exceeding energy will be released in the form of an x-ray photon which is called “Characteristic x-ray fluorescence” or used to excite another electron to a vacuum level which is called “Auger electron”, [75] as shown in figure 2.10.

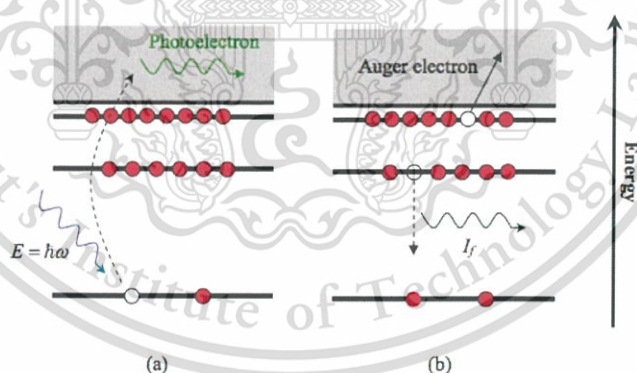


Figure 2.10 The schematic diagram showing the process of X-ray absorption [74].

X-ray absorption spectroscopy measures the absorption of x-ray or absorption as a function of x-ray photon energy,  $E = \hbar\omega$ . The x-ray absorption coefficient is assigned from the decay in the x-ray beam intensity  $I$  with distance  $x$ . The loss of intensity  $dI$  in each infinitesimal slab of material  $dx$  is shown in figure 2.11.

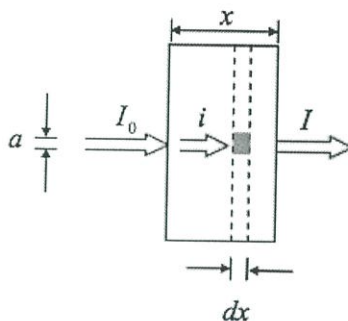


Figure 2.11 The schematic view of X-ray absorption [76].

The total intensity after passing through the sample can be written in the form:

$$I = I_0 e^{-\mu \cdot x} \quad (2.11)$$

The constant parameter  $\mu$  is defined to be an x-ray absorption coefficient which is found to be depending on energy and atomic number of sample. The x-ray absorption can be expressed in the term of multiplication of x-ray absorption coefficient,  $\mu$  and thickness,  $x$ .

$$\mu \cdot x = \ln \frac{I_0}{I_1} \quad (2.12)$$

The XAS spectrum is generally found that the x-ray absorption decreases with increasing photon energy. The presence of the sharp rise at certain energy is called “absorption edge”. Each absorption edge is related to the quantum-mechanical transition by exciting a particular atomic core-orbital electron to the continuum level, as shown in figure 2.12(a). The absorption edge is named after the electron origin in the core orbital, for example, *K*-edges referring to transition that excite the innermost 1s electron. The energy that provides the first maximum rise is called “edge energy”. The position of edge energy is unique to a given absorbing atom and will be shifted to the higher energy as the oxidation state increases, as shown in figure 2.12(b).

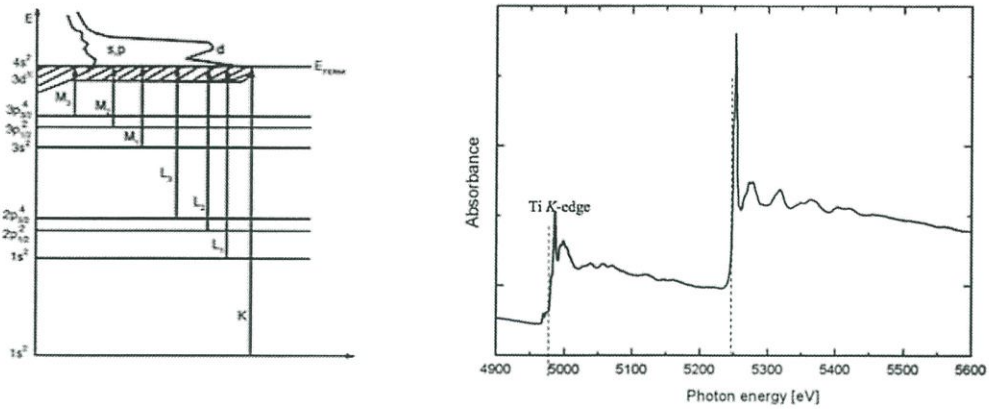


Figure 2.12 The XAS spectrum of Ti K-edge and Ba  $L_3$ -edge for  $\text{BaTiO}_3$  [74].

For the XAS spectrum, there are two regions of interest in XAS spectra as shown in figure 2.13. The first region is the x-ray absorption near edge structure (XANES). XANES covers the range between the thresholds of the absorption edge to the energy around 30 eV from the absorption edge. Since it gives a large signal, therefore XANES can be utilized at lower concentration and does not require a perfect sample condition. XANES contains information of oxidation state, the configuration of neighboring atom and gives a unique spectrum which can be used as fingerprint of any materials. The small feature presents before absorption edge in some kind of material is called “pre-edge” as shown in inset of figure 2.13. This feature which is caused by electronic transitions to empty bound states is also used for XANES analysis. The second region is the extended x-ray absorption fine structure (EXAFS). This region is extending to the energy about 500-1000 eV after the edge. The EXAFS spectrum,  $\chi(E)$  can be inferred to the oscillatory part of x-ray absorption above the given absorption edge [59], as seen in figure 2.13,

$$\chi(E) = \frac{\mu(E) - \mu_0(E)}{\Delta\mu_0} \quad (2.13)$$

where  $\mu_0(E)$  is the smoothly varying atomic-like background absorption and  $\Delta\mu_0$  is a normalization factor that arises from the net increase in the total atomic background absorption at the edge or edge step.

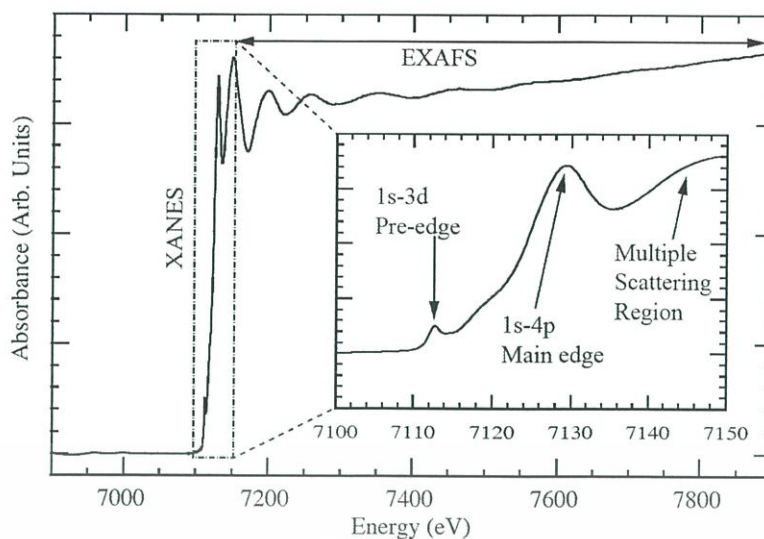


Figure 2.13 A schematic of XAS spectrum [75].

### 2.5.3 UV-visible spectroscopy

Many molecules absorb ultraviolet (UV) or visible light. The absorption of UV or visible radiation is caused by the excitation of outer electrons, from their ground state to an excited state. The Bouguer-Lambert-Beer law forms the mathematical physical basis for the light absorption measurements on gas and in solution [76]. According to this law, absorbance is directly proportional to the path length  $l$ , and the concentration of the absorbing substance  $c$ , and can be expressed as  $A = \alpha lc$ , where  $\alpha$  is a constant of proportionality, called the absorptivity. In addition, absorption strongly depends on the types of samples, and the environment of the sample. For example, molecules absorbing radiation of various wavelengths depending on the structural groups present within the molecules and show a number of absorption bands in the absorption spectrum. The solvent in which the absorbing species is dissolved also has an effect on the spectrum of the species. Moreover, the size of the particle is also important. If the size of the particle  $d \gg \lambda$ , light interacts with the samples instead of absorption, with parts of the light scattered and reflected.

When dealing with solid samples (figure 2.14), light penetrates into the sample; undergoes numerous reflections, refractions and diffraction and emerges finally diffusely at the surface. The Bouguer-Lambert-Beer law cannot handle solid samples [62], which is based on the assumption that the light intensity is not lost by scattering and reflection processes

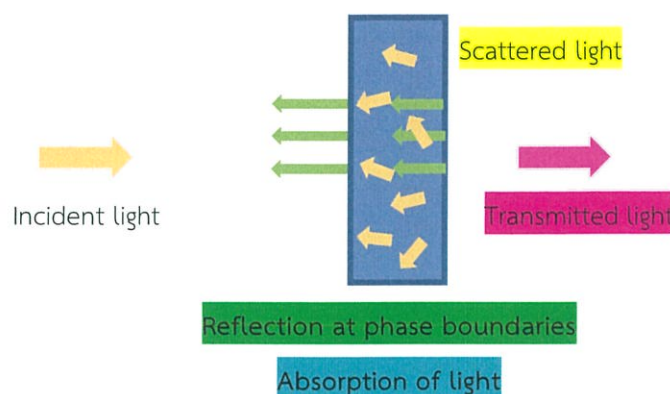


Figure 2.14 Interaction of light with solid samples [77].

#### 2.5.4 Field emission scanning electron microscope (FESEM)

An electron microscope, such as a transmission electron microscope (TEM), or a scanning electron microscope (SEM), is a microscope that uses a beam of electrons to illuminate a specimen and then create an enlarged image, which provides the surface and internal information on a nanometer scale. Electron microscopes have much higher resolving power than light microscopes, and can obtain much higher magnifications. The electron microscope is extensively used for inspection, quality assurance and failure analysis applications in industry. TEM and SEM have made crucial contributions to science and engineering, and made them indispensable tools in nanotechnology for analyzing nanostructures [78-79].

In the FESEM, a very fine beam of electrons with energy up to several tens keV is focused on the surface of a sample and is scanned across it in a parallel pattern. The intensity of emission of secondary and backscattered electrons is very sensitive to the angle at which the electron beam strikes the surface of the sample. The emitted electron current is collected and amplified. The magnification produced by the SEM is the ratio between the dimension of the final image display and the field scanning on the specimen. Usually, the magnification range of the SEM is between 10 to 222,000 times, and the resolution is between 4-10 nm. Generally, the TEM resolution is about an order of magnitude greater than the SEM resolution, however, because the SEM image relies on surface processes rather than transmission, it is able to image bulk samples and has a much greater depth of view, and so can produce images that are a good representation of the overall 3D structure of the sample. FESEM usually images conductive or semi-conductive materials. A common preparation technique is to coat the sample with a several-nanometer layer of conductive material, such as gold, or platinum, from a sputtering machine. However, this process can damage delicate samples. It should also be mentioned that This material is reserved for educational use only, not allowed for commercial use.

Forbidden to modify the content, and cite the document when use.

the specimen might be damaged by the electron-beam focusing for a long time on a small spot. FESEM measurements are conducted to determine the size and morphology of synthesized nanomaterials.

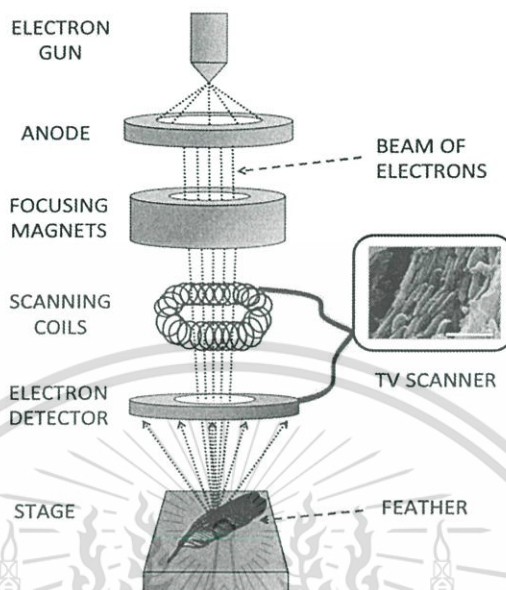


Figure 2.15 A Schematic for FESEM [79].

## 2.6 Literature review

### 2.5.1 TiO<sub>2</sub> doped with transition metal ions

In 2008, Y. Zhao *et al.* reported Zn-doped TiO<sub>2</sub> nanoparticles with high photocatalytic activity synthesized by hydrogen–oxygen diffusion flame [25]. They suggested that the photosensitized degradation activity could be enhanced by doping an appropriate amount of Zn. The improved properties by Zn doping could be attributed to the appropriate energetic position between ZnO and the excited state of dye, which enhanced the electron injection into the conduction band of TiO<sub>2</sub> by capturing electron, subsequently promoted the formation of reactive oxygen species.

T. B. Nguyen *et al.* [80] studied the synthesis and high photocatalytic activity of Zn-doped TiO<sub>2</sub> nanoparticles prepared by a novel sol-gel and ammonia-evaporation method. The results indicated that the Zn ions completely incorporated into TiO<sub>2</sub> lattice by using this method. The Zn-TiO<sub>2</sub> samples showed high photocatalytic activity for the degradation of methylene blue (MB). The highest photoactivity efficiency could remove ~91% of the MB after 4 h, while the pure TiO<sub>2</sub> only removed ~46% of the MB, as shown in figure 2.16. They also studied effects of the mol% of zinc ion doping in TiO<sub>2</sub> on photocatalytic activity.

This material is reserved for educational use only, not allowed for commercial use.

Forbidden to modify the content, and cite the document when use.

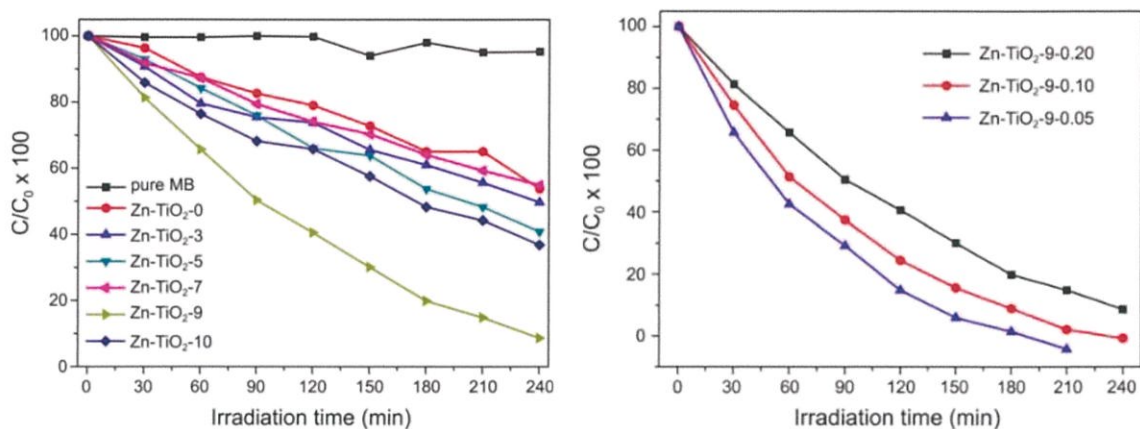


Figure 2.16 Effect of zinc content on photocatalytic activity and effect of initial concentration of ZnSO<sub>4</sub> on photo-catalytic activity [80].

M.M. Rashad *et al.* [81] studied the structural, optical, magnetic and photocatalytic properties of transition metal of Mn and Co ions doped TiO<sub>2</sub> nanoparticles by using hydrothermal method at 100°C with a post-annealing temperature process at 500°C. They reported that the anatase type structure in TiO<sub>2</sub> nanopowders with high crystallinity and high phase stability even after annealing at 500°C substantially indicated that the dopants might inhibit densification and crystallite growth in TiO<sub>2</sub> nanophasse by providing dissimilar boundaries. A suitable amount (ca. 0.2, 0.3 mol%), the Mn, Co dopants reduced anatase grain size and increased the specific surface area of TiO<sub>2</sub> powders. The energy band gap of prepared samples became narrow compared with bare TiO<sub>2</sub> as seen the optical spectra in the figure 2.17. Furthermore, magnetic measurement results revealed that all the samples exhibited the paramagnetic behavior at room temperature. Photocatalytic degradation of methylene blue (MB) under UV lights indicated that the meso-TiO<sub>2</sub> exhibited enhanced activity under UV lights. However, photodegradation of the MB under UV light was enhanced with the presence of Mn and Co with TiO<sub>2</sub>.

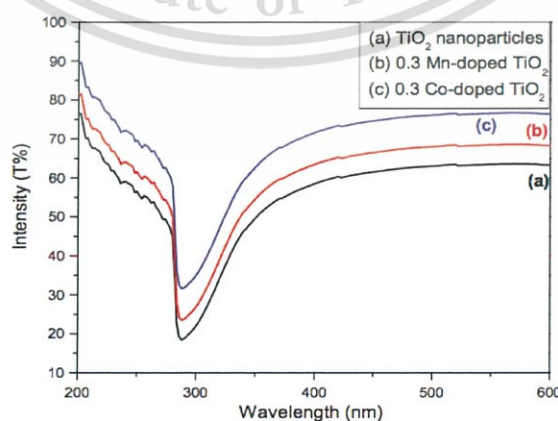


Figure 2.17 UV-visible transmittance spectrum T% of TiO<sub>2</sub> and Co [81]

This material is reserved for educational use only, not allowed for commercial use.

Forbidden to modify the content, and cite the document when use.

The effect of oxygen vacancy and dopant concentration on the magnetic properties of high spin  $\text{Co}^{2+}$  doped  $\text{TiO}_2$  nanoparticles was studied by B. Choudhury group [82]. They revealed that the Co-doped  $\text{TiO}_2$  nanoparticles have been synthesized by a simple sol-gel route taking 7.5, 9.5 and 10.5 mol% of cobalt concentration. Formation of nanoparticles was confirmed by XRD and TEM with increasing d-spacing for (0 0 4) and (2 0 0) peak and increasing impurity content. The weak ferromagnetic properties were found in the vacuum annealed samples. Increased magnetization was found for 9.5 mol% but this value again decreased for 10.5mol% due to antiferromagnetic interactions. In this work, they reported that oxygen vacancy and cobalt aggregation was a key factor for inducing ferromagnetism-superparamagnetism in the vacuum annealed samples. Appearance of negative Curie-Weiss temperature revealed the presence of antiferromagnetic  $\text{Co}_3\text{O}_4$ , which was the oxidation result of metallic Co or cobalt clusters presenting on the host  $\text{TiO}_2$ .

In addition, Meredith C.K. *et al.* [83] have claimed the room temperature ferromagnetism in Mn-doped  $\text{TiO}_2$  nanopillar matrices diluted magnetic semiconductors. They indicated that the morphology and microstructure exerted strong, but complicated, effects upon ferromagnetic behavior. To partially unravel such effects, the work compared room temperature ferromagnetism (RTFM) in Mn-doped anatase  $\text{TiO}_2$  films synthesized by two different atomic layer deposition protocols, leading to either nanopillars or more conventional columnar grains. RTFM was largely unaffected by this difference for undoped material, but nanopillaring greatly increased both the coercive field (100 Oe) and saturation magnetization (14–21  $\text{emu}/\text{cm}^3$ ) for Mn doping up to 2.7 at%. Nanopillaring seemed to enhance the congregation of defect-related bound magnetic polarons near grain boundaries, thereby increasing RTFM.

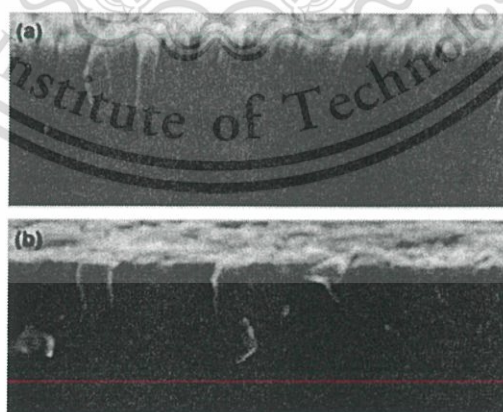


Figure 2.18 Typical cross-sectional micrographs of 100 nm thick (a) undoped and (b) Mn-doped  $\text{TiO}_2$ . [83]

The metal ion co-doping with series of Cr, Fe, Co, Ni, Cu, Zn, Ce and Zr on Mn/TiO<sub>2</sub> catalyst and its effect on selective reduction of NO with NH<sub>3</sub> were studied by B. Thirupathi *et al.* in 2011 [26]. They clearly showed that samples with the same atomic composition could have very different properties, depending on the co-doped metals and on their chemical properties. The in-situ N-FTIR results revealed that the titania-supported manganese and manganese–nickel surface sites had only Lewis acidity. BET and pore volume measurements suggested high surface area and pore volume of the Mn–Ni/TiO<sub>2</sub> catalyst. All the experimental results showed that NO conversion, N selectivity, broadening of temperature window and time on stream patterns of the catalyst were improved greatly by doping the Mn/TiO<sub>2</sub> catalyst with optimized ( $M/Mn = 0.4$ ) nickel. The N<sub>2</sub> selectivity and catalytic performance as shown in figure 2.19, among eight different types of co-dopants and five kind of  $M/Mn$  atomic ratios in each type, Mn–Ni(0.4)/TiO<sub>2</sub> catalyst was the best one for the low temperature SCR of NO with NH. This catalyst offered high NO conversion (100%), high N selectivity (100%), and broadening of the temperature window with stable time on stream patterns.

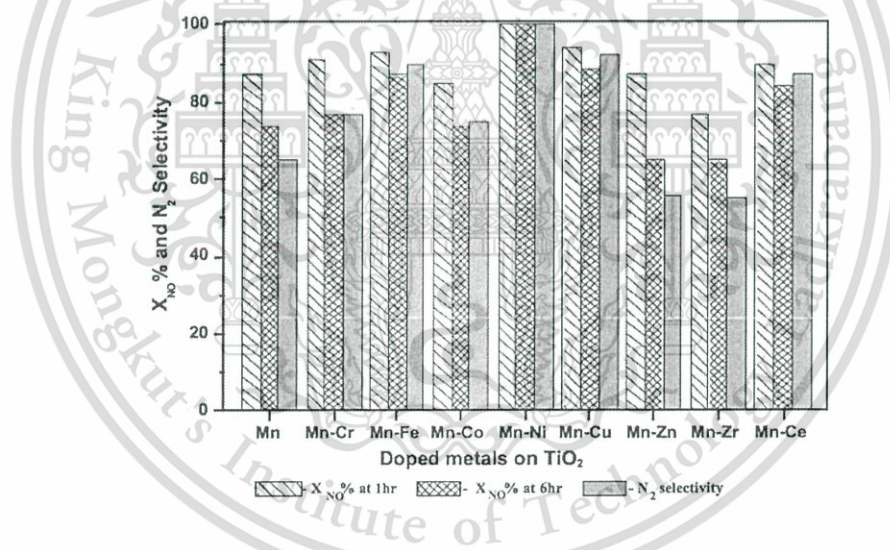


Figure 2.19 N<sub>2</sub> selectivity and catalytic performance of Mn-M/TiO<sub>2</sub> anatase catalyst: NH<sub>3</sub>=400 ppm; NO=400ppm [26].

## 2.6.2 ZTO and ZTO doping with metal ions

L. Wang *et al.* [84] reported the synthesis of ZnTiO<sub>3</sub> nanopowders at low temperature by using stearic acid gel method. XRD patterns are shown in figure 2.21, the results revealed the formation of ZnTiO<sub>3</sub> crystallites after heat treatment at 500°C. With increasing calcination temperature, the crystallinity of the as-prepared ZnTiO<sub>3</sub> powders was improved significantly. ZnTiO<sub>3</sub> powders could be synthesized at low temperature around 600°C. The average crystalline size of ZnTiO<sub>3</sub> synthesized at 600°C is about 20–50 nm. The optical analysis showed the higher visible responsibility with increasing of calcination temperature as seen in figure 2.21.

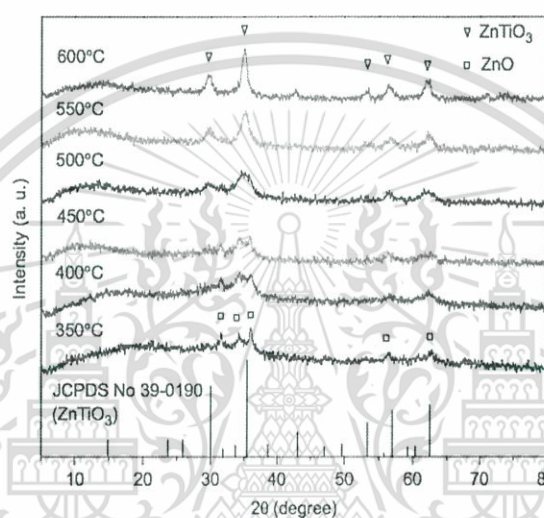


Figure 2.20 XRD patterns of the calcined samples at different temperatures (the standard diffraction XRD pattern of ZnTiO<sub>3</sub> is shown as a reference) [84].

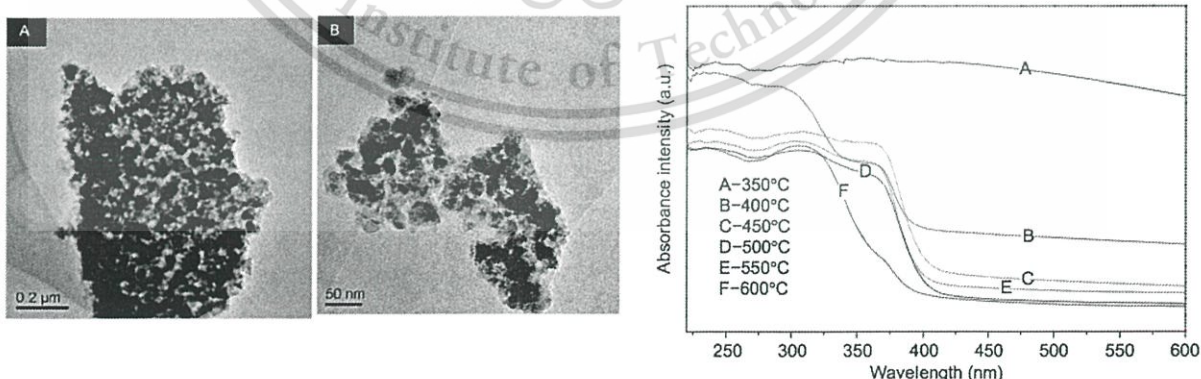


Figure 2.21 (A and B) TEM images of ZnTiO<sub>3</sub> powders calcined at 600°C. (C) UV/vis diffuse reflectance spectra of samples calcined at different temperatures [84].

This material is reserved for educational use only, not allowed for commercial use.

Forbidden to modify the content, and cite the document when use.

I. Bobowska *et al.* [85] conducted the synthesis and dielectric investigation of  $\text{ZnTiO}_3$  obtained by a soft chemistry route. In this paper, they reported a strategy for preparing an inorganic zinc titanate precursor by applying a chemical bath deposition method (CBD) to  $\text{ZnO}$  nanocrystals in an aqueous layered titanate colloid. The zinc titanate precursor, obtained as a precipitate, underwent profound changes under the influence of elevated temperatures in normal atmospheric conditions and allowed us to obtain zinc titanate  $\text{ZnTiO}_3$  with a rhombohedral symmetry. The investigations of its dielectric properties enabled as in figure 2.33 show a dielectric permittivity of 25, a low loss factor  $\tan(\delta) < 10^{-3}$ , and a temperature coefficient of 18 ppm at the frequency of 1.15MHz. The density of the zinc titanate ceramic was equal to approximately 80% of the theoretical density of the  $\text{ZnTiO}_3$  crystals.

Y. Wang *et al.* [40] reported the preparation of zinc titanate nanoparticles and their photocatalytic behaviors in the photodegradation of humic acid in water. They suggested that the zinc titanate nanoparticles had been prepared through sol-gel method using citric acid as chelating agent and ethylene glycol as stabilizer. The pure hexagonal ZTO was observed in samples calcined at  $800^\circ\text{C}$ . The prepared samples showed the extension in the visible light absorption as seen in figure 2.23. The photocatalytic activity of zinc titanate was evaluated by degrading the humic acid solution under the irradiation of sunlight and xenon lamp with the optimum catalyst loading of 0.8g/L. The holes ( $h^+$ ) and OH radicals are the major reactive species for the photocatalytic reactions. The enhancement of photocatalytic activity for the zinc titanate calcined might be attributed to the higher redox ability, coordination of Ti ions and smaller particle size.

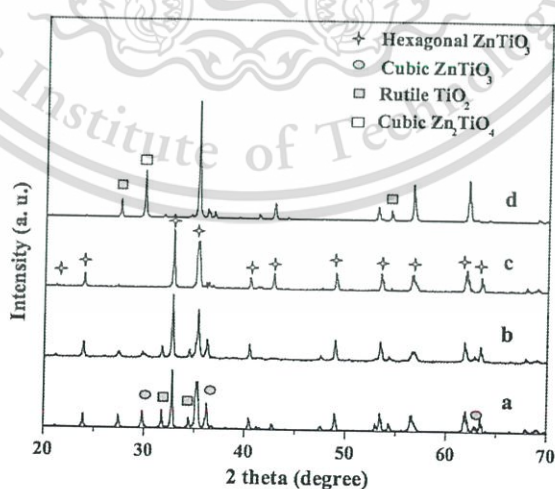


Figure 2.22 XRD patterns of the samples calcined at different temperatures (a)  $600^\circ\text{C}$ , (b)  $700^\circ\text{C}$  (c)  $800^\circ\text{C}$  and (d)  $900^\circ\text{C}$  [40].

This material is reserved for educational use only, not allowed for commercial use.

Forbidden to modify the content, and cite the document when use.

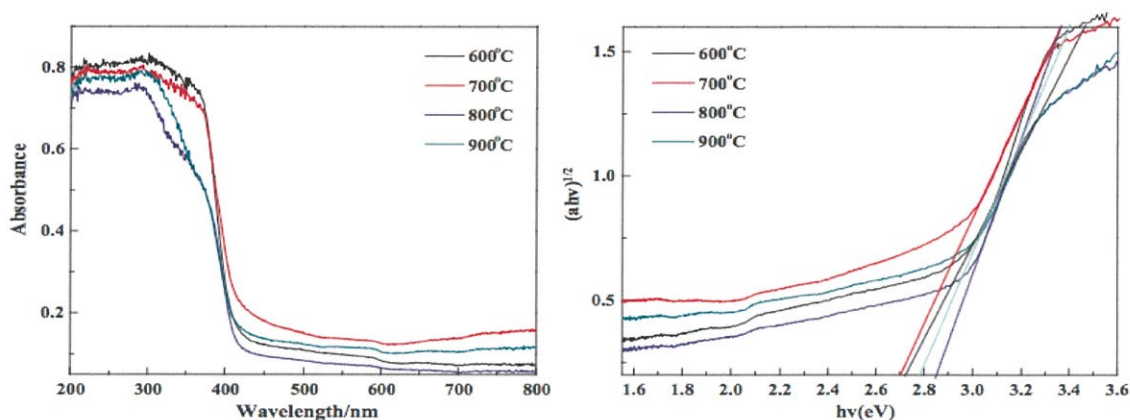


Figure 2.23 Optical properties of ZTO (a) absorption as a function wavelength and (b) energy band gap [40].

R.S. Raveendra *et al.* [86] studied the synthesis, structural characterization of nano  $\text{ZnTiO}_3$  ceramic with effective azo dye adsorbent and antibacterial agent. They showed that the nanocrystalline zinc titanate ceramic was successfully prepared by using a self-propagating solution combustion synthesis for the first time using urea as fuel. The sample was calcined at  $800^\circ\text{C}$  for 2h to improve the crystallinity. XRD result exhibited that the ilmenite type rhombohedral structure was formed when the sample calcined at  $800^\circ\text{C}$  for 2h. Adsorption experiments were performed with cationic malachite green (MG) dye. 96% dye was adsorbed onto nanocrystalline  $\text{ZnTiO}_3$  ceramic at pH 9 for 30min of the contact time. The optimum adsorbent dose was found to be 0.45g/L of dye. They used the Langmuir–Hinshelwood model to study adsorption kinetics and first order kinetic model well described the MG adsorption on  $\text{ZnTiO}_3$ . Antibacterial activity was investigated against gram negative *Klebsiella aerogenes*, *Pseudomonas desmolyticum*, *Escherichia coli*, and gram positive *Staphylococcus aureus* bacteria by agar well diffusion method. Nanocrystalline  $\text{ZnTiO}_3$  ceramic showed significant effect on all the four bacterial strains at the concentration of 1000 and 1500 g per well.

S. F. Wang group studied the photoluminescence of sol–gel derived  $\text{ZnTiO}_3$  doped with  $\text{Ni}^{2+}$  nanocrystals [34]. The studies exhibited that the introduction of  $\text{Ni}^{2+}$  ion has changed  $\text{ZnTiO}_3$  nanocrystal into a new luminescent material. With different excitation wavelength, three emission bands in blue, green and red region had all been observed as seen in figure 2.24. The emission intensities showed a dependence on the concentration of  $\text{Ni}^{2+}$  ion. They suggested that the luminescent phenomenon could be attributed to the optical transitions of  $\text{Ni}^{2+}$  ions in the  $\text{ZnTiO}_3$  nanocrystals.

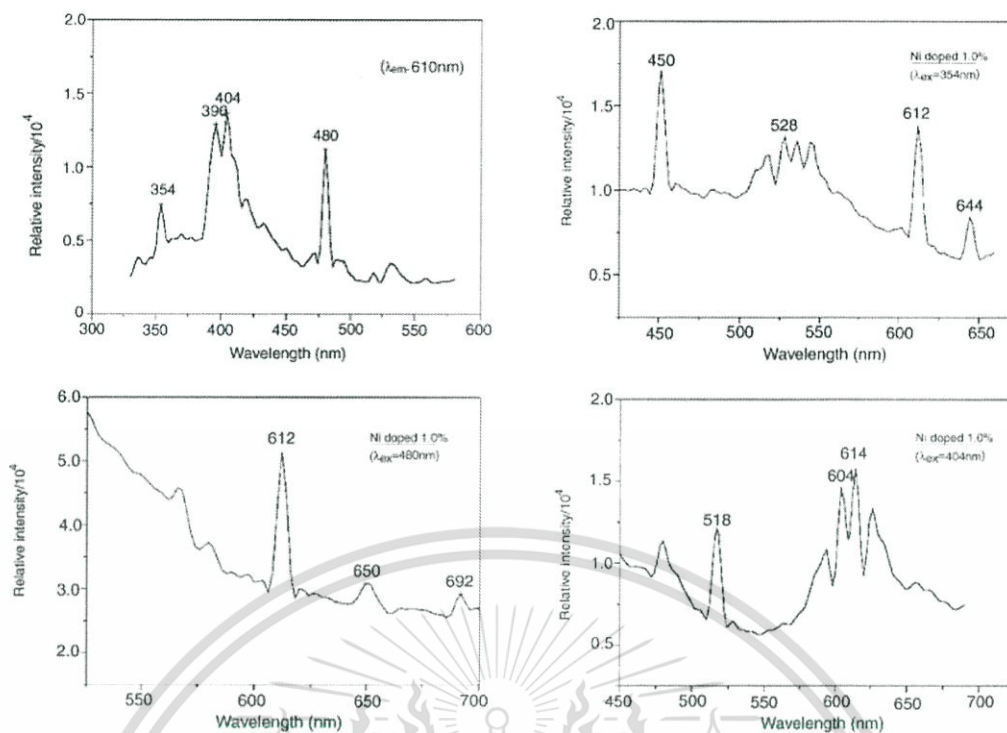


Figure 2.24 Excitation spectrum of the doped sample ( $\text{Ni}^{2+}$  ion is 1%). Emission spectra of the doped sample excited at different wavelength [34].

D. P. Dutta *et al.* [41] reported the Ag-doped and Ag-dispersed nano  $\text{ZnTiO}_3$  to improve photocatalytic organic pollutant degradation under solar irradiation and antibacterial activity. The results indicated that the structural phase product was sensitive to the annealing temperature of the as-synthesized product. The results also represented that the rhombohedral phase exhibited the highest photodegradation efficiency among all the undoped samples under UV as well as visible irradiation by degrading 100% of RhB within 150 min. For the Ag doping, the samples exhibited comparatively higher photocatalytic activity under solar irradiation compared to its undoped counterpart. Under sunlight, the  $\text{ZnTiO}_3:\text{Ag}(5\%)$  sample exhibited 100% RhB degradation within 45 min. It also showed promising antibacterial activity against strains of *E. coli* and *B. subtilize*, with a minimum growth inhibitory concentration value which was considerably lower than ciprofloxacin. They had also shown that the extension of photodegradation of RhB under solar irradiation was  $\sim 100\%$  even after five consecutive run using  $\text{ZnTiO}_3:\text{Ag}(5\%)$  as seen in figure 2.25.

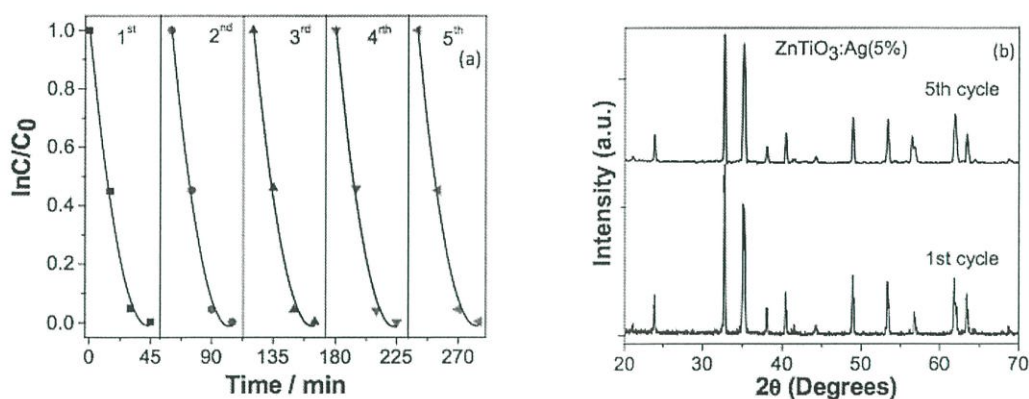


Figure 2.25 Photocatalytic activities under solar irradiation of the ZnTiO<sub>3</sub>:Ag(5%) photocatalysts for the degradation of RhB for five cycles and (b) XRD pattern of ZnTiO<sub>3</sub>:Ag(5%) after five cycles [41].

### 2.6.3 Sonochemical synthesis

A novel single-step synthesis of N-doped TiO<sub>2</sub> by a sonochemical method was reported by X. K. Wang *et al.* [87]. The TiO<sub>2</sub> nanoparticles were synthesized by sonication of the solution of tetraisopropyl titanium and urea in water and isopropyl alcohol. The XRD patterns exhibited the pure anatase phase for all prepared samples (figure 2.26). The crystallinity of anatase phase depended on the reaction temperature and reaction time. The photocatalytic activity of the as-prepared photocatalyst was evaluated via the photodegradation of an azo dye direct sky blue 5B, suggesting that the N-doped TiO<sub>2</sub> nanocrystalline prepared via sonication exhibited an excellent photocatalytic activity under UV light and simulated sunlight.

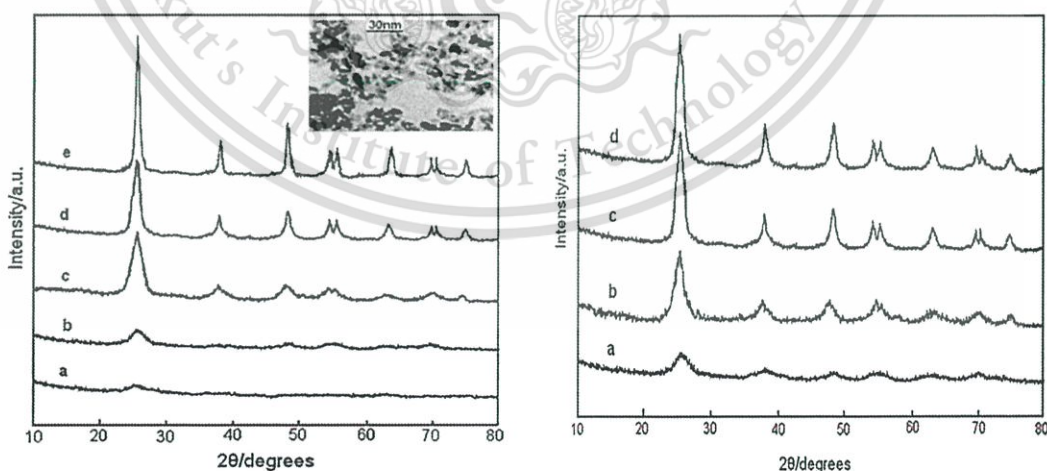


Figure 2.26 Powder XRD spectra of TiO<sub>2</sub> prepared by sonication for 150min at temperature (a) 30 °C, (b) 50 °C, (c) 70 °C, (d) 80 °C and (e) sample d calcined at 400 °C for 120 min. Powder XRD spectra of TiO<sub>2</sub> prepared at 80 °C after sonication (a) 60 min, (b) 120 min, (c) 150 min and (d) 180 min [87].

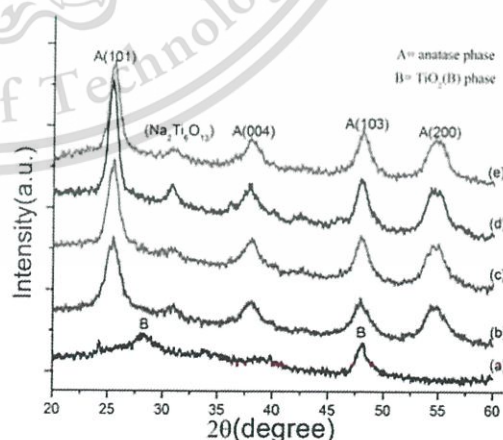
This material is reserved for educational use only, not allowed for commercial use.

Forbidden to modify the content, and cite the document when use.

W. Jiang *et al.* [88] reported the sonochemical synthesis and characterization of magnetic separable  $\text{Fe}_3\text{O}_4\text{-TiO}_2$  nanocomposites and their catalytic properties. A novel sonochemical method was described for the preparation of  $\text{Fe}_3\text{O}_4\text{-TiO}_2$  photocatalysts in which nanocrystalline titanium dioxide particles were directly coated onto a magnetic core. The  $\text{Fe}_3\text{O}_4$  nanoparticles were partially embedded in  $\text{TiO}_2$  agglomerates. nanocrystalline  $\text{TiO}_2$  was obtained by hydrolysis and condensation of titanium tetraisopropyl in the presence of ethanol and water under high-intensity ultrasound irradiation. This method is attractive since it eliminated the high-temperature heat treatment required in the conventional sol-gel method, which was important in transforming amorphous titanium dioxide into a photoactive crystalline phase. In comparison to other methods, the developed method is simple, mild, green and efficient.

$\text{TiO}_2$  nanostructure prepared by sonochemical method was studied by C. Kahatta *et al.* [45]. In this work,  $\text{TiO}_2$  particles were prepared by sonochemical-hydrothermal process from a precursor of titanium isopropoxide in the presence of polyvinyl alcohol aqueous solution. Sonication of the precursor was conducted using sonic horn operated at 20 kHz until the completely precipitated product was reached. As-obtained products were then loaded into a Teflon-lined stainless steel autoclave for hydrothermal process with 10M NaOH aqueous solution and heated under different temperature 80-120°C. The crystal analysis by XRD is shown in figure 2.27, the formation of anatase  $\text{TiO}_2$  phase was found after sonochemistry preparation for 30 min. The TEM analysis showed the nanosize and uniform nanoparticles as seen in figure 2.28. They also claimed that the sonochemical-hydrothermal process shows a good crystallinity and high purity titanium dioxide.

Figure 2.27 XRD patterns of  $\text{TiO}_2$  nanoparticles by  
 (a) hydrothermal at 120°C,  
 (b) sonochemical for 30 min,  
 (c) sonochemical-hydrothermal at 80°C,  
 (d) sonochemical-hydrothermal at 100°C,  
 (e) sonochemical-hydrothermal at 120°C [45].



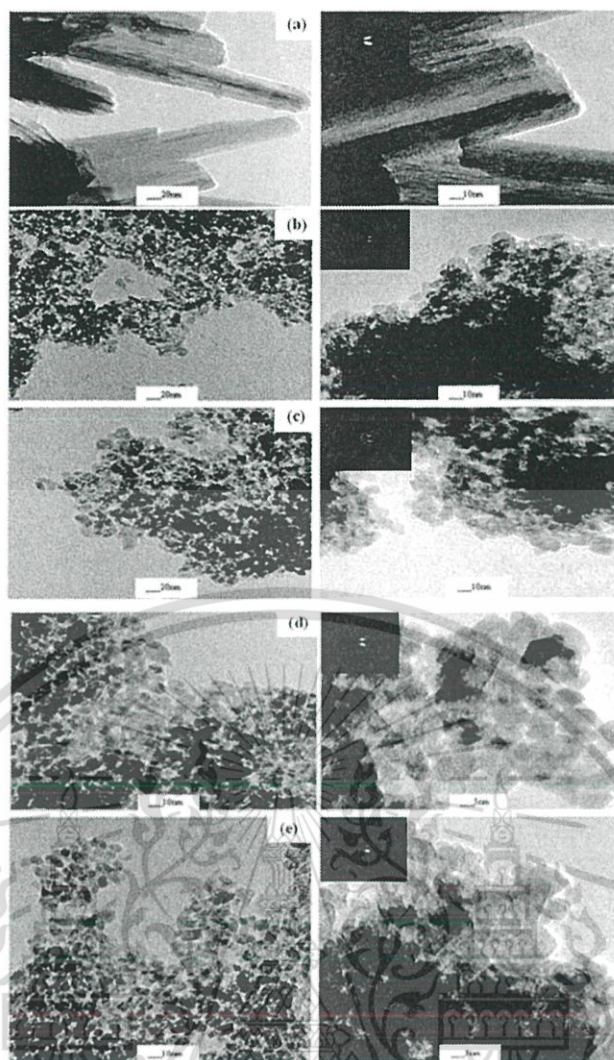


Figure 2.28 TEM images of  $\text{TiO}_2$  nanoparticles synthesized by (a) hydrothermal at  $120^\circ\text{C}$ , (b) sonochemical for 30 minute, (c) sonochemical-hydrothermal at  $80^\circ\text{C}$ , (d) sonochemical-hydrothermal at  $100^\circ\text{C}$ , (e) sonochemical-hydrothermal at  $120^\circ\text{C}$  [45].

## CHAPTER 3

### EXPERIMENTAL PROCEDURE

In this chapter, the applied experimental setups and methods are represented which can be divided into three main sections. The precursors, equipments for sample preparation are listed in section 3.1. The general procedure for synthesizing the samples are described in section 3.2 including fabrication of Zn-doped TiO<sub>2</sub>, zinc titanate and zinc titanate doped with transition metal ions of cobalt and manganese. Final part, the material characterizations are given in section 3.3. This part explains the detail information about the characterizations of the samples including: X-ray diffraction (XRD), Field Emission Electron Microscopy (FESEM), UV-visible spectroscopy (UV-vis), X-ray absorption spectroscopy (XAS), and photocatalytic measurement by rhodamine b dye degradation.

#### 3.1 Materials and equipment

##### Precursor materials

1. Titanium isopropoxide [Ti(OCH(CH<sub>3</sub>)<sub>2</sub>)<sub>4</sub>: TIIP]
2. Cobalt nitrate hexahydrate (Co(NO<sub>3</sub>)<sub>2</sub>·6H<sub>2</sub>O)
3. Manganese nitrate tetrahydrate (Mn(NO<sub>3</sub>)<sub>2</sub>·4H<sub>2</sub>O)
4. Zinc nitrate hexahydrate (Zn(NO<sub>3</sub>)<sub>2</sub>·6H<sub>2</sub>O)
5. Zinc acetate (Zn(CH<sub>3</sub>CO<sub>2</sub>)<sub>2</sub>)
6. Absolute ethanol 99.7% (CH<sub>3</sub>CH<sub>2</sub>OH)
7. Deionize water
8. Sodium hydroxide (NaOH)
9. Rhodamine B dye

##### Equipment

1. Sonometer
2. Hot oven
3. Furnace
4. Hotplate stirrer, model HTS-1003
5. Digital weight apparatus

## 3.2 Experimental procedure

### 3.2.1 Synthesis of Zn doped TiO<sub>2</sub> nanoparticle

The schematic of preparation process for Zn-doped TiO<sub>2</sub> is shown in figure 3.1. First, TIIP precursor was dissolved in absolute ethanol and acetylacetone under stirring for 15 min. Then, zinc acetate was slowly added into the solutions under vigorous stirring for 30 min to obtain the homogenous mixing solution. The mixing solution and deionized water was mixed together in the sonometer chamber as a ratio of 1:1. After that, the mixed solution was irradiated with high intensity ultrasound sonometer (750 W 20 kHz) at room temperature for 30 min until the completely precipitated product was obtained. After cooling down to room temperature, the precipitated products were washed by using deionized water. Then, the cleaned precipitate was dried at 100°C for 12 h to remove moisture and contaminants. Finally, the as-synthesized powders were calcined between 400 and 700°C for 2 h.

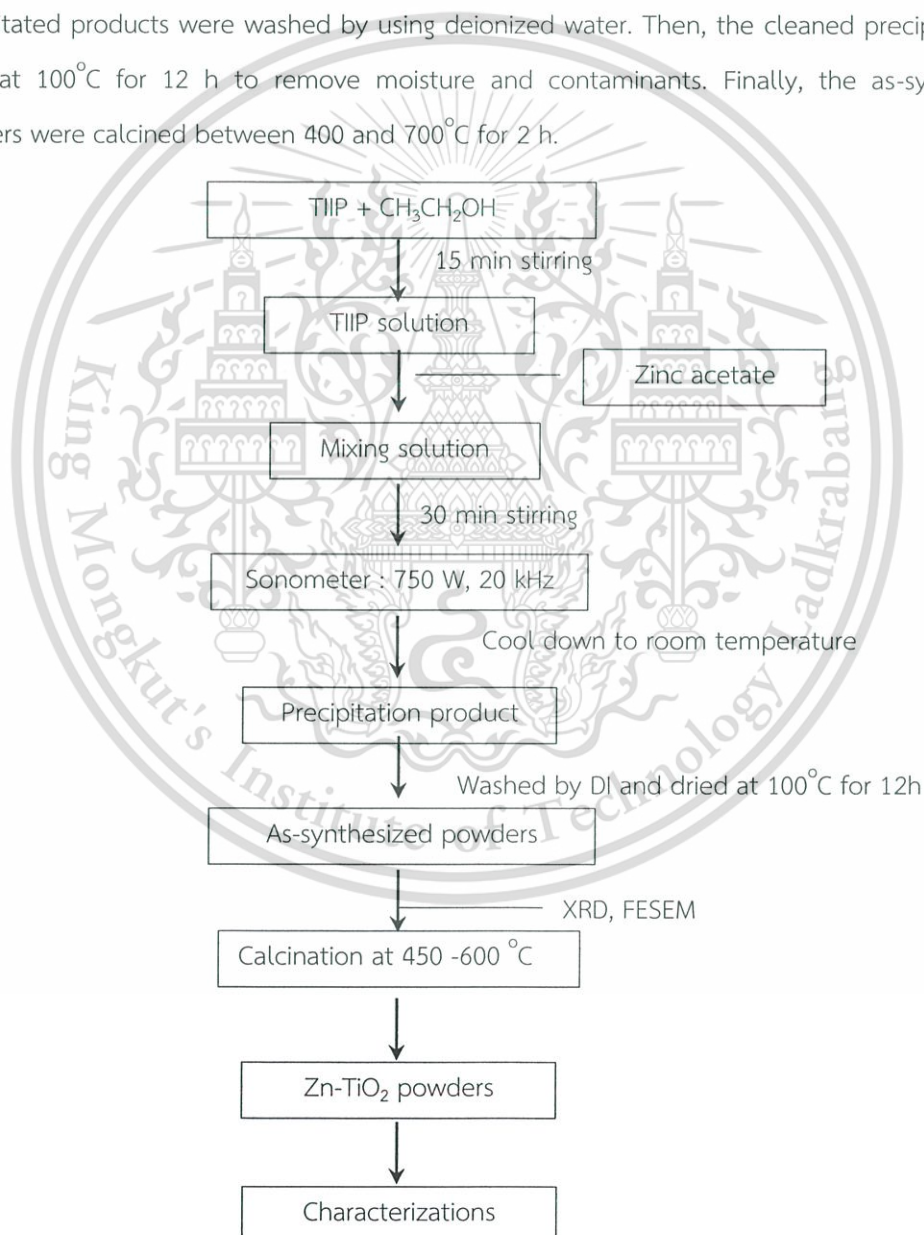


Figure 3.1 Schematic of preparation for Zn-doped TiO<sub>2</sub> nanoparticles

This material is reserved for educational use only, not allowed for commercial use.

Forbidden to modify the content, and cite the document when use.

### 3.2.2 Synthesis of Zn-Co and Zn-Mn co-doped TiO<sub>2</sub> nanoparticles

The preparation process diagram of co-doped TiO<sub>2</sub> is shown in figure 3.2. TIIP was dissolved in absolute ethanol under magnetic stirrer and zinc nitrate was then added in the solution. After that the Co or Mn dopants at different concentrations of 1-5mol% was added in the solution followed by DI water. The mixing solution was kept under stirring for 15 min. Finally, the mixed precursor was irradiated under high ultrasonic sonicator (750W, 20kHz) for 30 min at room temperature together with the slow addition of NaOH solution. The obtained solution was washed thoroughly with deionized water until the pH became to 7 and then dried at 120°C for 12 h.

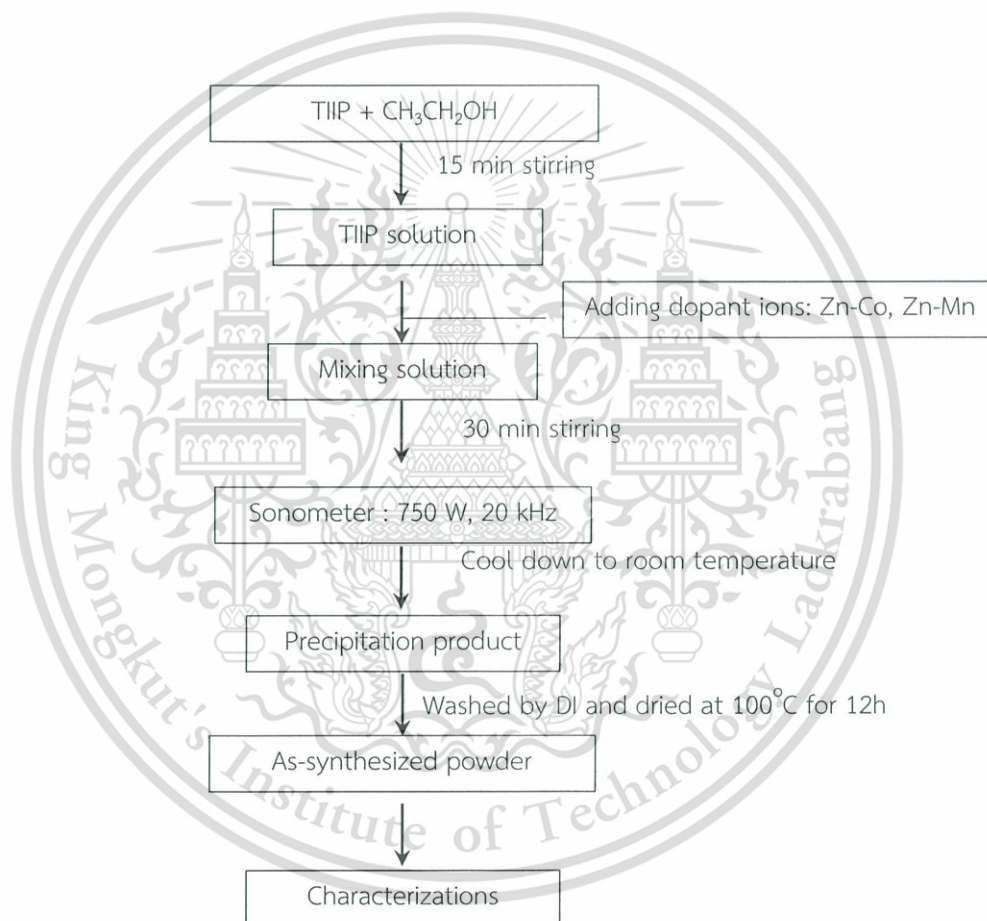


Figure 3.2 Schematic of preparation for co-doped TiO<sub>2</sub> nanoparticles

### 3.2.3 Synthesis of ZnTiO<sub>3</sub> nanoparticles

The preparation process chart of ZnTiO<sub>3</sub> is shown in figure 3.3. The ratio amount of TIIP and Zinc acetate stoichiometric is designated to 1:1. First, zinc acetate was dissolved in the absolute ethanol under magnetic stirring for 15 min. The oxalic acid was separately dissolved in absolute ethanol and slowly added into the zinc acetate solution to obtain a white cloudy like solution. Then, TIIP was dropped in the white cloudy suspension, immediately followed by DI water, and then the solution was kept under magnetic stirring for 30 min. The final mixing solution was irradiated with high ultrasonic sonometer (750 W, 20 kHz) for 30 min at room temperature to achieve the precipitate product. After that the green powders were washed by DI water and dried at 100°C for 12h. The green powders were calcined between 500°C and 900°C for 2 h.

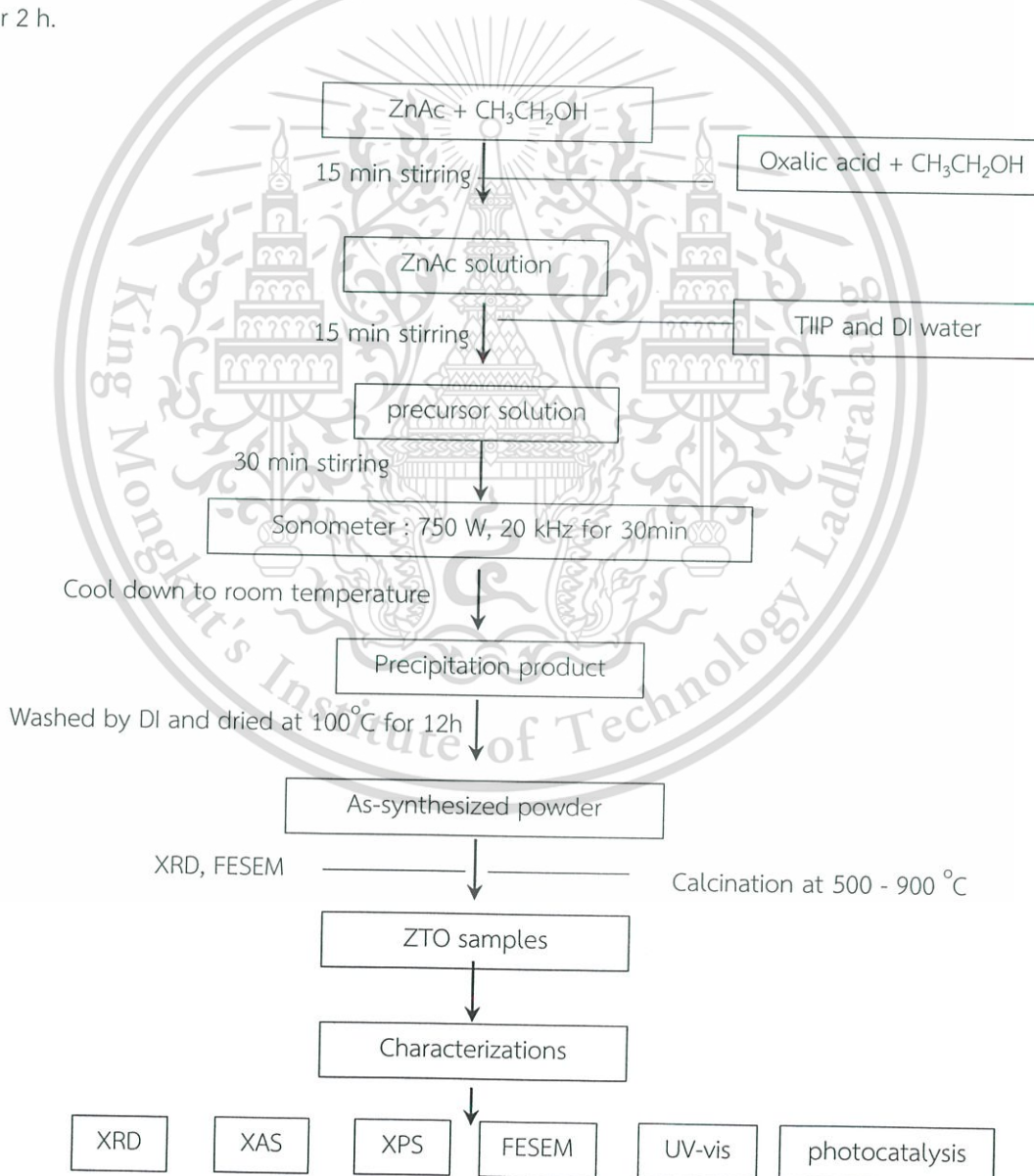


Figure 3.3 Schematic of preparation for ZnTiO<sub>3</sub> nanoparticles

This material is reserved for educational use only, not allowed for commercial use.

Forbidden to modify the content, and cite the document when use.

### 3.2.4 Synthesis of ZnTiO<sub>3</sub> doped with Co and Mn

The preparation process chart of ZnTiO<sub>3</sub> doped with Co and Mn is shown in figure 3.4. A stoichiometric amount of TIIP and zinc acetate was designated as a ratio 1:1. First, zinc acetate was dissolved in the absolute ethanol under magnetic stirring for 15 min. The oxalic acid was separately dissolved in absolute ethanol and slowly added into the zinc acetate solution to obtain a white cloudy like solution. TIIP was dropped in the white cloudy suspension, immediately followed by DI water under magnetic stirring. Cobalt nitrate (5, 7 and 10 mol%) or manganese nitrate (3, 5 and 7 mol%) were weighed and loaded into the mixing solution under continuous magnetic stirring for 1 h. after that the final mixing solution was irradiated with high ultrasonic sonometer (750 W, 20 kHz) for 30 min at room temperature to achieve the precipitate product. The green powders were washed by DI water and dried at 100°C for 12h. Finally, the green powders were calcined between 700°C for 2 h.

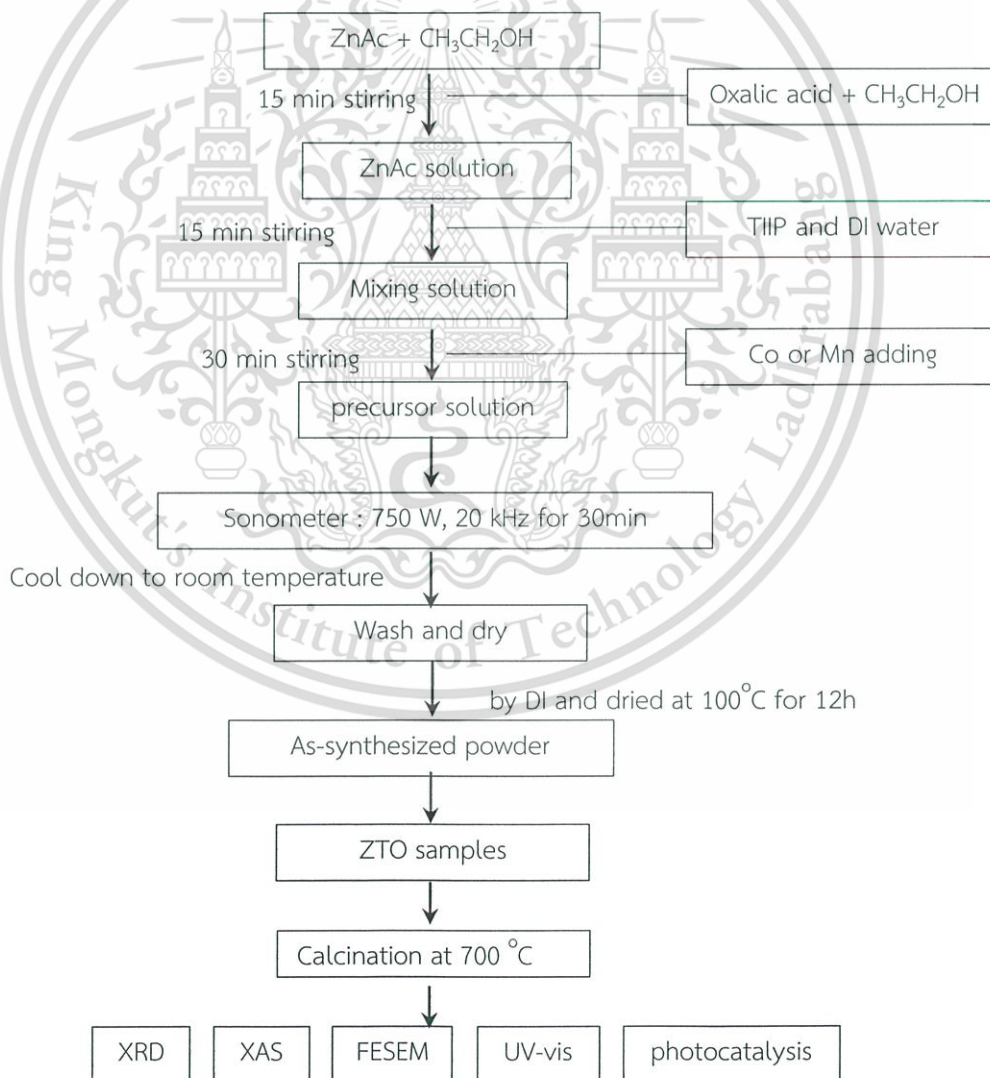


Figure 3.4 Schematic of preparation for ZnTiO<sub>3</sub> nanoparticles doped with Co and Mn.

### 3.3 Characterization methods

#### 3.3.1 X-ray diffraction (XRD)

The crystal structure and phase identification were investigated by XRD technique (PANalytical X'Pert Pro MPD model pw 3040/60) by using  $\text{CuK}\alpha$  irradiation ( $\lambda = 1.54 \text{ \AA}$ ). The broad scan analysis was typically conducted within the  $2\theta$  range of  $20 - 80^\circ$ . The strongest of XRD peak was used to determine the crystalline size ( $D$ ) of samples by using Debye-Sherrer's formula:

$$D = \frac{0.9\lambda}{b\cos\theta} \quad (3.1)$$

Where  $\lambda$  is wavelength of X-ray irradiation ( $\text{CuK}\alpha = 1.54 \text{ \AA}$ ),  $\theta$  is diffraction angle, and  $b$  is the full width at half maximum (FWHM) of the strongest peak.

The  $d$  spacing can be expressed through cell parameters and the Miller index by the following equation:

$$\frac{1}{d^2} = \frac{h^2}{a^2} + \frac{k^2}{b^2} + \frac{l^2}{c^2} \quad (3.2)$$

where,  $d$  is the d-spacing;  $a$ ,  $b$ , and  $c$  are sides of the unit cell; and  $h$ ,  $k$  and  $l$  are the Miller indices, which are used to describe the lattice planes and directions in a crystal.

In the cubic systems, the d-spacing is related to the lattice parameter and the Miller indices by the following relation:

$$\frac{1}{d^2} = \frac{h^2+k^2+l^2}{a^2} \quad (3.3)$$

On the other hand, the non-cubic systems such as hexagonal system, the Miller indices can be calculated by using the lattice parameter from Bravais lattice:

$$\frac{1}{d^2} = \frac{4}{3} \frac{h^2+hk+l^2}{a^2} + \frac{l^2}{c^2} \quad (3.4)$$

The percentage of hexagonal phase of prepared samples were calculated from the ratio of area for the hexagonal phase peak to the area of all peaks using the equation of

$$H\% = (A_h/A_{All}) \times 100 \quad (3.5)$$

This material is reserved for educational use only, not allowed for commercial use.

Forbidden to modify the content, and cite the document when use.

Where  $H\%$  is percentage of hexagonal phase (%),  $A_h$  is area of hexagonal phase peak and  $A_{all}$  is area of all peaks.

### 3.3.2 X-ray Absorption Spectroscopy

The X-ray absorption spectroscopy (XAS) technique was used to identify the chemical state and local structure of all samples. XAS measurement of Ti K-edge (4966 eV) Zn K-edge (9659 eV) in transmission mode and Co K-edge (7709 eV) and Mn K-edge (6539 eV) in fluorescent mode were recorded at room temperature using Ge(220) double crystal monochromater at Beamline-8, Synchrotron Light Research Institute (SLRI), Nakhonratchasima, Thailand. Reference standards of transition metal ions such as  $TiO_2$ ,  $CoO$ ,  $MnO$ ,  $Mn_2O_3$ ,  $MnO_2$  and  $ZnO$  which known decisive oxidation state were measured as well for comparison purpose. The recorded spectra were analyzed by using the ATHENA and ARTEMIS software packages.

### 3.3.3 UV-visible spectroscopy

The optical properties of prepared samples were characterized by UV/vis/NIR spectroscopy: PerkinElmer model LAMBDA 950 in reflection mode from 250 – 900 nm. The diffuse reflectance measurements are usually analyzed on the basis of the Kubelka-Munk equation:

$$F(R)_{\infty} = \frac{k}{s} = \frac{(1-R)^2}{2R} \quad (3.6)$$

where  $k$  and  $s$  are absorption and scattering coefficients respectively, and  $R$  is the reflectance at the front face.  $F(R)_{\infty}$  is termed the Kubelka-Munk function and is proportional to the concentration of the adsorbate molecules.

The energy band gap values were estimated following the Kubelka-Munk method combined with Tuac equation:

$$\alpha h\nu = A(h\nu - E_g)^m \quad (3.7)$$

Note that,  $\alpha$  is absorption coefficient,  $h\nu$  is photon energy,  $A$  is an energy dependent constant and  $m$  is integer depending on the nature of electronic transition: 2 for a direct allowed transition, 1/2 for indirect allowed transition, 3/2 for direct forbidden transition.

### 3.3.4 Field Emission Scanning Electron Microscope

Morphology and particles size of as-synthesis and calcined powders were observed by field emission electron microscope; Hitachi S-4700, measured at Thai Microelectronic Center (TMEC).

### 3.3.5 Photocatalytic system

Photocatalytic behavior of all prepared samples were investigated by using Rhodamine B (RhB) dye as a model for degradation under ultraviolet (UV) and visible light irradiation. The schematic for photocatalytic system in both UV and visible light irradiation are represented in figure 3.5. The conditions used: 0.08 mg of catalyst was added to 100 mL of dye solution with 0.01mmol of dye concentration. Before irradiation, the suspensions were stirred for 20 minute in the dark system to ensure the establishment of adsorption/desorption between dye and catalyst. The photocatalytic activity was carried out at room temperature using UV and LED lamp. The photocatalytic performance was evaluated by RhB decolorization by checking the absorbance at 554 nm, respectively, through a UV-Vis spectrometer. The decolorization efficiency of catalyst was calculated as:

$$C/C_0 = (A_0 - A)/A_0 = (C_0 - C)/C_0 \quad (3.8)$$

where  $A_0$ ,  $A$ ,  $C_0$  and  $C$  are initial absorbance, absorbance after irradiation at various time interval, initial concentration of solutions, and concentration of dye after irradiation at various time interval, respectively.

In order to find out the efficiency of the photocatalytic reaction, pseudo first order kinetic for photocatalytic oxidation was conducted by rate constant calculation followed the equation;

$$\ln(C/C_0) = kt \quad (3.9)$$

Where  $k$  is apparent first order rate constant of photodegradation,  $C$  and  $C_0$  are concentration of dye during reaction and initial concentration, respectively and  $t$  is the reaction time.

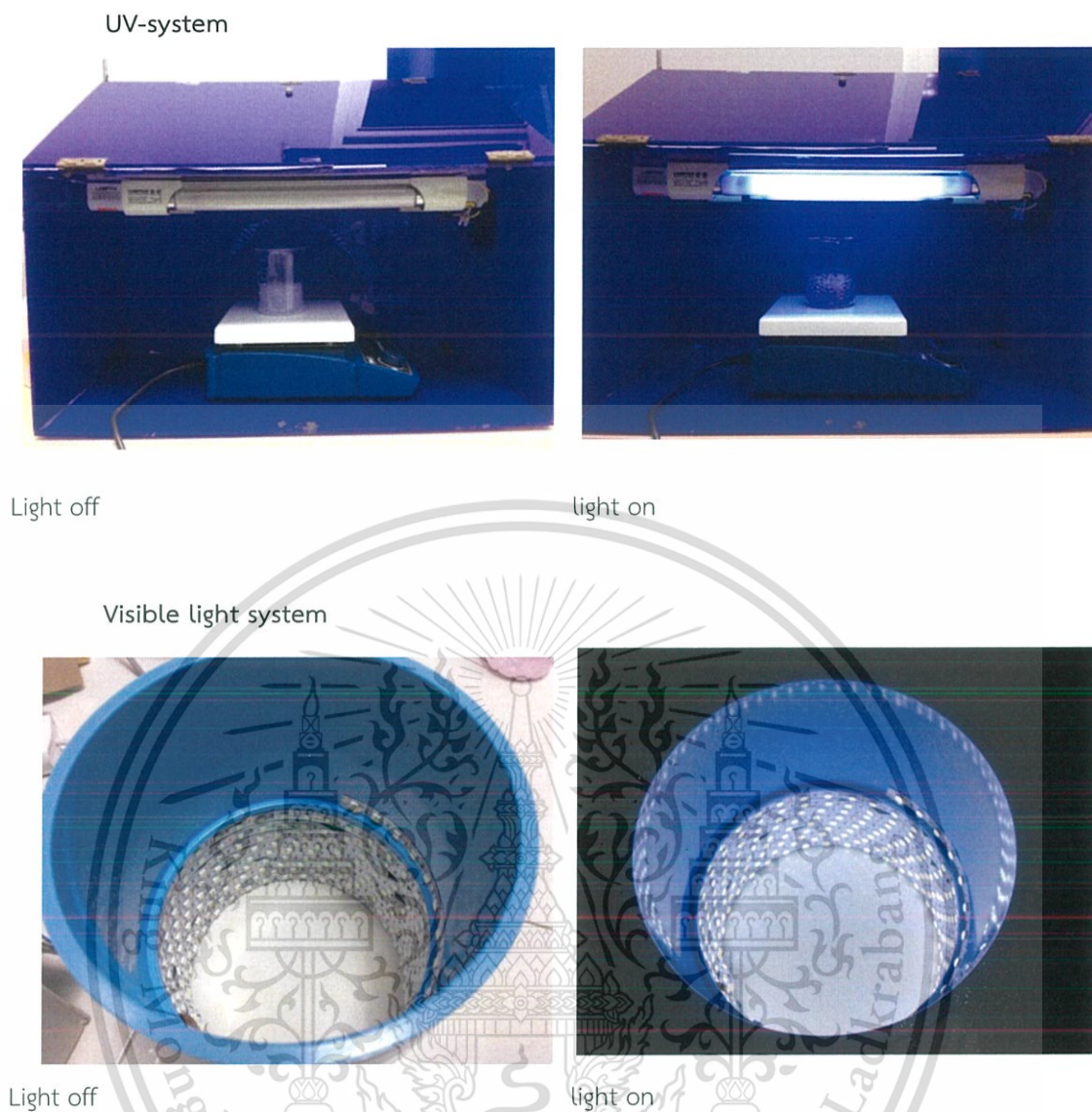


Figure 3.5 Schematic of photocatalytic system in UV- and visible light illumination.

## CHAPTER 4

### RESULTS AND DISCUSSION

#### 4.1 Zn-doped TiO<sub>2</sub> nanoparticles

##### 4.1.1 Structural phase

The structural phase of as-synthesized and calcined Zn-doped TiO<sub>2</sub> powders at different temperatures was investigated by X-ray diffraction and the results are shown in Figure 4.1. The XRD patterns of the as-synthesized powders present a small peak at around  $2\theta = 25.2^\circ$ ,  $48.2^\circ$  and  $62.5^\circ$ , which corresponded to (101), (200) and (204) plane of the anatase TiO<sub>2</sub> phase, respectively. This result indicated that the as-sonochemically synthesized fine-nanopowders of TiO<sub>2</sub> could be fabricated by single-step sonochemical process using the sonication time of 30 min without post annealing process. The formation mechanism of crystalline phase Zn-doped TiO<sub>2</sub> by the sonochemical process could be initiated by cavitation effect during high frequency ultrasound wave radiation via sudden collision forced by intense ultrasound energy. This collision is able to swiftly raise localized dominantly high temperature region, which speeds up the condensation of hydroxyl or intermediate hydroxide group to generate the nucleation of fine Zn-doped TiO<sub>2</sub> nanoparticles. In case of the samples calcined at 450–550°C, it is observed that the samples possess pronounce characteristic diffraction peaks with increasing peak intensity indicating the amelioration of crystallinity and anatase phase by calcinations process. As the calcination temperature elevated to 600°C, the rutile phase of TiO<sub>2</sub> and the secondary phase of ZnO were noticeably observed. This feature occurs because the anatase TiO<sub>2</sub> phase transforms into the rutile TiO<sub>2</sub> phase at this specific temperature vicinity [89]. In addition, the formation of ZnO phase was also initiated as the temperature rose to 600°C. This formation may be attributed to sufficient supplied thermal energy into the matrix that can induce the bonding between substituted Zn ion and surrounding oxygen atoms, leading to the formation of separated phase of ZnO. The crystallite size (*D*) of crystalline anatase and rutile phase was estimated by Scherrer's equation. The average crystallite size of Zn-doped TiO<sub>2</sub> nanoparticles slightly increases with increasing calcinations temperature. This result indicates that the calcinations temperature significantly affects the crystal of Zn-doped TiO<sub>2</sub> nanopowders.

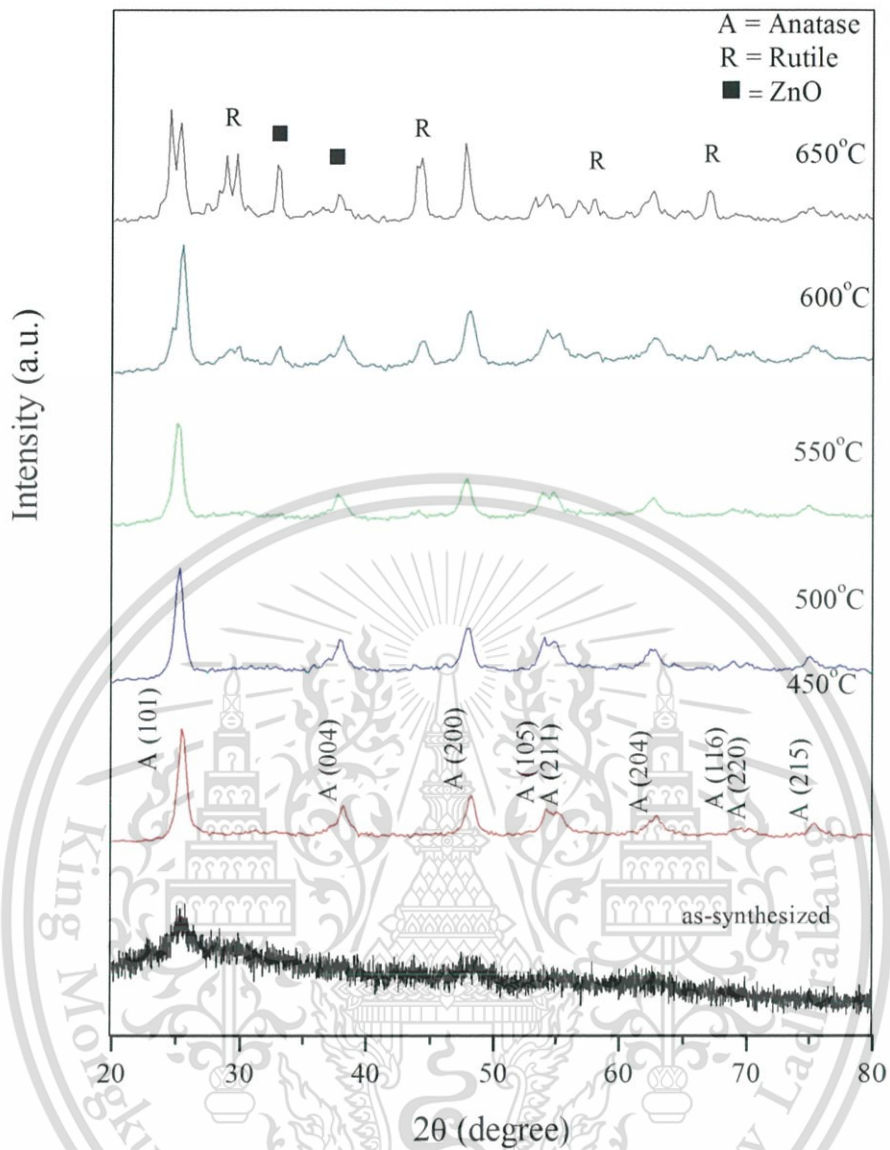


Figure 4.1 XRD patterns of as-synthesized and after-calcined of Zn-doped TiO<sub>2</sub> nanoparticles.

### 4.1.2 Morphology

Figure 4.2 shows the morphologies of as-synthesized Zn-doped TiO<sub>2</sub> nanopowders by transmission electron microscopy (TEM) technique. The TEM image clearly shows the finenanopowders with spherical shape and well-distribution. The average particle size is around 15 nm. The result confirms that the highly intense of ultrasound wave provided during the sonochemistry process can establish the uniform-fine Zn-doped TiO<sub>2</sub> nanopowder.

### 4.1.3 Optical properties

To study the optical properties of Zn-doped TiO<sub>2</sub> nanoparticles, the UV-VISdiffuse reflectance spectra were measured in a wavelength range of 200-700 nm, as shown in figure 4.3. The optical absorption of all samples shows that the absorption starts at about 370 nm, indicating the semiconducting feature with direct band gap of the samples. The UV-VIS reflectance of doped samples significantly shifts to a longer wavelength when comparing to pure TiO<sub>2</sub>. It could be deduced that the incorporation of low content of Zn ion into TiO<sub>2</sub> may significantly lower the effective optical band gap of TiO<sub>2</sub> by extending its absorption band to visible region that can enhance its performance in solar energy harvesting. The good substitution of Zn ions may create the defect sites and corresponding defect band tail between valence band and conduction band of TiO<sub>2</sub> that consequently reduces its effective band gap. The optical band gap energy ( $E_g$ ) was determined from reflectance spectra [90]. It is noticed that the correlated band gap energy of the sample tends to increase with increasing calcined temperature, i.e. at values of 2.82-3.02 eV for the sample calcined at 450-700°C, respectively. This feature may be originated from the fact that, at elevated temperature, the separated phase of ZnO takes place and the sample becomes intermixture of TiO<sub>2</sub> and ZnO that would cause the alternation the optical band gap of TiO<sub>2</sub>. The other possibility for this increment in optical band gap with increasing temperature is the anatase-to-rutile mixed phase of TiO<sub>2</sub> [91].

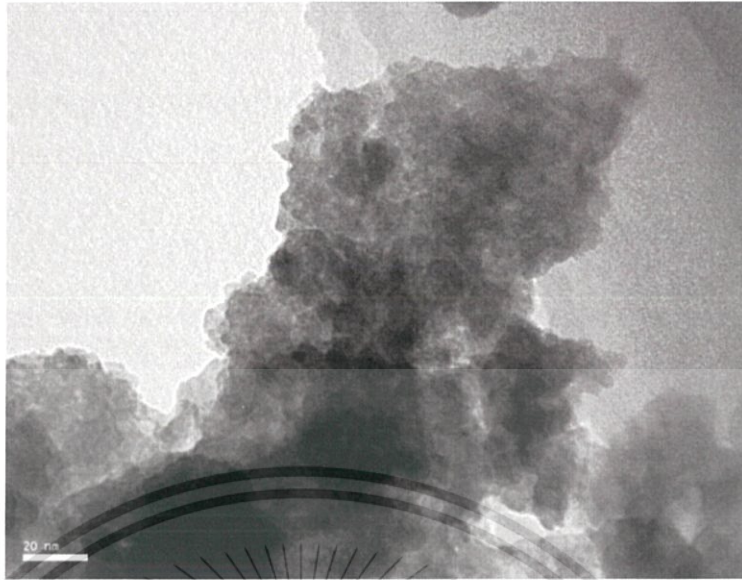


Figure 4.2 TEM image of as-synthesized Zn-doped  $\text{TiO}_2$  nanopowder synthesized by sonochemical method with sonication for 30 min.

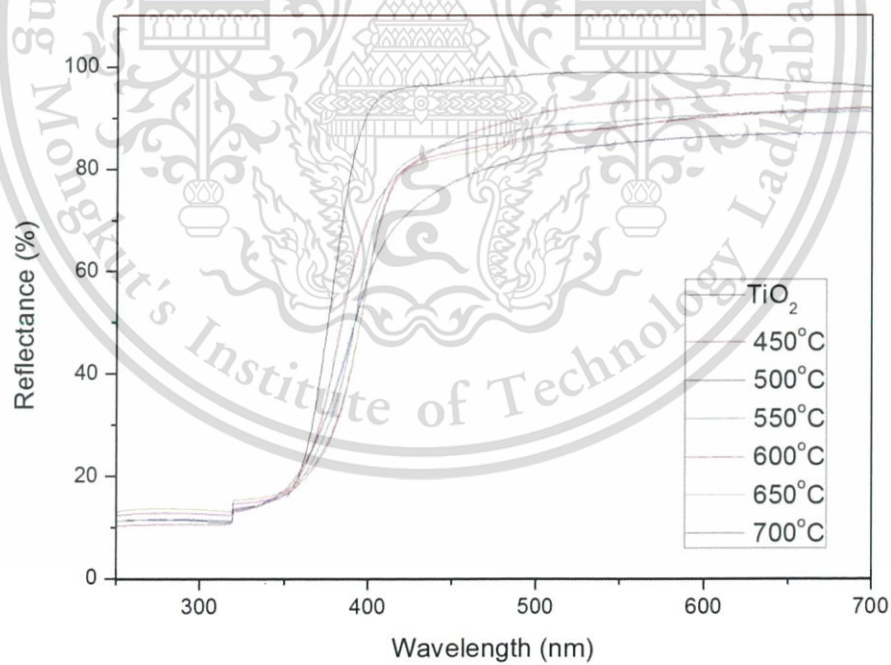


Figure 4.3 UV-VIS diffuse reflectance spectra of Zn-doped  $\text{TiO}_2$  nanoparticles calcined at various temperatures.

This material is reserved for educational use only, not allowed for commercial use.

Forbidden to modify the content, and cite the document when use.

Table 4.1 Crystalline size of Zn-doped TiO<sub>2</sub> samples.

Calcined temperature(°C)	Crystalline size (nm)
450	7.1
500	7.5
550	7.8
600	8.9
650	9.2
700	9.8



This material is reserved for educational use only, not allowed for commercial use.

Forbidden to modify the content, and cite the document when use.

## 4.2 Zn-Mn and Zn-Co co-doped TiO<sub>2</sub> nanoparticles

### 4.2.1 Structural phase

Figure 4.4(a)-(b) show the XRD patterns of as-prepared singly-doped and co-doped TiO<sub>2</sub> nanopowders. XRD diffractograms of all prepared samples clearly exhibit the formation of anatase TiO<sub>2</sub> phase without secondary phases of any metal oxides. In addition, broad peaks of diffracted pattern indicated low degree of crystallinity. Increase in co-dopant content results in slight shift of main (101) reflection to lower angle indicating the evidence of unit cell expansion. This expansion would originate from the replacement of Ti<sup>4+</sup> (0.74Å) by the slightly larger ionic radius of Zn<sup>2+</sup> (0.88Å), Mn<sup>2+</sup> (0.81Å) and Co<sup>2+</sup> (0.70Å) ions [92]. It is suggested that sonochemical synthesis is a potential technique for preparing the co-doped titania as single-step method at room temperature. The effect of ultrasonic irradiation on preparation process can be described by the localized spots and pressure generated from acoustic cavitation during sonication, which lead to the increase of the dispersion ability of dopant ion into the TiO<sub>2</sub> lattice. The possible sonochemical formation mechanism of nanocrystalline TiO<sub>2</sub>-metal is shown in figure 4.5 which as follows: The hydrolytic species of titanium precursor in solvent solution is condensed to form a large number of tiny nuclei, which aggregate to form larger cluster. Ultrasonic wave irradiation can generate many local hot spots within the gel, and the crystal structural unit is formed near the hot spots with decrease in the gel nuclei, which leads to the formation of nanocrystal particles.

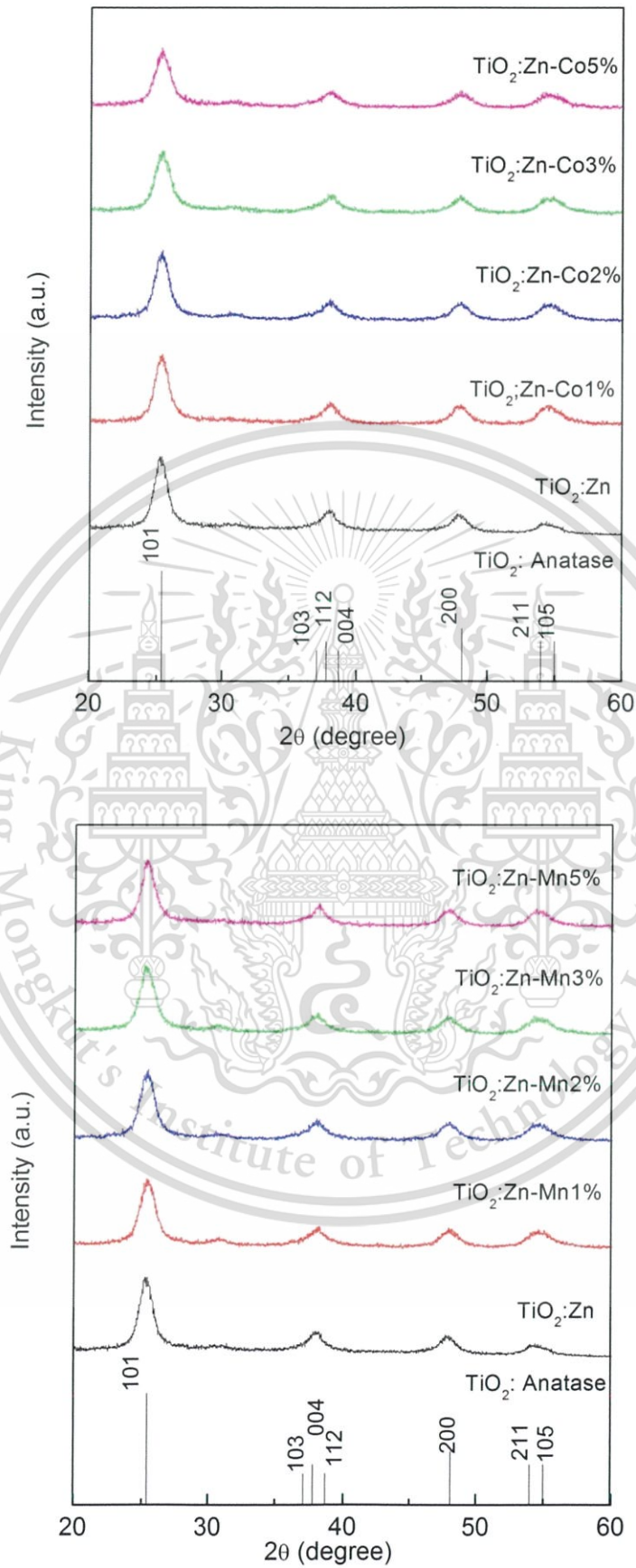


Figure 4.4 Powder XRD patterns of Zn-doped  $\text{TiO}_2$ , Co-Zn and Mn-Zn co-doped  $\text{TiO}_2$  nanoparticles.  
 This material is reserved for educational use only, not allowed for commercial use.

Forbidden to modify the content, and cite the document when use.

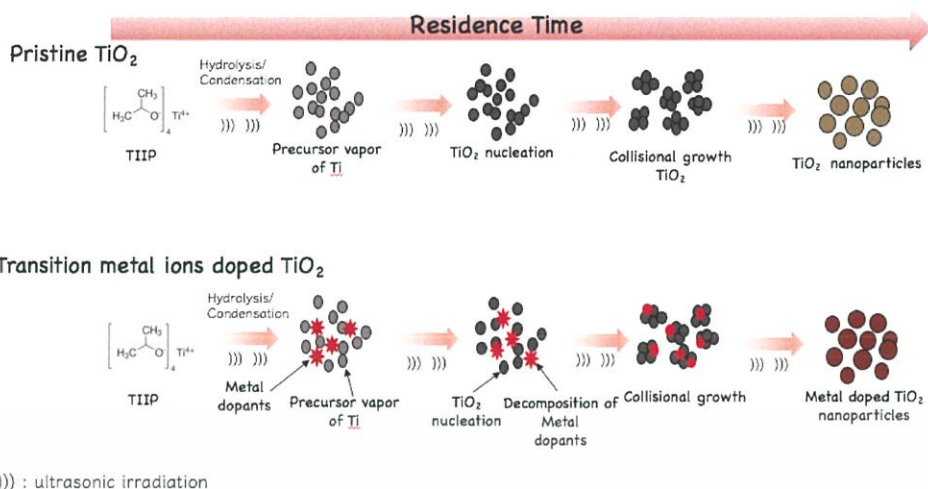


Figure 4.5 Schematic for the possible formation mechanisms of nanoparticles by sonication process: Top represents TiO<sub>2</sub> formation mechanism, Bottom is for low transition metal ions dopant concentration.

#### 4.2.2 Chemical composition and local structure

X-ray absorption spectroscopy including both X-ray absorption near edge structure (XANES) technique and extended X-ray absorption fine structure (EXAFS) were used to scrutinize details of chemical composition and local structure of as-prepared samples. The normalized XANES spectra of singly-doped, co-doped TiO<sub>2</sub> and their reference standards are shown in figure 4.6 and 4.7. As displayed in figure 4.6(a) and 4.7(a), the Ti K-edge of TiO<sub>2</sub>, singly-doped and co-doped TiO<sub>2</sub> samples clearly show the pre-edge spectra of A<sub>1</sub>, A<sub>2</sub>, A<sub>3</sub> and B peaks which correspond to the transition of core electron to Ti 3d4p4s hybridized states. The first pre-edge peak of A<sub>1</sub> arises from the t<sub>2g</sub> band-like state, while A<sub>2</sub> and A<sub>3</sub> peaks correlate to the e<sub>g</sub> band-like state. The t<sub>2g</sub> and e<sub>g</sub> states demonstrate the component of crystal field split Ti3d atomic orbital which is shifted relatively to each other in energy as a result of the octahedral oxygen surrounding of Ti [93-94]. However, the observation in pre-edge peak of co-doped samples exhibits the broadening of A<sub>1</sub> peak comparing to TiO<sub>2</sub> standard that may due to the lower crystallinity of as-synthesized samples. As the concentration of dopant increases, the contribution of A<sub>2</sub> and A<sub>3</sub> peak region is involved because of the larger fraction of Ti atom at the surface, suggesting the increasing distortion in octahedral TiO<sub>6</sub> unit. Meanwhile, the B peak has a predominant Ti4p character hybridized with Ti4s and O2s orbital [28]. The C peak represents transition of core electron toward O2p state that is hybridized with Ti4p state. The D peak is associated with the higher lying p atomic orbital [95]. The slight change in the pre-edge and post-edge feature of co-doped sample can be essentially associated to the distortion in the

octahedral  $\text{TiO}_2$ . These results suggest that co-dopant ions are able to substitutionally incorporate in Ti lattice.

The normalized XANES spectra for co-doped samples and ZnO for Zn K-edge for Co-Zn doped  $\text{TiO}_2$  and Mn-Zn doped  $\text{TiO}_2$  are shown in figure 4.6(b) and 4.7(b), respectively. The feature of all spectra shows the strong absorption edge in a range of 9660-9670 eV with no pre-edge region because the 3d orbital in  $\text{Zn}^{2+}$  ion is fully occupied by electrons. Therefore, only the electronic transition from 1s core level promoted to the higher unoccupied state exists, which is presented in  $\sim 9660\text{eV}$ . The energy absorption spectra of all samples correspond to the  $\text{Zn}^{2+}$  of ZnO reference standard. In addition, the post-edge of Zn K-XANES spectra demonstrates significantly different feature from ZnO spectrum implying that the  $\text{Zn}^{2+}$  ion in the prepared samples is not totally tetrahedral coordinated with O atom [96-97].

For the Co K-edge XANES spectra of co-doped samples, the spectra of all as-prepared samples reveal the main absorption energy at  $\sim 7710$  eV corresponding to the transition to higher energy levels as seen in figure 4.6(c). The strong absorption edge of Co-doped sample corresponds to the CoO reference standard. It can be concluded that the Co-Zn doped  $\text{TiO}_2$  contain Co  $2+$  of oxidation state. In case of Mn K-edge measurement, the normalized spectra of prepared samples and their reference standard are shown in figure 4.7(c). The corresponding spectra clearly show that the absorption edges of reference standard of  $\text{MnO}$ ,  $\text{Mn}_2\text{O}_3$  and  $\text{MnO}_4$  are located at 9644, 9650 and 9690 eV, respectively. The vigorous absorption edge of Mn-Zn co-doping is in the range of 9651-9670 eV, suggesting that the samples are composed of mixing oxidation states. The linear combination fitting (LCF) was conducted to identify the oxidation state using  $\text{MnO}$ ,  $\text{Mn}_2\text{O}_3$  and  $\text{MnO}_2$  as reference models. The best LCF reveals the reduction of  $\text{Mn}^{4+}$  into  $\text{Mn}^{3+}$  with increasing Mn-doping concentration as summarized in table 4.2.

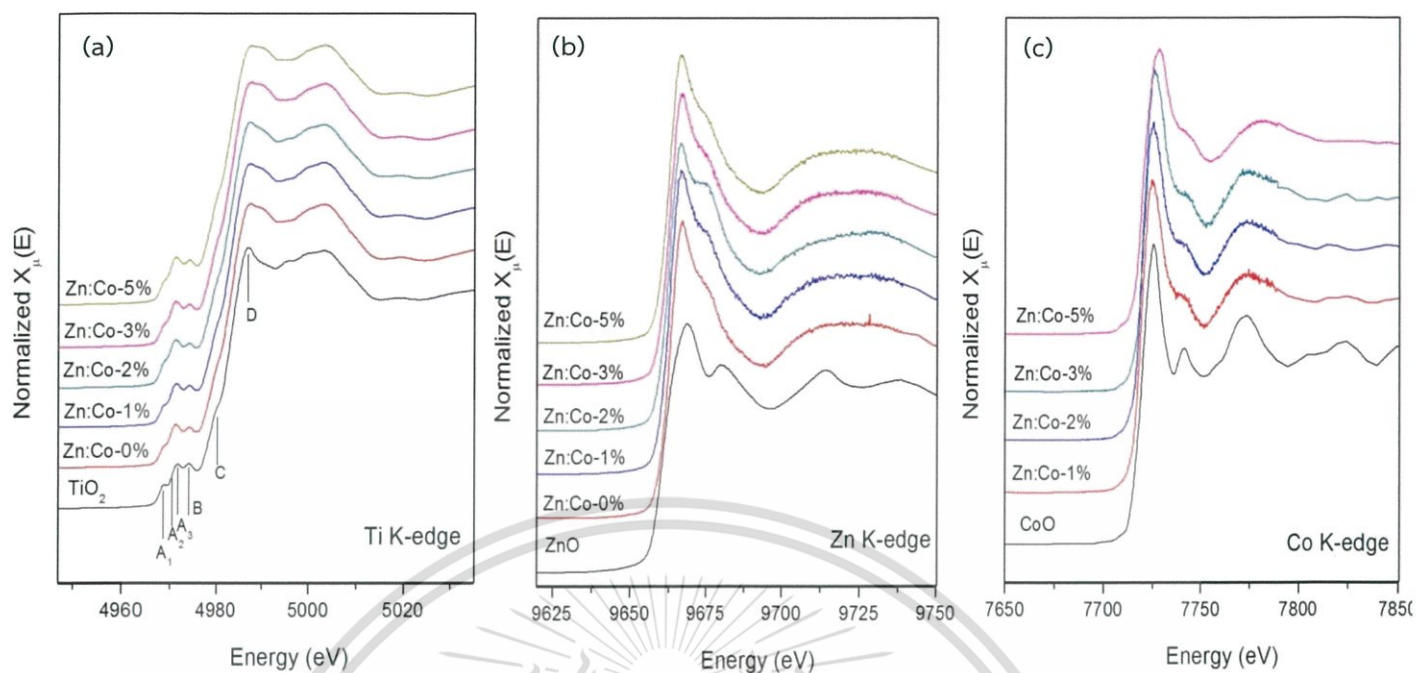


Figure 4.6 Normalized XANES spectra of Co-Zn co-doped  $\text{TiO}_2$  with (a) Ti K-edge, (b) Zn K-edge and (c) Co K-edge.

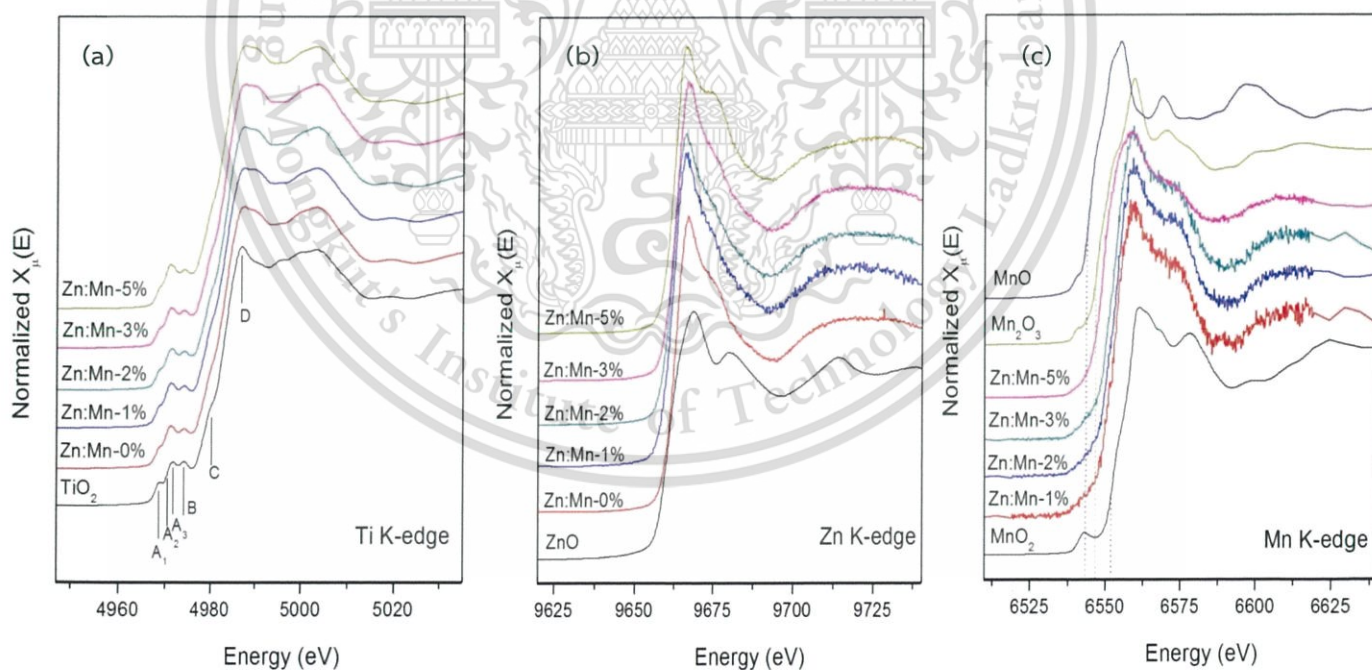


Figure 4.7 Normalized XANES spectra of Mn-Zn co-doped  $\text{TiO}_2$  with (a) Ti K-edge, (b) Zn K-edge and (c) Mn K-edge.

Table 4.2 Crystalline size, band gap energy and LCF of as-synthesized samples

sample	Eg (eV)	Component		
		MnO	Mn <sub>2</sub> O <sub>3</sub>	MnO <sub>2</sub>
TiO <sub>2</sub> :Zn	3.01	-	-	-
TiO <sub>2</sub> :Zn-Co1%	2.78	-	-	-
TiO <sub>2</sub> :Zn-Co2%	2.75	-	-	-
TiO <sub>2</sub> :Zn-Co3%	2.72	-	-	-
TiO <sub>2</sub> :Zn-Co5%	2.68	-	-	-
TiO <sub>2</sub> :Zn-Mn1%	2.60	0.00	0.74	0.26
TiO <sub>2</sub> :Zn-Mn2%	2.38	0.00	0.76	0.24
TiO <sub>2</sub> :Zn-Mn3%	2.30	0.00	0.85	0.15
TiO <sub>2</sub> :Zn-Mn5%	2.24	0.00	0.98	0.02

#### 4.2.4 Morphology

The SEM micrographs of singly-doped and co-doped samples are displayed in figure 4.8-4.9. As shown in figure 4.8(a), singly-doped TiO<sub>2</sub> is spherical in shape with uniform distribution. For the 3%Co- and 3% Mn-co-doped TiO<sub>2</sub> as observed in figure 4.8 (b) and (c), more agglomeration is observed. However, the micrograph exhibits the average particle size that is less than 10nm, indicating larger specific surface area which is suitable for photocatalytic activity.

#### 4.2.5 Optical properties

The diffuse reflectance spectra (DRS) of pure TiO<sub>2</sub>, singly-doped and co-doped samples are shown in figure 4.10. For the singly-doped samples, extended visible light absorption is observed comparing to pure TiO<sub>2</sub>. Furthermore, the greater absorption in visible region is noticed in the co-doped samples. It is suggested that increasing co-dopant concentration could result in the reduction of band gap energy and the enhancement in visible light harvesting of TiO<sub>2</sub>. This feature would be correlated to the incorporation of dopant ions in host lattice that could generate new electronic states in the TiO<sub>2</sub> band gap. Hence the distance of charge transfers between d electron of the dopant ion and the conduction or valence band is narrowed, leading to the increase in visible light response of the material. Moreover, the different valence states of dopants including Co<sup>2+</sup>, Mn<sup>3+</sup> and Zn<sup>2+</sup> from the host matrix Ti<sup>4+</sup> may induce the substantial generation of oxygen deficiencies. In addition, the DRS spectra of doped samples possess the shoulder peak with corresponding wavelength lower than 400 nm that should correspond to the photo-induced charge transfer from the valence band formed by 2p orbital of oxide anions to the conduction band formed by 3d<sub>t<sub>2g</sub></sub> orbital of Ti<sup>4+</sup> [98]. Furthermore, the broader peak observed around 500-650 nm may be attributed to 2+ oxidation state of dopant/Ti<sup>4+</sup> charge-

This material is reserved for educational use only, not allowed for commercial use.

transfer interaction. The band gap energies of all samples were calculated from the DRS spectra using Kubelka-Munk equation. It is obviously noticed that the incorporation of dual dopants significantly affects to the decrease of band gap energy of the host  $\text{TiO}_2$  as shown in table 4.2.



This material is reserved for educational use only, not allowed for commercial use.

Forbidden to modify the content, and cite the document when use.

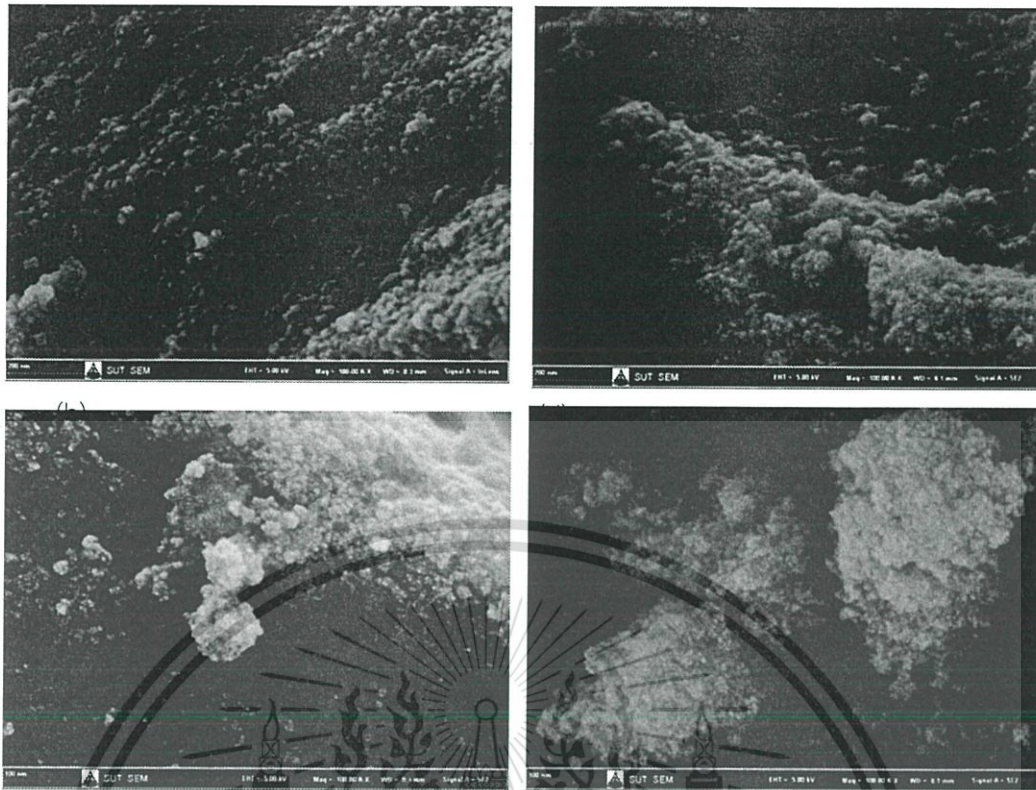


Figure 4.8 SEM images of co-doped  $\text{TiO}_2$  nanoparticles with (a)  $\text{TiO}_2$ , (b)  $\text{TiO}_2\text{:Zn-1\%Co}$ , (c)  $\text{TiO}_2\text{:Zn-3\%Co}$  and (d)  $\text{TiO}_2\text{:Zn-5\%Co}$ .

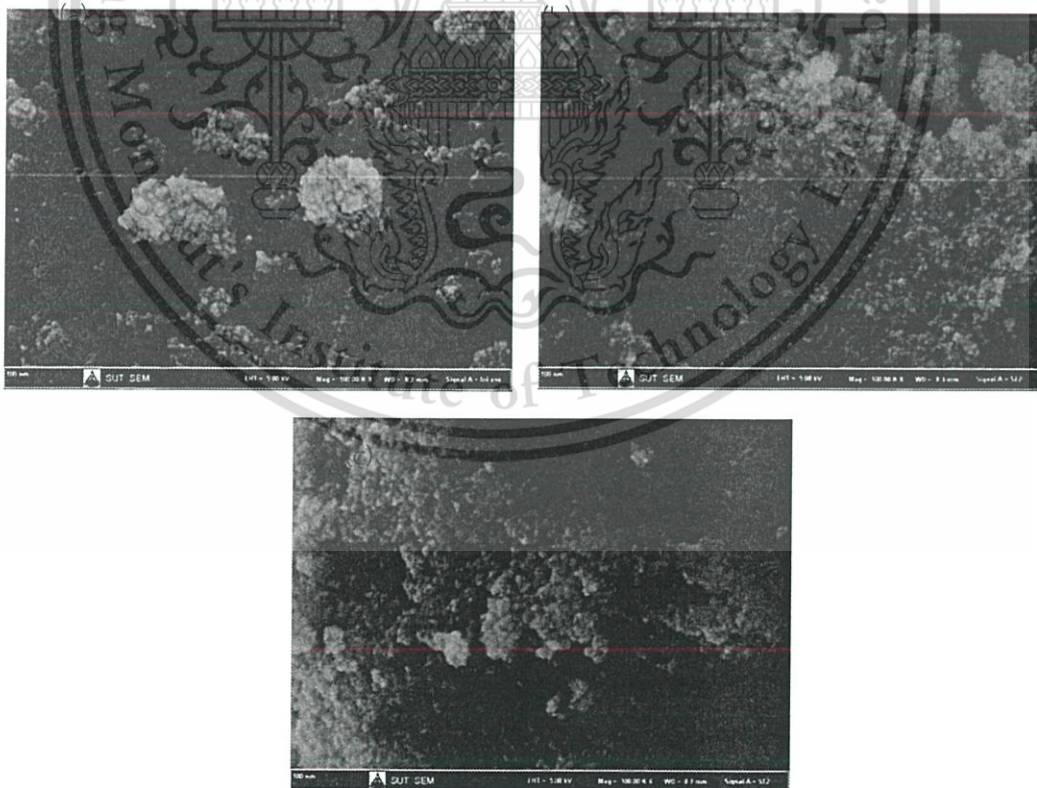


Figure 4.9 SEM images of co-doped  $\text{TiO}_2$  nanoparticles with (a)  $\text{TiO}_2\text{: Zn-1\%Mn}$ , (b)  $\text{TiO}_2\text{:Zn-3\%Mn}$  and (c)  $\text{TiO}_2\text{:Zn-5\%Mn}$ .

This material is reserved for educational use only, not allowed for commercial use.

Forbidden to modify the content, and cite the document when use.

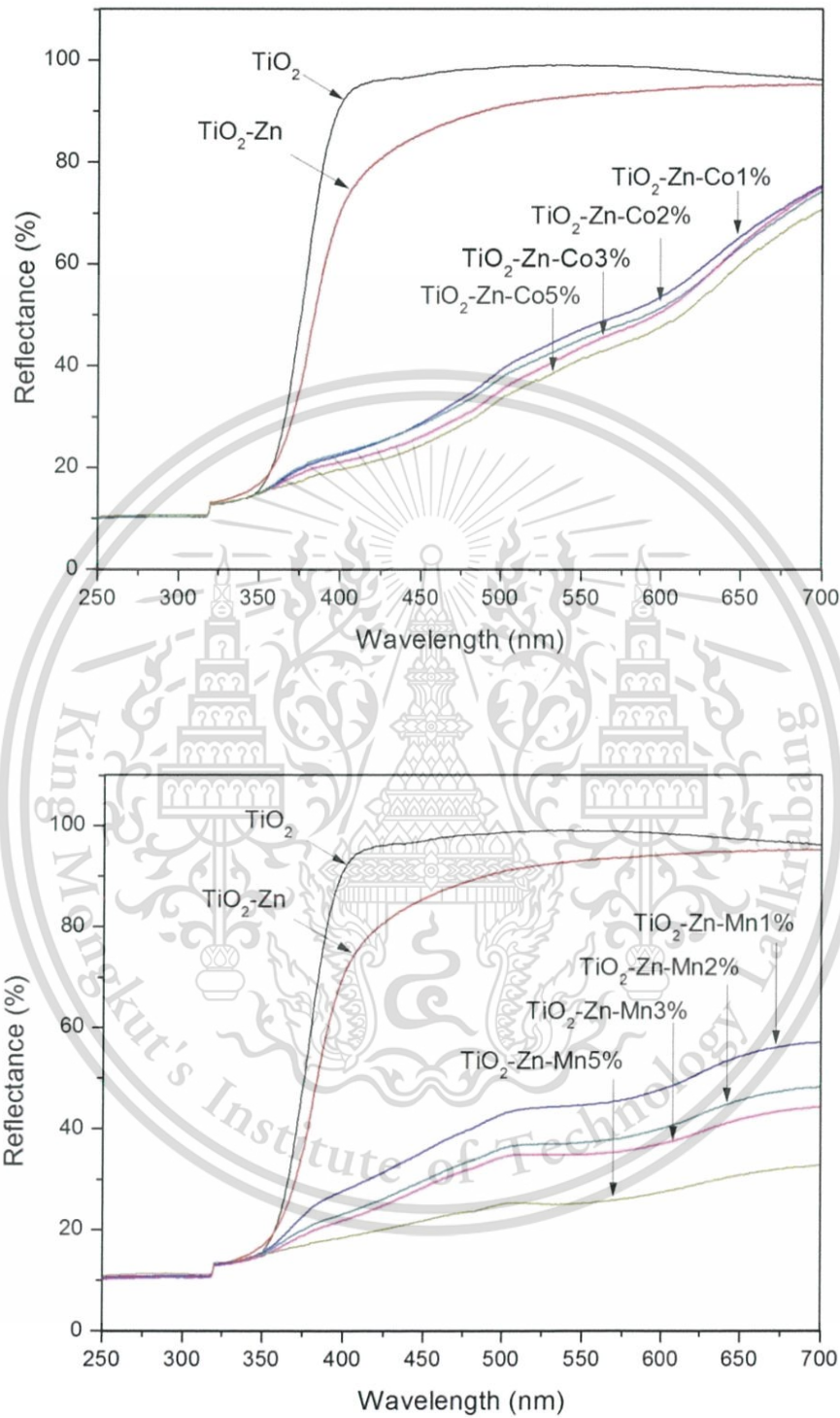


Figure 4.10 UV-VIS diffuse reflectance spectra of (a) Mn-Zn and (b) Mn-Zn co-doped  $\text{TiO}_2$ .

#### 4.2.6 Photocatalytic activity

The visible-light driven photocatalytic activities of the as-synthesized samples were evaluated through the photo-degradation of RhB dye solution. Figure 4.11 shows the RhB decolorization profiles by different catalysts under simulated visible irradiation. It is clearly observed that the dye solution was hardly degraded under visible light illuminated without the catalyst. Almost 40% of RhB degradation after 90 min was obtained in singly-doped sample. For the Co-Zn co-doped  $\text{TiO}_2$  (figure 4.11a), the superior degradation was found in the samples containing 3% of Co-content after 90 min of irradiation time while the sample with 1, 2 and 5% Co doping content exhibited 51, 73 and 71% of photo-decolorization, respectively. In case of Mn-doped samples as shown in Figure 4.12(a), highest removal of RhB was found in the 2% doped sample after 90 min of irradiated time. Whilst, 81%, 74% and 53% of dye degradation were obtained as the host material was doped with 1%, 3% and 5% Mn content, respectively. According to the results, all as-synthesized co-doped catalysts show higher degradation rates than singly-doped and bare  $\text{TiO}_2$ . In order to find out the decolorization rate of prepared samples, the first order kinetic degradation of Co-Zn and Mn-Zn doped  $\text{TiO}_2$  catalyst at each dopant concentration were calculated and shown in figure 4.11(b) and 4.12(b), respectively. The results show that the highest degradation rate constant of  $0.114 \text{ min}^{-1}$  was observed in 3%Co-doped sample. For the Mn-doping, the highest photodegradation rate was found in the 3%-Mn-doped sample with a value of  $0.0238 \text{ min}^{-1}$ . Obviously, a comparison in the plots of dye degradation shows that the concentration of as-prepared catalyst can indeed influence the degradation efficiency. The increase of dopant content to 3mol% (for Co-doping) and 2mol% (for Mn-doping) resulted in the increase in dye degradation. However, a slight decrease of dye decomposition was observed when the concentration of Co- and Mn-dopant was further increased to 5mol%, which might be attributed to the aggregation of the nanoparticle at high concentration, leading to the reduction of surface area of the catalyst. The degradation of RhB dye with respect to illuminated time in the presence of 2% Mn-co-doped catalyst is shown in fig. 4.11(c). It can be seen that the catalyst treated dye solution shows the noticeable decrease in optical absorption at 554nm of functional group of RhB with increasing irradiation time. Additionally, the absorption peak position is found to shift from 554 nm to 500 nm accompanying the alternation in color of RhB solution from pink to yellow as observed in figure 4.11(d). With further increase in irradiation time, almost 100% decrease in the peak intensity was obtained. This result indicates excellent photocatalytic performance of co-doped titania. The change in absorption spectra together with the color change from strong pink to yellow and colorless are corresponded to two processes of de-ethylation and destruction of conjugated dye structure [99-100]. Under the photocatalysis process, the ethyl groups are removed sequentially to form four intermediate groups, N,N,N'-triethylated Rhodamine, N,N,-diethylated Rhodamine, N-

This material is reserved for educational use only, not allowed for commercial use.

Forbidden to modify the content, and cite the document when use.

ethylate Rhodamine and Rhodamine, respectively. The destruction of the conjugated structures occurs concurrently, decomposing the rest to form the colorless dye solution [101]. Comparing between Co- and Mn- doping degradation efficiency, the results indicated that the Mn, Zn co-doped samples performed higher activity than Co, Zn co-doped sample. It may be described by two processes; the enhancement in visible light harvesting and greater hydroxyl radical from the conversion of  $Mn^{4+}$  to  $Mn^{3+}$  [102]. According to the photocatalytic behavior, the decomposition performance of co-doped sample is superior to the singly-doped and pure titania. This excellent degradation indicates that the Co-Zn and Mn-Zn co-doped  $TiO_2$  hold great promise for future application in organic pollutant removal.

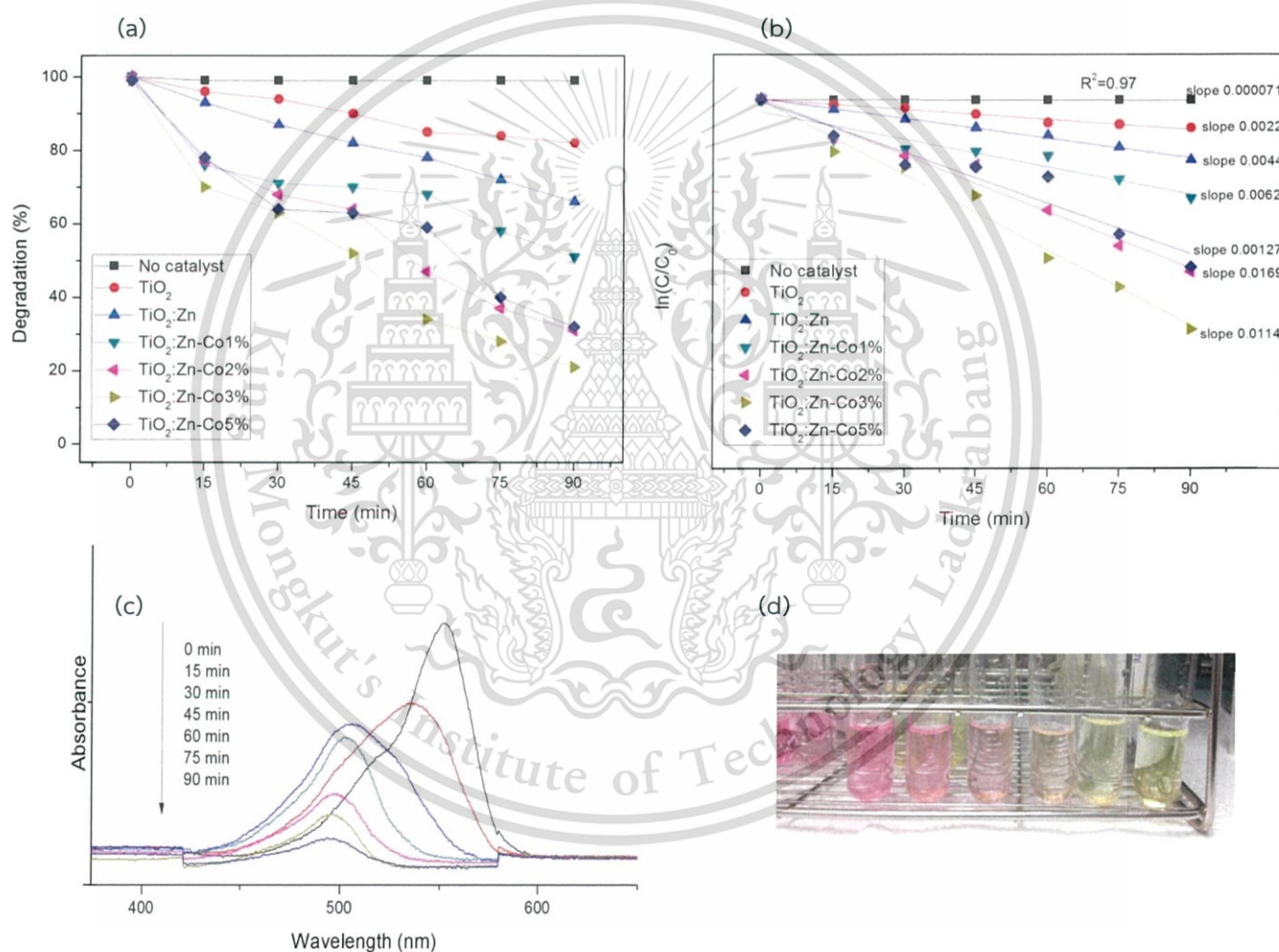


Figure 4.11 Photocatalytic degradation curve for different catalysts in the presence of RhB dye for Co-Zn co-doped  $TiO_2$  catalyst, (b) absorption kinetic of RhB over Co-Zn co-doped  $TiO_2$  catalyst (c) time independent variation of UV-vis spectra for RhB degradation of 2% Co-dopant and (d) Visual comparison of color fading in the degradation of RhB solution subsequent to being subjected to various degradation time for 0-90 min.

This material is reserved for educational use only, not allowed for commercial use.

Forbidden to modify the content, and cite the document when use.

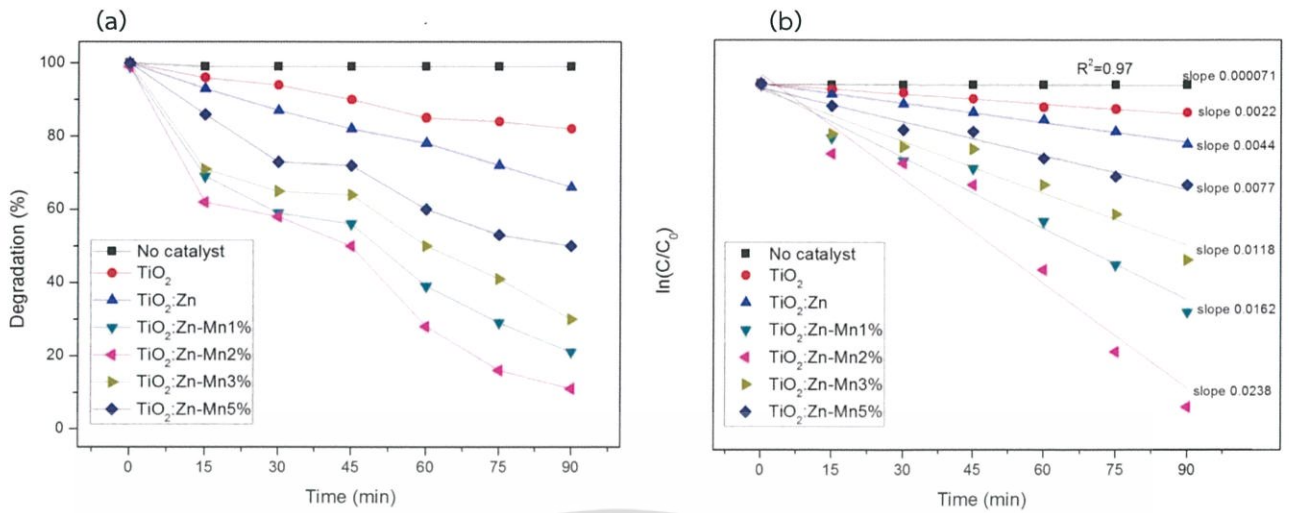


Figure 4.12 Photocatalytic degradation curve for different catalysts in the presence of RhB dye for Mn-Zn co-doped TiO<sub>2</sub> catalyst, (b) absorption kinetic of RhB over Mn-Zn co-doped TiO<sub>2</sub> catalyst and (c) Visual comparison of color fading in the degradation of RhB solution subsequent to being subjected to various degradation time for 0-90 min.

The feasible mechanism for the photocatalytic behavior of codoped catalysts may be described by the band gap structure of doubly-doped  $\text{TiO}_2$  as displayed in figure 4.13. As  $\text{TiO}_2$  has high energy band gap (3.2 eV), the direct excitation of electron from valance band (VB) to the conduction band (CB) in presence of visible light is not possible. On incorporation of Zn, Mn and Co ions into  $\text{TiO}_2$  lattice, the energy band gap of  $\text{TiO}_2$  decreases due to the formation of impurity levels below CB in the band gap, where electrons can transfer from VB of  $\text{TiO}_2$  to these energy levels. These electrons travel to surface and adsorbed by the  $\text{O}_2$  and produce the  $\cdot\text{O}_2$  ions, which can further converts to the strong redox species such as  $\text{H}_2\text{O}_2$  and  $\cdot\text{OH}$  ions [103-104]. These redox ions are responsible for the degradation of the surface adsorbed hazardous dye. In case of increasing transition metal co-doping ion, the density of new energy levels also increases, which ultimately enhances the recombination possibilities of electron and holes as they can be easily trapped on these recombination centers. Here due to the reduction of distances between the trapping sites, the increased recombination rate will compete with the photocatalytic redox process, which eventually slows down the photocatalytic rate.

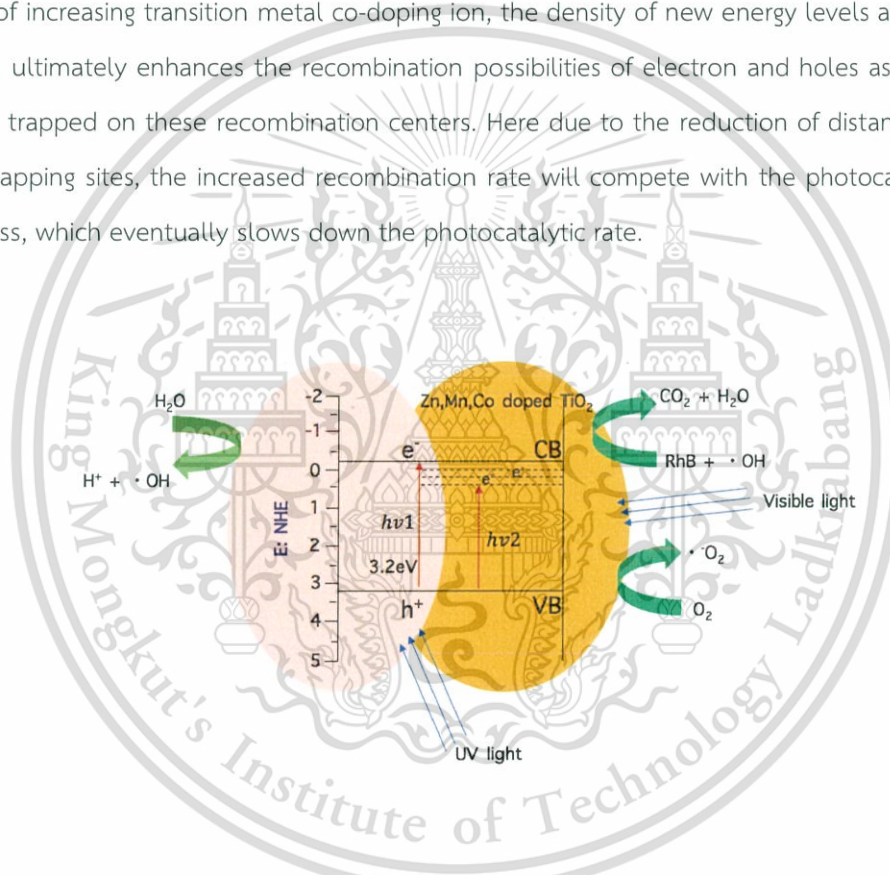


Figure 4.13 The possible mechanism of photocatalytic activity for co-doped  $\text{TiO}_2$

## 4.3 ZnTiO<sub>3</sub>

### 4.3.1 Structural phase

XRD patterns of ZnTiO<sub>3</sub> nanoparticles calcined between 500°C and 900°C are shown in figure 4.14. At calcination temperature of 500°C, the diffraction pattern exhibits broaden peaks around 25°, 35°, 48°, 57° and 63°, which suggests the initial formation of cubic ZTO structure. The sharpness XRD peak of sample calcined at 600°C exhibits high crystallinity of the particle with cubic ZnTiO<sub>3</sub> phase. The mixing phases between cubic and hexagonal ZTO phases are observed in samples calcined at 700-800°C. This feature shows good correspondence to previous work reporting that the unstable cubic ZTO at low temperature can transform into stable hexagonal structure at higher temperature [105]. When the calcination temperature elevated to 900°C, the hexagonal ZTO structure was retained and no significant change into other structures. In addition, the secondary phase of spinel Zn<sub>2</sub>TiO<sub>4</sub> at around 30° and rutile phase at around 28° are observed resulting from the decomposition of ZTO at high temperature. The percentage of hexagonal phase was calculated from the ratio of area of hexagonal phase peaks to the area of all peaks using equation of  $H\% = (A_h/A_{all}) \times 100$  when  $A_h$  and  $A_{all}$  is the area of hexagonal phase ZTO and area of all peaks, respectively. The results are shown in table 4.3.

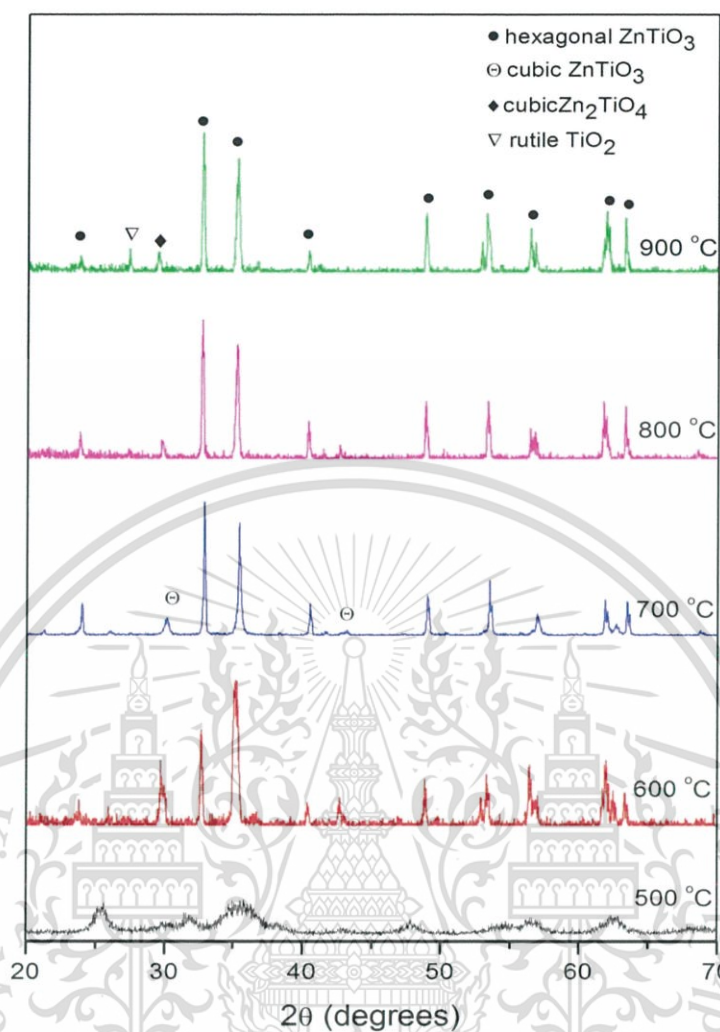


Figure 4.14 XRD patterns of perovskite  $\text{ZnTiO}_3$  nanoparticles calcined at 500-900°C for 2 h.

Table 4.3 Percentage of hexagonal phase

sample	% of hexagonal phase (%)
ZTO-500°C	23
ZTO-600°C	87
ZTO-700°C	93
ZTO-800°C	89
ZTO-900°C	75

### 4.3.2 Chemical composition

The chemical composition of Zn and Ti ions in ZTO sample was performed and characterized by XANES. Figure 4.14 shows the normalized Zn K-edge and Ti K-edge of ZTO at the calcination temperature between 500°C and 900°C accompanying reference standards. For the Zn K-edge, Figure 4.15(a), the spectrum lines of all prepared samples represent strong absorption edge at around 9665 eV. All Zn K-edge XANES spectra do not possess any pre-edge peaks because all 3d bands of Zn are occupied by 3d electrons [106]. This study confirms that the oxidation state of Zn for ZTO sample is 2+. The normalized XANES spectra of Ti K-edge of ZTO nanoparticle including reference standard are displayed in Figure 4.15(b). The XANES spectra illustrate the triplet pre-edge electronic step ahead the large absorption edge at around 4966 eV, which is a powerful finger print of Ti characteristic. This character can be attributed to the transition of 1s electron p-d hybridization of Ti coordination in the ZTO structure [107]. Hence, it is summarized that the ZTO has a perovskite structure comprising six coordinated  $Ti^{4+}$  ions.

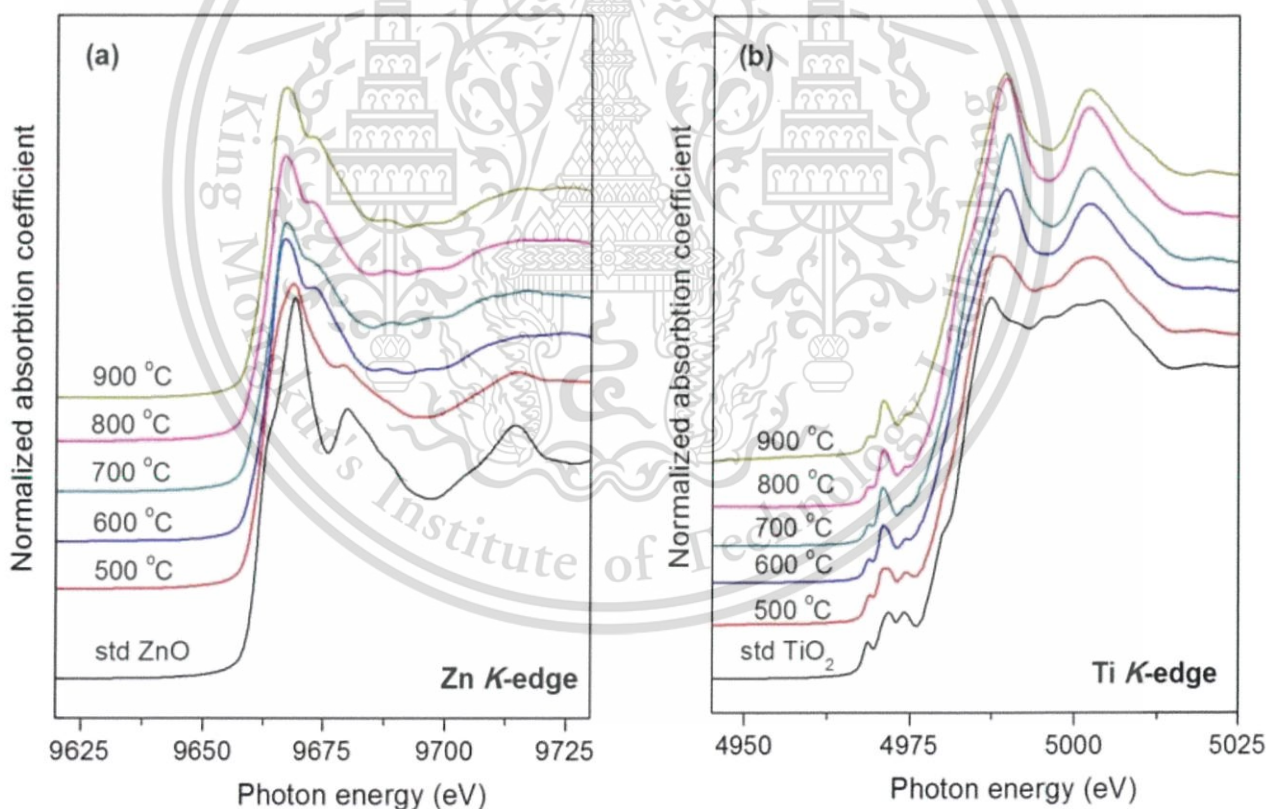


Figure 4.15 Measured XANES spectra of ZTO nanoparticle for (a) Zn K-edge and (b) Ti K-edge.

### 4.3.3 Morphology

Figure 4.16 shows FE-SEM image of perovskite ZTO nanoparticles. The micrograph of samples calcined at 600°C and 700°C in Figure 4.16 (a)-(c) reveal that the particle is nearly spherical in shape with uniform size and distribution. The average particle size is approximately 25 nm. When the calcination temperature rose up to 900°C, as seen in figure 4.16(c), the grain boundary began to melt and smaller particles merged together to be larger grains. However, the particle size became larger with increasing calcination temperature attributing to the better crystal growth with elevated heat treatment temperature.

### 4.3.4 Optical properties

To determine the optical properties of perovskite ZTO nanoparticles, the UV-vis absorption spectra were recorded in the range of 250-700 nm. No significant absorption spectrum observed in the sample calcined at 600°C, as seen in black line spectra in figure 4.17(a). For the sample calcined at 700°C and 900°C, the UV-VIS spectra indicate that the ZTO has such strong absorption in the UV region. This can be attributed to the photo excitation of electron from valence band to conduction band, indicating semiconductor feature of calcined samples. The wide band gap energy in the range of 3.07–3.21 eV is obtained for the samples calcined at 500–700°C. Meanwhile, the band gap energy value for ZTO calcined at 900°C is around 3.71 eV that may be due to the formation of spinel and rutile phases in the sample.

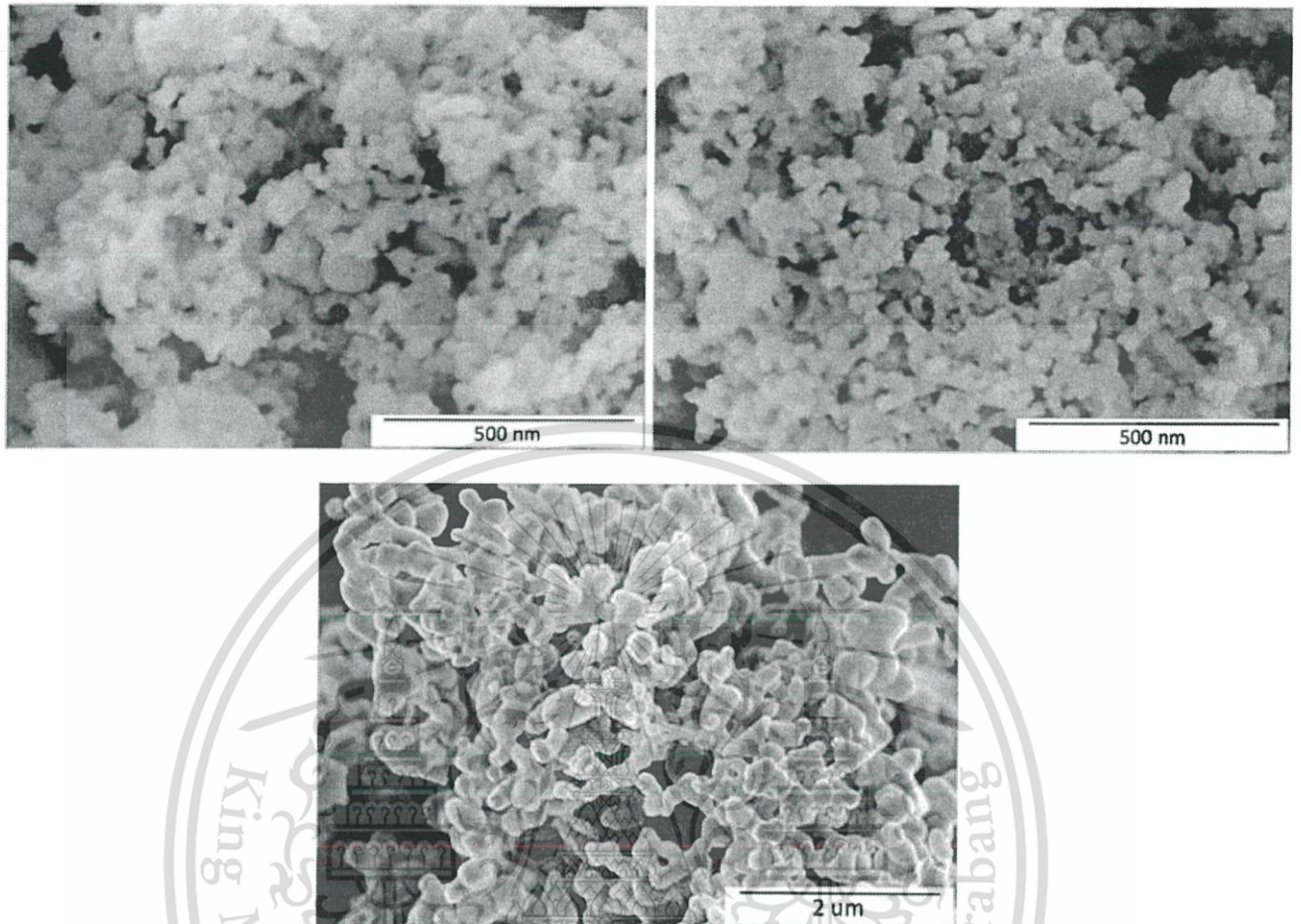


Figure 4.16 FE-SEM micrograph of ZTO nanoparticles calcined at (a) 600°C, (b) 700°C and (c) 900°C.

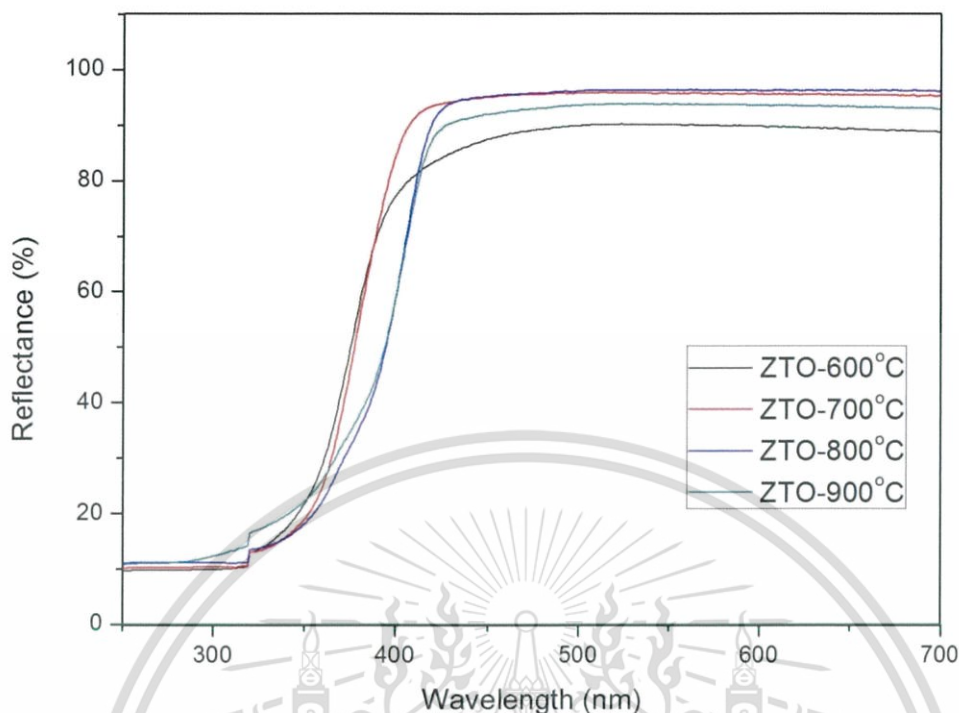


Figure 4.17 Optical reflection spectra of  $\text{ZnTiO}_3$  nanoparticle at difference annealing temperatures.

#### 4.4.4 Photocatalytic behavior

Typically, the structural phase and heat treatment processes are major role factors in the photocatalytic performance of the catalysts. The photocatalytic activities of perovskite ZTO nanoparticles were performed on degradation of RhB under both UV and visible light illumination. Figure 4.18 displays the photodegradation ability of ZTO catalyst under excitation with UV irradiation. It is clearly seen that the sample calcined at  $700^\circ\text{C}$  exhibits superior performance under UV excitation, with 100% of decolorization within 75 min. In contrast, about 95%, 84%, 80% and 49 % of RhB decolorization were obtained by ZTO catalysts calcined at  $800^\circ\text{C}$ ,  $900^\circ\text{C}$ ,  $600^\circ\text{C}$  and  $500^\circ\text{C}$  in 75 min, respectively. These results suggest that the high percentage of hexagonal phase of ZTO samples exhibits the better photocatalytic efficiency compared to low mixing of cubic/hexagonal phase. Better photocatalytic behavior of hexagonal phase has been reported in the literature and it has been ascribed to the change in its crystal phase structure [108]. Figure 4.19 represents the photocatalytic activity of the  $\text{ZnTiO}_3$  catalyst

calcined at 700°C at different irradiation times from 0 to 75 min by mean of the decrement of the absorbance at 554 nm of RhB absorption. The ZTO catalyst performed complete removal the RhB within 75 min. Under visible irradiation, the sample calcined at 700°C performed, as shown in figure 4.20(a). About 55% of the RhB was photocatalytically degraded after 210 min exposure over ZTO samples. The sample calcined at 700°C demonstrated excellent photocatalytic behavior that may be due to the higher hexagonal-phase with a large energy band gap providing powerful redox ability for photocatalytic decomposition of organics contaminant under UV and visible light irradiation [109-110]. Another possible reason may be due to the fact that the tetragonal coordinate in the Ti ions can adsorb more water and oxygen molecules to produce more hydroxyl groups on the surface of ZTO catalyst [111] leading to greater catalytic performance.

In order to find out the efficiency of the photocatalytic reaction, pseudo first order kinetic for photochemical oxidation was established. Figure 4.21(a) represents the absorption rate of ZTO catalyst calcined under UV light illumination. For the UV irradiation system, the kinetic simulation with reaction time ( $t$ ) and  $\ln C/C_0$  is close to a linear curve with the fitting constant  $R$  greater than 0.94. It is observed that the ZTO catalyst exhibit a good activity with  $k = 0.047 \text{ min}^{-1}$  for the samples calcined at 700°C. To compare the photocatalytic performance under UV and visible light irradiation, the first order kinetic rate of samples calcined at 700°C with the UV and visible light photo-degradation were plotted in the figure 4.21(b). The best fitting shows the photocatalytic rate of  $0.047 \text{ min}^{-1}$  and  $0.002 \text{ min}^{-1}$  for UV and visible light illumination, respectively. The superior performance of perovskite ZTO catalyst under UV to visible light is correlated to the higher vigorous absorption in the UV region and the wide band gap energy of the powder.

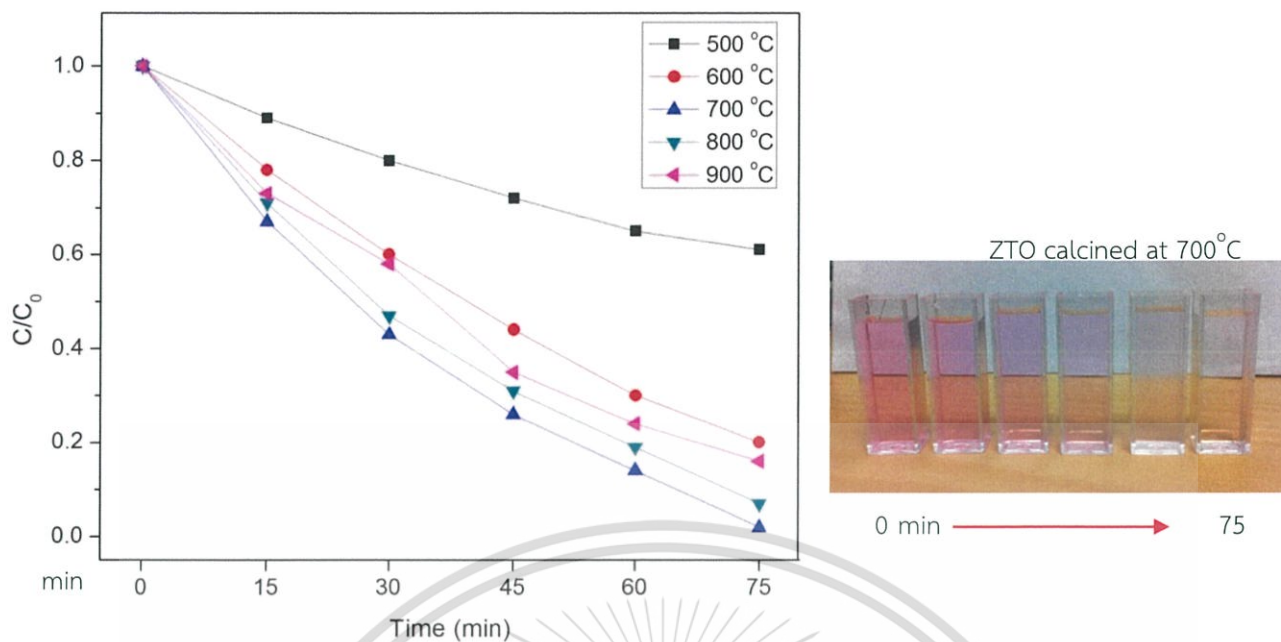


Figure 4.18 (a) Photocatalytic behavior for RhB degradation as a function of time of ZnTiO<sub>3</sub> calcined at 500-900 °C under UV irradiation.

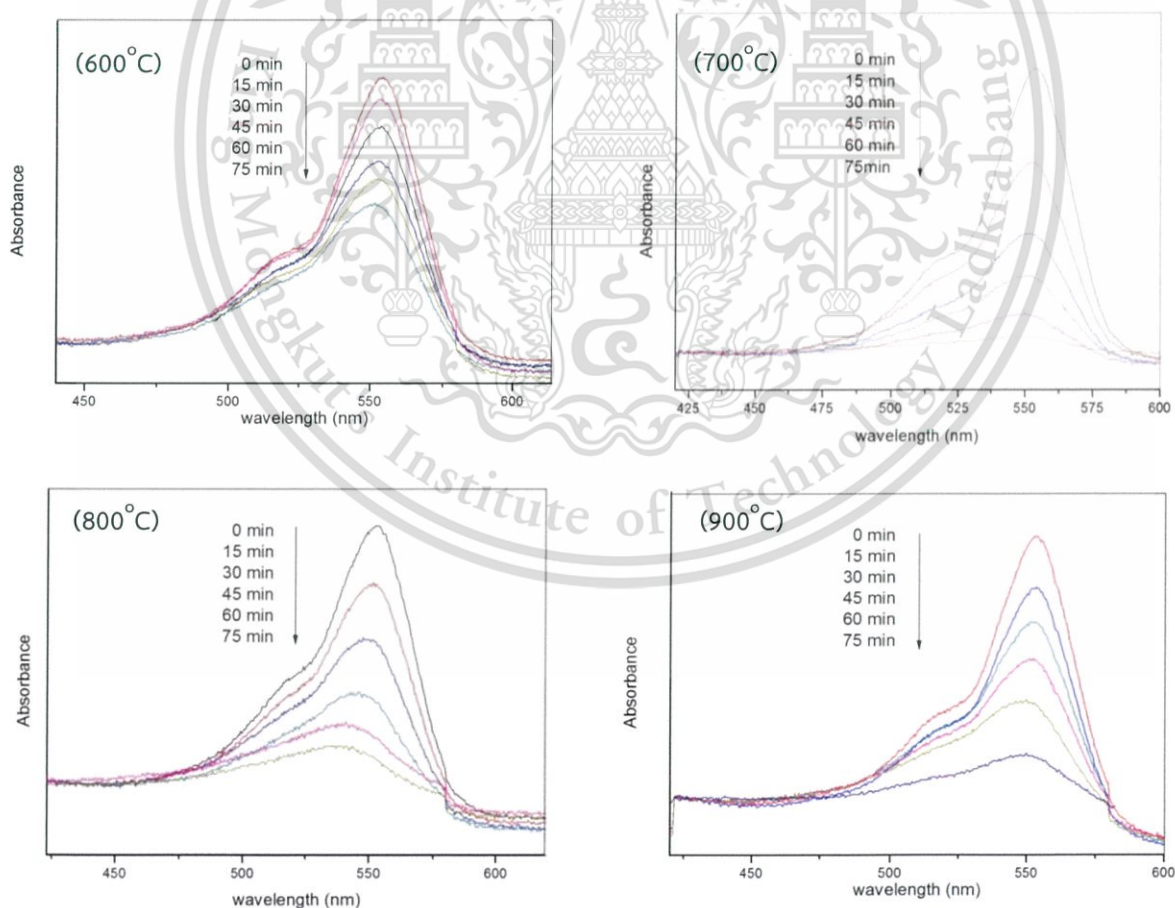


Figure 4.19 Time dependent variation of UV-vis spectra for RhB degradation of ZnTiO<sub>3</sub> calcined at 600-900 °C.

This material is reserved for educational use only, not allowed for commercial use.

Forbidden to modify the content, and cite the document when use.

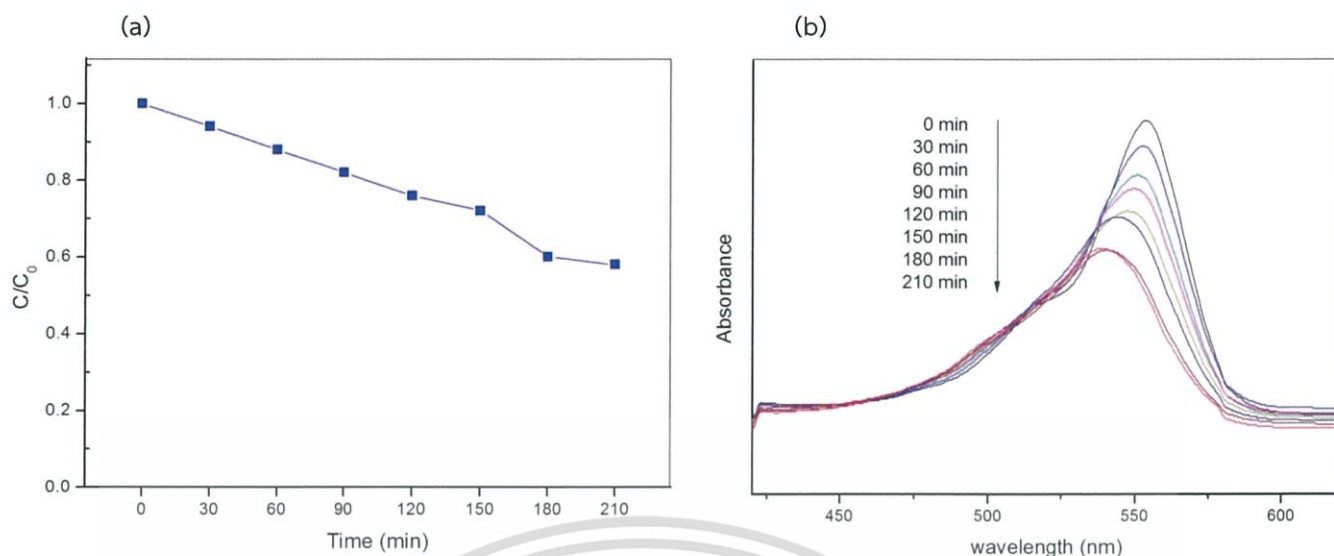


Figure 4.20 (a) Photocatalytic behavior for RhB degradation as a function of time for ZTO calcined at 700°C under visible irradiation and (b) Time dependent variation of UV-vis spectra for RhB degradation for ZTO calcined at 700°C.

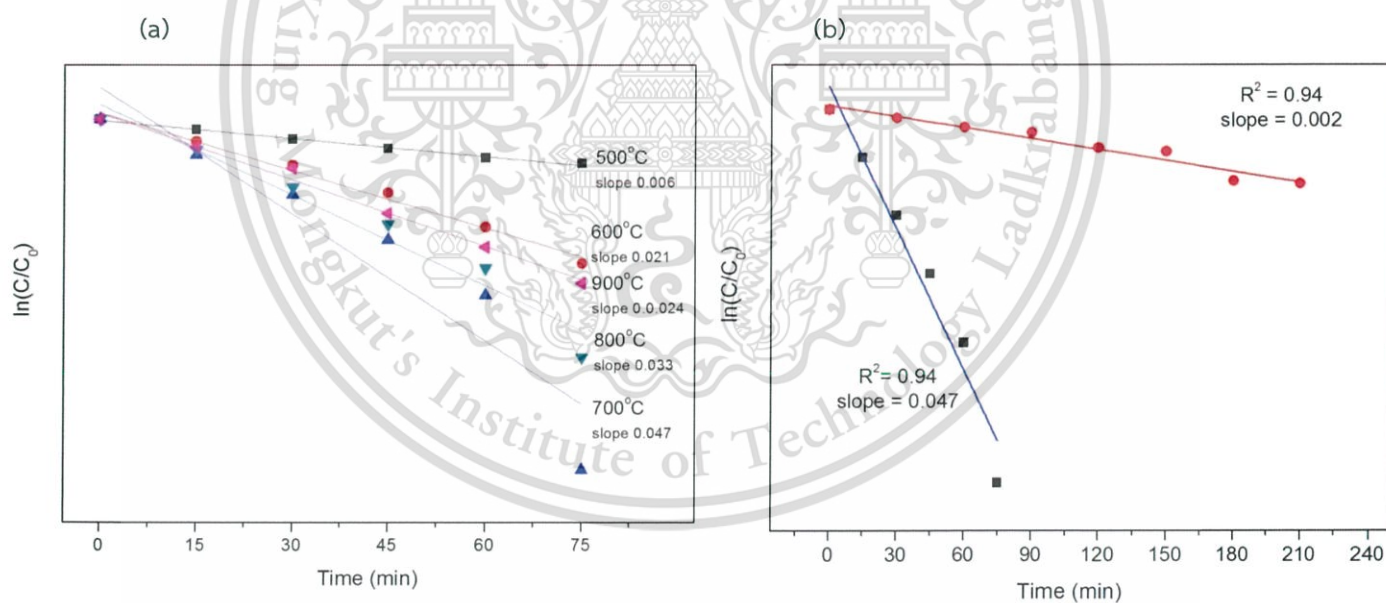


Figure 4.21 Adsorption kinetic of RhB over ZTO catalyst (a) under UV irradiation and (b) samples calcined at 700°C under UV and visible irradiation.

## 4.4 ZTO doped with Co and Mn

### 4.4.1 Structural phase

The XRD patterns of Co-ZTO and Mn-ZTO calcined at 800°C for 3 h are shown in figure 4.22. The figure, shows that all diffractograms of Co-ZTO and Mn-ZTO samples exhibit hexagonal ZnTiO<sub>3</sub> phase accompanying small cubic phase ZTO structure. The XRD patterns of both Co-ZTO and Mn-ZTO samples indicate strong and sharp peaks, ensuring the high crystallinity of the samples. The average crystalline sizes of Co-ZTO and Mn-ZTO calculated by the diffraction peak with highest intensity using Sherrer's equation are approximately 18 nm and 24 nm, respectively. The impurity phases of any metal oxides are not observed in the XRD pattern, indicating a good incorporation of dopant ions into the ZTO host.

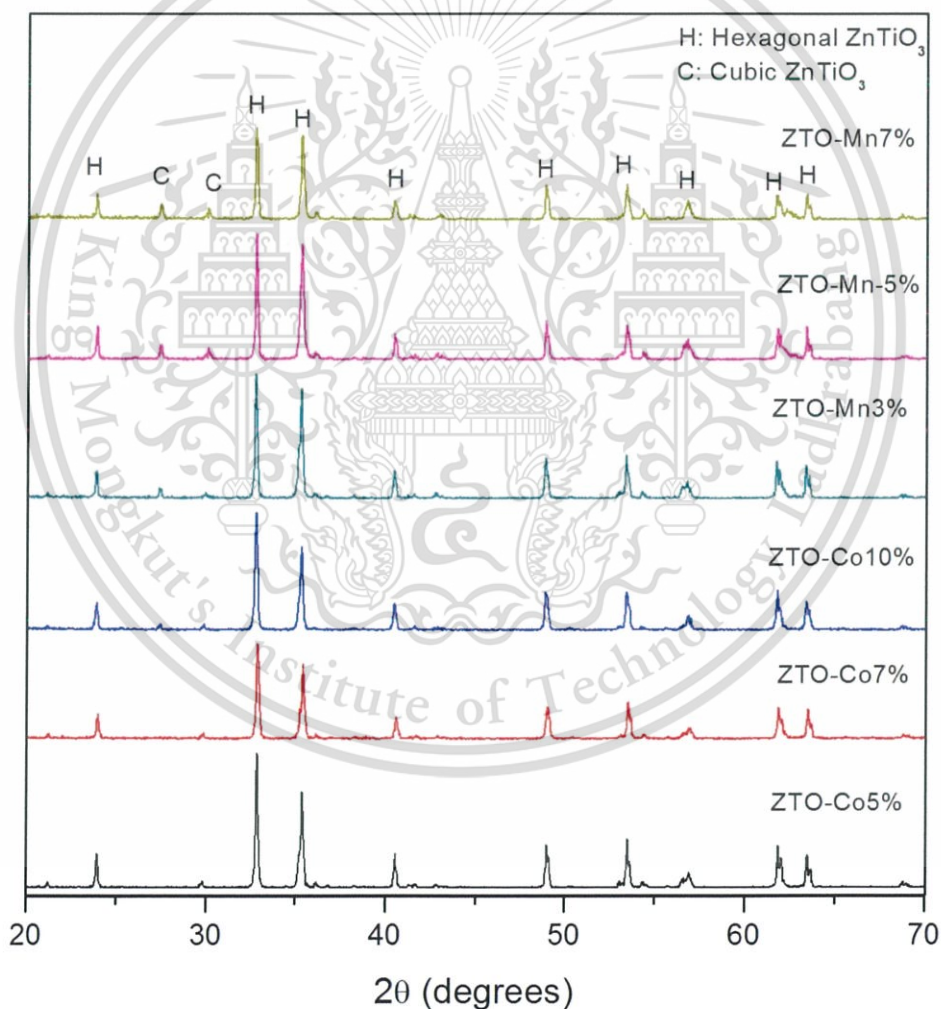


Figure 4.22 XRD patterns of ZTO doped with Co and Mn at various concentrations.

#### 4.4.2 Chemical composition

XANES measurement was conducted to confirm the existence of Co and Mn in the samples, and to study the valence states of Zn, Ti, Co and Mn ions in the Co-ZTO and Mn-ZTO as shown in figure 4.23. The Zn- and Ti *K*-edge (figure a and b) was performed in transmission mode and Co- and Mn- *K*-edge (figure c and d) was performed in fluorescent mode. Figure 4.23 (a) shows the normalized Zn *K*-edge XANES spectra without noticeable pre-edge region in all spectra due to the 3d orbital of Zn<sup>2+</sup> being fully occupied by electrons. Thus, the strong energy absorption edge of 9664 eV presents only the core level of electronic transition from 1s to 4p unoccupied states. This result indicates the existence of Zn<sup>2+</sup> oxidation state in the Co-ZTO and Mn-ZTO samples. Figure 4.23(b) shows the normalized Ti *K*-edge XANES spectra with reference standard of Co-ZTO and Mn-ZTO samples. All spectra represent three pre-edge electronic transition steps before the strong absorption peak of 4966 eV. The triplet pre-edge peaks are typically associated with the strong fingerprint that defines the coordination number of the materials. We can also implicate this to transition of the 1s electron p-d hybridized state in tetrahedral symmetry [112]. The strong energy absorption spectra of all samples are close to the Ti<sup>4+</sup> reference standard. Hence, it can be deduced that the Co-ZTO and Mn-ZTO samples have perovskite structure consisting of six coordinated Ti<sup>4+</sup> ions. The inset of figure 4.23(c) represents experimental XANES spectra of Co *K*-edge with their reference standard. The XANES spectra show a small pre-edge shoulder located at 7708 eV. The large absorption energy positioned at 7715 eV is almost identical to the Co<sup>2+</sup> standard spectrum. This result confirms that the oxidation state of Co ion in Co-ZTO samples is 2+. Figure 4.23(d) shows the strong absorption peaks of Mn *K*-edge located between 6345 and 6555 eV. This characteristic feature suggests the existence of Mn ion with different oxidation states (Mn<sup>2+</sup>, Mn<sup>3+</sup> and Mn<sup>4+</sup>) in samples due to the environmental sensitivity of Mn ion. Moreover, figure 4.23(e) shows that increasing Mn content leads to a shift in edge position to higher energy, indicating an increase in the Mn oxidation state.

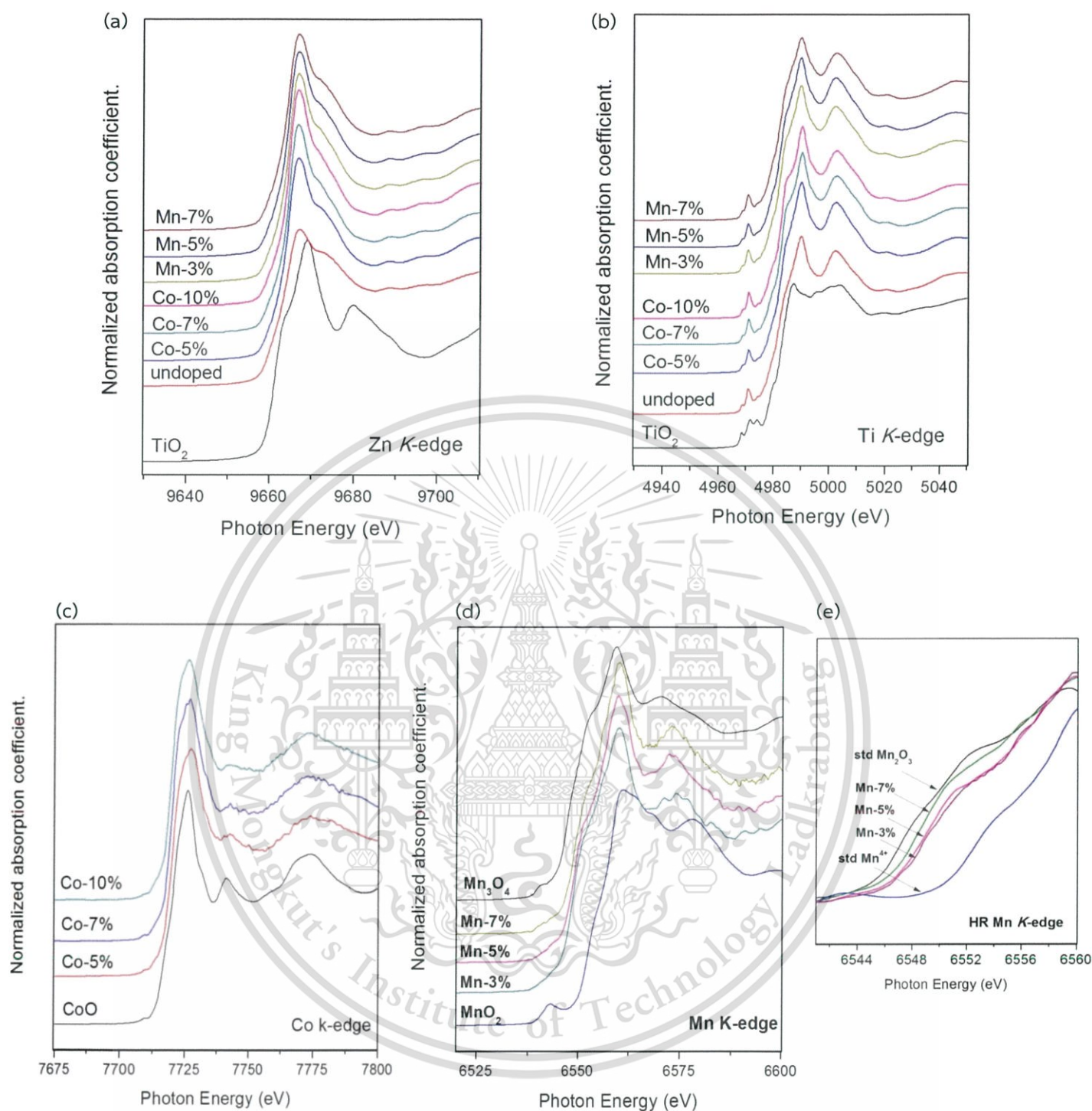


Figure 4.23 Measured XANES spectra of Co-ZTO and Mn-ZTO for Co K-edge and Mn K-edge with reference standard in fluorescent mode.

#### 4.4.3 Local structure

The local environment of Co- and Mn-doped ZTO samples were determined by EXAFS measurement. The data identification of all EXAFS measurement was carried out by using the ATHENA and ATHEMIS program [113-114]. The EXAFS data in  $k=3-10 \text{ \AA}^{-1}$  range were transformed by Fourier transform. The data were fitted in the real space in  $R=1-5 \text{ \AA}^{-1}$  range to obtain the best fitting result using the Hanning window function with  $k^2$ -weighted. The  $k^2$ -weighted and the best fitting curve of corresponding experiment data are shown in figure 4.24(a) and (b). In the Co-ZTO samples, the first two peaks were fitted using ARTHEMIS including single and multiple scattering as seen in figure 4.24(b). The EXAFS analysis indicates that the Zn atom is surrounded by six nearest oxygen atoms, corresponding to the first main peak of  $R$ -space at around  $1.5 \text{ \AA}$ . The second and third peaks are observed at  $\sim 2.5$  and  $3.7 \text{ \AA}$ , corresponding to the metal oxides of Ti and Zn atoms in the next nearest shell. The coordination numbers and inter-atomic distance in the ZTO-host sample agree well with structural values of hexagonal ZTO. For the Mn-ZTO samples,  $k^2$ -weighted and the corresponding Fourier transform curve are displayed in figure 4.25(a) and (b). The best fit analysis of the oscillation and the first two peaks in Fourier transform were done by using the single and multiple scattering. Fitted peaks harmonize to the first two coordination shells around the Zn atom. The first three peaks are found at around  $1.6$ ,  $2.4$  and  $3.7 \text{ \AA}^{-1}$ , which can be assigned to the nearest of O-, Ti- and Zn-atom, respectively. In addition, when the Co- and Mn-contents increased, poor fitting was observed at  $R > 3.5 \text{ \AA}$ . This result confirms that the crystal system of ZTO host could be disturbed by Co- and Mn- dopant, indicating the increasing defect in the sample.

In order to determine the preferred site occupation of Co dopants in ZTO unit cell, the Fourier transform of EXAFS spectra for hexagonal ZTO with ion dopant dominating A(Zn)- and B(Ti)-sites were simulated. As seen in figure 4.26(a), the feature of EXAFS oscillation for Co-doped sample is nearly similar to the A-site of ZTO but different from that of B-site and CoO reference. In addition, the radial distribution function of Co-doped samples around the Co-atom exhibits nearly harmonic peak position with those of ZTO around Zn atoms as shown in figure 4.26(b). These results indicate that the local atomic environment around the Co-atoms in ZTO is similar to the Zn atom in ZTO, demonstrating the  $\text{Co}^{2+}$  ions substituted in A(Zn)-site position in ZTO crystal lattice. Moreover, the increasing shoulder peak around  $2.5 \text{ \AA}^{-1}$  in  $k$ -space was observed, corresponding to the  $k$ -space of CoO. It can be attributed to some parts of Co-dopants forming into CoO cluster in the ZTO-based samples. In case of Mn-doped sample, as the  $k^2$ -spectra and

*R*-space spectra compared with A- and B-site MnO, Mn<sub>2</sub>O<sub>3</sub> and Mn<sub>3</sub>O<sub>4</sub> were simulated which was shown in figure 4.27(a)-(b). The shape of  $k^2$ -weighted and radial distribution function for all Mn-doped samples are significantly similar to both of A(Zn)-site and Mn<sub>2</sub>O<sub>3</sub> oscillation. So, it may conclude that some Mn-ions might substitute in B(Zn)-site in the ZTO lattice and some of them might form in a small Mn<sub>2</sub>O<sub>3</sub> cluster. The possible reason for the substitution difficulty of Zn-site by Mn ions than Co ions may attribute to the radii of the dopant ions. The ionic radius of Mn is 0.066nm, which bigger than Co (0.058nm) and Zn (0.060nm). Therefore, the substitution of Zn-site with the Co ions is anticipated to arise more commonly than with Mn ions [115].

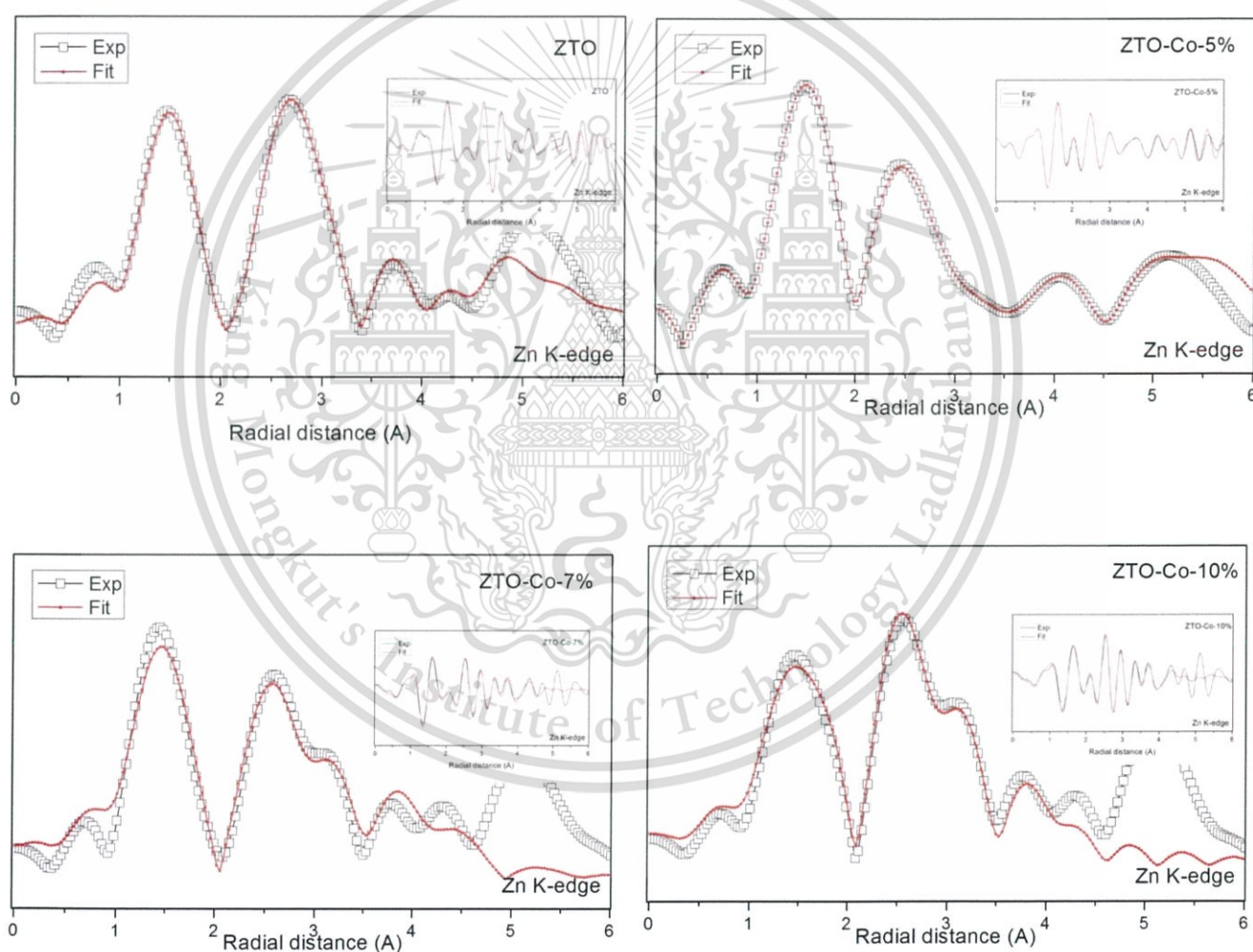


Figure 4.24 The Fourier transform magnitudes of EXAFS spectra of  $k^2$ -weighted data with fit at Zn K-edge into *R*-space and EXAFS function  $k^2\chi(k)$  with fit for Zn K-edge (small picture) of Co-ZTO.

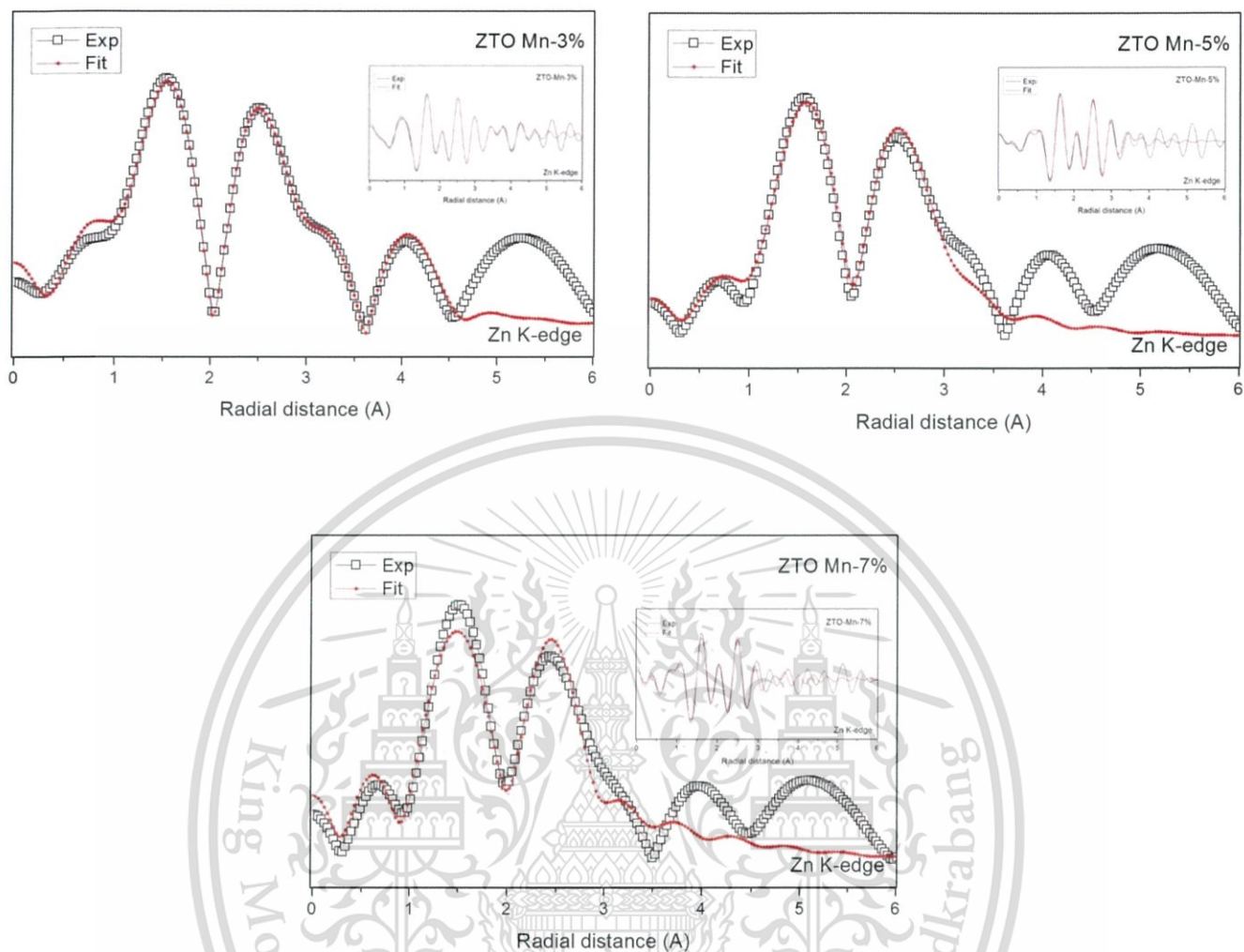


Fig.4.25 The Fourier transform magnitudes of EXAFS spectra of  $k^2$ -weighted data with fit at Zn K-edge into R space and EXAFS function  $k^2\chi(k)$  with fit for Zn K-edge (small picture) of Mn-ZTO.

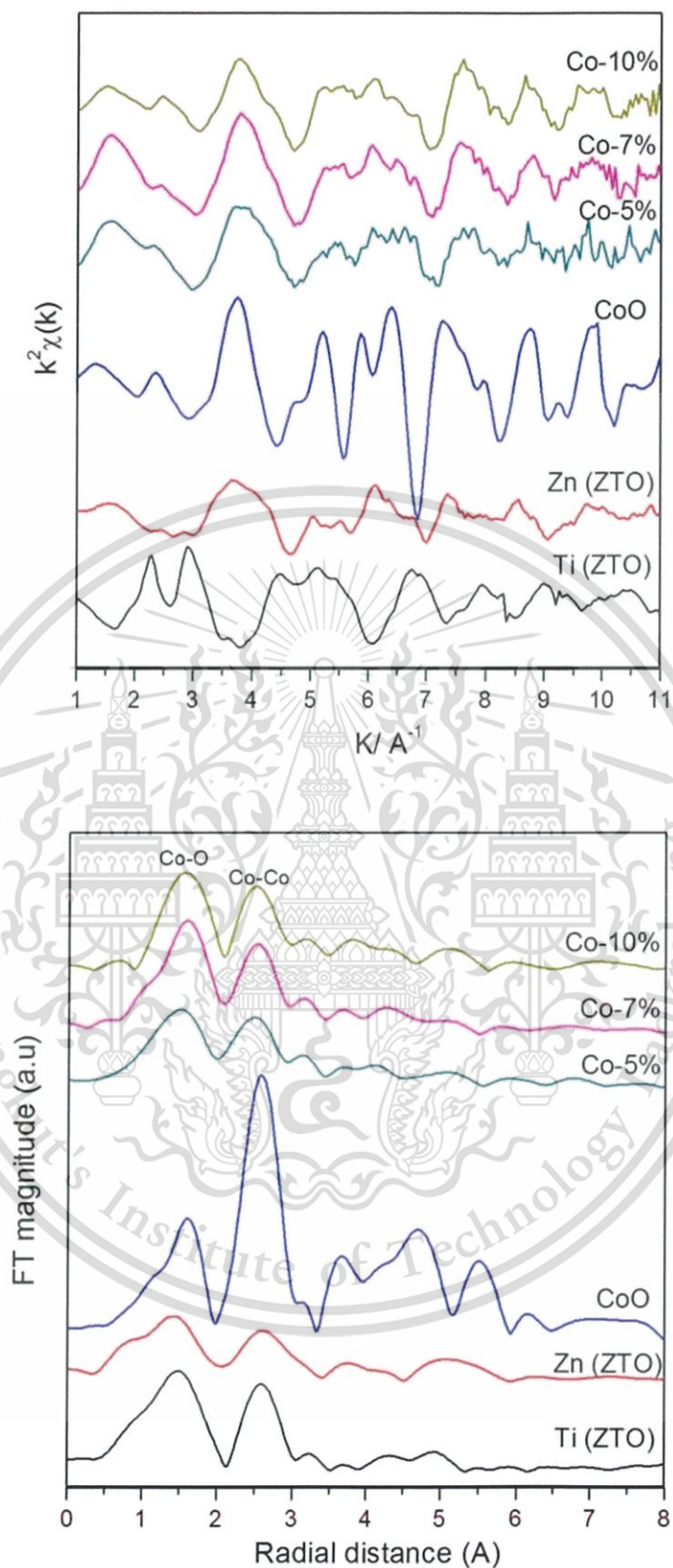


Figure 4.26 EXAFS oscillations and their corresponding Fourier transform of dopant spectra compared to A-site, B-site and their reference standard of Co-ZTO samples.

This material is reserved for educational use only, not allowed for commercial use.

Forbidden to modify the content, and cite the document when use.

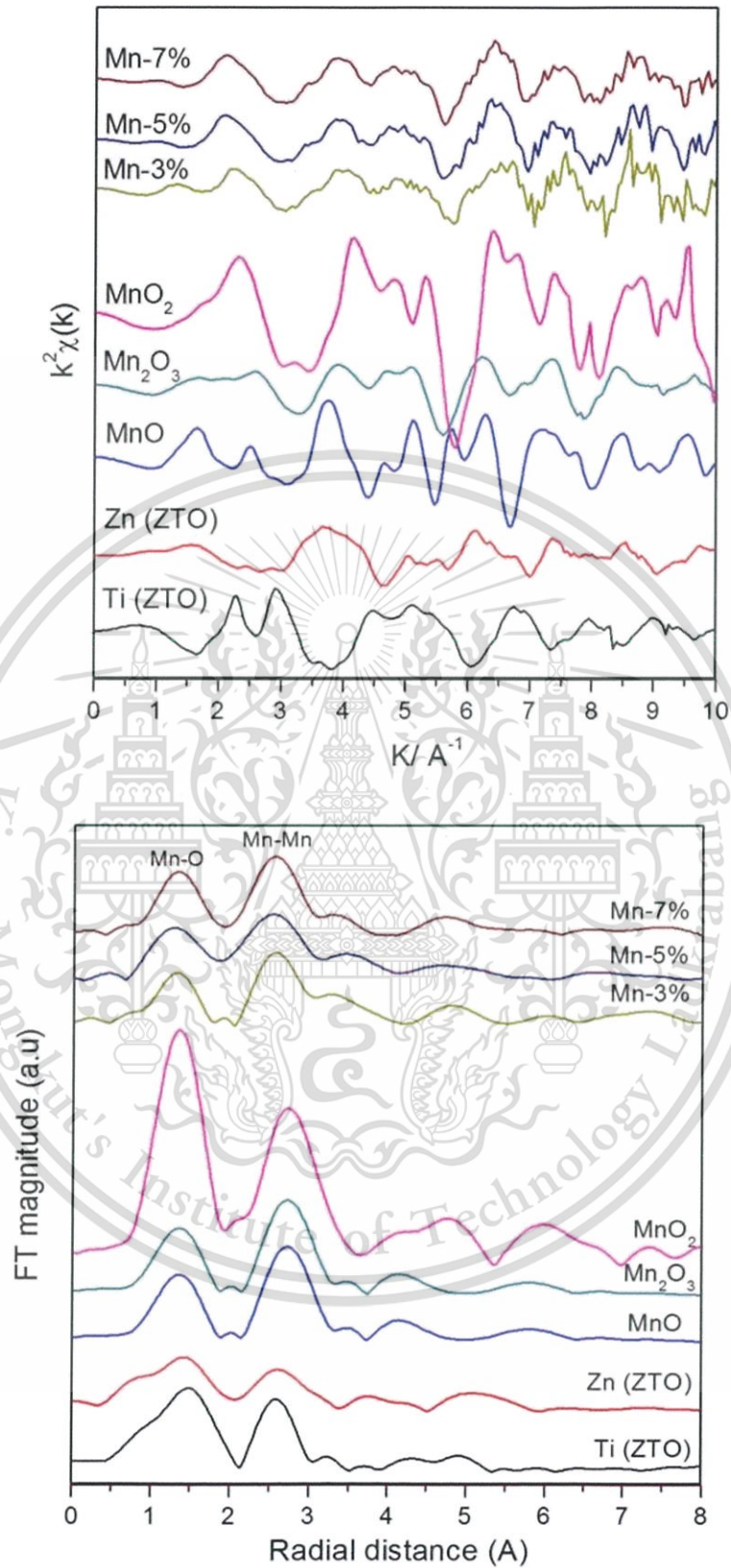


Figure 4.27 EXAFS oscillations and their corresponding Fourier transform of dopant spectra compared to A-site, B-site and their reference standard of Mn-ZTO samples.

This material is reserved for educational use only, not allowed for commercial use.

Forbidden to modify the content, and cite the document when use.

#### 4.4.4 Optical properties

The optical properties of samples were investigated by diffuse reflectance spectroscopy (DRS). The plots of reflectance as a function of wavelength for Co-ZTO samples are shown in Figure 4.28. All of spectra exhibit significant strong absorption in UV region. The Co-ZTO spectra also show broad peak around 550-650 nm region, that is possibly originated by additional impurity state  $\text{Co}^{2+}$  formed in the host semiconductor energy gap. These results are well agreeable with previous work of Co-doped  $\text{TiO}_2$  [116]. For the Mn-ZTO, the plots of reflectance and wavelength are shown in figure 4.28 (b). It can be seen that the spectra reveal absorption in UV region. The absorption edge clearly shifts to higher wavelength implying significant decrease of the energy band gap of the samples. The band gap energy values of all samples were estimated as shown in figure 4.28. It can be seen that the indirect energy gap value of Co-ZTO increases from 3.26 to 3.51 eV when Co content increases from 5 to 10%. On the other hand, the energy gap of Mn-ZTO slightly decreases with increasing of Mn concentration. Such decrease of energy band gap of samples can be described that the dopant ion incorporated into ZTO matrix can replace some  $\text{Zn}^{2+}$  ions and induce structural changes and defects affecting the change in electrical and optical properties of the host matrix. It is supported by XAS results showing that the Co- and Mn-dopants exist in the doped samples. The change in energy band gap of ZTO-based samples has a strong bearing on the photocatalytic properties of the samples.

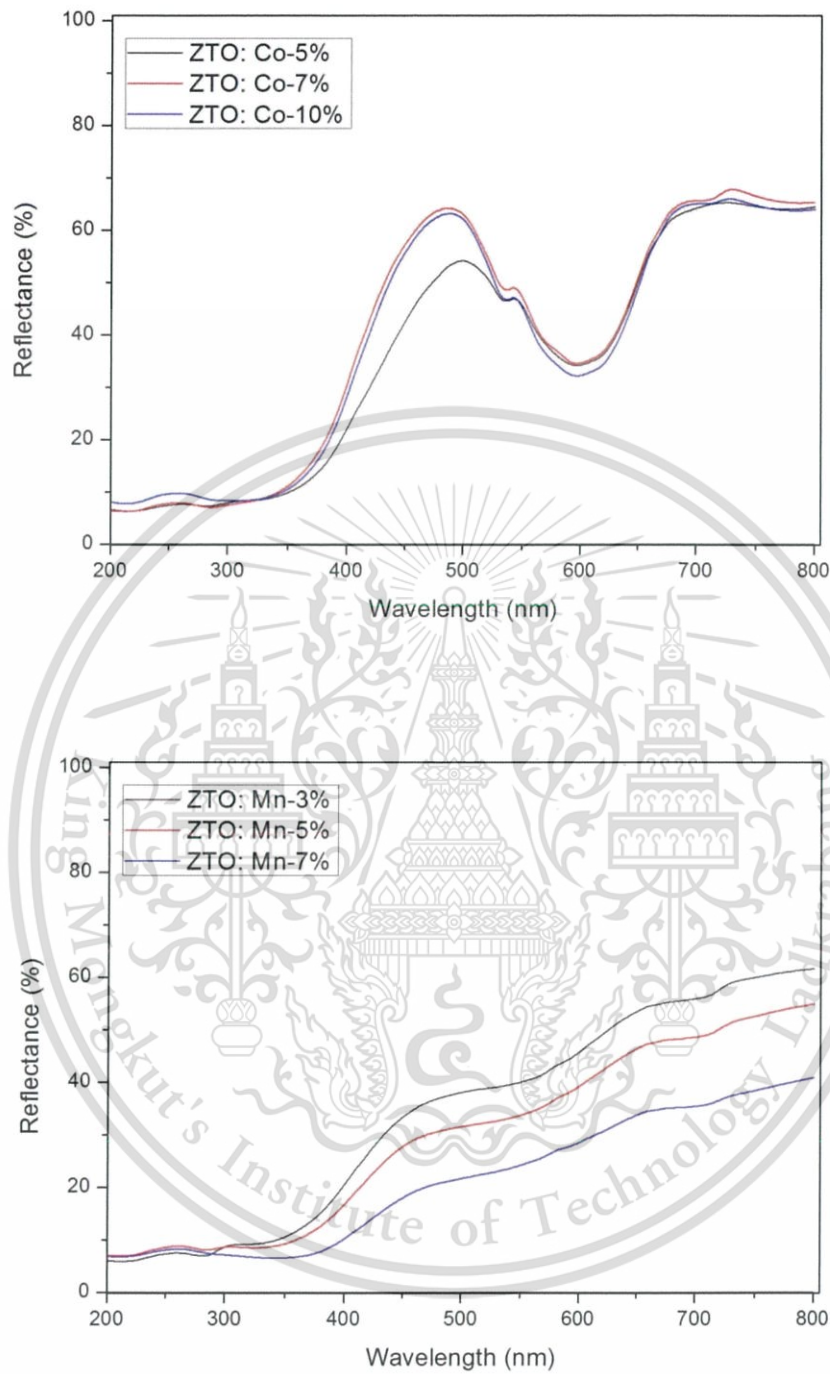


Figure 4.28 Diffuse reflectance spectra versus wavelength of Co-ZTO and Mn-ZTO.

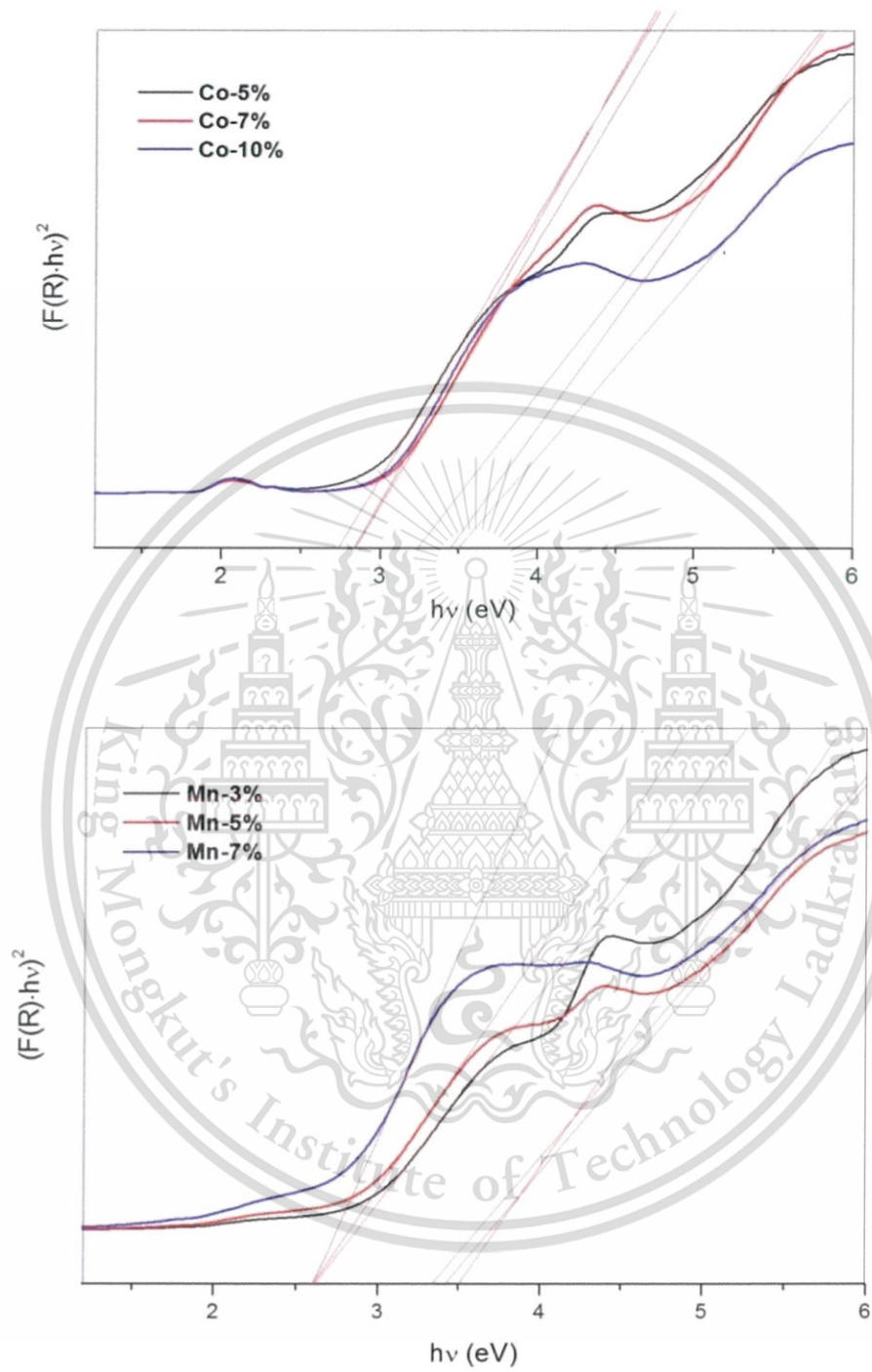


Figure 4.29 Direct and indirect energy band gap determination for Co-ZTO and Mn-ZTO.

This material is reserved for educational use only, not allowed for commercial use.

Forbidden to modify the content, and cite the document when use.

#### 4.4.5 Morphology

The particle size and distribution of Co-ZTO and Mn-ZTO samples were studied by FESEM. Figures 4.30(a)–(c) show the image of ZTO samples with different Co doping concentrations. It can be observed that the average particles size slightly increases with increasing Co content, with estimated value of 218, 222 and 243 nm for Co contents of 5, 7 and 10%, respectively. Figures 4.30 (d)–(f) represent the microphotographs of Mn-ZTO. The images emphasize that the particle sizes are 136, 158 and 224 nm for Mn concentrations of 3, 5 and 7%, respectively. Moreover, the FESEM images exhibit morphologies of Co-ZTO and Mn-ZTO that are of irregularly granular structure with observable agglomeration. The experimental results indicate that the Co and Mn ion doping may be inserted into the ZTO lattice, and inhibit crystalline and particle growth. The average particle size obtained from FESEM characterization is in accordance with the crystalline size calculated from the XRD results.

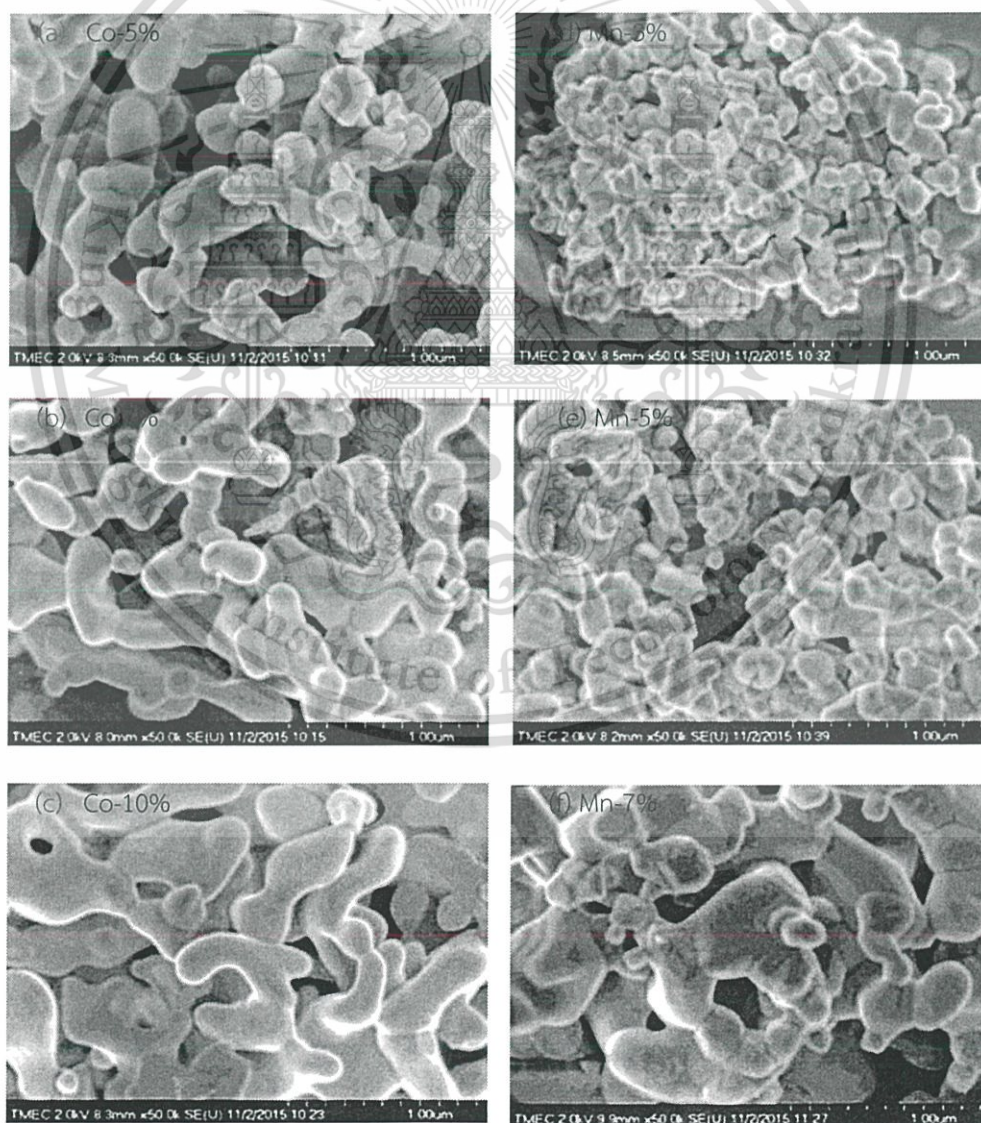


Figure 4.30 SEM images of ZTO doped by Co and Mn.

This material is reserved for educational use only, not allowed for commercial use.

Forbidden to modify the content, and cite the document when use.

#### 4.4.6 Photocatalytic activity

According to the UV-VIS spectroscopy measurement, the optical analysis reveals that the ZTO-based catalyst is active under the visible light irradiation. In this work, the photocatalytic decomposition experiments of Rhodamine-B by ZTO-based samples were conducted under visible light illumination. As seen in the figure 4.31(a), ~36% of RhB photo-degradation was obtained in the ZTO-bare catalyst under visible light irradiation. For the Co-doped, after 150 min under visible light irradiation, the total RhB removal of 68%, 54% and 52% were found in the 7, 5 and 10 mol% of dopant concentration, respectively. The pseudo first order kinetic for photocatalytic oxidation was calculated and displayed in figure 4.31 (b). The degradation rate constant of 0.0043, 0.0061 and 0.0036  $\text{min}^{-1}$  were found in the 5%, 7% and 10% of Co-dopant concentration. In case of Mn-doped samples, the highest RhB degradation of 67% were obtained by ZTO doped with 7% of Mn after 150 min of irradiation time as shown in figure 4.32(a). Whilst, 55% and 51% of dye degradation were found in ZTO doped with Mn 5% and 3%, respectively. Figure 4.32 (b) exhibits the photodegradation rate of Mn-ZTO samples, the highest rate of 0.007  $\text{min}^{-1}$  found in 7%Mn-doped sample. The enhanced photocatalytic efficiency exhibited by the doped samples might be due to the increasing of optical absorption in the visible region probably arising from the high point defects in the crystal lattice. The crystal defects in photocatalyst semiconductor allow the excitation of electron from the valence band to the conduction band with the comparatively low energy photon. A further increase in the photocatalytic activity in the presence of Co and Mn dopants may be due to the deposition of oxide cluster on the ZTO matrix, which efficiently enhances the charge separation of photogenerated electron-hole pairs and prolongs the light absorption range in ZTO, resulting in the higher photocatalytic activity under visible light illumination [117]. In addition, the Mn-doped samples can possess the greater photo-degradation than Co-doped sample owing to the highly generated hydroxyl radical originated from the conversion of different oxidation states of Mn.

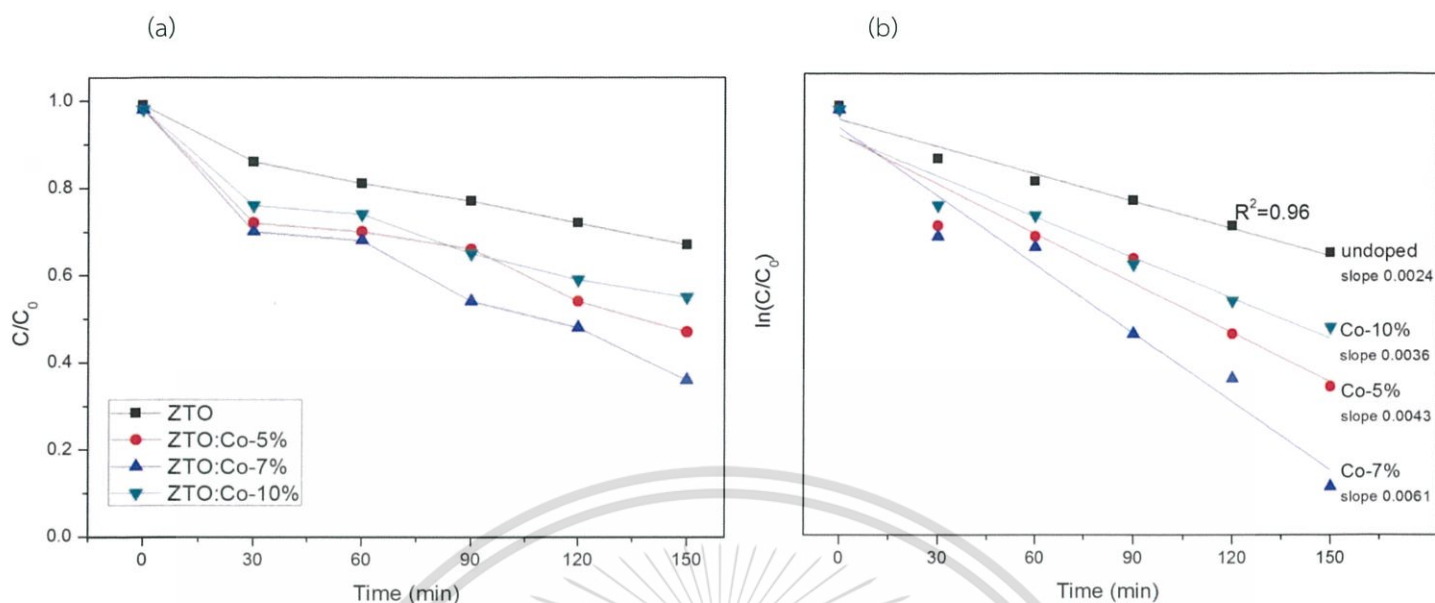


Figure 4.31 (a) Photocatalytic degradation curve for different catalyst in the presence of RhB dye for Co-ZTO catalyst and (b) Adsorption kinetic of RhB over Co-ZTO catalyst.

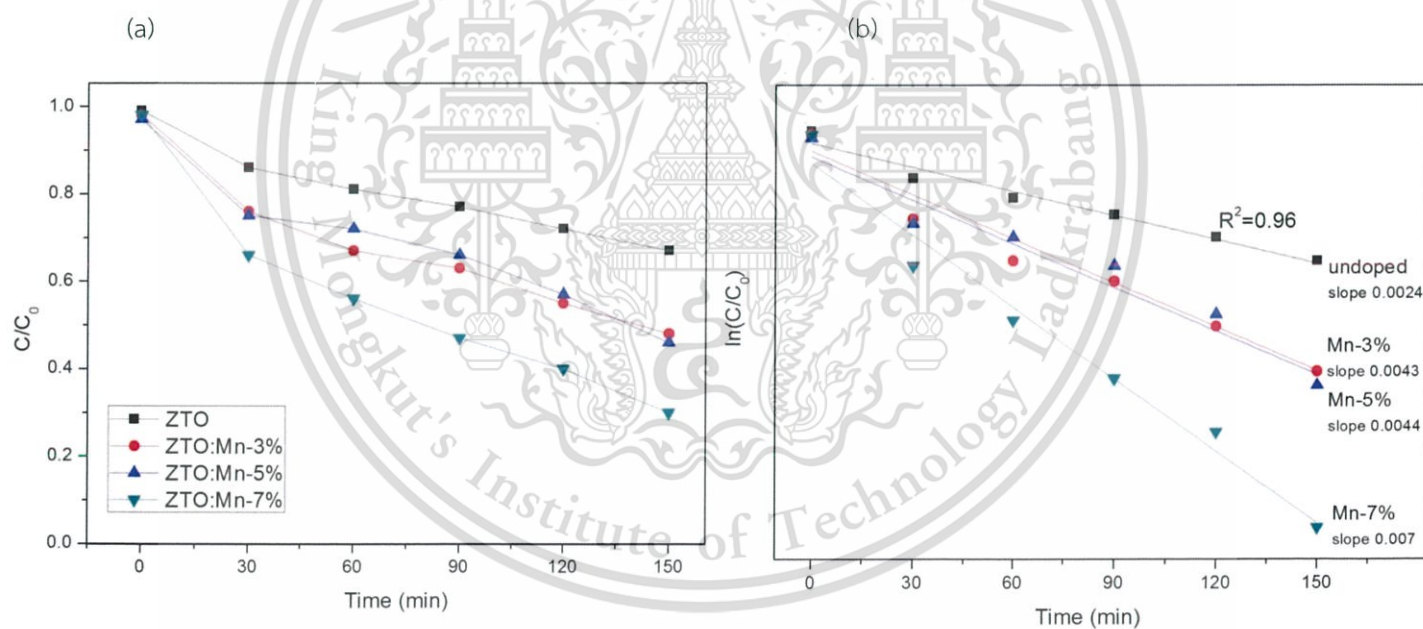


Figure 4.32 (a) Photocatalytic degradation curve for different catalyst in the presence of RhB dye for Mn-ZTO catalyst and (b) Adsorption kinetic of RhB over Mn-ZTO catalyst.

## CHAPTER 5

### Conclusion

The first system in this research is bare-TiO<sub>2</sub> and Zn-doped TiO<sub>2</sub> nanopowders prepared by sonochemical method using sonometer (20kHz, 750W) for 30 min of sonication time. The structural phase studies revealed that the anatase TiO<sub>2</sub> phase was formed after sonication process. The crystallinity of as-synthesized nanopowders was improved by heat treatment process at 450-550°C for 2 h. The high crystallinity phase of anatase TiO<sub>2</sub> was obtained after calcined at 450-550°C. While, the rutile phase and impurity phase of ZnO were detected at the calcination temperature above 550°C. The TEM image shows the good distribution of nanoparticles with an average particle size of 15 nm. The energy gaps of calcined samples are found to be increased with increasing calcination temperature. The incorporation of Zn ions into the TiO<sub>2</sub> lattice can extend its effective band gap into the visible region. The calcination temperature and Zn dopant have considerable influence on the structure phase, and optical properties of TiO<sub>2</sub> nanoparticles.

For the series of double-doping system, Co-Zn and Mn-Zn co-doped TiO<sub>2</sub> were synthesized by single-step of sonochemical method using sonication time for 30min. The characterization tests indicate that the co-dopant ions could be incorporated in the TiO<sub>2</sub> lattice. The structural phase of as-synthesized powders belongs to the anatase TiO<sub>2</sub> phase without secondary phase of any oxide phases. The average size of as-synthesized nanoparticles is in value around 5-10 nm. The XANES measurement confirmed the oxidation state of 4+, 2+ and 2+ for Ti, Zn and Co, respectively, while the mixing of oxidation state of 3+ and 4+ was obtained in the Mn-doped samples. The EXAFS studies represent that the Co- and Mn- ions both were incorporated in Ti- site and formed as a small cluster in the TiO<sub>2</sub> host. The effective co-doping of Co-Zn and Mn-Zn could significantly decrease the optical band gap of titania, making them suitable for application in visible-light-driven photocatalysis. The photocatalytic activity for RhB dye testing revealed that the presence of co-doped samples has superior performance than singly-doped samples. The best decolorization performance was achieved in the content of 3% for Co- and 2% for Mn-doping content. The rapid and excellent photocatalytic behavior is attributed to the large visible light capacity and great surface area of co-doped samples.

For the perovskite ZnTiO<sub>3</sub>-based compounds, pure ZnTiO<sub>3</sub>, and ZnTiO<sub>3</sub> doped with Co and Mn were successfully fabricated by sonochemical method. XRD results exhibit the cubic ZnTiO<sub>3</sub> phase for the samples calcined at 600°C. The mixed phases of cubic and tetragonal

This material is reserved for educational use only, not allowed for commercial use.

Forbidden to modify the content, and cite the document when use.

ZnTiO<sub>3</sub> were observed in the sample calcined at 700°C, while the spinel and rutile phase could be noticed as calcination is beyond 700°C. The XAS experiment confirms the oxidation state of Zn<sup>2+</sup> and Ti<sup>4+</sup> in perovskite ZnTiO<sub>3</sub> nanopowders. The ZnTiO<sub>3</sub> sample calcined at 700°C with highest percentage of hexagonal phase exhibited the excellent photocatalytic efficiency for the complete decolorization of RhB within 70 min under UV exposure and 40% of RhB degradation within 3 h under visible light irradiation. In case of perovskite ZnTiO<sub>3</sub> doped with Co and Mn transition ions, the samples were prepared by sonochemical method combined with calcinations at 800°C for 3 h. Co-ZTO shows the pure hexagonal ZnTiO<sub>3</sub> phase, while Mn-ZTO exhibits mixed phases of cubic and hexagonal ZnTiO<sub>3</sub> phases. The existence of Co and Mn and the valence states of each ion in the samples were characterized by XANES. EXAFS measurements indicate that the Co-dopant ions seems to be A(Zn)-site favored dopant together with small cluster of CoO oxide. For Mn-doped ZnTiO<sub>3</sub>, the Mn-dopant ions appear to be both of A(Zn)-site and Mn<sub>2</sub>O<sub>3</sub> cluster in the ZTO lattice. The incorporation and formation of cluster of Co and Mn dopant in ZTO-based samples exhibit the better photocatalytic activity for RhB dye degradation under visible light irradiation compared to pure ZTO. These studies indicate that the uncomplicated and eco-environmental method can be useful for synthesizing the potential catalysts with highly efficient degradation of organic pollutants for environmental renewal. In addition, the incorporation of transition metal ions of Zn, Co and Mn dopants is an effective way to improve the catalytic efficiency of both TiO<sub>2</sub>-based and perovskite ZTO-based compounds.

## References :

- [1] A. Fujishima, X. Zhang, D.A. Tryk, TiO<sub>2</sub> photocatalysis and related surface phenomena, *Surf. Sci. Rep.*, 63 (2008), 515-582.
- [2] A. Fujishima, T.N. Rao, D.A. Tryk, Titanium dioxide photocatalysis *J. Photochem. Photobiol. C*, 1 (2000), 1-21.
- [3] M.I. Litter, Heterogeneous photocatalysis: Transition metal ion in photocatalytic system, *Appl. Catal. B*: 23 (1999) 89-114.
- [4] D. S. Bhatkhande, V. G. Pangarkar and A. A. Beenackers, Photocatalytic degradation for environmental applications: a review, *J. Chem. Technol. Biotechnol.* 77 (2001) 102-116.
- [5] M.R. Hoffmann, S.T. Martin, W. Choi and D.W. Bahnemann, Environmental Application of semiconductor photocatalysis, *Chem. Rev.* 95 (1995) 69-96.
- [6] A. Fujishima and K. Honda, Electrochemical photolysis of water at a semiconductor electrode *Nature*, 238 (1972) 37-38.
- [7] R. Chauhan, A. Kumar and R. P. Chaudhary, Structural and photocatalytic studies of Mn doped TiO<sub>2</sub> nanoparticles, *Spectrochemi. Acta. Mol. Biomol. Spectrosc.* 98 (2012) 256-264.
- [8] H. Moradi, A. Eshaghi, S.R. Hosseini and K. Ghani, *Ultrason. Sonochem.* 32 (2016) 314-319.
- [9] H.M. Yadav, S.V. Otari, R.A. Bohara, S.S. Mali, S.H. Pawar and S.D. Delekar, *J. Photochem. Photobiol. A Chem.* 294 (2014) 130-136.
- [10] Y. Lv, X. Cao, H. Jiang, W. Song, C. Chen and J. Zhao, *Appl. Catal. B*. 194 (2016) 150-156.
- [11] SNR. Reddy, T. Boningari and M. Suidan, Visible-light-induced photodegradation of gas phase acetonitrile using aerosol-made transition metal (V, Cr, Fe, Co, Mn, Mo, Ni, Cu, Y, Ce, and Zr) doped TiO<sub>2</sub>, *Appl. Catal. B*: 114 (2014) 333-342.
- [12] A.K. Tripathi, M.C. Mathpal, P. Kumer, M.K. Singh, M.A.G. Soler and A.A. garwal, Structural, optical and photoconductivity of Sn and Mn doped TiO<sub>2</sub> nanoparticles, *J. Alloys. Comp.* 622 (2015) 37-47.
- [13] J.Y. Park, K.I. Choi, J.H. Lee, C.H. Hwang, D.Y. Choi and J.W. Lee, Fabrication and characterization of metal-doped TiO<sub>2</sub> nanofibers for photocatalytic reactions *Mater. Lett.* 97 (2013) 64-66.
- [14] M. Anpo, Use of visible light. Second-generation titanium dioxide photocatalysts prepared by the application of an advanced metal ion-implantation method. *Pure Appl Chem* 2000; 72: 1787-1792.
- [15] H. Yamashita, M. Harada, J. Misaka, M. Takeuchi, K. Ikeue, M. Anpo, Degradation of propanol diluted in water under visible light irradiation using metal ion-implanted titanium dioxide photocatalysts. *J Photochem Photobiol A* 148 (200) 257-261.
- [16] J. Zhu, W. Zheng, B. He, J. Zhang, M. Anpo. Characterization of Fe-TiO<sub>2</sub> photocatalysts synthesized by hydrothermal method and their photocatalytic reactivity for degradation of XRG dye diluted in water. *J Mol Catal A* 216 (2004) 35-43.
- [17] X. Li and F. Li, Study of Au/Au<sup>3+</sup>-TiO<sub>2</sub> photocatalysts towards visible photooxidation for water and wastewater treatment. *Environ Sci Technol* 35 (2001) 2381-2387.
- [18] M. Fuerte, A. Maira, M. Arias, M. Fernandez-Garcia, J. Conesa, J. Soria J. Visible light-activated nanosized doped-TiO<sub>2</sub> photocatalysts. *Chem Commun* 24 (2001) 2718-2719.

- [19] H. Yamashita, M. Harada, J. Misaka, Application of ion beam techniques for preparation of metal ion-implanted TiO<sub>2</sub> thin film photocatalyst available under visible light irradiation: Metal ion-implantation and ionized cluster beam method. *J Synchrotron Rad* 8 (2001) 569-571.
- [20] Z. Ambrus, N. Balazs, T. Alapi, Synthesis, structure and photocatalytic properties of Fe(III)-doped TiO<sub>2</sub> prepared from TiCl<sub>3</sub>, *Applied Catalysis B*, 81, (2008) 27–37.
- [21] W. Sun, S. Zhang, Z. Liu, C. Wang, and Z. Mao, Studies on the enhanced photocatalytic hydrogen evolution over Pt/PEG-modified TiO<sub>2</sub> photocatalysts, *International Journal of Hydrogen Energy*, 33 (2008) 1112–1117.
- [22] J. R. Xiao, T. Y. Peng, R. Li, Z. H. Peng, and C. H. Yan, Preparation, phase transformation and photocatalytic activities of cerium-doped mesoporous titania nanoparticles, *Journal of Solid State Chemistry*, 179 (2006) 1161–1170.
- [23] E. A. Kozlova and A. V. Vorontsov, Influence of mesoporous and platinum-modified titanium dioxide preparation methods on photocatalytic activity in liquid and gas phase,” *Applied Catalysis B*, vol. 77, no. 1-2, pp. 35–45, 2007.
- [24] L. Jing, B. Xin, F. Yuan, L. Xue, B. Wang and H. Fu Effects of surface oxygen vacancies on photophysical and photochemical processes of Zn-doped TiO<sub>2</sub> nanoparticles and their relationships, *J. Phys. Chem. B* 110 (2006) 17860-17865.
- [25] Y. Zhao, C. Li, X. Liu, F. Gu and H.L. Du and L. shi, Zn-doped TiO<sub>2</sub> nanoparticles with high photocatalytic activity synthesized by hydrogen–oxygen diffusion flame *Applied Catalysis B: Environmental* 79 (2008) 208-215
- [26] B. Thirupathia and G. Smirniotis, Co-doping a metal (Cr, Fe, Co, Ni, Cu, Zn, Ce, and Zr) on Mn/TiO<sub>2</sub> catalyst and its effect on the selective reduction of NO with NH<sub>3</sub> at low-temperatures, *Applied Catalysis B: Environmental* 110 (2011) 195–206.
- [27] T. Sun, J. Fan, E. Liu, Y. Wang, H. Dai, Y. Yang, W. Hou, X. Hu and Z. Jiang, Fe and Ni co-doped TiO<sub>2</sub> nanoparticles prepared by alcohol-thermal method: Application in hydrogen evolution by water splitting under visible light irradiation, *Powder Technol.* 228 (2012) 210-218.
- [28] B. Li, X. Cheng, X. Yu, L. Yan and Z. Xing, Fe-N-S-tri-Doped Photocatalyst and Its Enhanced Visible Light Photocatalytic Activity, *Advances in Materials Science and Engineering* 2012 (2012)
- [29] Z. Yuan, J. Jia, and L. Zhang, Influence of codoping of Zn (II)+Fe (III) on the photocatalytic activity of TiO<sub>2</sub> for phenol degradation, *Mater. Chem. Phys.* 73 (2002) 323–326.
- [30] N. Pal, M. Paul, A. Bhaumik, New mesoporous perovskite ZnTiO<sub>3</sub> and its excellent catalytic activity in liquid phase organic transformations, *Appl. Catal. A*, 393 (2011), 153-160.
- [31] F.H. Dulin, D.E. RasePhase equilibria in the system ZnO–TiO<sub>2</sub>, *J. Am. Ceram. Soc.* 43 (1960) 125-131.
- [32] H. Obayashi, Y. Sakurai, T. Gejo, Perovskite-type oxides as ethanol sensors, *J. Solid State Chem.*, 17 (1976) 299-303.
- [33] Z.X. Chen, A. Derking, W. Koot, M.P. van, Dehydrogenation of isobutane over zinc titanate thin film catalysts, *J. Catal.*, 161 (1996) 730-741.
- [34] S.F. Wang, F. Gu, M.K. Lü, C.F. Song, D. Xu, D.R. Yuan, S.W. Liu, Photoluminescence of sol–gel derived ZnTiO<sub>3</sub>:Ni<sup>2+</sup> nanocrystals, *Chem. Phys. Lett.*, 373 (2003) 223-227.
- [35] H.T. Kim, J.D. Byun, Y. Kim, Microstructure and microwave dielectric properties of modified zinc titanates (II) *Mater. Res. Bull.*, 33 (1998) 975-986.

- [36] Y. J. Silva, R.C. Perez, G.T. Delgado, A.M. Lopez and O.Z. Angel, Analysis of the photocatalytic activity of CdS+ZnTiO<sub>3</sub> nanocomposite films prepared by sputtering process, *Superlattices and Microstructures*, 100 (2016) 148-157.
- [37] N. Pal, M.Paul and A. Bhaumik, New mesoporous perovskite ZnTiO<sub>3</sub> and its excellent catalytic activity in liquid phase organic transformations *Applied Catalysis A: General* 393 (2011) 153-160.
- [38] C. Ke, X. Cheng, Q. Wang, Y. Wang and Z. Pan, Preparation of a photocatalytic TiO<sub>2</sub>/ZnTiO<sub>3</sub> coating on glazed ceramic tiles *Ceramics International* 40 (2014) 8891-8895.
- [39] C. Miao, M. Wang, Z. Yue and J. Zhou and Q. Li, Co-firing behavior of ZnTiO<sub>3</sub> dielectric ceramics/Ag composites for MLCCs, *Ceramics International* 32 (2006) 471-474.
- [40] Y. W. Wang, P.H. Yuan, C.M. Fan, Y. Wang, G.Y. Ding and Y. F. Wang, Preparation of zinc titanate nanoparticles and their photocatalytic behaviors in the photodegradation of humic acid in water, *Ceramics International*, 38 (2012) 4173-4180.
- [41] D. P. Dutta, Ag doped and Ag dispersed nano ZnTiO<sub>3</sub>: Improved photocatalytic organic pollutant degradation under solar irradiation and antibacterial activity *Journal of Environmental Chemical Engineering* 2, (2014) pp. 2177-2187
- [42] S. Ramandi, M.H. Entezari and N. Ghows, Sono-synthesis of solar light responsive S–N–C–tri doped TiO<sub>2</sub> photo-catalyst under optimized conditions for degradation and mineralization of Diclofenac, *Ultrasonics Sonochemistry*, 38 (2017) 234-245.
- [43] U. O. Bangwat, J. J. Wu, A. M. Asiri and S. Anandan, Sonochemical Synthesis of Mg-TiO<sub>2</sub> nanoparticles for persistent Congo red dye degradation. *J. Photochem. Photobio. A. Chem.* 346 (2017) 559-569.
- [44] T. J. Mason and J. P. Lorimer, *Applied Sonochemistry*, Wiley, VCH, Weinheim (2002).
- [45] N. Wongpisutpaisan, C. Kahattha, N. Vittayakorn, A. Ruangphanit and W. Pecharapa, Titanium Dioxide Nanostructures Synthesized by Sonochemical-hydrothermal Process, *Journal of Metals, Materials and Minerals*, 23 (2013) 19-24.
- [46] Zhang, H. Chen, G.; Bahnemann, D. W. *Journal of Materials Chemistry* 19 (2009) 5089.
- [47] Augustynski, J. *Electrochim. Acta*, 38 (1993), 43–46.
- [48] J. Zhang, P. Zhou, J. Liu and J. Yu, *Phys. Chem. Chem. Phys.* (2014) 20382–20386.
- [49] M.E. A Dompablo, A.M. Garcia and M. Taravillo, DFT+U Calculations of Crystal Lattice, Electronic Structure, and Phase Stability under Pressure of TiO<sub>2</sub> Polymorphs, *J. Chemical Physics* 135 (2011) 054503.
- [50] Z. L. Wang and J. H. Song, *Science* 312 (206) 242.
- [51] X. D. Wang, J. H. Song, J. Liu, et al., *Science* 316 (2007) 102.
- [52] U. Ozgur, Y. I. Alivov, C. Liu, A. Teke, M. A. Reshchikov, G. S. Dogan, V. Avrutin, S. J. Cho, S. and H. Morkoç, A comprehensive review of ZnO materials and devices, *Journal of Applied Physics*, 98 (2005), 041301
- [53] M. A. Pena, J. Fierro, Chemical Structures and Performance of Perovskite Oxides, *Chem. Rev.* 2001, 101, 1981.

- [54] M. A. Pena and J. L. G. Fierro, *Chem. Rev.*, 101 (2001) p.1981.
- [55] F. Galasso and W. Darby, *J. Phys. Chem.*, 66 (1962) p.131.
- [56] M. Chergui, *Structural dynamic* 4 (2017) 044002.
- [57] V. M. Goldschmidt, *Naturwissenschaften*, 1926, 14, 477.
- [58] C. Li, X. Lu, W. Ding, L. Feng, Y. Gao and Z. Guo, *Acta Crystallogr., Sect. B: Struct. Sci.*, 2008, 64, 702–707.
- [59] M. J. Herrmann, *Topics in Catalysis*, 34 (2005) 49-65.
- [60] Ristante, V. M. Prado, A. G. S. Jorge, S. M. A. Valente, J. P. S. Florentino, A. O. Padilha, P. M. *Journal of Photochemistry & Photobiology, A: Chemistry*, 195 (2008) 23-29.
- [61] Murakami, Y.; Kenji, E.; Nosaka, A. Y.; Nosaka, Y. *J. Phys. Chem. B* 108 (2006) 8751-8755.
- [62] R. Beranek *electrochemical Methods for the Determination of the Band Edge Positions of TiO<sub>2</sub>-Based Nanomaterials: Article review, Advances in Physical Chemistry* 2011 (2011), Article ID 786759,1-20.
- [63] Pilli S, Bhunia P, Yan S, LeBlanc RJ, Tyagi RD (2011) Ultrasonic pretreatment of sludge: a review. *Ultrason Sonochem* 18:1–18.
- [65] Suslick KS (1989) The chemical effect of ultrasound. *Sci. Am.* 260:80–86.
- [66] Pang YL, Abdullah AZ, Bhatia S (2011) Review on sonochemical methods in the presence of catalysts and chemical additives for treatment of organic pollutants in wastewater. *Desalination* 277:1–14
- [67] P. Chowdhury, T. Viraraghavan, Sonochemical degradation of chlorinated organic compounds, phenolic compounds and organic dyes—a review. *Sci Total Environ* 407:2474–2492
- [68] Suslick KS (1990) Sonochemistry. *Science* 247:1438–1445
- [69] B. D. Cullity, *Elements of X-ray Diffraction*. Addison-Wesley Publishing Company, London; (1987).
- [70] D. Bish and J. E. Post, *Modern Powder Diffraction*. Reviews in Mineralogy, 20. Mineralogical Society of America (1989).
- [71] H. P. Klug, and L. E. Alexander. *X-ray diffraction procedures for polycrystalline and amorphous materials*. 2nd ed. Wiley, New York (1974).
- [72] D.C. Koningsberger, R. Prins, *X-ray Absorption: Principles, Applications, Techniques of EXAFS, SEXAFS and XANES* (Wiley, New York, 1988)
- [73] G.Bunker, *Introduction to XAFS* (Cambridge University Press, Cambridge, 2010)
- [74] S.D. Kelly, D. Hesterberg, B. Ravel, Analysis of soils and minerals using X-ray absorption spectroscopy, in *Methods of Soil Analysis—Part 5: Mineralogical Methods*, Soil Science Society of America Book Series No. 5, Madison (2008).
- [75] C. S. Schnorr and M. C. Ridgway, *X-ray Absorption Spectroscopy Semiconductors*, 361 (2015) 185.
- [76] Perkampus, H.-H., *UV-VIS spectroscopy and its applications*. Springer-Verlag: Berlin ; New York, (1992) 244.
- [77] Barrett, E. P.; Joyner, L.; Halenda, P. P. *J. Am. Chem. Soc.* 73 (1951) 373.
- [78] A. Bogner, P.H. Jouneau, G. Thollet, D. Basset, C. Gauthier A history of scanning electron microscopy developments: Towards “wet-STEM” imaging *Micron* 38 (2007) 390–401.
- [79] E. Uska, *The development of the electron microscope and of electron microscopy*. Nobel Lecture (1986).

This material is reserved for educational use only, not allowed for commercial use.

Forbidden to modify the content, and cite the document when use.

- [80] T. B. Nguyen, K.S. Ryu and M. J. Hwang, studied the synthesis and High Photocatalytic activity of Zn-doped TiO<sub>2</sub> nanoparticles prepared by a novel sol-gel and ammonia-evaporation method, *Bull. Korean. Chem. Soc.* 33 (2012) 243.
- [81] M.M. Rashad, E.M Elsayed, M.S. Al-Kotb and A.E. Shalan, The structural, optical, magnetic and photocatalytic properties of transition metal ions doped TiO<sub>2</sub> nanoparticles, *J. Alloy. Comp.* 581 (2013), 71-78.
- [82] B. Choudhury, A. K. M. Islam, A. Choudhury and M. Mukherjee, The effect of oxygen vacancy and dopant concentration on the magnetic properties of high spin Co<sup>2+</sup> doped TiO<sub>2</sub> nanoparticles was studied *Journal of Magnetism and Magnetic Materials* 323(2011) 440-446. *J. Magn. Magn. Mater.* 323 (2011) 440-446.
- [83] M. Sellers and E. G. Seebauer, room temperature ferromagnetism in Mn-doped TiO<sub>2</sub> nanopillar matrices diluted magnetic semiconductors, *Matter. Lett.* 114 (2014) 44-47.
- [84] L. Wang, H. Kang, D. Xue and C. Liu, Low-temperature synthesis of ZnTiO<sub>3</sub> nanopowders, *J. Crystal. Growth* 311 (2009) 611-614.
- [85] I. Bobowska, A. Opasinska, A. Wypych and P. Wojciechowski, showed the synthesis and dielectric investigations of ZnTiO<sub>3</sub> obtained by a soft chemistry route, *Matter. Chem. Phys.* 134 (2012) 87-92.
- [86] R.S.Raveendra, P.A.Prashanth, R.H. Krishna, N.P.Bhagya, B.M.Nagabhushana, H.Raja Naika, K.Lingaraju, H.Nagabhushana, and B.Daruka Prasad, synthesis, structural characterization of nano ZnTiO<sub>3</sub> ceramic with effective azo dye adsorbent and antibacterial agent, *J. Asian Ceramic Societies*, 2 (2014) 357-365.
- [87] D. P. Dutta, A. Singh and A.K.T yagi, Ag doped and Ag dispersed nano ZnTiO<sub>3</sub> ceramics: Improve photocatalytic organic pollutant degradation under solar irradiation and antibacterial activity *J. Environ. Chem. Eng.* 2 (2014) 2177-2187.
- [88] W. Jiang, X. Zhang, X. Gong, F. Yan and Z. Zhang, the sonochemical synthesis and characterization of magnetic separable Fe<sub>3</sub>O<sub>4</sub>-TiO<sub>2</sub> nanocomposites and their catalytic properties, *International Journal of smart and Nanomaterials*, 1 (2010).
- [89] A. D. Hanaor. and C. C. Sorrell, Review of the anatase to rutile phase transformation. *J. Mater. Sci.* 46 6823-6829 (2011).
- [90] J. Tauc, *Amorphous and Liquid Semiconductors*. Plenum Press, London and New York; (1974).
- [91] C. Biswajit. and C. Amarjyoti, Oxygen defect dependent variation of band gap, Urbach energy and luminescence property of anatase, anatase-rutile mixed phase and of rutile phases of TiO<sub>2</sub> nanoparticles. *Physica E.* 56, 364-371 (2014).
- [92] R. D. Shannon and C. T. Prewitt, *Acta Cryst.* B25 (1969), 925-946.
- [93] P. C. Angelome, L. Andriani, M. E. Calvo, F. Requejo, S. Bilmes and G. J. Soler-Illia, Mesoporous Anatase TiO<sub>2</sub> Films: Use of Ti K XANES for the Quantification of the Nanocrystalline Character and Substrate Effects in the Photocatalysis Behavior, *J. Phys. Chem. C* 111 (2007) 10886-10893.
- [94] T. Yamamoto, Assignment of pre-edge peaks in K-edge X-ray absorption spectra of 3d transition metal compounds: Electric dipole or quadrupole X-Ray Spectrometry, 37, 6, pp. 572-584, 2008.

- [95] P. C. Angelome, L. Andrini, M. E. Calvo, F. Requejo, S. Bilmes and G. J. Soler-Illia, Mesoporous Anatase TiO<sub>2</sub> Films: Use of Ti K XANES for the Quantification of the Nanocrystalline Character and Substrate Effects in the Photocatalysis Behavior, *J. Phys. Chem. C* 111 (2007) 10886-10893.
- [96] F. Farges, G. E. Brown and J. J. Rehr, Ti K-edge XANES studies of Ti coordination and disorder in oxide compounds: comparison theory and experiment, *Phys. Rev. B* 56 (1997) 1809–1819.
- [97] Zn occupied T. Yamamoto, “Assignment of pre-edge peaks in K-edge X-ray absorption spectra of 3d transition metal compounds: Electric dipole or quadrupole?” *X-Ray Spectrometry*, 37 (2008) 572–584.
- [98] G. Sadanandam, K. Lalitha, V.D. Kumari, M.V. Shankar, M. Subrahmanyam, Cobalt doped TiO<sub>2</sub>: a stable and efficient photocatalyst for continuous hydrogen production from glycerol: water mixtures under solar light irradiation, *Int. J. Hydrogen Energy* 38 (23) (2013) 9655–9664.
- [99] F. Chen, J. Zhao, and H. Hidaka, Highly selective deethylation of rhodamine B: Adsorption and photooxidation pathways of the dye on the TiO<sub>2</sub>/SiO<sub>2</sub> composite photocatalyst, *International Journal of Photoenergy* 5 (2005) 209-217.
- [100] X. Li and J. Ye, Photocatalytic degradation of Rhodamine B over Pb<sub>3</sub>Nb<sub>4</sub>O<sub>13</sub>/fumed SiO<sub>2</sub>, composite under visible light irradiation, *Journal of Physical chemistry. C* 111 (2007) 13109-13116.
- [101] T. Liu, L. Wang, X. Lu, J. Fan, X. Cai, B. Gao, R. Miao, J. Wang and Y. Lv, Comparative study of the photocatalytic performance for the degradation of different dyes by ZnIn<sub>2</sub>S<sub>4</sub>: adsorption, active species, and pathways *RSC Adv*, 7 (2017) 12292-12300.
- [102] L. Wang, X. Zhang, P. Zhang, Z. Cao and J. Hu, Photoelectric conversion performances of Mn doped TiO<sub>2</sub> under >420 nm visible light irradiation, *Journal of Saudi Chemical Society* 19 (2015), 595–601.
- [103] A. Ajmal, I. Majeed, R. N. Malik, H. Idriss and M. A. Nadeem, *RSC Adv*. 4 (2014) 37003-37026.
- [104] J. Zhu, F. Chen, J. Zhang, H. Chen and M. Anpo, *J. Photochem. Photobiol. A. Chem.* 180 (2006) 196-204.
- [105] L. Hou et al., “Formation and transformation of ZnTiO<sub>3</sub> prepared by sol-gel process,” *Mater. Lett.* 59 (2005). 197–200.
- [106] T. Yamamoto, Assignment of pre-edge peaks in K-edge X-ray absorption spectra of 3d transition metal compounds: Electric dipole or quadrupole, *X-Ray Spectrometry*, vol. 37, no. 6, pp. 572–584, 2008.
- [107] G. Akgül, Synthesis and structural characterization of zinc titanates, *J. Molecular Struct.*, vol. 1037, pp. 35–39, Apr. 2013.
- [108] X. Yan, V. Zhao, Y. Zhou, Z. Wu, J. Yuan, W. Li, Synthesis and characterization of ZnTiO<sub>3</sub> with high photocatalytic activity, *Transactions of Nonferrous Metals Society of China* 25 (2015) 2272-2278.
- [109] J. Z. Kong, Preparation, characterization and photocatalytic properties of ZnTiO<sub>3</sub> powders, *J. Hazardous Mater.* 171 (2009) 918–923.
- [110] Y.W. Wang, P.-H. Yuan, C.M. Fan, Y. Wang, G.-Y. Ding, and Y.-F. Wang, Preparation of zinc titanate nanoparticles and their photocatalytic behaviors in the photodegradation of humic acid in water, *Ceram. Int.*, vol. 38, 4173–4180, Jul. 2012
- [111] R. S. Raveendra, Synthesis, structural characterization of nano ZnTiO<sub>3</sub> ceramic: An effective azo dye adsorbent and antibacterial agent, *J. Asian Ceram. Soc.* 2 (2014) 357–365.
- [112] T. Yamamoto, *X-ray Spectrometry*, *X-ray Spectrum* 37, 572 (2008).

This material is reserved for educational use only, not allowed for commercial use.

Forbidden to modify the content, and cite the document when use.

- [113] B. Ravel, A practical introduction to multiple scattering theory, *Journal of Alloys and Compounds*, 401 (2005) 118-126.
- [114] B. Ravel and E. A. Stern, Local disorder and near edge structure in titanate perovskites, *Physica B: Condensed Matter* 208–209 (1995) 316-318.
- [115] Rongliang He, Rosalie K. Hocking and T. Tsuzuki, *J Matter. Sci.* 47 (2012) 3150-3158.
- [116] L. Samet, J. B. Nasserur, R. Chtourou, K. March, and O. Stephan, *Mater. Charact.* 85, 1 (2013).
- [117] A. Molea, V. Popescu, and N. R. Anthony, *Powder. Technol.* 230, 203 (2012).



This material is reserved for educational use only, not allowed for commercial use.

Forbidden to modify the content, and cite the document when use.



This material is reserved for educational use only, not allowed for commercial use.

Forbidden to modify the content, and cite the document when use.

# Synthesis and Characterization of Zn-Doped TiO<sub>2</sub> Nanoparticles via Sonochemical Method

C. Wattanawikkam & W. Pecharapa

To cite this article: C. Wattanawikkam & W. Pecharapa (2015) Synthesis and Characterization of Zn-Doped TiO<sub>2</sub> Nanoparticles via Sonochemical Method, Integrated Ferroelectrics, 165:1, 167-175, DOI: [10.1080/10584587.2015.1063928](https://doi.org/10.1080/10584587.2015.1063928)

To link to this article: <http://dx.doi.org/10.1080/10584587.2015.1063928>



Published online: 22 Oct 2015.



Submit your article to this journal [↗](#)



Article views: 8



View related articles [↗](#)



View Crossmark data [↗](#)

# Synthesis and Characterization of Zn-Doped TiO<sub>2</sub> Nanoparticles via Sonochemical Method

C. WATTANAWIKKAM AND W. PECHARAPA\*

College of Nanotechnology, King Mongkut's Institute of Technology  
Ladkrabang, Bangkok 10520, Thailand

*Zn-doped TiO<sub>2</sub> nanoparticles were successfully fabricated using sonochemical method accompanying post calcination process. Titanium isopropoxide (Ti[OC<sub>3</sub>H<sub>7</sub>]<sub>4</sub>) and Zinc chloride (ZnCl<sub>2</sub>) were used as starting precursors for Ti and Zn sources, respectively. The homogeneous mixing solution of different Zn (0–1 mol%) and Ti ratio were irradiated in high intensity ultrasound sonometer (750 W 20 kHz) for 30 min at room temperature to obtain as-synthesized Zn-doped TiO<sub>2</sub> nanoparticles followed by calcination at 400–700°C. To evaluate the structure and phase identification of prepared powders, the X-ray diffraction (XRD) and Raman spectroscopy were employed. The results reveal that the as-synthesized Zn-doped TiO<sub>2</sub> nanoparticles are in anatase phase and their crystallinity increases with increasing calcined temperature. The morphology of as-synthesized powders was investigated by transmission electron microscope (TEM). The effect of Zn content and calcinations temperature on TiO<sub>2</sub> properties was also discussed.*

**Keywords** Sonochemical; Zn-doped TiO<sub>2</sub>; nanoparticles

## 1. Introduction

In recent years, dye-sensitized solar cells (DSSC) based on TiO<sub>2</sub> electrode layer have attractive considerable interest due to their relatively high efficiency and cost-effective fabrication [1–6]. In general, DSSCs are composed of a layer of TiO<sub>2</sub> nanoparticles with rather high surface area acting as photoanode covered by a monolayer of dye molecule, a redox and counter electrode. In DSSC, the TiO<sub>2</sub> layer plays a major role in defining the performance of DSSC by collecting and transporting the photoelectrons that are injected from the photo excited dye of TiO<sub>2</sub> conduction band to the conducting substrate and then to the external circuit [7–8]. High injection of electrons results to good performance of DSSCs because the increasing of injection electron concentration could consequently enhance the electron transport efficiency and promote an improved short circuit current [9]. To enhance TiO<sub>2</sub> performance in DSSCs, many pioneered works have been devoted such as decreasing of large band gap of TiO<sub>2</sub> by doping foreign ion into the TiO<sub>2</sub> lattice. During recent years many researches have attained successful works regarding doping different ions into the TiO<sub>2</sub> lattice. Previous studies suggested that the incorporation of Zn<sup>2+</sup> to TiO<sub>2</sub> host led to a significant increase of photoelectric properties [10–16]. Since, a number of valence electrons of Zn<sup>2+</sup> is lower than Ti<sup>4+</sup>, the excess of hole can create

Received December 22, 2014; in final form May 22, 2015.

\*Corresponding authors. E-mail: ithree43@gmail.com; kpewisan@gmail.com

Color versions of one or more of the figures in the article can be found online at [www.tandfonline.com/ginf](http://www.tandfonline.com/ginf).

an acceptor band near that of the TiO<sub>2</sub>. Y. Zhang *et al.* [10] had recently fabricated the Zn-doped TiO<sub>2</sub> layer (with Zn = 0-1%) served as a photoanode. They revealed that the slightly doping content of Zn (0.5-1%) ion can promote the increasing photoelectron concentrations and also separation of the photo-generated charge as well as restrain the recombinations. A.H. Ghanbari *et al.* [11] additionally reported that the introduction of Zn into TiO<sub>2</sub> resulted to the enhancement of electron injection and photon capture assisted by light scattering effect. K.P. Wang *et al.* synchronously [12] expressed that the insertion of Zn ions into the titania layer had capability to heighten electron transport performance in DSSCs.

Recently, different methods have been employed to prepare Zn-doped TiO<sub>2</sub> nanostructures, such as thermal hydrolysis [9] and sol-precipitate method [13–16]. Sonochemical method is one of alternatively effective process for the fabrication of functional nanomaterials owing to simplicity of apparatus, low equipment cost and ease to synthesis [14–20]. The sonochemical method typically applies high frequency of ultrasonic wave to initiate chemical reaction of the starting precursor and induce the particle formation during irradiation. The sonication acoustic cavitation phenomenon generates cavities in the liquid solution of reactants. The cavitations processes consist of the creation, growth and implosive collapse of gas vacuoles in the solution. According to the hot-spot theory, extreme temperature and high pressure occur in the bubbles during the cavitation collapse [21]. However, from the literature survey, the Zn-doped TiO<sub>2</sub> nanoparticles prepared by the sonochemical method have not yet been studied. In this paper, an effort has been made to synthesize of Zn-doped TiO<sub>2</sub> nanoparticles via the sonochemical method accompanying calcinations and to investigate the effect of Zn doping content and calcination temperature on phase structure, microstructure and optical properties of Zn-doped TiO<sub>2</sub> nanoparticles that could be potential photoanode material for DSSCs application.

## 2. Experimental Details

Titanium isopropoxide (Ti[OC<sub>3</sub>H<sub>7</sub>]<sub>4</sub>, TIIP 97%) and Zinc chloride (ZnCl<sub>2</sub>) were used as precursors for Ti and Zn source, respectively. TIIP was dissolved in absolute ethanol (99.7%) and acetylacetone under stirring for 15 min. ZnCl<sub>2</sub> was slowly added into the solutions under vigorous stirring for 30 min to obtain the homogenous mixing solution. The mixing solution and deionized water was mixed together in the sonometer chamber as a ratio of 1:1. Then the mixed solution was irradiated with high intensity ultrasound sonometer (750 W 20 kHz) at room temperature for 30 min until the completely precipitated product was obtained. After cooling down to room temperature, the completely precipitated product was washed using deionized water. After that the cleaned precipitate was dried at 100°C for 12 h to remove moisture and contaminants. Then, the as-synthesized powders were calcined at 450–700°C for 2 h. To evaluate of the structure and phase identification of as-synthesized powders, the X-ray diffraction (XRD) and Raman spectroscopy were used. The microstructure was investigated by transmission electron microscope (TEM) meanwhile the optical properties were studied by typical UV-vis spectroscopy.

## 3. Results and Discussion

The crystal structures of as-synthesized and after-calcined Zn-doped TiO<sub>2</sub> powder at various calcinations temperature were studied by X-ray diffraction analysis and the corresponding

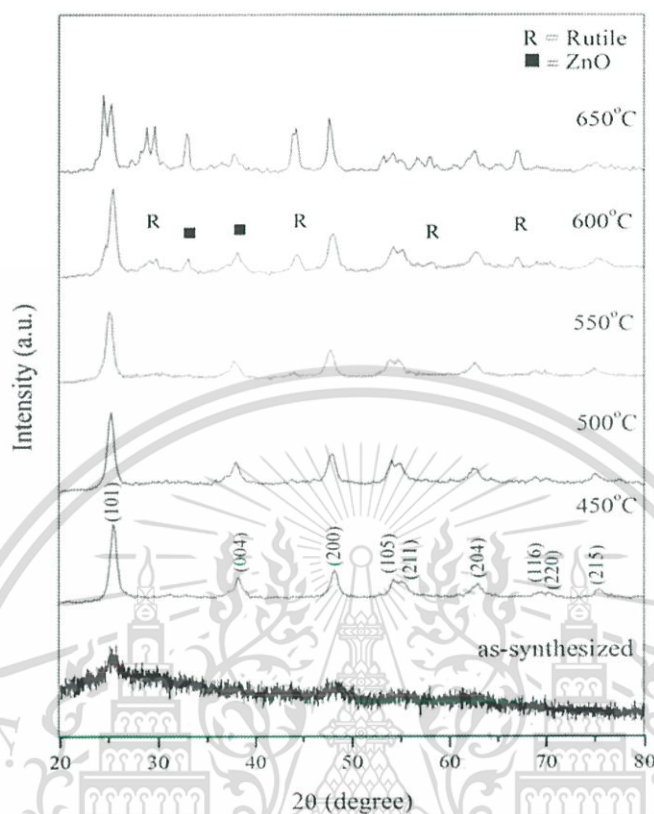
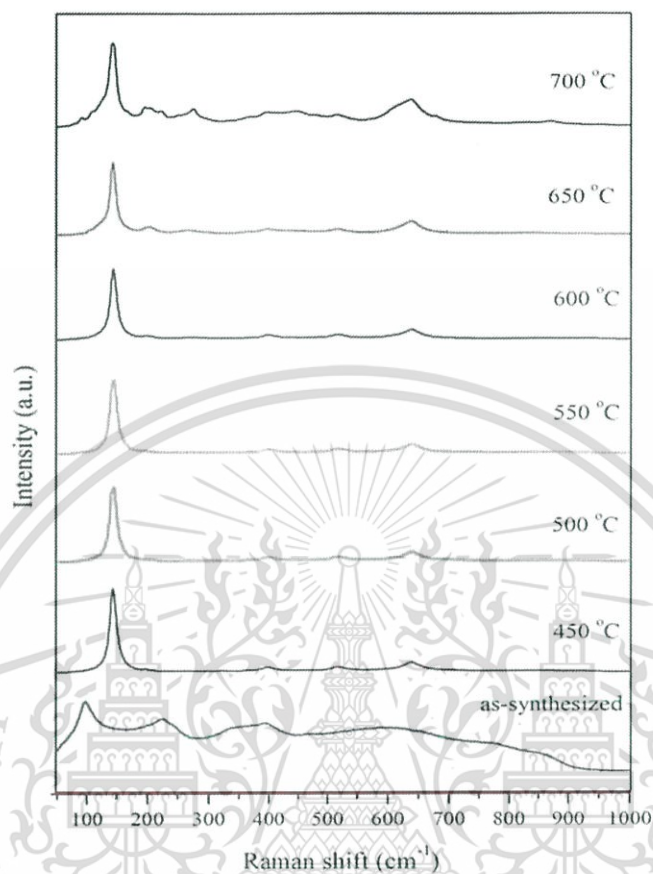


Figure 1. XRD patterns of as-synthesized and after calcined of Zn-doped TiO<sub>2</sub> nanoparticles.

results are illustrated in Fig. 1. It can be seen that the as-synthesized powders showed a small peak at around  $2\theta = 25.2^\circ$ ,  $48.2^\circ$  and  $62.5^\circ$ , which corresponded to (101), (200) and (204) plane of the anatase TiO<sub>2</sub> phase, respectively. The results indicated the as-sonochemically synthesized fine-nanopowders of TiO<sub>2</sub> could be fabricated by one-step sonochemical process using the sonication time of 30 min without heat treatment process. The formation mechanism of crystalline phase Zn-doped TiO<sub>2</sub> during the sonochemical process could be initiated by cavitation effect during high frequency ultrasound wave radiation via sudden collision forced by intense ultrasound energy. This collision is able to swiftly raise localized dominantly high temperature region, which speeds up the condensation of hydroxyl or intermediate hydroxide group to generate the nucleation of fine Zn-doped TiO<sub>2</sub> nanoparticles. For the samples calcined at 450–550°C, it is observed that the samples possess pronounce characteristic diffraction peaks with increasing peak intensity indicating the amelioration of crystallinity and anatase phase by calcinations process. As the calcination temperature elevated to 600°C, the rutile phase of TiO<sub>2</sub> and the secondary phase of ZnO were noticeably observed. This feature is because the anatase TiO<sub>2</sub> phase transforms into the rutile TiO<sub>2</sub> phase at this specific temperature vicinity [22]. In addition, the formation of ZnO phase was also initiated as the temperature raised to 600°C. This formation may be attributed sufficient supplied thermal energy into the matrix that can induce the bonding between substituted Zn ion and surrounding oxygen atoms, leading to the formation of separated phase of ZnO. The crystallite size ( $D$ ) of crystalline anatase and rutile phase was estimated



**Figure 2.** Raman spectra of as-synthesized and calcined Zn-doped TiO<sub>2</sub> nanoparticles.



**Figure 3.** TEM image of as-synthesized powder synthesized by sonochemical method with sonication time of 30 min.

**Table 1**  
Crystal sizes of Zn-doped TiO<sub>2</sub> nanoparticles.

Temperature (°C)	Crystal size (nm)
450	7.1
500	7.5
550	7.8
600	8.9
650	9.2
700	9.8

by Scherrer's equation as follows [23]

$$D = \frac{0.9\lambda}{\beta \cos \theta} \quad (1)$$

Note that  $D$  is the crystallite size,  $K$  is the shape factor (0.9),  $\lambda$  is the X-ray wavelength of Cu  $K_{\alpha}$  (0.154 nm),  $\beta$  is the full-width at half maximum (FWHM) and  $\theta$  is the diffraction angle of the major peak of anatase phase located at  $2\theta = 25.4^{\circ}$ . The average crystallite size of Zn-doped TiO<sub>2</sub> nanoparticles slightly increase with increasing calcinations temperature as shown in Table 1. This result indicates that the calcinations temperature significantly affects the crystal of Zn-doped TiO<sub>2</sub> nanopowders.

Fig. 2 shows Raman spectra of as-synthesized and calcined samples at various temperatures. Raman spectra of as-synthesized and samples calcined at 450–550°C for 2 h show the prominent bands assigned to the modes of anatase TiO<sub>2</sub>. The dominant bands assigned to E<sub>g</sub> modes are centered at 145 cm<sup>-1</sup> and 638 cm<sup>-1</sup>. The bands positioned at 397 cm<sup>-1</sup> and 516 cm<sup>-1</sup> are attributed to B<sub>1g</sub> and A<sub>1g</sub> modes. As calcination temperature increases to be beyond 550°C, the results exhibited mixing of anatase-rutile phase and secondary phase

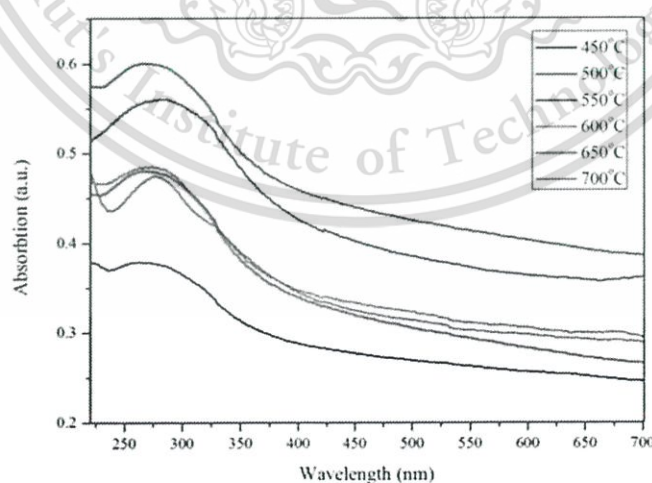


**Figure 4.** UV-vis absorbance spectra of Zn-doped TiO<sub>2</sub> nanoparticles.

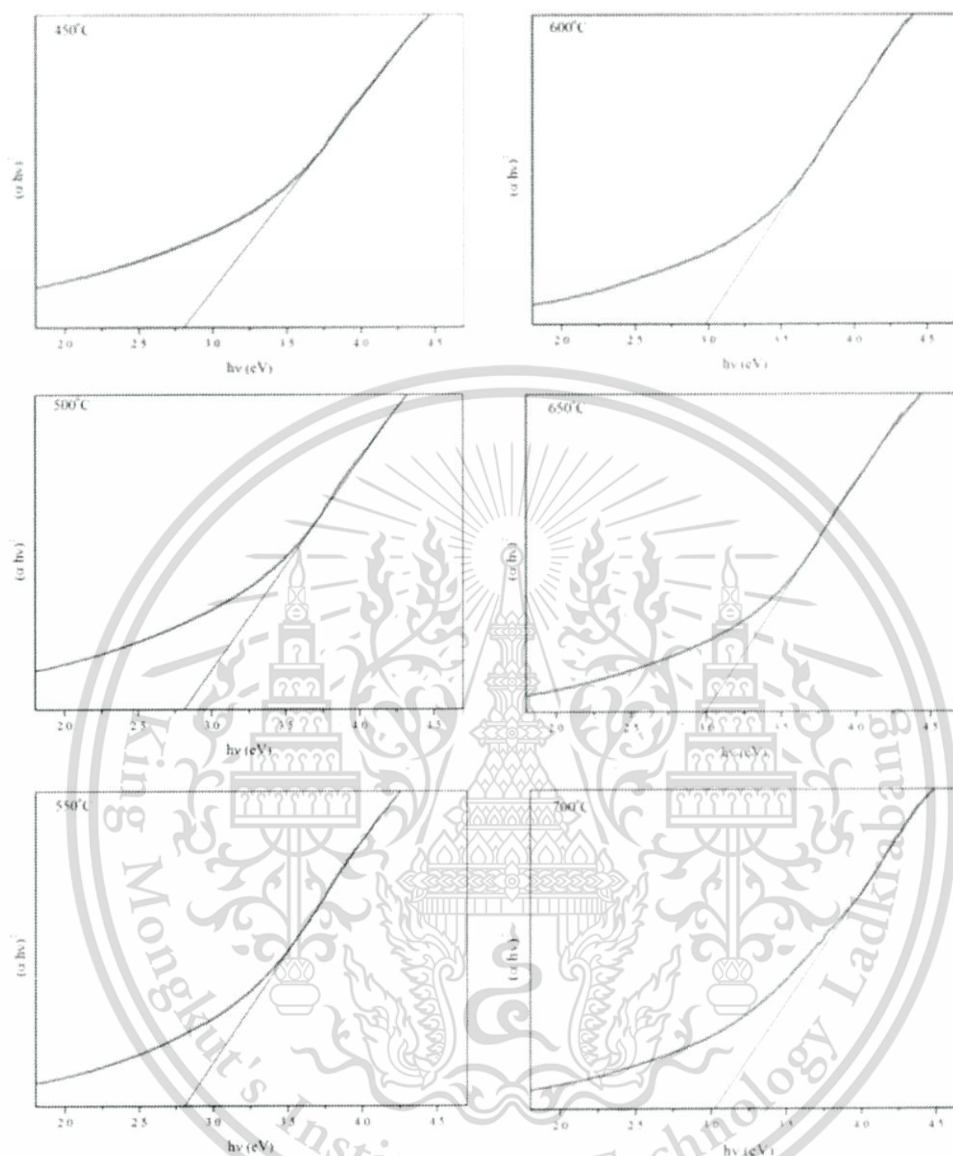


Figure 5. Optical band gaps of Zn-doped  $\text{TiO}_2$  nanoparticles calcined at different temperatures.

of ZnO with the corresponding band peaks around  $200\text{ cm}^{-1}$ ,  $270\text{ cm}^{-1}$  and  $445\text{ cm}^{-1}$  [20,24]. It is indicated that the Raman results are in good accordance with the XRD results.

As observed in Fig. 3, TEM image reveals the morphology of nanocrystalline of as-synthesized Zn-doped  $\text{TiO}_2$  fine powder. It is clearly seen that the fine as-synthesized nanopowders have nearly spherical shape with the average size is about 10–15 nm. The TEM results confirm that the highly intense of ultrasound energy provided during sonochemical process can create the uniform fine nanoparticles of Zn-doped  $\text{TiO}_2$ .

The optical absorbance spectra of Zn-doped  $\text{TiO}_2$  nanoparticles in a wavelength range of 200–700 nm are displayed in Fig. 4. It can be seen that the optical absorption of all

samples starts at about 370 nm, indicating the semiconducting feature with direct bandgap of the samples. The UV-vis absorbance of doped samples significantly shifts to a longer wavelength when comparing to pure TiO<sub>2</sub> [25]. It could be deduced that the incorporation of low content of Zn ion into TiO<sub>2</sub> may significantly lower the effective optical band gap of TiO<sub>2</sub> by extending its absorption band to visible region, that can enhance its performance in solar energy harvest. The good substitution of Zn ions may create the defect sites and corresponding defect band tail between valence band and conduction band of TiO<sub>2</sub>, that consequently reduces its effective band gap. The optical band gap energy ( $E_g$ ) was determined from absorbance spectra using the Tauc's equation [26], given as

$$(\alpha h\nu) = A(h\nu - E_g)^n$$

where  $\alpha$  is absorption coefficient,  $\nu$  is light frequency,  $h$  is Planck's constant,  $A$  is proportionality constant,  $E_g$  is band gap energy and exponent  $n$  depends on type of transition. For a direct-allowed transition,  $n = 1/2$ , for an indirect-allowed transition,  $n = 2$  and for indirect forbidden transition,  $n = 3/2$ . For TiO<sub>2</sub>, known as a direct semiconductor,  $n$  was chosen as  $1/2$ . The optical band gap of samples estimated by intercept of slope to x-axis from plot of  $(\alpha h\nu)^2$  versus the photon energy  $h\nu$  are shown in Fig 5. It is noticed that the correlated band gap energy of the sample tends to increase with increasing calcined temperature, i.e. at values of 2.82, 2.83, 2.85, 2.95, 2.98 and 3.02 eV for the sample calcined at 450, 500, 550, 600, 650 and 700°C, respectively. This feature may be originated from the fact that, at elevated temperature, the separated phase of ZnO takes place and the sample becomes intermixture of TiO<sub>2</sub> and ZnO that would cause the alternation the optical band gap of TiO<sub>2</sub>. The other possibility for this increment in optical band gap with increasing temperature is the anatase-to-rutile mixed phase of TiO<sub>2</sub> [27].

#### 4. Conclusion

Nanocrystalline Zn-doped TiO<sub>2</sub> particles were synthesized by effective sonochemical method using the sonication time for 30 min. The pure anatase TiO<sub>2</sub> phase with a high crystallinity of nanoparticles can be obtained after calcination process at moderate temperature of 450–550°C for 2 h. At the calcination temperature above 550°C, the rutile phase and impurity phase of ZnO were detected. The morphology of as-synthesized fine powder monitored by TEM displays the average particle size in the range of 10–15 nm. The energy gaps of calcined samples are found to be increased with increasing calcination temperature. The incorporation of Zn ions into the TiO<sub>2</sub> lattice can extend its effective band gap into the visible region. The calcination temperature and Zn dopant have considerable influence on the structure phase, and optical properties of TiO<sub>2</sub> nanoparticles.

#### Acknowledgments

Authors gratefully acknowledge the support from College of Nanotechnology, King Mongkut's Institute of Technology Ladkrabang.

#### Funding

This work has been partially supported by Thailand Research Fund (TRF) through the Royal Golden Jubilee Ph.D. Program (Grant No. PHD/0193/2556) and KMITL research fund.

## References

1. M. S. Kang, Y. J. Kim, J. Won and Y. and S. Kang, Roles of terminal groups of oligomer electrolytes in determining photovoltaic performances of dye-sensitized solar cells. *Chem. Commun.* **21**, 2686–2688 (2005).
2. B. O'Regan. and M. Gratzel, A low-cost, high-efficiency solar cell based on dye-sensitized colloidal TiO<sub>2</sub> films. *Nature.* **353**, 737–739 (1991).
3. F. Sauvage, D. H. Chen, P. Comte, F. Z. Huang, L. P. Heiniger, Y. B. Cheng, R. A. Caruso. and M. Gratzel, Dye-Sensitized solar cells employing a single film of mesoporous TiO<sub>2</sub> Beads achieve power conversion efficiencies over 10%. *ACS. Nano.* **4** 442–4425 (2010).
4. C. Shen, Z. Q. Ma, L. Shen, L. Zhao, F. Xu, Y. H. Li, Z. X. Zhao, F. Hong. and W. Wu, Fabrication of highly oriented TiO<sub>2</sub> nanotube arrays and their application in DSSC. *Integr. Ferroelectr.* **128**, 130–134 (2011).
5. H. J. Jo, Y. C. Choi, D. K. Lee, S. H. Lee, N. K. Park, T. J. Lee. and J. H. Kim, Synthesis and photovoltaic properties of mesoporous TiO<sub>2</sub> for the dye-sensitized solar cell. *Mol. Cryst. Liq. Cryst.* **512**, 92–98 (2009).
6. Q. Kang, S. Liu, L. Yang. and Q. Cai, The photoelectric performances of TiO<sub>2</sub> nanotube arrays-sensitized with organometallic complexes. *Anal. Lett.* **44**, 1371–1380 (2011).
7. X. Chen and S. S. Mao, Titanium dioxide nanomaterials: synthesis, properties, modifications, and applications. *Chem. Rev.* **107** (7), 2891–2959 (2007).
8. D. Wang, B. Yu, C. Wang, F. Zhou and W. Liu, A novel protocol toward perfect alignment of anodized TiO<sub>2</sub> nanotubes. *Adv. Mater.* **21**, 1964–1967 (2009).
9. H. H. Ou, S. L. Lo. and Sep. Purif, Review of titania nanotubes synthesized via the hydrothermal treatment: Fabrication, modification, and application. *Technol.* **58**, 179–191 (2007).
10. D. Zhang, enhancement of the photocatalytic activity of modified TiO<sub>2</sub> nanoparticles with Zn<sup>2+</sup> correlation between structure and properties. *Russ. J. Phys. Chem. A* **86**, 489–494 (2012).
11. A. H. Ghanbari, A. M. Bakhshayesh. and M. R. Mohammadi, Double-layer dye-sensitized solar cells based on Zn-doped TiO<sub>2</sub> transparent and light scattering layers: Improving electron injection and light scattering effect Solar Energy. *Sol. Energ.* **103**, 210–222 (2014).
12. K. P. Wang. and H. S. Teng, Zinc-doping in TiO<sub>2</sub> films to enhance electron transport in dye-sensitized solar cells under low-intensity illumination. *Chem. Phys.* **11**, 9489–9496 (2009).
13. L. Yang, Y. Lin, J. Jia, X. Xiao, X. Li. and X. Zhou, Light harvesting enhancement for dye-sensitized solar cells by novel anode containing cauliflower-like TiO<sub>2</sub> spheres. *J. Power. Sources.* **182**, 370–376 (2008).
14. F. Zhu, P. Zhang, X. Wu, L. Fu, J. Zhang. and D. Xu, The origin of higher open-circuit voltage in Zn-doped TiO<sub>2</sub> nanoparticle-based dyesensitized solar cells. *Chem. Phys. Chem.* **13**, 3731–3737 (2012).
15. Y. Zhang, L. Wang, B. Liu, J. Zhai, H. Fan, D. Wang, Y. Lin. and T. Xie, Synthesis of Zn-doped TiO<sub>2</sub> microspheres with enhanced photovoltaic performance and application for dye-sensitized solar cells. *Electrochim. Acta.* **56**, 6517–6523 (2011).
16. M. R. Mohammadi. and D. J. Fray, Low temperature nanostructured zinc titanate by an aqueous particulate sol-gel route: Optimization of heat treatment condition based on Zn:Ti molar ratio. *J. Eur. Ceram. Soc.* **30**, 947–961 (2010).
17. A. H. Roshan, S. M. Kazemzadeh, M. R. Vaezi. and A. Shokuhfar, The effect of sonication power on the sonochemical synthesis of titania nanoparticles. *Ceram. Process.* **12**, 299–303 (2011).
18. S. Vuttivong, S. Niemcharoen, P. Seeharaj, W. Vittayakorn. and N. Vittayakorn, Sonochemical synthesis of spherical BaTiO<sub>3</sub> nanoparticles. *Ferroelectrics* **457**, 44–52 (2013).
19. N. Wongpisutpaisan, N. Vittayakorn, A. Ruangphanit. and W. Pecharapa, CaCu<sub>3</sub>Ti<sub>14</sub>O<sub>12</sub> ceramics synthesized by sonochemical-assisted process. *Integr. Ferroelectr.* **149**, 56–60 (2013).
20. C. Kahattha, N. Wongpisutpaisan, N. Vittayakorn. and W. Pecharapa, Physical properties of V-doped TiO<sub>2</sub> nanoparticles synthesized by sonochemical-assisted process. *Ceram. Int.* **39**, S389–393 (2013).

21. T. J. Mason. and J. P. Lorimer, *The Uses of Power Ultrasound in Chemistry and Processing*. Applied Sonochemistry. Wiley, VCH, Weinheim. (2002).
22. A. D. Hanaor. and C. C. Sorrell, Review of the anatase to rutile phase transformation. *J. Mater. Sci.* **46** 6823–6829 (2011).
23. B. D. Cullity, *Elements of X-ray Diffraction*. Addison-Wesley Publishing Company, London; (1987).
24. N. Thaweesaeng, S. Suphankij, W. Techitdheera. and W. Pecharapa, Structural properties of Cu-doped ZnO nanopowder synthesized by co-precipitation method. *Energ. Proc.* **34**, 682–688 (2013).
25. S. Valencia, J. M. Marín. and G. Restrepo, Study of the band gap of synthesized titanium dioxide nanoparticles using the sol-gel method and a hydrothermal treatment. *Mater. Sci.* **4**, 9–14 (2010).
26. J. Tauc, *Amorphous and Liquid Semiconductors*. Plenum Press, London and New York; (1974).
27. C. Biswajit. and C. Amarjyoti, Oxygen defect dependent variation of band gap, Urbach energy and luminescence property of anatase, anatase-rutile mixed phase and of rutile phases of TiO<sub>2</sub> nanoparticles. *Physica E.* **56**, 364–371 (2014).



# Sonochemical Synthesis, Characterization, and Photocatalytic Activity of Perovskite ZnTiO<sub>3</sub> Nanopowders

Chakkaphan Wattanawikkam and Wisanu Pecharapa

**Abstract**—Perovskite zinc titanate (ZnTiO<sub>3</sub>) nanopowders were synthesized using the sonochemical method combined with calcinations at 500 °C and 900 °C for 2 h to improve their crystallinity. The effect of calcination temperature on their structural, optical, and photocatalytic properties has been studied. The cubic phase and the mixing phase of cubic and hexagonal were observed in sample calcined at 600 °C and 700 °C, respectively, while the spinel ZnTiO<sub>3</sub> and rutile TiO<sub>2</sub> phase arises in sample calcined over 700 °C. The valence state was investigated by the X-ray absorption near-edge spectroscopy technique, and the corresponding results indicate the existence of Zn<sup>2+</sup> and Ti<sup>4+</sup> in the powders. The chemical states of the samples were scrutinized by X-ray photoelectron spectroscopy. The average particle size is approximately 20–240 nm. The excellent photocatalytic performance of ZnTiO<sub>3</sub> nanoparticle calcined at 700 °C gave complete degradation Rhodamine B (RhB) in 75 min under ultraviolet light exposure with the *k* rate of 0.033 min<sup>-1</sup> and 55% of decolorization RhB in 210 min under visible irradiation. The sample calcined at 700 °C ensures a good dielectric permittivity with a value 20 and the loss tangent of about 10<sup>-2</sup>.

**Index Terms**—Perovskite, sonochemical method, X-ray absorption near-edge spectroscopy (XANES), zinc titanate (ZnTiO<sub>3</sub>) nanoparticles.

## I. INTRODUCTION

WIDE bandgap semiconductor of titanium-based oxides with a general formula of ATiO<sub>3</sub> has been the subject of numerous applications for over decades due to their outstanding electrical, chemical, and optical properties [1]. Recent studies have revealed that zinc titanate (ZnTiO<sub>3</sub>) is a potential functional material for catalytic sorbent, dielectric material for microwave devices, paint pigment, and CO and NO sensing and photoluminescence material [2]–[6]. ZnTiO<sub>3</sub> is an ABO<sub>3</sub> perovskite oxide material having BO<sub>6</sub> octahedral with cations A<sup>2+</sup> inserting in the framework. This compound belongs to the binary system of ZnO–TiO<sub>2</sub> that typically exists in three compounds, including perovskite ZnTiO<sub>3</sub> (cubic and hexagonal), spinel Zn<sub>2</sub>TiO<sub>4</sub> (cubic and tetragonal), and

defect spinel Zn<sub>2</sub>Ti<sub>3</sub>O<sub>8</sub> (cubic) [7]–[10]. The cubic perovskite has thermodynamically stability at low temperature and it would decompose into spinel Zn<sub>2</sub>TiO<sub>4</sub> and rutile phase at around 950 °C. At higher temperature, ZnO can transform to volatile Zn element resulting in a deficiency of Zn in ZnTiO<sub>3</sub>, which becomes substoichiometric and consequently results to its decomposition [11]. Therefore, it is still a challenge to develop the novel process to fabricate high purity perovskite ZnTiO<sub>3</sub> nanoparticle at lower temperature.

Recently, various synthesis techniques, including solid-state reaction method, evaporation-induced self-assembly, chemical bath deposition, and sol–gel method, have been employed to synthesize Zn–Ti–O compounds [10]–[12]. Wang *et al.* [10] prepared ZnTiO<sub>3</sub> nanopowders by a sol–gel process combined with calcinations at 800 °C and investigated their photocatalytic behavior in the photodegradation of humic acid. Bobowska *et al.* [11] synthesized ZnTiO<sub>3</sub> ceramics by soft chemical route and studied its dielectric properties. They reported that the prepared ceramics had the dielectric permittivity ( $\epsilon$ ) of 25 and the low-loss factor ( $\tan \delta$ ) < 10<sup>-3</sup> at the frequency of 1.15 GHz.

Recently, the considerable attention has been focused on the application of ultrasound in advanced chemical synthesis for the fabrication of ultrafine nanoparticle materials [13]. The sonochemical process is sonoluminescence applications, which is a high-emission phenomenon assigned with the collapse of bubble oscillating under high ultrasonic frequencies. The enormous local heating and high pressure inside the bubble and adjacent bubble wall from such collapses can give rise to an unusual phenomena in chemical reaction [14]. However, multifunctional ZnTiO<sub>3</sub> material synthesized by the sonochemical process has not been reported in the literature. In the present investigation, an effort has been carried out to synthesize multifunctional perovskite ZnTiO<sub>3</sub> nanopowders by sonochemical-assisted process. The structural phase and the morphological characterization are conducted with X-ray diffraction, Raman spectroscopy, and field-emission scanning electron microscope (FE-SEM). The valence state and the surface chemical bonding were investigated using the X-ray absorption near-edge spectroscopy (XANES) and X-ray photoelectron spectroscopy (XPS) techniques, respectively. The photocatalytic behavior was tested on the Rhodamine B (RhB) in water under ultraviolet (UV) and visible (Vis) light illumination. The dielectric constant and the loss tangent were studied by LCR meter. The effect of

Manuscript received January 15, 2016; accepted July 14, 2016. Date of publication July 21, 2016; date of current version October 1, 2016. This work was supported by Thailand Research Fund (TRF) through the Royal Golden Jubilee Ph.D. Program (Grant PHD/0193/2556) and National Science and Technology Development Agency, Ministry of Science and Technology, Thailand (Grant JRA-CO-2558-857-TH). (Corresponding author: Wisanu Pecharapa.)

The authors are with the College of Nanotechnology, King Mongkut's Institute of Technology Ladkrabang, Bangkok 10520, Thailand (e-mail: kpevisan@gmail.com; ithree43@gmail.com).

Digital Object Identifier 10.1109/TUFFC.2016.2593002

0885-3010 © 2016 IEEE. Personal use is permitted, but republication/redistribution requires IEEE permission.

This material is intended for personal use only. All rights reserved. See [http://www.ieee.org/publications\\_standards/publications/rights/index.html](http://www.ieee.org/publications_standards/publications/rights/index.html) for more information.

Forbidden to modify the content, and cite the document when use.

firing temperature on structural phase, morphology, optical properties, dielectric properties, and photocatalytic properties was also discussed.

## II. EXPERIMENT

The analytical grade of titanium isopropoxide ( $\text{Ti}[\text{OC}_3\text{H}_7]_4$ : TIIP 97%) and zinc acetate dihydrate [ $\text{Zn}(\text{CH}_3\text{CO}_2)_2 \cdot 2\text{H}_2\text{O}$ , 99.9%] supplied by Aldrich was used as a Ti and Zn precursor, respectively. The ratio amount of TIIP and zinc acetate stoichiometric is designated at 1:1. First, zinc acetate was dissolved in the absolute ethanol under magnetic stirring for 15 min. The oxalic acid was separately dissolved in absolute ethanol and slowly added into the zinc acetate solution to obtain a white cloudy like solution. The TIIP was dropped in the white cloudy suspension, immediately followed by DI water, and then, the solution was kept under magnetic stirring for 1 h. The final mixing solution was irradiated with high ultrasonic sonometer (750 W, 20 kHz) for 30 min at room temperature to achieve the precipitate product. After cooling down, the green powders were washed by DI water and dried at 100 °C for 12 h. The green powders were calcined between 500 °C and 900 °C for 2 h.

The crystal structure and the phase identification of all calcined samples were characterized by X-ray diffractometer (XRD; PANalytical X'Pert Pro). To investigate the valence state of samples, the X-ray absorption spectroscopy (XAS) technique of Ti K-edge (4966 eV) and Zn K-edge (9659 eV) was recorded in transmission mode at room temperature using Ge(220) grid at Beamline-8 of the Synchrotron Light Research Institute, Nakhon Ratchasima, Thailand. The surface analysis was investigated by XPS (AXIS Ultra DLD). The FE-SEM was used to determine the powder morphology. The photocatalytic behaviors of all samples were studied toward on the degradation of RhB under UV and Vis light illumination. The 4 g/L of  $\text{ZnTiO}_3$  catalysts were dispersed in the 0.1 mM of RhB and stirred for 15 min in the dark area to obtained adsorption/desorption equilibrium between RhB and catalyst surface. The solution was illuminated by UV light and Vis light at room temperature until the color of dye completely disappeared. RhB degradation was investigated by means of the decrease in its absorbance at maximum wavelength by UV-Vis spectrometer. The photodegradation performance was calculated by  $C/C_0$  as a function of time, where  $C_0$  and  $C$  are the concentration of RhB at initial and after irradiation, respectively. The dielectric properties of samples were investigated by using LCR dielectric spectrometer measuring at 1 MHz and the temperature range from -50 °C to 100 °C. To fabricate a pellet of  $\text{ZnTiO}_3$  sample for dielectric measurement, the as-prepared powder was pressed into a pellet at 3 ton for 3 min, and then, the pellet was further calcined at 500 °C–900 °C for 2 h.

## III. RESULTS AND DISCUSSION

Fig. 1 shows the XRD pattern of  $\text{ZnTiO}_3$  nanoparticles calcined between 500 °C and 900 °C. At the calcination temperature of 500 °C, the diffractogram exhibits broaden peak around 25°, 35°, 48°, 57°, and 63°, which suggests the initial formation of cubic  $\text{ZnTiO}_3$  structure. The sharpness XRD peak

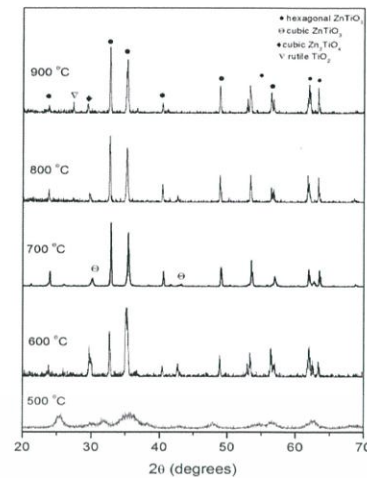


Fig. 1. XRD pattern of perovskite  $\text{ZnTiO}_3$  nanoparticles calcined at 500 °C–900 °C for 2 h.

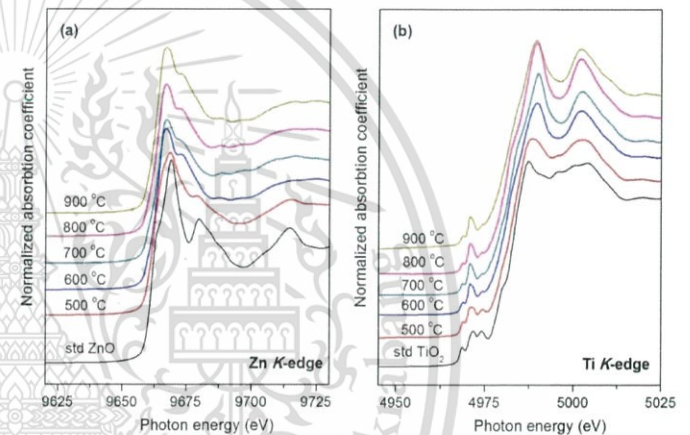


Fig. 2. Measured XANES spectra of  $\text{ZnTiO}_3$  nanoparticle for (a) Zn K-edge and (b) Ti K-edge.

of sample calcined at 600 °C exhibits high crystallinity of the particle with cubic  $\text{ZnTiO}_3$  structure, while the mixing phases of cubic and hexagonal  $\text{ZnTiO}_3$  phase were observed in samples calcined at 700 °C–800 °C. This feature shows good correspondence to the previous work reporting that the unstable cubic  $\text{ZnTiO}_3$  at low temperature can transform into stable hexagonal structure at higher temperature [7]. When the calcination temperature elevated to 900 °C, the hexagonal  $\text{ZnTiO}_3$  structure was retained and did not significantly change into another structure. In addition, the secondary phase of spinel  $\text{Zn}_2\text{TiO}_4$  at around 30° and rutile phase at around 28° was appeared resulting from the decomposition of  $\text{ZnTiO}_3$  at high temperature. The percentage of hexagonal phase was calculated from the ratio of area of hexagonal phase peaks to the area of all peaks using the equation of  $H\% = (A_h/A_{\text{all}}) \times 100$  when  $A_h$  and  $A_{\text{all}}$  are the area of hexagonal phase  $\text{ZnTiO}_3$  and area of all peaks, respectively. The results indicate that the highest H% observed in the samples calcined at 700 °C with a value of 93%.

XANES measurement was employed for studying the valence states of Zn and Ti ion in  $\text{ZnTiO}_3$  nanoparticles. Fig. 2 shows the normalized Zn K-edge and Ti K-edge of

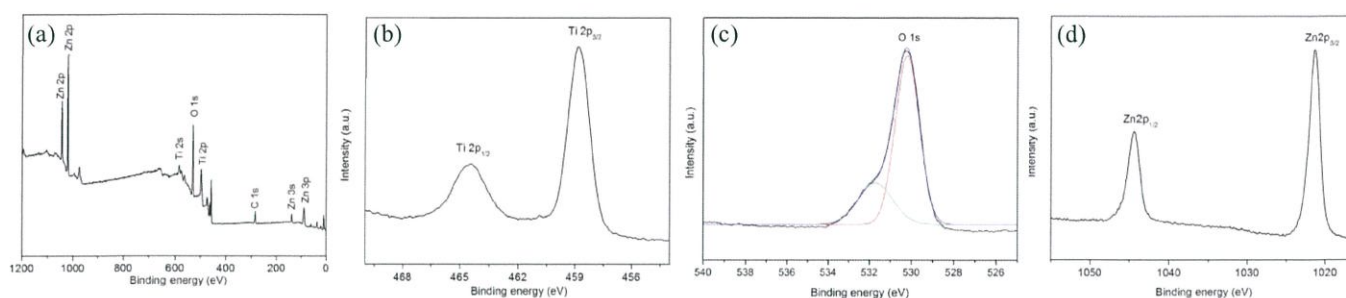


Fig. 3. XPS core level spectra of ZnTiO<sub>3</sub> nanoparticles for (a) survey spectra, (b) Ti 2p, (c) O 1s, and (d) Zn 2p.

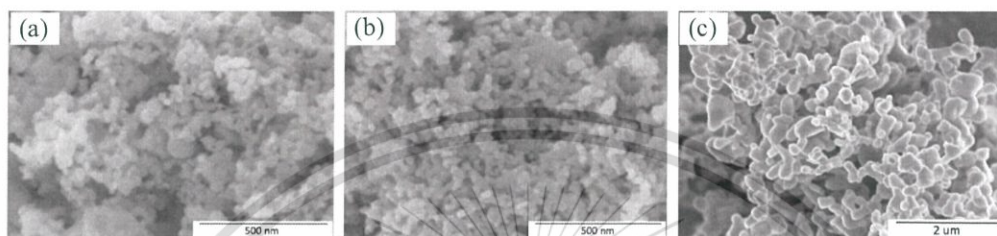


Fig. 4. FE-SEM micrograph of ZnTiO<sub>3</sub> nanoparticles calcined at (a) 600 °C, (b) 700 °C, and (c) 900 °C.

ZnTiO<sub>3</sub> at the calcination temperature of 500 °C–900 °C accompanying reference standards. For the Zn K-edge, as shown in Fig. 2(a), the spectrum line represents strong absorption edge at around 9665 eV. All Zn K-edge XANES spectra do not possess any preedge peak, because all 3d bands of Zn are occupied by 3d electrons [15]. This result confirms that the oxidation state of Zn for ZnTiO<sub>3</sub> sample is 2<sup>+</sup>. The normalized XANES spectra for Ti K-edge of ZnTiO<sub>3</sub> nanoparticle, including reference standard, are demonstrated in Fig. 2(b). The XANES spectra illustrate the triplet preedge electronic step ahead the large absorption edge at around 4966 eV, which is a powerful finger print of Ti characteristic. This character can be attributed to the transition of 1s electron p–d hybridization of Ti coordination in the ZnTiO<sub>3</sub> structure [16]. Hence, it is summarized that the ZnTiO<sub>3</sub> has a perovskite structure comprising six coordinated Ti<sup>4+</sup> ions.

XPS measurements were also conducted on perovskite ZnTiO<sub>3</sub> nanoparticle to ascertain surface composition and chemical status. Fig. 3(a) shows the survey XPS spectra from 0 to 1000 eV for ZnTiO<sub>3</sub> nanoparticle calcined at 700 °C. It is observed that the main peaks are C 1s, Ti 2p, O 1s, and Zn 2p centered at 258.06, 458.81, 530.37, and 1019.37 eV, respectively. The high resolution of Ti 2p XPS spectra in Fig. 2(b) exhibit the binding energy of Ti 2p<sub>3/2</sub> and 2p<sub>1/2</sub> spin orbit doublet at 458.81 and 464.46 eV, respectively, that is well agreeable with the reported data for ZnTiO<sub>3</sub> [17]. Fig. 3(c) demonstrates the XPS peak of O 1s, including the best fitted data. The O 1s peak binding energy located at 530.23 eV attributes to O<sup>2-</sup> in ZnTiO<sub>3</sub>, while the binding energy at 531.28 and 532.29 can be ascribed to oxygen deficiency and hydroxide OH groups [18]. The binding energy for Zn 2p<sub>3/2</sub> and 2p<sub>1/2</sub> is observed at around 285.66 and 286.40 eV, indicating the typical XPS spectra of Zn<sup>2+</sup> ion [19].

Fig. 4 shows the FE-SEM image of perovskite ZnTiO<sub>3</sub> nanoparticles. The micrograph of the samples calcined at 600 °C and 700 °C in Fig. 4(a) and (b) reveals that the particle is nearly spherical in shape with uniform size and distribution. The average particle size is ~25 nm. When the calcination temperature rose up to 900 °C, as shown in Fig. 4(c), the grain boundary began to melt and smaller particles merged together to be a larger grains. However, the particle size became larger with increasing calcination temperature attributing to the better crystal growth with elevated heat treatment temperature.

To determine the optical energy bandgap of perovskite ZnTiO<sub>3</sub> nanoparticles, the UV–Vis absorption spectra were recorded in the range of 250–700 nm. No significant absorption spectrum is observed in the sample calcined at 500 °C, as shown in black line spectra in Fig. 5(a). For the sample calcined at 600 °C–900 °C, the UV–Vis spectra indicate that the ZnTiO<sub>3</sub> has such strong absorption in the UV region. This can be attributed to the photoexcitation of electron from valence band to conduction band, indicating semiconductor feature of calcined samples. The bandgap energy of samples was estimated by the method proposed by Tauc according to the following equation:

$$(ah\nu) = A(h\nu - E_g)^{1/2}$$

where  $\alpha$  is the absorption coefficient that can be obtained from the scattering and reflectance spectra according to the Kubelka–Munk theory,  $h\nu$  is the photon energy, and  $A$  is the constant relevant to the material. The bandgap energy was determined from the plot of  $(ah\nu)$  versus photon energy ( $h\nu$ ) by the intercept of the tangent to the plot, as shown in Fig. 5(b). The wide bandgap energy in the range of 3.07–3.21 eV is obtained for the samples calcined at 500 °C–700 °C. Meanwhile, the bandgap energy value for

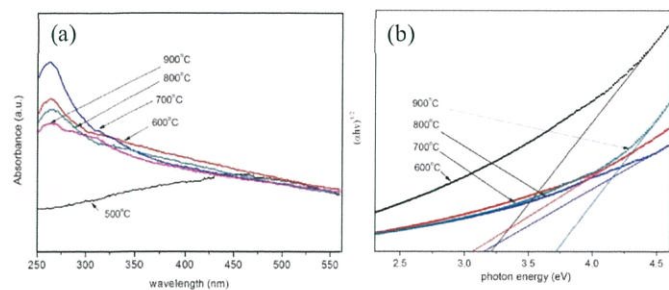


Fig. 5. (a) Optical absorption spectra of ZnTiO<sub>3</sub> nanoparticle at different annealing temperatures. (b) Plot of  $(ah\nu)^{1/2}$  as a function of photon energy for ZnTiO<sub>3</sub> nanoparticle.

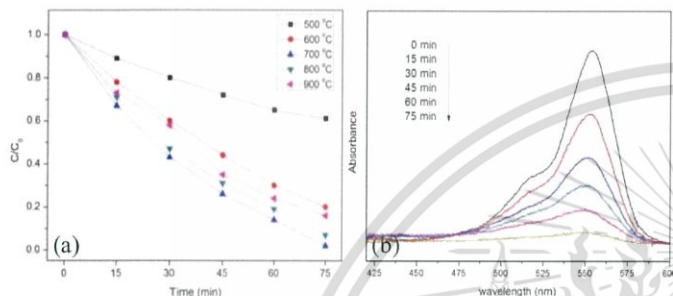


Fig. 6. (a) Photocatalytic behavior for RhB degradation as a function of time of ZnTiO<sub>3</sub> calcined at 500 °C–900 °C under UV irradiation. (b) Time-dependent variation of UV-Vis spectra for RhB degradation of ZnTiO<sub>3</sub> calcined at 700 °C.

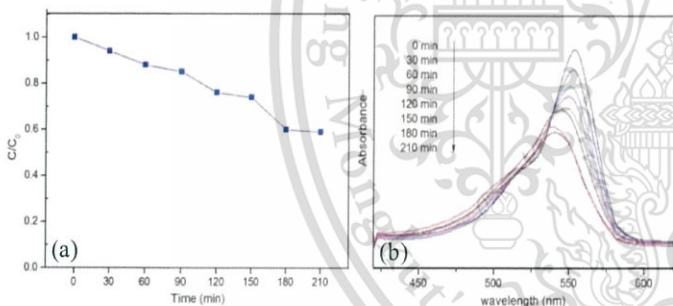


Fig. 7. (a) Photocatalytic behavior for RhB degradation as a function of time of ZnTiO<sub>3</sub> calcined at 700 °C under Vis irradiation. (b) Time-dependent variation of UV-Vis spectra for RhB degradation of ZnTiO<sub>3</sub> calcined at 700 °C.

ZnTiO<sub>3</sub> calcined at 900 °C is  $\sim 3.71$  eV that may be due to the formation of spinel and rutile phase in the sample.

In fact, the structural phase and calcination temperature are the major role factor in the photocatalytic performance. The photocatalytic activities of perovskite ZnTiO<sub>3</sub> nanoparticles were performed on the degradation of RhB under both UV and Vis light. Figs. 6 and 7 show the photodegradation ability of ZnTiO<sub>3</sub> catalyst under excitation with UV and Vis light, respectively. It is clearly seen that the sample calcined at 700 °C exhibits superior performance under UV excitation, with 100% of decolorization within 75 min. In contrast,  $\sim 95\%$ ,  $\sim 84\%$ ,  $\sim 80\%$ , and  $\sim 49\%$  of RhB decolorization were obtained by ZnTiO<sub>3</sub> catalysts calcined at 800 °C, 900 °C, 600 °C, and 500 °C in 75 min, respectively. These results suggest that the hexagonal phase ZnTiO<sub>3</sub> would be the proper phase providing photocatalytic efficiency. Fig. 6(b) represents

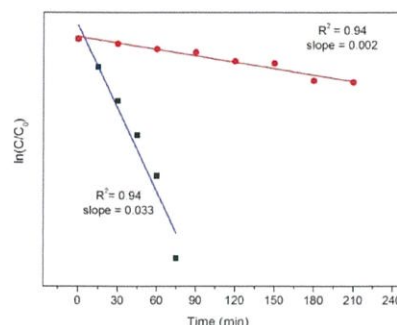


Fig. 8. Adsorption kinetic of RhB over ZnTiO<sub>3</sub> catalyst calcined at 700 °C for UV and Vis irradiation.

the photocatalytic activity of the ZnTiO<sub>3</sub> catalyst calcined at 700 °C at different irradiation times from 0 to 75 min by means of the decrement in the absorbance at 554 nm of RhB absorption. The ZnTiO<sub>3</sub> catalyst performed complete removal of the RhB within 75 min. For the Vis irradiation, the sample calcined at 700 °C was performed, as shown in Fig. 7(b). About 55% of the RhB was photocatalytically degraded after 210 min exposure over ZnTiO<sub>3</sub> samples. The sample calcined at 700 °C demonstrated excellent photocatalytic behavior that may be due to the higher hexagonal phase with a large energy bandgap, providing powerful redox ability for photocatalytic decomposition of organics contaminant under UV and Vis light irradiation [9], [10]. Another possible reason may be due to the fact that the tetragonal coordinate in the Ti ions can adsorb more water and oxygen molecules to produce more hydroxyl group on the surface of ZnTiO<sub>3</sub> catalyst [10], leading to greater catalytic performance.

In order to find out the efficiency of the photocatalytic reaction, pseudo first-order kinetic for photochemical oxidation was established. This model was used for calculating the rate constant of activity [20]

$$\ln(C/C_0) = kt$$

where  $k$  is the apparent first-order rate constant of photodegradation,  $C$  is the concentration of RhB during reaction,  $C_0$  is the initial concentration, and  $t$  is the reaction time. Fig. 8 represents the absorption rate of ZnTiO<sub>3</sub> catalyst calcined at 700 °C under UV and Vis light illumination. The kinetic simulation with reaction time ( $t$ ) and  $\ln C/C_0$  is close to a linear curve with the fitting constant  $R$  greater than 0.94. It is observed that the ZnTiO<sub>3</sub> catalyst exhibits a good activity with  $k = 0.033$  and 0.002 under UV and Vis excitation, respectively. The superior performance of perovskite ZnTiO<sub>3</sub> catalyst under UV to Vis light is correlated with the higher vigorous absorption in the UV region and the wide bandgap energy of the powder.

Fig. 9 shows the temperature-dependent dielectric constant ( $\epsilon$ ) and dielectric loss of ZnTiO<sub>3</sub> nanoparticles calcined at 700 °C measured at 1 MHz. It can be obviously seen that the dielectric response is flat over very broad temperature range with an approximate value of 20, while the dielectric loss is  $\sim 10^{-2}$ . The obtained dielectric constant from this paper is slightly lower than the previous published paper by solid-state reaction method and soft chemical route [11] with the value of 28 and 25, respectively. This may be caused by the

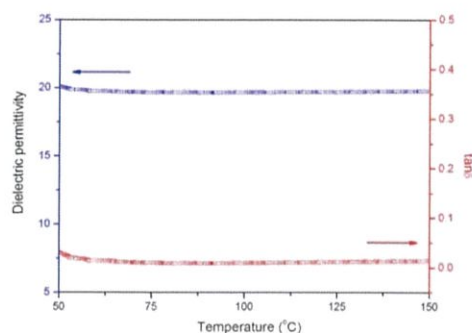


Fig. 9. Temperature dependence of dielectric permittivity and loss tangent of  $\text{ZnTiO}_3$  calcined at  $700\text{ }^\circ\text{C}$ .

relation between the dielectric constant and their density pellet. The dielectric measurement for the samples calcined at  $800\text{ }^\circ\text{C}$  and  $900\text{ }^\circ\text{C}$  was not operated, since the sample calcined over  $700\text{ }^\circ\text{C}$  exhibits the completed secondary phase of spinel and rutile.

#### IV. CONCLUSION

This report investigated the structural phase, valence state, optical properties, dielectric properties, and photocatalytic behavior under UV and Vis irradiation of the multifunctional perovskite  $\text{ZnTiO}_3$  nanoparticles synthesized by the sonochemical method. The XRD results exhibit the cubic  $\text{ZnTiO}_3$  phase for the samples calcined at  $600\text{ }^\circ\text{C}$ . The mixing phases of cubic and tetragonal  $\text{ZnTiO}_3$  were observed in the sample calcined at  $700\text{ }^\circ\text{C}$ , while the spinel and rutile phase could be noticed as calcination is beyond  $700\text{ }^\circ\text{C}$ . The XAS experiment confirms the oxidation state of  $\text{Zn}^{2+}$  and  $\text{Ti}^{4+}$  in perovskite  $\text{ZnTiO}_3$  nanopowders. The  $\text{ZnTiO}_3$  shows the excellent photocatalytic efficiency for the decolorization of RhB within 75 min under UV exposure. The dielectric permittivity of samples calcined at  $700\text{ }^\circ\text{C}$  is  $\sim 20$ . The effect of calcination temperature directly affects its phase structure, microstructure, optical properties, dielectric properties, and photocatalytic behavior. Moreover, the perovskite  $\text{ZnTiO}_3$  nanoparticles prepared by this method may be the promising material for application in photocatalyst and dielectric materials.

#### ACKNOWLEDGMENT

The authors would like to thank Beamline 8 (BL8) at Synchrotron Light Research Institute (SLRI) for XANES measurement.

#### REFERENCES

- [1] H. T. Kim, S. Nahm, J. D. Byun, and Y. Kim, "Low-fired  $(\text{Zn},\text{Mg})\text{TiO}_3$  microwave dielectrics," *J. Amer. Ceram. Soc.*, vol. 82, pp. 3476–3480, Dec. 1999.
- [2] C. Wattanawikkam and W. Pecharapa, "Optical, dielectric and photocatalytic properties of perovskite  $\text{ZnTiO}_3$  nanoparticle synthesized by sonochemical process," in *Proc. ISAF-ISIF-PFM*, May 2015, pp. 280–283.
- [3] H. T. Kim, J. D. Byun, and Y. Kim, "Microstructure and microwave dielectric properties of modified zinc titanates (II)," *Mater. Res. Bull.*, vol. 33, pp. 975–986, Jun. 1998.
- [4] S. F. Wang *et al.*, "Photoluminescence of sol-gel derived  $\text{ZnTiO}_3:\text{Ni}^{2+}$  nanocrystals," *Chem. Phys. Lett.*, vol. 373, pp. 223–227, 2003.
- [5] H. Obayashi, Y. Sakurai, and T. Gejo, "Perovskite-type oxides as ethanol sensors," *J. Solid State Chem.*, vol. 17, pp. 299–303, Mar. 1976.

- [6] W. Wu, Y.-W. Cai, J.-F. Chen, S.-L. Shen, A. Martin, and L.-X. Wen, "Preparation and properties of composite particles made by nano zinc oxide coated with titanium dioxide," *J. Mater. Sci.*, vol. 41, no. 18, pp. 5845–5850, 2006.
- [7] L. Hou *et al.*, "Formation and transformation of  $\text{ZnTiO}_3$  prepared by sol-gel process," *Mater. Lett.*, vol. 59, pp. 197–200, Feb. 2005.
- [8] Y.-H. Yu and M. Xia, "Preparation and characterization of  $\text{ZnTiO}_3$  powders by sol-gel process," *Mater. Lett.*, vol. 77, pp. 10–12, Jun. 2012.
- [9] J.-Z. Kong *et al.*, "Preparation, characterization and photocatalytic properties of  $\text{ZnTiO}_3$  powders," *J. Hazardous Mater.*, vol. 171, pp. 918–923, Nov. 2009.
- [10] Y.-W. Wang, P.-H. Yuan, C.-M. Fan, Y. Wang, G.-Y. Ding, and Y.-F. Wang, "Preparation of zinc titanate nanoparticles and their photocatalytic behaviors in the photodegradation of humic acid in water," *Ceram. Int.*, vol. 38, pp. 4173–4180, Jul. 2012.
- [11] I. Bobowska, A. Opasińska, A. Wypych, and P. Wojciechowski, "Synthesis and dielectric investigations of  $\text{ZnTiO}_3$  obtained by a soft chemistry route," *Mater. Chem. Phys.*, vol. 134, pp. 87–92, May 2012.
- [12] N. Pal, M. Paul, and A. Bhaumik, "New mesoporous perovskite  $\text{ZnTiO}_3$  and its excellent catalytic activity in liquid phase organic transformations," *Appl. Catalysis A, General*, vol. 393, pp. 153–160, Feb. 2011.
- [13] C. Wattanawikkam and W. Pecharapa, "Synthesis and characterization of Zn-doped  $\text{TiO}_2$  nanoparticles via sonochemical method," *Integr. Ferroelectr., Int. J.*, vol. 165, no. 1, pp. 167–175, 2015.
- [14] S. S. Lee *et al.*, "Homogeneous ZnS coating onto  $\text{TiO}_2$  nanoparticles by a simple one pot sonochemical method," *Chem. Eng. J.*, vol. 139, pp. 194–197, May 2008.
- [15] T. Yamamoto, "Assignment of pre-edge peaks in K-edge X-ray absorption spectra of 3d transition metal compounds: Electric dipole or quadrupole?" *X-Ray Spectrometry*, vol. 37, no. 6, pp. 572–584, 2008.
- [16] G. Akgül, "Synthesis and structural characterization of zinc titanates," *J. Molecular Struct.*, vol. 1037, pp. 35–39, Apr. 2013.
- [17] C. D. Wagner, W. H. Riggs, L. E. Davis, J. F. Moulder, and G. E. Muilenberg, *Handbook of X-Ray Photoelectron Spectroscopy*. Waltham, MA, USA: Perkin-Elmer, 1979.
- [18] B. Gilbert *et al.*, "X-ray absorption spectroscopy of the cubic and hexagonal polytypes of zinc sulfide," *Phys. Rev. B*, vol. 66, p. 245205, Dec. 2002.
- [19] D. Chu, A. Younis, and S. Li, "Direct growth of  $\text{TiO}_2$  nanotubes on transparent substrates and their resistive switching characteristics," *J. Phys. D, Appl. Phys.*, vol. 45, pp. 355306–355309, 2012.
- [20] R. S. Ravendra *et al.*, "Synthesis, structural characterization of nano  $\text{ZnTiO}_3$  ceramic: An effective azo dye adsorbent and antibacterial agent?" *J. Asian Ceram. Soc.*, vol. 2, pp. 357–365, 2014.



**Chakkaphan Wattanawikkam** received the B.S. degree in physics in 2009 and the M.S. degree in applied physics in 2012 from Naresuan University. He is currently pursuing the Ph.D. degree with the College of Nanotechnology, King Mongkut's Institute of Technology Ladkrabang, Bangkok, Thailand.

His current research interests include the synthesis of multifunctional material oxide compound Zn-Ti system using the sonochemical technique and photocatalyst materials.



**Wisanu Pecharapa** received the B.S. degree in physics from Chiang Mai University, Chiang Mai, Thailand, in 1992, the M.S. degree in physics from the University of Central Florida, Orlando, FL, USA, in 1997, and the Ph.D. degree in applied physics from the King Mongkut's Institute of Technology Ladkrabang, Bangkok, Thailand, in 2007.

His current research interests include the synthesis processes and the characterization techniques of metal oxide-based materials, such as  $\text{TiO}_2$ ,  $\text{ZnO}$ ,  $\text{WO}_3$ ,  $\text{NiO}$ ,  $\text{SnO}_2$ , and their alloys and composite, especially in low-dimensional structures that can be applied for optical, optoelectronics, catalysts, and energy applications.

# Structural, Optical and Magnetic Properties of Diluted Magnetic Perovskite ZnTiO<sub>3</sub> Doped with Co and Mn Prepared by Sonochemical Method

Chakkaphan Wattanawikkam, Weerachon Phoohinkong, and Wisanu Pecharapa\*

*College of Nanotechnology, King Mongkut's Institute of Technology Ladkrabang, 10520, Thailand*

We employed a sonochemical method to fabricate transition metal ion doped perovskite ZnTiO<sub>3</sub> (M-ZnTiO<sub>3</sub>) nanoparticles, including individual Co and Mn ions. The Zn:Ti was mixed in molar ratio of 1:1 to obtain starting precursor for ZnTiO<sub>3</sub>. The different concentrations of Co (5–10 mol%) and Mn (3–7 mol%) were doped in ZnTiO<sub>3</sub>, then the mixing solution were irradiated in high frequency ultrasound of a sonometer (20 kHz, 750 W) at room temperature to obtain the as-prepared samples. The final products were calcined at 800 °C for 3 h to improve the crystallinity. We confirmed formation structures of M-ZnTiO<sub>3</sub> nanoparticles by X-ray diffraction (XRD), and used X-ray absorption near edge spectroscopy (XANES) and X-ray photoelectron spectroscopy (XPS) technique to investigate the crystal structure and valence states of the sample. Meanwhile, we studied their optical properties by diffuse reflectance spectroscopy, and evaluated magnetic properties of the samples at room temperature by vibrating sample magnetometer (VSM). Magnetization measurements revealed the paramagnetic behavior for Co-ZnTiO<sub>3</sub> and weak ferromagnetic behavior for Mn-ZnTiO<sub>3</sub>. We also investigated and discussed the effect of metal ion doping concentration on the structural, optical and magnetic properties.

**Keywords:** Zinc Titanate, Sonochemical, Magnetic Properties, XANES.

## 1. INTRODUCTION

Perovskite-type oxide materials with a formula of ABO<sub>3</sub> have attracted interest over the past decade, owing to their unique physical and chemical properties.<sup>1</sup> Perovskite structures are generally mixed oxide having BO<sub>6</sub> octahedral with A<sup>2+</sup> cations inserted in the framework. Recently, great interest has been paid to multi-functional perovskite zinc titanate (ZnTiO<sub>3</sub>; ZTO), which is a precious compound for practical industrial applications, including regenerable catalysts, pigment, and dielectric material in the microwave frequency region.<sup>2,3</sup> The adaptability in the electronic properties of perovskite materials arises from changing the concentration of cation dopants with different valence states. Doping technique has been considered an effective route to modify the structural and relevant properties of perovskite-type oxides. Transition metal ions such as Fe, Co, Mn and Ni have been determined to be potential candidates as effective doping elements for Ti-based

oxides.<sup>4–6</sup> Up to now, there have been few detailed studies on the incorporation of transition magnetic metal ions into ATiO<sub>3</sub> structure resulting in dilute magnetic behaving semiconductor. Lately, dilute magnetic semiconductors (DMSs) have been expected to play an important role in the fields of optoelectronics, magnetoelectronics, and microwave devices.<sup>7,8</sup> Previous work reported the DMS behavior of the transition magnetic ion doped TiO<sub>2</sub>; its behavior is mediated by the oxygen vacancies in the gap of the host oxide, and the spurious phase, such as transition metal ion or cluster, in the host matrix.<sup>9–11</sup> Rashad and colleague studied the Co and Mn individually doped TiO<sub>2</sub> synthesized by a hydrothermal method.<sup>9</sup> They suggested that metal doped TiO<sub>2</sub> exhibited a blue shift in band energy TiO<sub>2</sub>. The corresponding results additionally revealed weak paramagnetic behavior of the doped samples at room temperature, and that increasing Co and Mn doping concentration could increase its paramagnetic order. Choudhury et al.<sup>10</sup> studied the effect of oxygen vacancy and doping concentration on the magnetic properties of high spin Co-doped TiO<sub>2</sub> nanoparticles

\* Author to whom correspondence should be addressed.

prepared by a sol–gel route. They observed that the air annealed samples showed paramagnetic properties, while the vacuum annealed sample displayed ferromagnetic-superparamagnetic behavior. They concluded that the oxygen vacancy and cobalt aggregates were key factors for magnetic behavior variation.

Recently, a sonochemical method for fabricating diverse kinds of nanomaterials has attracted considerable interest, owing to simplicity of apparatus, low equipment cost, and the uniform nanoparticle size of the obtained products.<sup>12</sup> The sonochemical process typically provides high frequency and energy of ultrasonic wave to initiate chemical reaction of the starting precursor, and induce particle formation during irradiation. The sonication acoustic cavitation phenomenon abruptly generates cavities in the liquid solution of reactants. In general, the cavitation processes consist of the creation, growth and implosive collapse of gas vacuoles in the solution. Regarding the hot-spot theory, extreme temperature and high pressure occur in the bubbles during cavitation collapse.<sup>13</sup> To our best knowledge, no literature or research work has been reported that deals with transition magnetic metal ion doped ZTO nanoparticles. In the present work, we employ the sonochemical method to prepare Co and Mn doped perovskite ZTO nanoparticles. We investigate the phase structures by X-ray diffractometer (XRD), and determine their valence states by X-ray absorption near edge spectroscopy (XANES). We study their morphologies by field emission scanning electron microscope (FESEM), while elucidating their optical properties by diffuse reflectance spectroscopy. We study the magnetic properties of all samples using vibrating sample magnetometer (VSM), and discuss the effect of Co and Mn concentration on phase structures, morphologies, and optical and magnetic properties.

## 2. EXPERIMENTAL DETAILS

We prepared the Co-doped ZTO and Mn-doped ZTO nanoparticles by a sonochemical method. Titanium isopropoxide (Ti[OC<sub>3</sub>H<sub>7</sub>]<sub>4</sub>: TIIP) and zinc acetate (Zn(CH<sub>3</sub>CO<sub>2</sub>)<sub>2</sub>), purchased from Aldrich were used as Ti and Zn sources, respectively. Cobalt nitrate hexahydrate (Co(NO<sub>3</sub>)<sub>2</sub> · 6H<sub>2</sub>O) and manganese nitrate tetrahydrate (Mn(NO<sub>3</sub>)<sub>2</sub> · 4H<sub>2</sub>O) purchased from Adrich were utilized as sources of Co and Mn dopant, respectively. A stoichiometric amount of TIIP and zinc acetate was designated as ratio 1:1. First, zinc acetate was dissolved in the absolute ethanol under magnetic stirring for 15 min. Oxalic acid was separately dissolved in the absolute ethanol, and was then slowly added into the zinc acetate solution under constant stirring to obtain a white solution. The TIIP was added, suddenly followed by DI water. Cobalt concentrations of 5, 7 and 10% and Mn concentrations of 3, 5 and 7% were loaded in the solution. The mixing solution was kept under constant magnetic stirring for another

30 min. The final solution was irradiated in high ultrasonic sonometer (20 kHz, 750 W) for 30 min at room temperature to obtain the precipitate product. After that, the precipitate sample was washed by DI water, and dried at 100 °C for 12 h. The as-synthesized powders were calcined at 800 °C for 3 h.

We characterized the calcined samples for the phase structure by X-ray diffractometer (XRD; PANalytical X'Pert PRO), using CuK $\alpha$  irradiation ( $\lambda = 1.54 \text{ \AA}$ ) in the range of  $2\theta$  between 20° and 80°. For the valence state investigation of samples, we conducted X-ray absorption spectroscopy (XAS) at Zn, Ti, Co and Mn *K*-edge using the Beamline-8 (BL8) of the Synchrotron Light Research Institute (SLRI), Nakhon Ratchasima, Thailand. We performed data collection in the transmission mode (for Zn *K*-edge (9659 eV) and Ti *K*-edge (4966 eV)), and fluorescent mode (for Co *K*-edge (7709 eV) and Mn *K*-edge (6539 eV)) by Ge(220) double crystal monochromator. The BL8 is a bending storage ring at 1.2 GeV with a beam current of 80–120 mA during the measurement. We investigated the optical properties of samples by diffuse reflectance spectroscopy performed from 200–800 nm. We used the field emission scanning electron microscope (FE-SEM) to determine the morphologies of samples, and studied the magnetic properties of samples by the vibrating sample magnetometer (VSM) in a maximum applied field of 15 kOe.

## 3. RESULTS AND DISCUSSION

Figure 1 shows the XRD patterns of Co-ZTO and Mn-ZTO calcined at 800 °C for 3 h. Figure 1(a) shows that all diffractograms of Co-ZTO exhibit pure hexagonal ZnTiO<sub>3</sub> phase, while Figure 1(b) shows that the XRD patterns of Mn-ZTO samples exhibit the mixing phase of cubic ZnTiO<sub>3</sub> and hexagonal ZnTiO<sub>3</sub>. The XRD patterns of both Co-ZTO and Mn-ZTO indicate strong and sharp peaks, ensuring the high crystallinity of the samples. The average crystalline sizes of Co-ZTO and Mn-ZTO calculated by the diffraction peak with highest intensity using Sherrer's equation are approximately 18 nm and 24 nm, respectively. Interestingly, we observed no peak corresponding to the secondary phase of cobalt oxide or manganese oxide in XRD patterns, suggesting the good incorporation of these dopants in ZTO structure.

We conducted XANES measurement to confirm the existence of Co and Mn in the samples, and to study the valence states of Zn, Ti, Co and Mn ion in the Co-ZTO and Mn-ZTO. Figure 2 compares the normalized XANES spectra for Co-ZTO and Mn-ZTO samples with the reference standard samples, where (a)–(b) show the Zn *K*-edge and Ti *K*-edge in transmission mode and (c)–(d) the Co *K*-edge and Mn *K*-edge in fluorescent mode, respectively. Figure 2(a) shows the normalized Zn *K*-edge XANES spectra without noticeable pre-edge region in all spectra

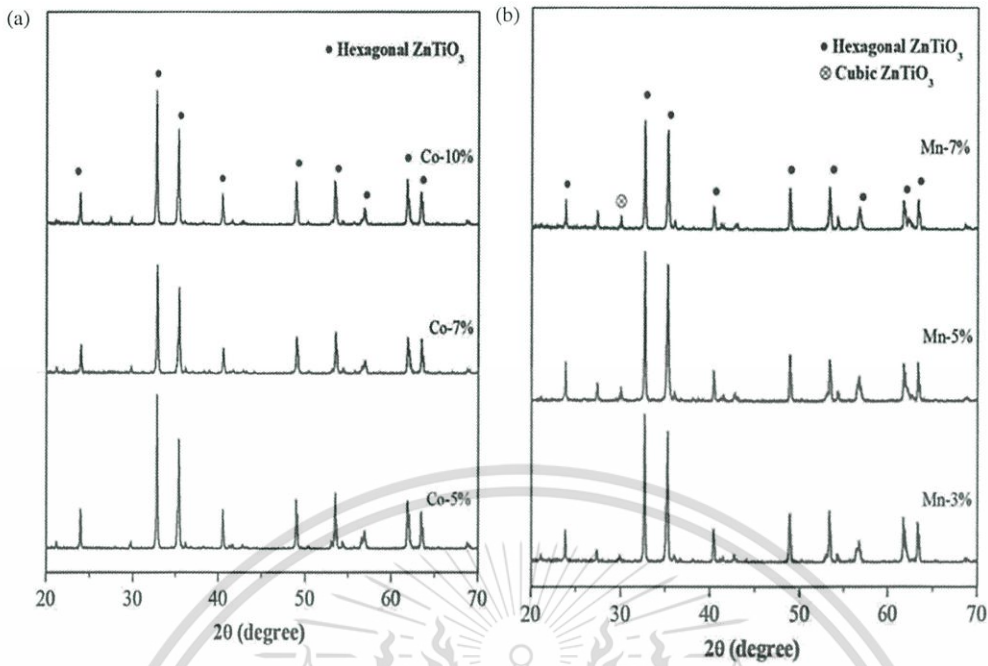


Figure 1. XRD patterns of ZTO doped with (a) Co, and (b) Mn, calcined at 800 °C for 3 h.

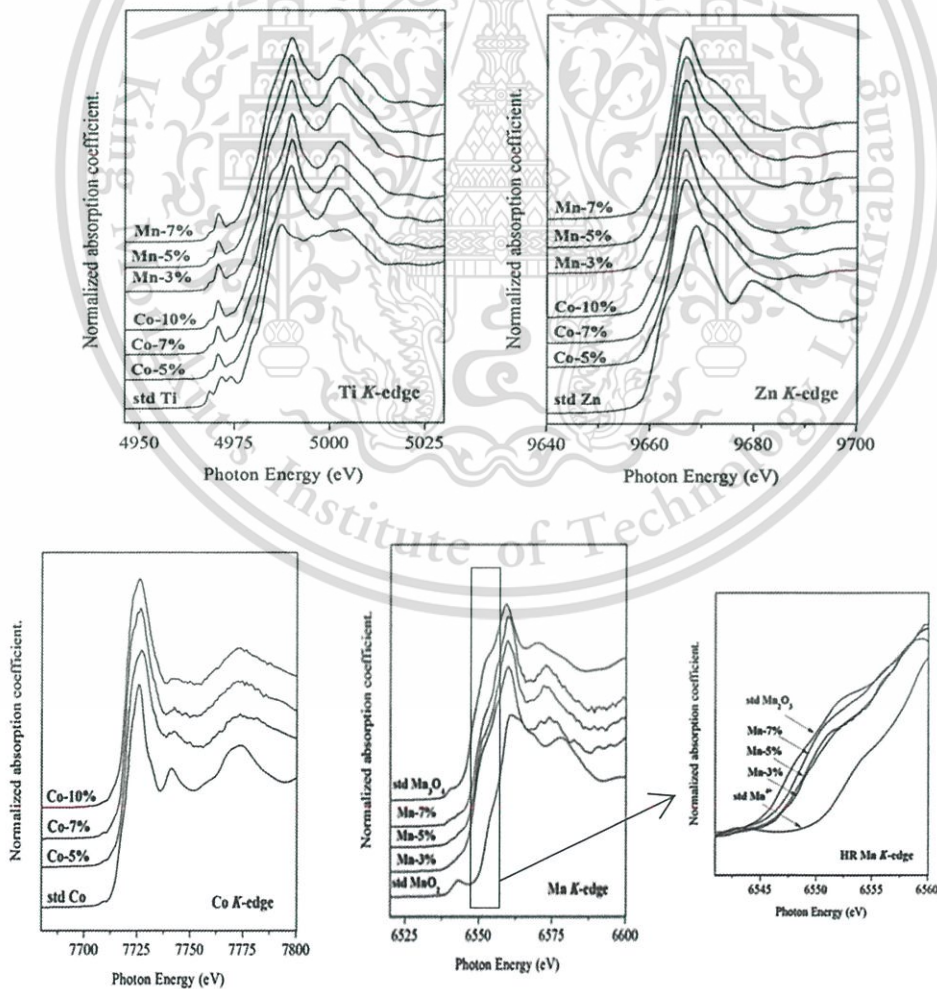


Figure 2. Measured XANES spectra of Co-ZTO and Mn-ZTO at Zn K-edge, Ti K-edge, Co K-edge, Mn K-edge, and high resolution of Mn K-edge.

due to the  $3d$  orbital of  $Zn^{2+}$  being fully occupied by electrons. Thus, the strong energy absorption edge of 9664 eV presents only the core level of electronic transition from  $1s$  to  $4p$  unoccupied state. This result indicates the existence of  $Zn^{2+}$  oxidation state in the Co-ZTO and Mn-ZTO samples. Figure 2(b) shows the normalized Ti  $K$ -edge XANES spectra with reference standard of Co-ZTO and Mn-ZTO samples. All spectra represent three pre-edge electronic transition steps before the strong absorption peak of 4966 eV. The triplet pre-edge peaks are typically associated with the strong fingerprint that defines the coordination number of the materials. We can also implicate this to transition of the  $1s$  electron  $p$ - $d$  hybridized state in tetrahedral symmetry.<sup>14</sup>

The strong energy absorption of all samples are close to the  $Ti^{4+}$  reference standard. Hence, we could conclude that the Co-ZTO and Mn-ZTO samples have perovskite structure consisting of six coordinated  $Ti^{4+}$  ions.<sup>15</sup> The inset of Figure 2(c) represents experimental XANES spectra of Co  $K$ -edge with their reference standard. The XANES spectra show a small pre-edge shoulder located at 7708 eV. The large absorption energy positioned at 7715 eV is almost identical to the  $Co^{2+}$  standard spectrum. This result confirms that the oxidation states of Co ion in Co-ZTO samples are 2+. Figure 2(d) shows the strong absorption peaks between 6345 and 6555 eV we observed in the case of Mn  $K$ -edge. This characteristic feature suggests the existence of Mn ion with different oxidation states ( $Mn^{2+}$ ,  $Mn^{3+}$  and

$Mn^{4+}$ ) in samples due to the environmental sensitivity of Mn ion.<sup>16</sup> Moreover, Figure 2(f) shows that increasing Mn content leads to a shift in edge position to higher energy, indicating an increase in the Mn oxidation state.

We carried out XPS measurement to investigate the surface composition of Co-ZTO and Mn-ZTO samples. Figure 3(a) shows that the survey spectra from 0–1200 eV of Co-ZTO sample show binding energy of Zn  $2p$ , Ti  $2p$ , O  $1s$ , C  $1s$  and Co  $2p$ , thus confirming the chemical composition of the samples. Figures 3(b–e) also show the high resolution XPS of Zn, Ti, O and Co. For the Ti  $2p$  spectra. Figure 3(b) shows that the splitting of spin-orbit for Ti  $2p_{3/2}$  and Ti  $2p_{1/2}$  appears at binding energies of 458.30 and 463.97 eV, respectively. The difference in binding energy:  $\Delta$  ( $\Delta = Ti\ 2p_{1/2} - Ti\ 2p_{3/2}$ ) of 5.61 eV is well agreeable to the characteristic for  $Ti^{4+}$  in the ZTO.<sup>17</sup> Figure 3(c) shows that the Zn  $2p$  spectra reveal double spin-orbit feature occurring at binding energies of 1044.48 and 1021.42 eV. The difference  $\Delta = 23.06$  eV between Zn  $2p_{1/2}$  and Zn  $2p_{3/2}$  nicely matches with 2+ of Zn oxidation state in ZTO.<sup>18</sup> The O  $1s$  spectra of Co-ZTO can be fitted by three components of 529.60, 530.75 and 531.72 eV.

The binding energy of 529.60 eV implies an oxygen bonding in the lattice of Co-ZTO, while we can attribute binding energy located at 530.75 eV to the oxygen deficiencies of Co-ZTO. The small shoulder peak at 531.72 eV suggests that the surface is partially covered by OH group.<sup>19</sup>

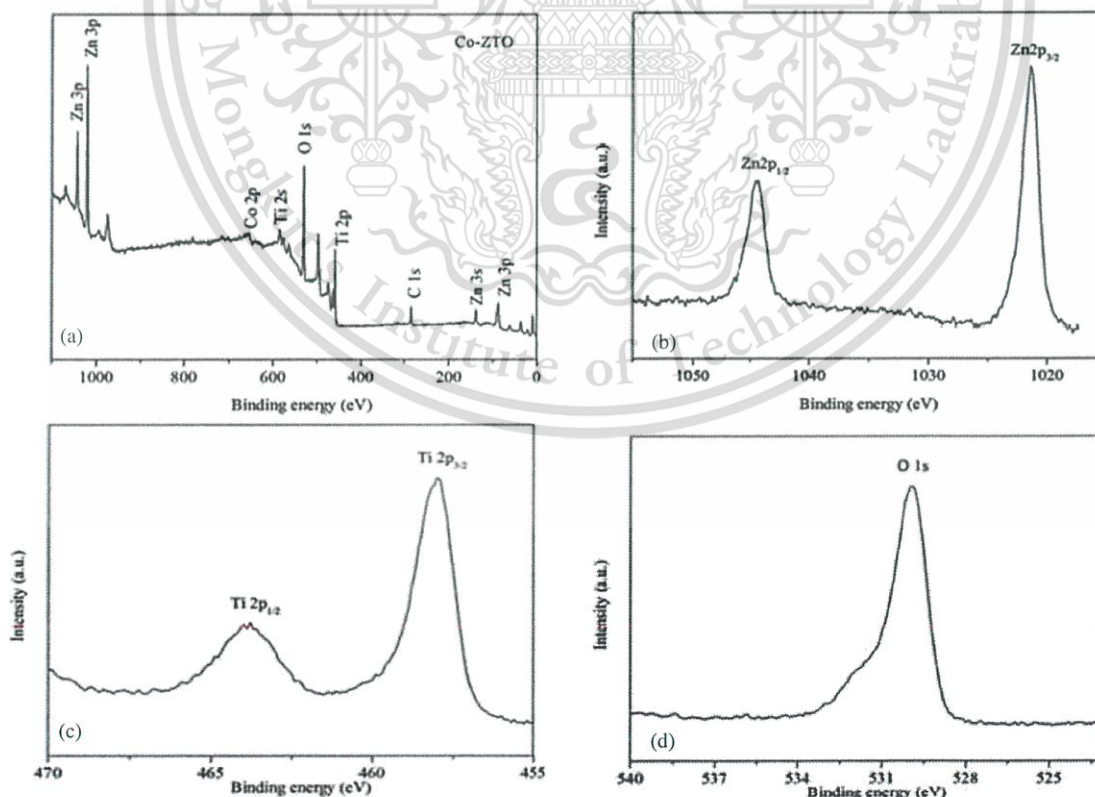


Figure 3. XPS survey spectrum of (a) Co-ZTO, and high resolution of (b) Zn  $2p$ , (c) Ti  $2p$ , and (d) O  $1s$ .

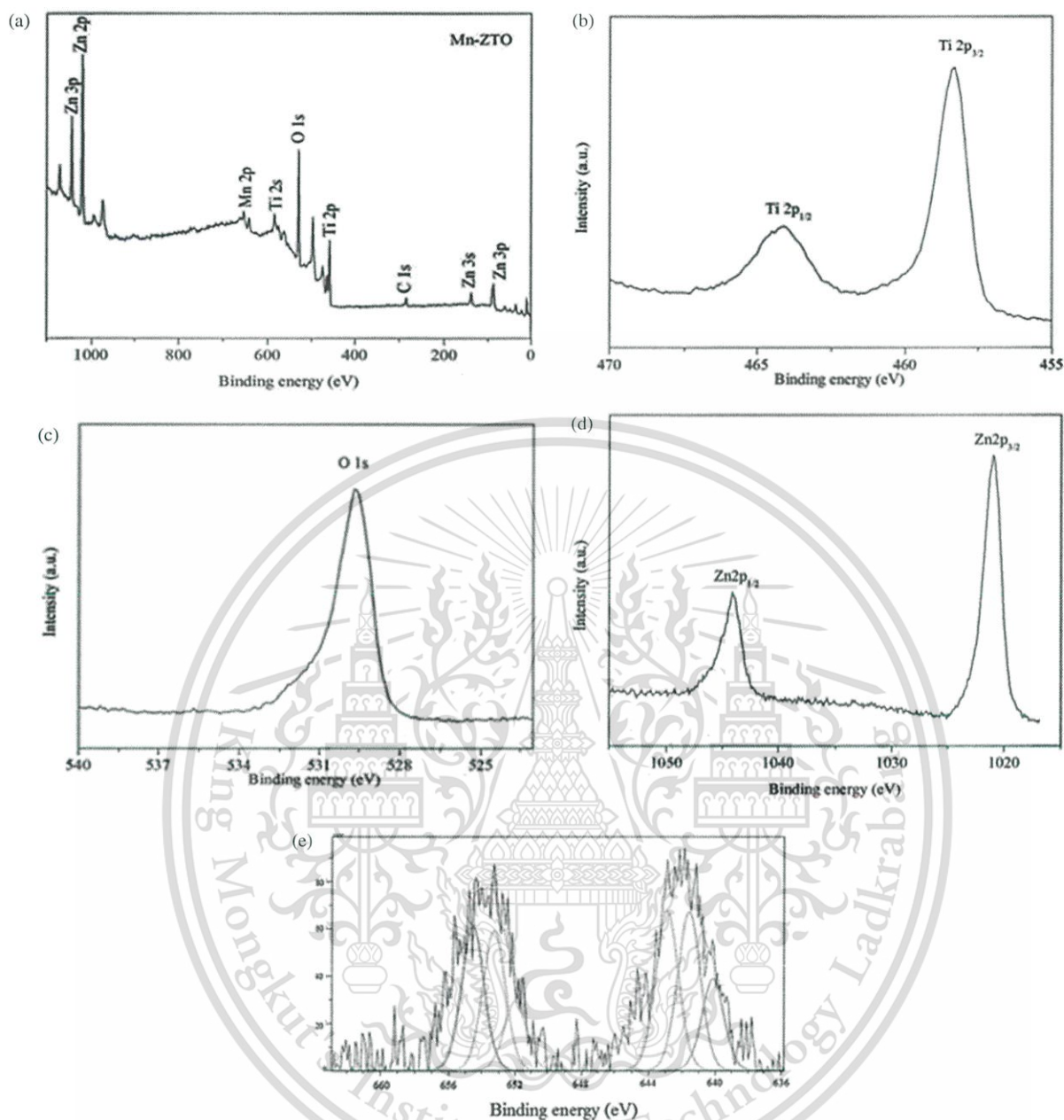


Figure 4. XPS survey spectrum of (a) Mn-ZTO, and high resolution of (b) Zn 2p, (c) Ti 2p, (d) O 1s, and (e) Mn 2p.

We conducted XPS determination of Mn-ZTO, and Figures 4(a–e) present the corresponding results. Figure 4(a) shows the survey spectra representing the binding energies of Zn 2p, Ti 2p, O 1s, C 1s and Mn 2p. Figure 4(b) displays two peaks of Ti spectra at 463.67 and 457.98 eV that associate with Ti 2p<sub>3/2</sub> and 2p<sub>1/2</sub>, respectively. The triplets O 1s peaks at 529.60, 530.75 and 531.74 eV ascribed to lattice oxygen, oxygen deficiencies and hydroxyl oxygens, respectively. The Mn 2p<sub>3/2</sub> spectra in Figure 4(e) possess three peaks situated at 640.17, 641.62 and 642.94 eV in their fitting. We could attribute the lowest intensity peak of 640.17 eV to the 2+ oxidation state, whilst we attribute the higher fitting peak of

641.62 and 642.94 eV to the 3+ and 4+ oxidation states, respectively.<sup>20, 21</sup> Furthermore, the XPS fitting spectra of Mn 2p<sub>3/2</sub> demonstrate the intensity percentages of 39, 38 and 23% for Mn<sup>4+</sup>, Mn<sup>3+</sup> and Mn<sup>2+</sup> oxidation states, respectively. The summation percentage oxidation states of Mn<sup>2+</sup> and Mn<sup>3+</sup> are higher than Mn<sup>4+</sup>, that is in harmony with the XANES results of Mn K-edge showing the closer edge spectrum to reference standard Mn<sub>2</sub>O<sub>3</sub> (Mn<sup>2+</sup>, Mn<sup>3+</sup>) than reference standard MnO<sub>2</sub> (Mn<sup>4+</sup>). Thus, we can conclude that the main oxidation states in sample are Mn<sup>2+</sup> and Mn<sup>3+</sup>.

We characterized the particle size and distribution of Co-ZTO and Mn-ZTO samples by FE-SEM.

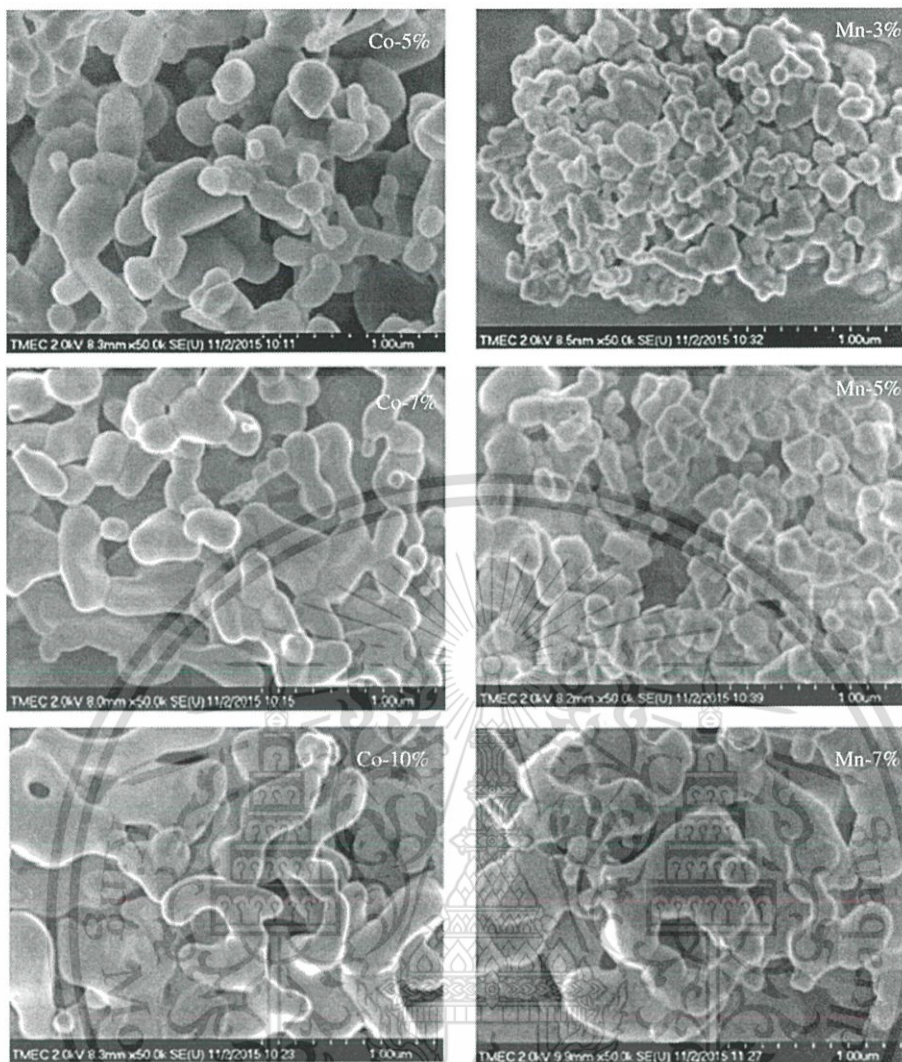


Figure 5. SEM images of ZTO doped by Co and Mn, calcined at 800 °C for 3 h.

Figures 5(a–c) show images of ZTO with different Co doping concentrations. We can see that the average particles size slightly increases with increasing Co content, with estimated value of 218, 222 and 243 nm for Co contents of 5, 7 and 10%, respectively. Figures 3(d–f) represent the microphotographs of Mn-ZTO. The images emphasize that the particle sizes are 136, 158 and 224 nm for Mn concentrations of 3, 5 and 7%, respectively. Moreover, the FESEM images exhibit morphologies of Co-ZTO and Mn-ZTO that are of irregularly granular structure with observable agglomeration. The experimental results indicate that the Co and Mn ion doping may be inserted into the ZTO lattice, and inhibit crystalline and particle growth. The average particle size obtained from FE-SEM characterization accords with the crystalline size calculated from the XRD results.

The optical properties of samples were investigated by diffuse reflectance spectroscopy. The Kubelka-Munk function  $F(R)$  was employed to investigate the energy band

gap of the samples. The plots of  $F(R)$  versus wavelength of Co-ZTO are shown in Figure 6(a). All of spectra exhibit significant strong absorption in UV region. The Co-ZTO spectra also show broad peak around 550–650 nm region, that is possibly originated by additional impurity state  $\text{Co}^{2+}$  species formed in the host semiconductor energy gap.<sup>22</sup> These results match well with previous work of Co doped  $\text{TiO}_2$ .<sup>22</sup> For the Mn-ZTO, the plots of  $F(R)$  and wavelength are shown in Figure 6(C). It can be seen that the spectra reveal absorption in UV region. The absorption edge clearly shifts to higher wavelength implying significant decrease of the energy band gap of the samples. The energy band gap values of all samples were estimated following the Kubelka-Munk method combined with the Tauc equation;

$$\alpha hv = A(hv - E_g)^m \quad (1)$$

Note that,  $\alpha$  is absorption coefficient,  $hv$  is photon energy,  $A$  is an energy dependent constant and  $m$  is integer depending on the nature of electronic transition.<sup>23</sup> For an

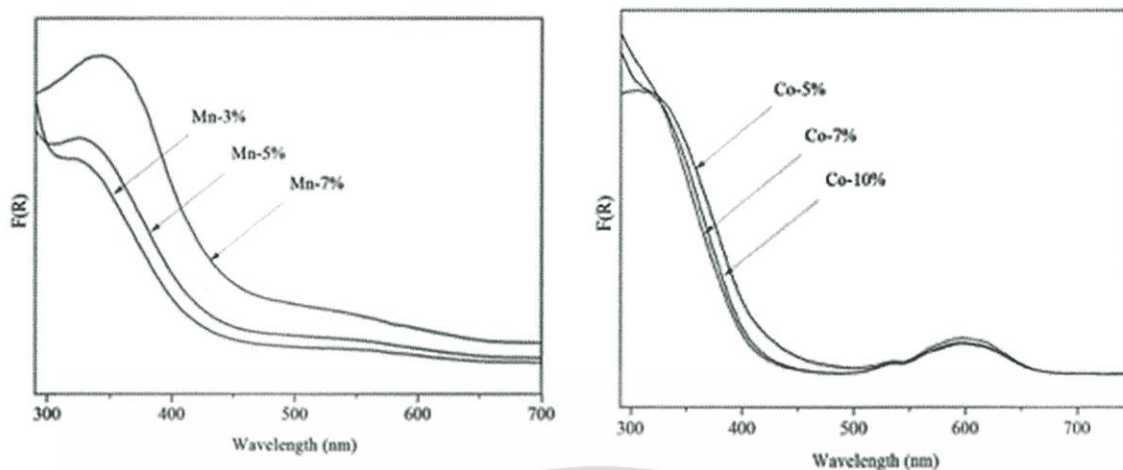


Figure 6. Diffuse reflectance spectra versus wavelength of Co-ZTO and Mn-ZTO.

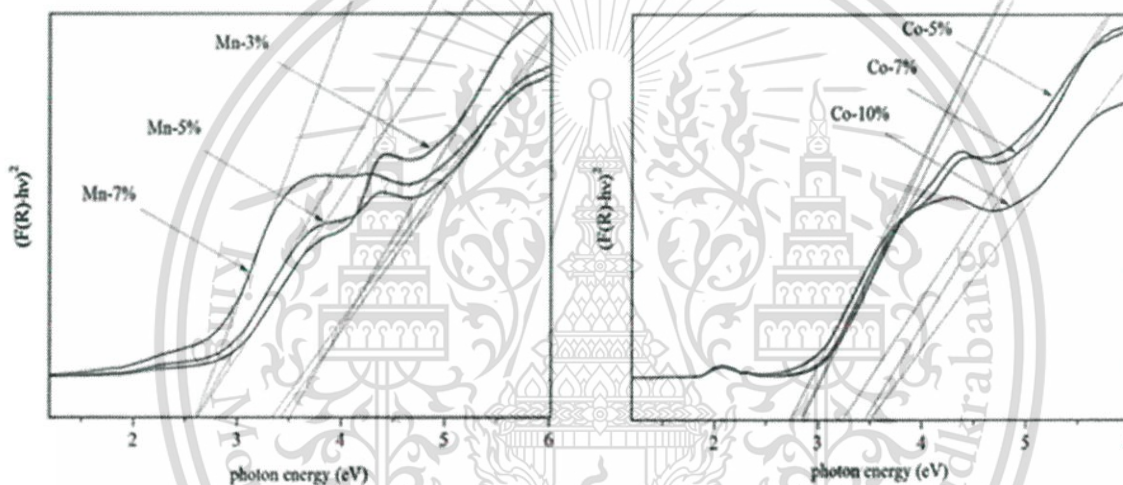


Figure 7. Direct and indirect energy band gap determination for Co-ZTO and Mn-ZTO.

indirect transition  $m = 2$  and for direct transition  $m = 1/2$ . The energy band gap can be conducted from a plot of  $(\alpha hv)^2$  and photon energy  $(hv)$  as shown in Figure 7. It can be seen that the indirect energy gap value of Co-ZTO increases from 3.26 to 3.51 eV when Co content increases from 5 to 10%. On the other hand, the energy gap of Mn-ZTO slightly decreases with increasing of Mn concentration, as seen in Table I. Such decrease of energy

band gap of samples can be described that the dopant ion incorporated into ZTO matrix can replace some Zn<sup>2+</sup> or Ti<sup>4+</sup> ions and induce structural changes and defects affecting the change in electrical and optical properties of the host matrix.<sup>22</sup>

To study the influence of transition magnetic ion doping on relevant magnetic properties of ZTO, room temperature magnetic measurement ( $M-H$ ) was carried out

Table I. Phase structure, crystallite size, energy band gap and magnetic properties of ZTO doped with Co and Mn.

	Phase	Crystallite size (nm)	Particles size (nm)	$E_g^i$ (eV)	$E_g^d$ (eV)	$M_s$ (emu/g)	$M_r$ (emu/g)	$H_c$ (kOe)
Co 5%	H	16	218	2.74	3.26	0.25	0.005	709
Co 7%	H	22	220	2.84	3.44	0.28	0.025	199
Co 10%	H	23	243	2.84	3.52	0.12	0.060	1290
Mn 3%	H+C	14	136	2.63	3.51	0/35	0.023	2565
Mn 5%	H+C	18	158	2.63	3.43	0.32	0.023	2754
Mn 7%	H+C	24	224	2.63	3.33	0.25	0.015	2298

Note: \*H: hexagonal phase, C: cubic phase.

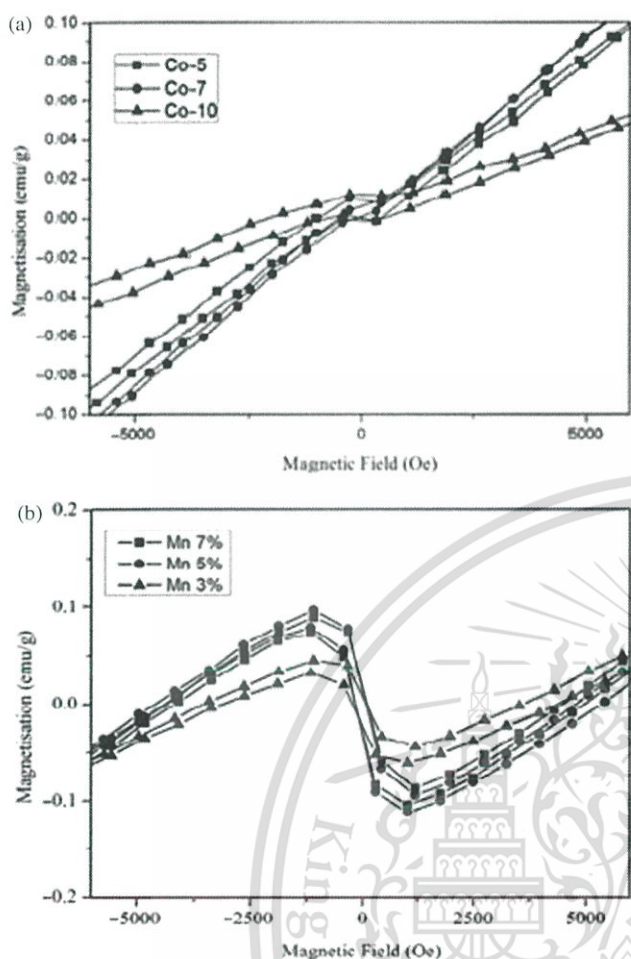


Figure 8. The  $M-H$  curve of (a) Co-ZTO and (b) Mn-ZTO operated at room temperature.

in the field range of  $\pm 15$  kOe. Figure 8(a) shows the  $M-H$  curve of Co-ZTO samples at various Co concentrations. All the samples exhibit weak paramagnetic behavior and the paramagnetic order increases with an increase in Co content to 7% and then drop as a concentration increases to 10%. The saturate magnetization value is 0.25, 0.28 and 0.12 emu/g for 5%, 7% and 10% of Co dopant concentration, respectively, as seen in Table I. At low doping concentration, the magnetic cations are situated apart and the net magnetization comes from isolated ion of  $\text{Co}^{2+}$ . After further Co content increases, the  $\text{Co}^{2+}$  are paired up resulting in the antiferromagnetic superexchange interaction between the nearest neighboring Co cations. These antiferromagnetic coupling could lead to the antiferromagnetic alignment of the magnetic moment, thus the reduction of average moment per magnetic dopant ion.<sup>24</sup> Figure 8(b) illustrates the  $M-H$  curve of Mn-ZTO at room temperature. It is clear that the curve assumes  $s$ -type shape. It suggests the emergence of ferromagnetic long range ordering. The magnetization ( $M_s$ ), retentivity ( $M_r$ ), and coercivity ( $H_c$ ) of all samples are shown in Table I. However, this small value of magnetization in all samples

may relate to the magnetic ion of  $\text{Co}^{2+}$  and  $\text{Mn}^{2+}$  ion located in the ZTO host matrix.<sup>25</sup> From the structural, morphology, optical properties, and magnetic behavior results, the Co and Mn doped ZnTiO<sub>3</sub> nanoparticles prepared by sonochemical method may be promising application for magnetic semiconductor materials and also the photocatalytic materials.

#### 4. CONCLUSION

We successfully synthesized perovskite ZnTiO<sub>3</sub> doped with Co and Mn transition ions by a sonochemical method combined with calcinations at 800 °C for 3 h. Co-ZTO shows the pure hexagonal ZnTiO<sub>3</sub> phase, while Mn-ZTO exhibits mixing phase of cubic and hexagonal ZnTiO<sub>3</sub> phases. We confirmed the existence of Co and Mn and the valence states of each ion in the samples by XANES and XPS technique. Both Co-ZTO and Mn-ZTO exhibit two strong absorption peaks in UV and visible light. Co-ZTO exhibits weak paramagnetic, while Mn-ZTO represents weak ferromagnetic behavior at room temperature. We can deduce that Co and Mn dopants have significant effects on the phase structure, optical properties and magnetic properties of ZTO.

**Acknowledgments:** This work has been partially supported by the Thailand Research Fund (TRF) through the Royal Golden Jubilee Ph.D. Program (Grant No. PHD/0193/2556) and National Science and Technology Development Agency, Ministry of Science and Technology, Thailand (Grant No. JRA-CO-2558-857-TH). The authors gratefully acknowledge the support from the College of Nanotechnology, King Mongkut's Institute of Technology, Ladkrabang. The authors would like to also thank Beamline 8 (BL8) at the Synchrotron Light Research Institute (SLRI) for XAS measurement.

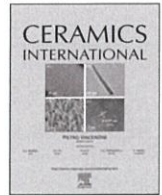
#### References and Notes

1. C. D. Chandler, C. Roger, and M. J. Hampden, *Chem. Rev.* 193, 1205 (1993).
2. Y. S. Chang, Y. H. Chang, I. G. Chen, G. J. Chen, Y. L. Chap, S. Wu, and T. H. Fang, *J. Alloys Compd.* 354, 303 (2003).
3. H. T. Kim, Y. Kim, M. Valant, and D. Suvorov, *J. Am. Ceram. Soc.* 84, 1081 (2001).
4. N. Pal, M. Paul, and A. Bhaumik, *Appl. Catal. A* 393, 153 (2011).
5. H. Eskandarloo, A. Badii, M. A. Behnajady, A. Tavakoli, and G. M. Ziarani, *Ultrasonic Sonochem.* 29, 258 (2016).
6. D. P. Dutta, A. Singh, and A. K. Tyagi, *J. Environ. Chem. Eng.* 2, 2177 (2014).
7. R. Fiederling, M. Kerm, G. Reuscher, W. Ossau, G. Schmidt, A. Waag, and L. W. Molenkamp, *Nature* 402, 787 (1999).
8. S. A. Wolf, D. D. Awschalom, R. A. Buhrman, J. M. Daughton, S. Molnar, M. L. Roukes, A. Y. Chatchelkanova, and D. M. Treger, *Science* 294, 1488 (2011).
9. M. M. Rashad, E. M. Elsayed, M. S. Al-Kotb, and A. E. Shalan, *J. Alloys Compd.* 13, 1025 (2013).
10. B. Choudhury, A. Choudhury, A. M. Maidul Islam, P. Alagaramy, and M. Mukherjee, *J. Magn. Magn. Mater.* 323, 440 (2011).
11. K. Karthik, S. K. Pandian, K. S. Kumar, and N. V. Jaya, *Appl. Surf. Sci.* 256, 4757 (2011).

12. C. Kahattha, N. Wongpisutpaisan, N. Vittayakorn, and W. Pecharapa, *Ceram. Int.* 39, S389 (2013).
13. T. J. Mason and J. P. Lorimer, *Applied Sonochemistry*, Wiley, VCH, Weinheim (2002).
14. T. Yamamoto, *X-ray Spectrometry, X-ray Spectrum* 37, 572 (2008).
15. G. Akgul, *J. Mol. Struct.* 1037, 35 (2013).
16. M. C. Biesinger, L. M. Lan, A. R. Gerson, and R. L. Smart, *Appl. Surf. Sci.* 257, 88 (2010).
17. C. D. Wanger, W. M. Riggs, L. E. Davis, J. F. Moulder, and G. E. Muilenberg, *Handbook of X-ray Photoelectron Spectroscopy*, Perkin-Elmer Corp., Physical Electronics Division, Eden Prairie, Minnesota, USA (1979), p. 190.
18. B. Gilbert, B. H. Frazer, H. Zhang, F. Huang, J. F. Banfield, D. Haskel, J. C. Lang G. Srajer, and G. D. Stasio, *Phys. Rev. B* 66, 245205 (2002).
19. D. Chu, A. Younis, and S. Li, *J. Phys. D: Appl. Phys.* 45, 355306 (2012).
20. H. W. Nesbiyy and D. Banerjee, *American Mineralogist.* 83, 305 (1998).
21. M. C. Biesinger, B. P. Payne, A. P. Grovenor, L. W. Lau, A. R. Gerson, and R. St. C. Smart, *Appl. Surf. Sci.* 257, 2717 (2011).
22. L. Samet, J. B. Nasserur, R. Chtourou, K. March, and O. Stephan, *Mater. Charact.* 85, 1 (2013).
23. A. Molea, V. Popescu, and N. R. Anthony, *Powder. Technol.* 230, 203 (2012).
24. M. A. White, S. T. Ochesbein, and D. R. Gamelin, *Chem. Mater.* 20, 7101 (2008).
25. N. Dragan, M. Crisan, M. Raileanu, D. Chisan, A. Ianculescu, P. Oancea, S. Somacescum, L. Todan, N. Stanica, and B. Vasile, *Ceram. Int.* 40, 12273 (2014).

Received: 27 January 2016. Accepted: 28 July 2016.





# X-ray absorption spectroscopy analysis and magnetic properties of M-doped TiO<sub>2</sub> nanoparticles (M=Co, Mn, Ni and Zn) prepared by co-precipitation method



Chakkaphan Wattanawikkam<sup>a,\*</sup>, Wisanu Pecharapa<sup>a</sup>, Keiichi N. Ishihara<sup>b</sup>

<sup>a</sup> College of Nanotechnology, King Mongkut's Institute of Technology Ladkrabang, Bangkok, Thailand

<sup>b</sup> Graduate school of Energy Science, Kyoto University, Kyoto, Japan

## ARTICLE INFO

### Keywords:

TiO<sub>2</sub>  
Transition ions doped  
XANES  
Magnetic properties

## ABSTRACT

M-doped TiO<sub>2</sub> nanoparticles (M=Co, Mn, Ni and Zn) were synthesized by co-precipitation method combined with annealing at 500 °C for 2 h. X-ray diffraction (XRD) was used to identify their structural phases. X-ray absorption near edge structure (XANES) was conducted to probe the chemical state and crystal atomic structure of prepared samples. Magnetic properties of all samples were characterized by vibrating sample magnetometer (VSM). The XRD analyses reveal that all samples crystallize in anatase tetragonal structure with no additional peaks. The XANES spectra exhibit triple pre-edge fingerprint of Ti4+ of oxidation state with six-fold octahedral coordinate structure. Co-, Ni- and Zn- K-edge results indicate that the Co, Ni and Zn ions in M-doped TiO<sub>2</sub> are in 2+ formal oxidation state. Meanwhile, Mn-doped TiO<sub>2</sub> sample contains the different oxidation states of 3+ and 4+. The amount of each oxidation state is confirmed by using linear combination fitting method. The magnetic measurement illustrates the paramagnetic behavior for Co-, Mn- and Ni- doped samples that strongly depend on the doping content and no hysteresis loop is observed in undoped and Zn-doped samples.

## 1. Introduction

Titanium dioxide (TiO<sub>2</sub>)-based materials have been extensively studied and researched for decades because of their excellent potential chemical, electrical and optical properties. TiO<sub>2</sub> represents the high chemical, electrical and mechanical stability and ease of doping with active ions [1]. During recent decades, the exhibition of magnetic behavior on TiO<sub>2</sub> semiconductor materials by doping with a small percent of magnetic impurity ions have attracted great attention (as call dilute magnetic semiconductors; DMSs) with promising application for use in the spintronic and magnetoelectronic devices [2–4]. Numerous experiments and researches have been performed on DMSs of TiO<sub>2</sub>-based materials doped with transition magnetic ions. Among these transition magnetic ions with high magnetic ions behavior such as Co, Mn and Ni are the most selected ions dopants [5–10] Choudry et al. [6] and Bouaine et al. [5] reported the ferromagnetic and paramagnetic properties of Co-doped TiO<sub>2</sub>. The magnetism at room-temperature of transition metal ions (Mn and Co) doped TiO<sub>2</sub> was claimed by M. M. Rashad and colleague [11]. The mechanisms for the occurrence of magnetic behavior in DMSs still remain controversial. Many experimental investigations have claimed that the oxygen vacancy or the

F-centers in a gap of host matrix played crucial roles on the ferromagnetic behaviors of DMSs [12]. A super-exchange mechanism between the 3d ions dopant associated to the oxygen vacancy is also the key factor for the magnetic properties of DMSs [13]. Furthermore, it had been reported that the transition metal dopant is essential for paramagnetic and ferromagnetic behavior to the spurious phase such as the metal oxide or clusters [14].

The structural phase and effect of transition metal ions dopant on TiO<sub>2</sub> structure attracts interesting as well, herein, it is important to accurately understand local structure and the doping effectiveness. X-ray absorption spectroscopy (XAS) technique is a powerful technique which provides insight into the electronic structure and local order around a selected type of atom. XAS can be divided into two techniques, the X-ray absorption near edge spectroscopy (XANES) and extended X-ray absorption fine structure (EXAFS). XANES technique provides the information on oxidation state, coordination number and site symmetry of absorbing atoms [15]. Meanwhile, EXAFS region spectra offer short-order information on the crystal structure and local structure information of elements such as a number and type of coordinating atom, the distances to neighboring atom and distance order [16]. Some research reports revealed the XAS analysis

\* Corresponding author.

E-mail address: [ithree43@gmail.com](mailto:ithree43@gmail.com) (C. Wattanawikkam).

<http://dx.doi.org/10.1016/j.ceramint.2017.05.188>

Available online 26 May 2017

0272-8842/ © 2017 Elsevier Ltd and Techna Group S.r.l. All rights reserved.

for transition metal incorporated in TiO<sub>2</sub> matrix such as Yildirim et al. (2015) investigated a non-magnet-to-ferromagnet and the local structure of Mn<sup>+</sup>-implanted TiO<sub>2</sub> employing the XAS technique. [17].

However, there are few publications focusing on the local structure investigation for transition metal ion incorporated into TiO<sub>2</sub> nanoparticles. Thus, this work aims to investigate of structural phase and magnetic properties of TiO<sub>2</sub> nanoparticles doped with different transition metal ions at various dopant concentrations. The influence of transition metal ions doping on phase structure, physicochemical state and magnetic properties of TiO<sub>2</sub> samples have been evaluated using X-ray diffractometer (XRD), X-ray absorption near edge spectroscopy (XANES) and vibrating samples magnetometer (VSM). The effect of different dopant ions with different doping concentrations on the structural phase and magnetic properties of TiO<sub>2</sub> nanoparticles were also discussed in this paper.

## 2. Material and methods

M-doped TiO<sub>2</sub> nanoparticles (M=Co, Mn, Ni and Zn) with doping concentrations of 0.5, 1, 3 and 5 mol% were synthesized by co-precipitation method. Titanium isopropoxide [Ti(OCH(CH<sub>3</sub>)<sub>2</sub>)<sub>4</sub>] purchased from Nacalai tesque, was used as a precursor of Ti source. Cobalt nitrate hexahydrate (Co(NO<sub>3</sub>)<sub>2</sub>·6H<sub>2</sub>O), manganese nitrate tetrahydrate (Mn(NO<sub>3</sub>)<sub>2</sub>·4H<sub>2</sub>O), zinc nitrate hexahydrate (Zn(NO<sub>3</sub>)<sub>2</sub>·6H<sub>2</sub>O) and nickel nitrate hexahydrate (Ni(NO<sub>3</sub>)<sub>2</sub>·6H<sub>2</sub>O) purchased from Wako were used as precursors of Co, Mn, Zn and Ni source, respectively. Ammonium solution (NH<sub>3</sub>) and absolute ethanol was employed as a precipitation agent and solvent, respectively.

The starting precursor of cobalt nitrate and titanium isopropoxide were weighed according to the required stoichiometric proportion and separately dissolved in absolute ethanol under magnetic stirring to form the starting precursor solution. The starting precursors were mixed together under magnetic stirring to form the homogeneous solution. The precipitation agent of NH<sub>3</sub> was slowly added in the homogeneous solution until the pH became 9. The mixing solution was constantly stirred for 3 h then the solution was aged for 12 h to obtain the precipitated product. After this stage, the precipitate was washed by DI water until the pH became neutral and then dried at 100 °C for 12 h. Finally, the green powders were annealed at 500 °C in atmosphere for 2 h.

The phase structure of M-TiO<sub>2</sub> samples was identified by XRD diffractometer model Rigaku Rint2100 CMJ with CuK<sub>α</sub> radiation (λ = 0.154 nm) in the scan range from 20 to 60°. The X-ray absorption spectroscopy (XAS) technique was used to identify the chemical state of all samples. X-ray absorption near edge structure (XANES) of Ti K-edge in transmission mode and Co K-edge, Mn K-edge, Ni K-edge and Zn K-edge in fluorescent mode were recorded at room temperature using Ge(220) double crystal monochromator at Beamline-8, Synchrotron Light Research Institute (SLRI), Nakhonratchasima, Thailand. Reference standards of transition metal ions such as TiO<sub>2</sub>, CoO, MnO, Mn<sub>2</sub>O<sub>3</sub>, MnO<sub>2</sub>, NiO and ZnO which known decisive oxidation state were measured as well for comparison purpose. The magnetic behavior of all samples was observed at room temperature by vibrating samples magnetometer (VSM); Riken Denshi, BHV-50 model with the external applied magnetic field range of ± 10 kOe.

## 3. Results and discussion

### 3.1. XRD

X-ray diffraction pattern of undoped and TiO<sub>2</sub> nanoparticles doped with transition metal ions of Co, Mn, Ni and Zn at different concentration are shown in Fig. 1. All diffractogram peaks of undoped and doped samples exhibit main diffraction peaks of (101), (004), (200), (105) and (211) positioned at around 25.4°, 36.8°, 48.9° and 54.7°, respectively, which confirmed the tetragonal anatase phase of TiO<sub>2</sub>. It is noteworthy that no diffraction peak corresponding to metal oxide

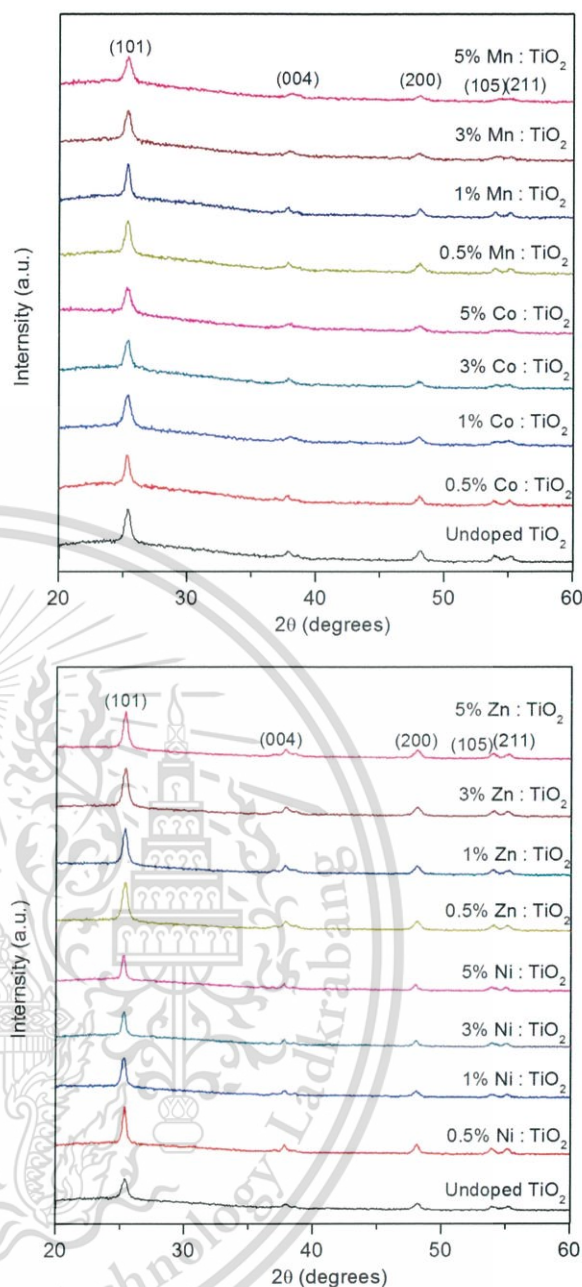


Fig. 1. XRD patterns of M-TiO<sub>2</sub> nanoparticles calcined at 500 °C for 2 h.

dopant and any impurity peak, indicating that the transition metal ions dopants are well dispersed within the TiO<sub>2</sub> matrix.

### 3.2. XAS

To investigate the atomic structure of TiO<sub>2</sub> doped with Co, Mn, Ni and Zn, K-edge XANES data analysis for each ion was performed. The normalized Ti K-edge XANES spectra of TiO<sub>2</sub> reference standard and M-TiO<sub>2</sub> samples are shown in Fig. 2(a)–(d). The Ti K-edges of M-TiO<sub>2</sub> samples represent the feature of spectra similar to TiO<sub>2</sub> reference standard comprising a triplet pre-edge peak. This major feature of pre-edge peak (A<sub>1</sub>, A<sub>2</sub> and A<sub>3</sub>) is a characteristic fingerprint to assign the coordination number of materials, which arises from the X-ray induced electronic transitions from the valence band to the conduction band. The pre-edge features were observed at ~4968 eV (A<sub>1</sub>), ~4970 eV (A<sub>2</sub>) and ~4972 eV (A<sub>3</sub>). A<sub>1</sub> peak generally attributes to a quadrupole transition from 1s to 3d (t<sub>2g</sub>) in the Ti absorber, A<sub>2</sub> peak arises from a dipole

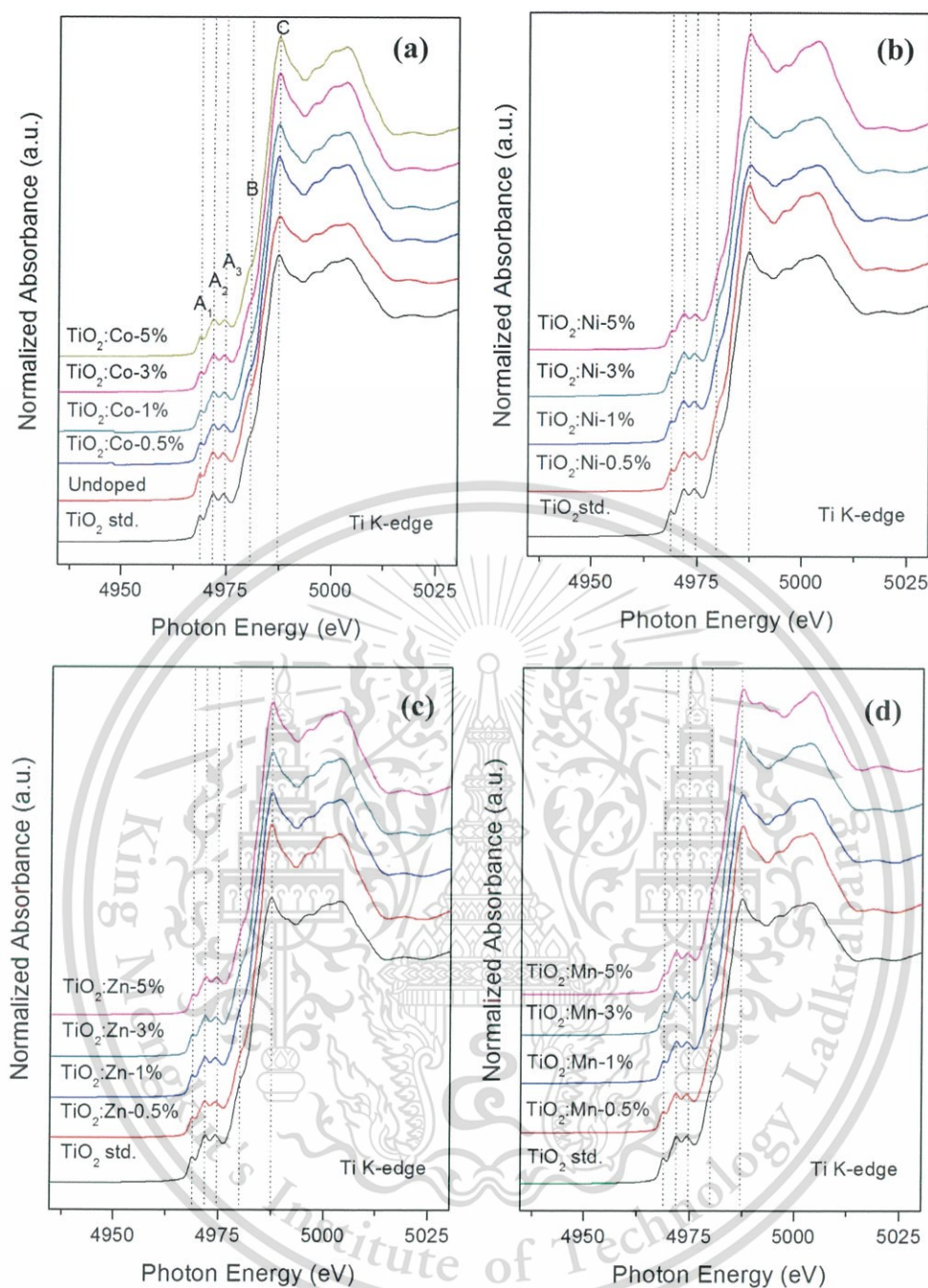


Fig. 2. Normalized XANES spectra of M-TiO<sub>2</sub> samples for Ti K-edge with (a) Co-TiO<sub>2</sub>, (b) Ni-TiO<sub>2</sub>, (c) Zn-TiO<sub>2</sub> and (d) Mn-TiO<sub>2</sub> samples.

transition from 1 s to hybridized p-d ( $t_{2g}$ ) on the neighboring Ti atom and  $A_3$  peak is dipole transition from 1 s to hybridized p-d ( $e_g$ ) on the Ti neighboring atom [18–21]. The shoulder B feature peak of XANES spectra may attribute to the interactions of the central Ti 4p orbital hybridized with the near Ti and O atom. For the post-edge spectrum, C feature (~4988 eV) can be assigned to 3s- $np$  dipole-allowed transition [22,23]. From the pre-edge and post-edge feature data of all samples, it could be concluded that the Ti in Co-, Mn-, Ni- and Zn-TiO<sub>2</sub> samples contains six coordinated Ti<sup>4+</sup> ions. In addition, a small change in proportion of  $A_1$ ,  $A_2$  and  $A_3$  feature implies the substitution of Ti<sup>4+</sup> ion in the samples by the transition metal ions dopant.

The normalized X-ray absorption near edge structure (XANES) of Co-, Mn-, Ni- and Zn-doped TiO<sub>2</sub> nanoparticles including their reference standard in fluorescent mode are shown in Fig. 3(a)–(d). Fig. 3(a) displays the Co K-edge for Co-TiO<sub>2</sub> nanoparticles with doping

content of 0.5–5 mol%. It can be clearly seen that the position of absorption edge spectra is observed at ~7710 eV without pre-edge peak which similar to the CoO reference standard. This result suggests that the oxidation state of Co ions in Co-doped TiO<sub>2</sub> samples is 2+. When the Co concentration increases to 3 and 5 mol%, the XANES spectrum character shows small broaden peak around ~7745 eV situated at same location with CoO standard peak. This manner may originate from the beginning formation of CoO cluster in the samples. For Ni-doped TiO<sub>2</sub> samples, the XANES spectra are represented in Fig. 3(b). The absorption-pre-edge and post-edge spectra obviously exhibit the strong absorption energy of ~8336–8345 eV that is similar to NiO standard. This result confirm that it contains 2+ formal valence state of Ni ions for Ni-doped TiO<sub>2</sub> sample. At the higher Ni concentration, a small broaden peak around ~8365 eV is observed due to the NiO phase formation in the sample. As seen in Fig. 3(c) displaying the XANES

This material is reserved for educational use only, not allowed for commercial use.

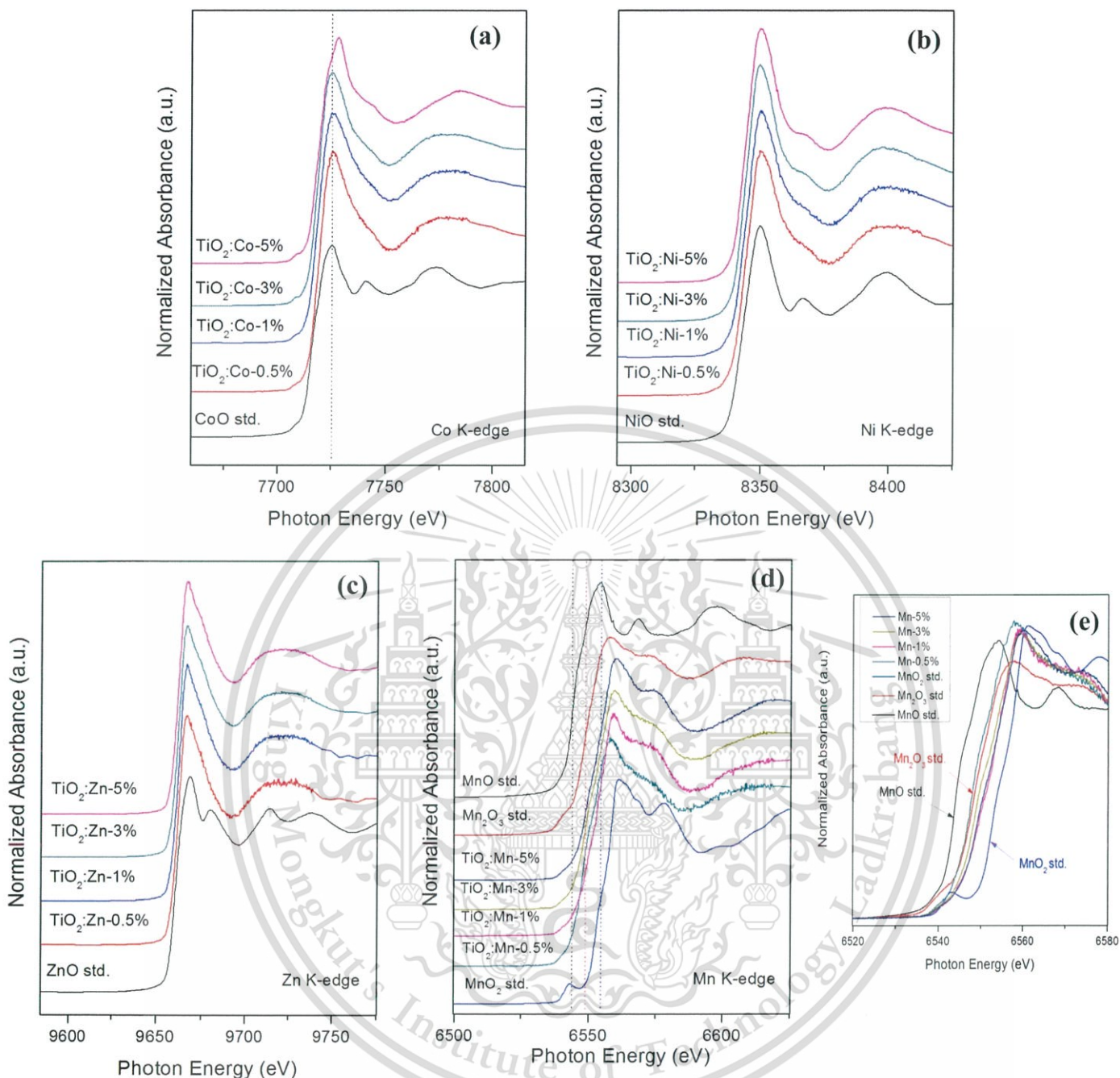


Fig. 3. Normalized XANES spectra of M-TiO<sub>2</sub> samples for (a) Co K-edge (b) Ni K-edge, (c) Zn K-edge, (d) Mn K-edge and (e) high resolution Mn K-edge.

Table 1

Weight of component from XANES linear combination fitting in TiO<sub>2</sub> doped with Mn at various concentrations.

Samples	Component		
	MnO	Mn <sub>2</sub> O <sub>3</sub>	MnO <sub>2</sub>
TiO <sub>2</sub> : Mn-0.5%	0.021	0.885	0.094
TiO <sub>2</sub> : Mn-1%	0	0.613	0.387
TiO <sub>2</sub> : Mn-3%	0	0.767	0.233
TiO <sub>2</sub> : Mn-5%	0	0.591	0.409

spectra of Zn K-edge, it is noticeable that there is the strong absorption edge around 9653 eV for all dopant concentrations, which corresponds to the oxidation state of 2+. In case of Mn-doped TiO<sub>2</sub> samples, the Mn K-edge XANES spectra are shown in Fig. 3(d). The spectra of all

samples represent strong absorption energy edge in a range of ~6538–6553 eV between the standard spectrum of Mn<sub>2</sub>O<sub>3</sub> and MnO<sub>2</sub>, as clearly seen in Fig. 3(e). This tendency of data suggests the existence of mixture of Mn ions in different oxidation states in Mn-doped TiO<sub>2</sub> sample. Linear combination fitting (LCF) of Mn spectra was performed to confirm the oxidation states of Mn dopant in Mn-doped TiO<sub>2</sub> sample using MnO, Mn<sub>2</sub>O<sub>3</sub> and MnO<sub>2</sub> as a reference model. The best LCF with three of reference standards suggests that the decrease of Mn<sup>3+</sup> component and the increase of Mn<sup>4+</sup> of oxidation state occurs when the Mn dopant concentration increases, as seen in Table 1.

### 3.3. VSM

The magnetic properties of the samples were investigated by VSM for ± 10 kOe at room temperature. Fig. 4 shows the plot of magnetization; *M* and magnetic field; *H* curve recorded for Co-, Mn-, Ni- and Zn-doped

This material is reserved for educational use only, not allowed for commercial use.

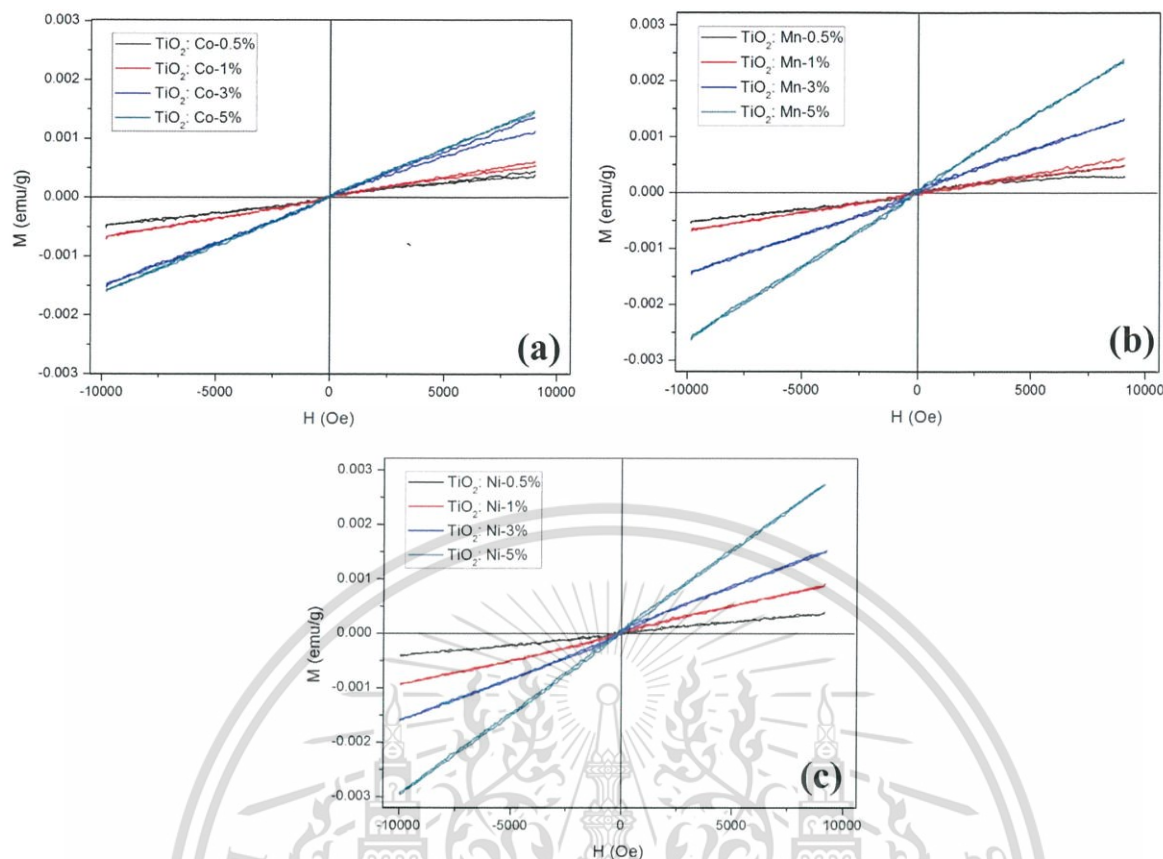


Fig. 4. The plot of  $M$ - $H$  hysteresis loop at room temperature of  $M$ - $\text{TiO}_2$  samples with (a) Co- $\text{TiO}_2$ , (b) Mn- $\text{TiO}_2$  and (c) Ni- $\text{TiO}_2$ .

$\text{TiO}_2$  samples. Pure  $\text{TiO}_2$  sample presents the diamagnetic behavior. Meanwhile, all transition metal ion doped samples exhibit typical magnetization loop indicating paramagnetic behavior. The slope of linear paramagnetic increases with the increase of Co-, Mn-, Ni- doping concentration. The magnetic properties of the samples were investigated by VSM for  $\pm 10$  kOe at room temperature. Fig. 4(a)–(c) shows the plot of magnetization;  $M$  and magnetic field;  $H$  curve recorded for Co-, Mn- and Ni-doped  $\text{TiO}_2$  samples. Pure  $\text{TiO}_2$  sample presents the diamagnetic behavior. Meanwhile, all transition metal ion doped samples exhibit typical magnetization loop indicating paramagnetic behavior. The paramagnetism presented in prepared samples may be originated from the isolated transition metal dopant ions dispersed on the  $\text{TiO}_2$  host matrix. This result is in harmony with the XANES results that indicate the existence of Co-, Mn- and Ni-dopant occurring as  $\text{Co}^{2+}$ ,  $\text{Ni}^{2+}$  and  $\text{Mn}^{3+,4+}$  insertion into the  $\text{TiO}_2$  lattice [11]. In addition, the substitution of  $\text{Ti}^{4+}$  ions in  $\text{TiO}_2$  by  $\text{Co}^{2+}$ ,  $\text{Ni}^{2+}$  and  $\text{Mn}^{3+,4+}$  will result in the creation of oxygen vacancies and charge carriers playing significant role for the magnetism origin in magnetic oxide.

#### 4. Conclusions

$\text{TiO}_2$  nanoparticles doped with different transition metal ions of Co, Mn, Ni and Zn at various concentrations were prepared by co-precipitation method and calcinations at  $500^\circ\text{C}$  for 2 h. The XRD results confirm the structural phase belonging to tetragonal anatase  $\text{TiO}_2$  phase for all samples without secondary phase of doped metal oxide phase. XANES results clearly show tripped pre-edge fingerprint of Ti with 4+ of valence state for Ti in all samples. The 2+ oxidation state was found in Co-, Ni- and Zn- doped samples. The mixing oxidation state of 3+ and 4+ was observed in the Mn-doped  $\text{TiO}_2$  samples. Magnetic measurement on the samples indicates the existence of paramagnetic behavior at room temperature for Co- Mn- and Ni-doped samples, and diamagnetic behavior for undoped and Zn doped

samples. Higher Co-, Mn- and Ni- concentration leads to greater magnetization value. The isolate magnetic ion of Co, Mn and Zn dispersed in the host oxide matrix is a key factor for magnetic behavior.

#### Conflict of interest

We declare that we do not have any commercial or associative interest that represents a conflict of interest in connection with the work submitted.

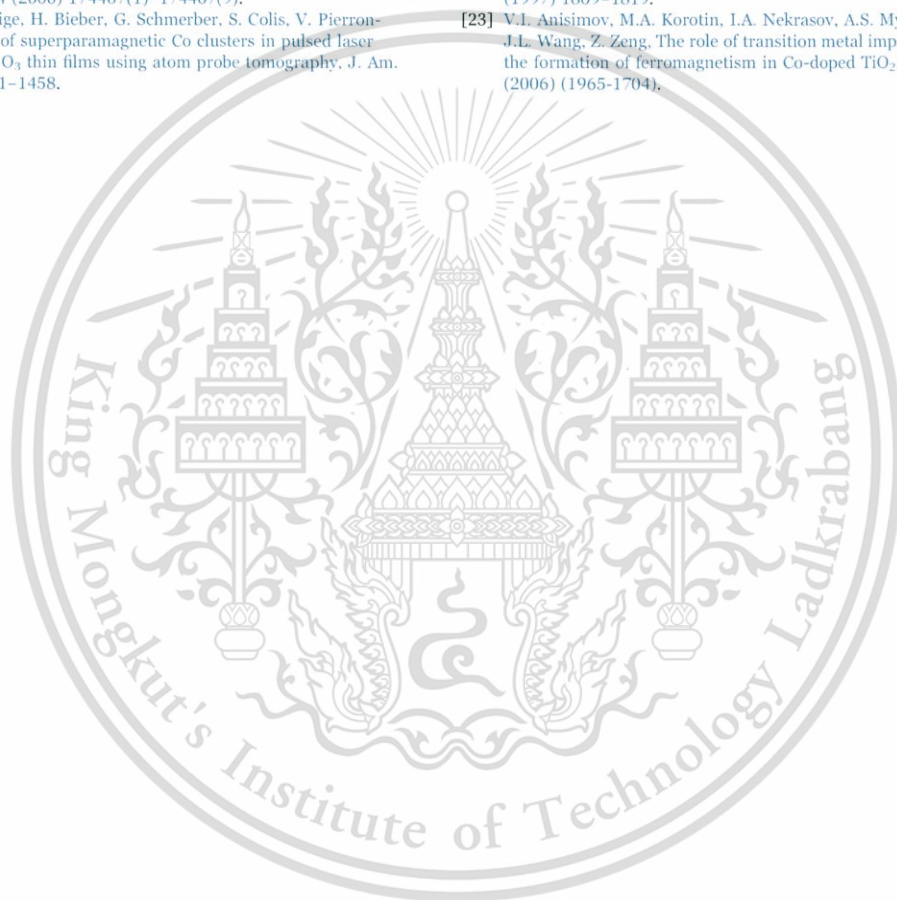
#### Acknowledgements

This work has been supported by Thailand Research Fund (TRF) within the Royal Golden Jubilee Ph.D. Program (Grant no. PHD/0193/2556) and National Science and Technology Development Agency, Ministry of Science and Technology, Thailand (Grant no. JRA-CO-2558-857-TH). We would like to thank College of Nanotechnology, King Mongkut's Institute of Technology Ladkrabang and Graduate School of Energy Science, Kyoto University for supported the facility and the Beamline-8 at Synchrotron Light Research Institute (SLRI) for XAS measurement.

#### References

- [1] M.H. Henderson, A surface science perspective on  $\text{TiO}_2$  photocatalysis, *Surf. Sci., Rep.* 66 (2011) 185–278.
- [2] S.A. Wolf, D.D. Awschalom, R.A. Buhrman, J.M. Daughton, S.V. Molnar, M.L. Roukes, A.Y. Chtchelkanova, D.M. Treger, Spintronics: a spin-based electronics vision for the future, *Science* 294 (2001) 1488.
- [3] G.A. Prinz, *Magneto-electronics*, Science 282 (1998) 1660–1663.
- [4] J.M. Kikkawa, I.P. Smorchkova, N. Samarth, D.D. Awschalom, Room-temperature spin memory in two dimensional electron gases, *Science* 277 (1997) 1284–1287.
- [5] A. Bouaine, G. Schmerber, D. Ihiwakrim, A. Derory, Structural, optical, and magnetic properties of polycrystalline Co-doped  $\text{TiO}_2$  synthesized by solid-state method, *Mater. Sci. Eng. B* 177 (2012) 1618–1622.

- [6] B. Choudhury, A. Choudhury, A.K.M. Maidul Islam, P. Alagarsamy, M. Mukherjee, Effect of oxygen vacancy and dopant concentration on the magnetic properties of high spin  $\text{Co}^{2+}$  doped  $\text{TiO}_2$  nanoparticles, *J. Magn. Magn. Mater.* 323 (2011) 440–446.
- [7] K. Karthik, S.K. Pandian, K.S. Kumar, N.V. Jaya, Influence of dopant level on structural, optical and magnetic properties of Co-doped anatase  $\text{TiO}_2$  nanoparticles, *Appl. Surf. Sci.* 256 (2010) 4757–4760.
- [8] D. Vokoun, M. Svatuška, J. Olejníček, M. Kohout, J. Drahoukoupil, M. Rameš, J. Vejpravová, A. Mantliková, L. Fekete, J. Kopeček, L. Klimša, O. Hezko, Ni– $\text{TiO}_2$  nanocomposite films and their magnetic properties, *Phys. B: Condens. Matter* 503 (2016) 44–50.
- [9] B. Choudhury, A. Choudhury, Oxygen vacancy and dopant concentration dependent magnetic properties of Mn doped  $\text{TiO}_2$  nanoparticle, *Curr. Appl. Phys.* 13 (2013) 1025e1031.
- [10] C.K. Sellers, E.G. Seebauer, Room temperature ferromagnetism in Mn-doped  $\text{TiO}_2$  nanopillar matrices, *Mater. Lett.* 114 (2014) 44–47.
- [11] M.M. Rashad, E.M. Elsayed, M.S. Al-Kotb, A.E. Shalan, The structural, optical, magnetic and photocatalytic properties of transition metal ions doped  $\text{TiO}_2$  nanoparticles, *J. Alloy. Compd.* 581 (2013) 71–78.
- [12] M.D. Coey, M. Venkatesan, C.B. Fitzgerald, Donor impurity band exchange in dilute ferromagnetic oxides, *Nat. Mater.* 4 (2005) 173–179.
- [13] K. Kikoin, V. Fleurov, Superexchange in dilute magnetic dielectrics: application to  $(\text{Ti},\text{Co})\text{O}_2$ , *Phys. Rev. B* 74 (2006) 174407(1)–174407(9).
- [14] R. Lardé, E. Talbot, P. Pareige, H. Bieber, G. Schmerber, S. Colis, V. Pierron-Bohnes, A. Dinia, Evidence of superparamagnetic Co clusters in pulsed laser deposition-grown  $\text{Zn}_{0.9}\text{Co}_{0.1}\text{O}_3$  thin films using atom probe tomography, *J. Am. Chem. Soc.* 133 (2011) 1451–1458.
- [15] S.J. Stewart, S.J.A. Figueroa, J.M. Ramallo López, S.G. Marchetti, J.F. Bengoa, R.J. Prado, F.G. Requejo, Cationic exchange in nanosized  $\text{ZnFe}_2\text{O}_4$  spinel revealed by experimental and simulated near-edge absorption structure, *Phys. Rev. B* 75, 073408.
- [16] D. Makovec, A. Kodrežtók, A. Drogenik, The structure of compositionally constrained zinc-ferrite spinel nanoparticles, *J. Nanopart. Res.* 13 (2011) 1781–1790.
- [17] T.L. Hsiuna, H.P. Wang, H.P. Lin, Chemical structure of photocatalytic active sites in nanosize  $\text{TiO}_2$ , *J. Phys. Chem. Solids* 69 (2008) 383–385.
- [18] M. Ghaffari, T. Liu, H. Huang, O.K. Tan, M. Shannon, Investigation of local structure effect and X-ray absorption characteristics (EXAFS) of Fe (Ti) K-edge on photocatalyst properties of  $\text{SrTi}_{1-x}\text{Fe}_x\text{O}$ , *Mater. Chem. Phys.* 136 (2012) 347e357.
- [19] T. Yamamoto, T. Mizoguchi, I. Tanaka, Core-hole effect on dipolar and quadrupolar transitions of  $\text{SrTiO}_3$  and  $\text{BaTiO}_3$  at Ti K edge, *Phys. Rev. B* 71 (2005) 245113.
- [20] V. Luca, S. Djajanti, R.F. Howe, Structural and electronic properties of sol-gel titanium oxides studied by X-ray absorption spectroscopy, *J. Phys. Chem. B* 102 (1998) 10650–10657.
- [21] Z.Y. Wu, G. Ouvrard, P. Gressier, C.R. Natoli, Ti and O K-edges for titanium oxides by multiple scattering calculations: comparison to XAS and EELS spectra, *Phys. Rev. B* 55 (1997) 10382–10391.
- [22] F. Farges, G.E. Brown, J.J. Rehr, Ti K-edge XANES studies of Ti coordination and disorder in oxide compounds: comparison theory and experiment, *Phys. Rev. B* 56 (1997) 1809–1819.
- [23] V.I. Anisimov, M.A. Korotin, I.A. Nekrasov, A.S. Mynnikova, A.V. Lukyanov, J.L. Wang, Z. Zeng, The role of transition metal impurities and oxygen vacancies in the formation of ferromagnetism in Co-doped  $\text{TiO}_2$ , *J. Phys. Condens. Matter* 18 (2006) 1965–1704.



## BIOGRAPHY

Name Mr. Chakkaphan Wattanawikkam  
Date of Birth 24 June 1986  
Place of Birth Uthai thani  
Address 52 M.9, Khaokwangthong, Nongchang, Uthai thani 61110  
Education **2009:** Bachelor of Science in Physics,  
Faculty of Science, Naresuan University.

**2012:** Master of Science in Applied Physics,  
Faculty of Science, Naresuan University.

Scholarship The Royal Golden Jubilee Ph.D. Program  
(grant no. PHD/0193/2556)

Exchange program **2016:** Exchange student at Graduate School of Energy  
Science, Kyoto University, Kyoto, Japan.

### Publications:

1. C. Wattanawikkam, W. Pecharapa and K.N. Ishihara “X-ray absorption spectroscopy analysis and magnetic properties of M-doped TiO<sub>2</sub> nanoparticles (M=Co, Mn, Ni and Zn) prepared by co-precipitation method” *Ceram. Int.* 43, (2017) pp. s397-s402 (IF = 2.605).
2. C. Wattanawikkam, W. Phoohinkong and W. Pecharapa “Structural, optical and magnetic properties of diluted magnetic perovskite ZnTiO<sub>3</sub> doped with Co and Mn prepared by sonochemical method” *J. Nanosci. Nanotechnol.* 17, (2017) pp. 3620-3628 (IF = 1.339).
3. C. Wattanawikkam and W. Pecharapa “Sonochemical Synthesis, Characterization, and Photocatalytic Activity of Perovskite ZnTiO<sub>3</sub> Nanopowders” *IEEE Trans. Ultrason. Ferroelect. Freq. Control.* 63 (2016) pp.1663-1667 (IF = 2.21).
4. C. Wattanawikkam, W. Pecharapa “Synthesis and Characterization of Zn-Doped TiO<sub>2</sub> Nanoparticles via Sonochemical Method” *Integr. Ferroelectr.* 165, (2015) pp.167-175 (IF = 0.37).

#### Conference:

1. Southeast Asia Conference on Thermoelectrics, (SACT-2014) Pakse, Lao PDR.
2. Joint IEEE International Symposium on Applications of Ferroelectric (ISAF), International Symposium on Integrated Functionalities (ISIF), and Piezoresponse Force Microscopy Workshop (PFM), (ISAF-ISIF-PFM 2015), Singapore.
3. International Conference on Advanced Electromaterials (ICAE-2015), Jeju, South Korea.
4. International Conference on Powder and Powder Metallurgy, (JSPM-2016) spring meeting, Kyoto, Japan.
5. 23<sup>rd</sup> International Symposium on Metastable, Amorphous and Nanostructured Materials (ISMANAM 2016), Nara, Japan.
6. Eco-Energy and Materials Science and Engineering Symposium (EMSES-2016), Udon thani, Thailand.
7. 10<sup>th</sup> Asian Meeting on Electroceramics (AMEC-2016), Taipei, Taiwan.
8. Nanokorea-2017, Seoul, South Korea.
9. International Conference on Advanced Energy Materials (AEM-2017), Guildford, England.

